Physiological coupling in multi-person collaborative tasks: An intrinsic multi-scale synchrony approach

Apit Hemakom

Supervisor: Prof. Danilo P. Mandic

A thesis submitted for the degree of
Doctor of Philosophy (Ph.D.)

Communications and Signal Processing Group
Department of Electrical and Electronic Engineering
Imperial College London
January 2018

Abstract

Expert human performance in team scenarios (choir singing, surgical team) critically depends on the degree of collaboration between the individuals involved, and is reflected in elevated synchrony levels of their neuronal and physiological responses. Objective and physically meaningful synchrony metrics, however, are only just emerging, but are desperately needed in cognitive and behavioural science, education, robotics and gaming.

Motivated by the multi-scale nature of human physiological and neuronal responses, such as the standard frequency bands in the electroencephalogram (EEG), this thesis sets out to explore and extend the so-called intrinsic multi-scale analysis framework in order to derive robust and physically meaningful metrics for the quantification of physiological and neuronal inter-component dependence across the scales of interest. In this way, standard data-association measures, such as correlation, coherence and phase synchrony, are equipped with the ability to operate at the intrinsic scale level, for example, through the noise-assisted multivariate empirical mode decomposition (NA-MEMD) algorithm.

This thesis introduces three new intrinsic data-association measures for quantifying inter-individual physiological and neuronal couplings: (i) intrinsic coherence (ICoh), (ii) intrinsic synchrosqueezing coherence (ISC), and (iii) nested intrinsic phase synchrony (N-IPS). These measures are employed to robustly and accurately quantify physiological (respiration and heart rate variability) and neuronal (through electroencephalography) couplings between participants in several notoriously noisy and prone to artefacts real-world collective tasks, such as choir singing, multi-player gaming and performing a surgical procedure.

The radically enhanced scale discrimination ability of the proposed approach is demonstrated over so-called hyperscanning (brain-to-brain communication) experiments using the next generation ear-EEG device for simultaneously recording neuronal function from multiple brains. The various EEG synchrony levels are evaluated against standard EEG in cooperative multi-player games, termed Bar Balancing and Ninjas, developed specifically for the work in this thesis to induce neuronal coupling

between participants during the experiments. The ISC algorithm is shown to be capable of identifying inter-person neuronal coupling despite the detrimental effects from a variety of artefacts arising from the background brain activity and the sensing system, highly complex and nonlinear systems.

Finally, to deal with power imbalances between physiological data channels (e.g. due to different electrode impedances), which is detrimental to the analysis, a robust extension of the adaptive, data-driven algorithm for the analysis of nonlinear and non-stationary multivariate signals, termed multivariate empirical mode decomposition (MEMD), is proposed and is referred to as adaptive-projection intrinsically transformed MEMD (APIT-MEMD). The APIT-MEMD algorithm in the intrinsic multi-scale analysis framework is validated on cooperative steady-state visual evoked potential (SSVEP) and P300-based brain-computer interface (BCI).

The proposed data-association measures, together with the APIT-MEMD algorithm, offer a new avenue for the analysis of coupled physiological and neuronal signals, and are the underpinning technology for collaborative research and applications, including performance science and eSports.

Acknowledgements

I gratefully wish to acknowledge the support I have received during my time at Imperial College. First and foremost, I would like to express my sincere gratitude to my supervisor Professor Danilo P. Mandic. It has been an immense honour for me to work with him. This work would not have been completed without his great support, enthusiasm and encouragement. During the last four years, his countless invaluable pieces of advice have been crucial to my developments both as a researcher and as a person. Valuable and insightful comments of him, fellow PhD students and post-doctoral researchers given in our regular group meetings have also been essential to the progress of my PhD studies.

Next, I am particularly grateful for the assistance given by Dr. Valentin Goverdovsky on our publications, i-Amp data loggers and ear-EEG sensors. Without these important pieces of equipment, several studies of mine would have been impossible. I am indebt to Theerasak Chanwimalueang and Wilhem von Rosenberg for our fruitful academic discussion and their generous help. I would like to show my gratitude to Dr. David Looney for guiding me through the early years of my PhD. I would like to thank Alicia C. Garcia for her effort put on our financial studies during her academic visits to London. I would like to thank Dr. Alireza Ahrabian for introducing me the concept of signal decomposition catering for power imbalances. I am thankful to have been given the privilege to work with Prof. Anthony G. Constantinides. I am grateful to the CSP group administrator, Ms. Charlotte Grady, and graduate tutor, Dr. Imad Jaimoukha, for all their help during my PhD.

I would like to thank Takashi, Tricia, Sithan, Pouria, Alex, Min, Ilia and Thayne for their help and chats on various topics. I am thankful for the help given by Giuseppe, Bruno and Allan, who helped me with several studies while pursuing their Master's degrees. I would like to thank Katarzyna for our productive collaboration.

I would like to express gratitude to Dr. Pasin Israsena, who gave me the opportunity to pursue higher degree studies in the UK. I would like to acknowledge the Royal Thai Government, National Science and Technology Development Agency (NSTDA, Thailand) and National Electronics and Computer Technology Center (NECTEC, Thailand) for the PhD funding.

Last but not least, my heartfelt gratitude goes to my family for their love, understanding and support during the last few years. I would not be here without them.

"Live the life of your dreams. When you start living the life of your dreams, there will always be obstacles, doubters, mistakes and setbacks along the way, but with hard work, perseverance and self-belief there is no limit to what you can achieve."

Roy T. Bennett, The Light in the Heart [2016]

"Anyone who acquires more than the usual amount of knowledge concerning a subject is bound to leave it as his contribution to the knowledge of the world."

Liberty H. Bailey [1858–1954]

Contents

Abstract **2**

Acknowledgements **4**

Contents **6**

List of Figures **10**

List of Tables **15**

Statement of Originality **16**

Copyright Declaration **17**

List of Principal Symbols **18**

List of Abbreviations **20**

Publications **22**

1 Introduction **24**

1.1 Respiration and Heart Rate Variability 26

1.2 Hyperscanning via EEG 27

1.3 Ear-EEG Recording Concept 29

1.4 Empirical Mode Decomposition and Its Variants 32

1.5 Quantifying Inter-channel Dependence 35

1.6 Synchrosqueezing Transform 36

1.7 Original Contributions 37
1.8 Thesis Organisation 38

2 Algorithms and Background 42

2.1 Stationarity of a Random Process 42
2.2 Phase Response of a Filter 43
2.3 Empirical Mode Decomposition (EMD) 43
2.4 Multivariate Extensions of Empirical Mode Decomposition 45
2.5 Noise-assisted Multivariate Empirical Mode Decomposition (NA-MEMD) 47
2.6 Intrinsic Phase Synchrony (IPS) 48
2.7 Synchrosqueezing Transform (SST) 50
2.8 Multivariate Synchrosqueezing Transform (MSST) 52
2.9 Bias and Variance of an Estimator 54
2.10 Matched Filtering 55
2.11 Hilbert Transform 55
2.12 The Matched Filtering and Hilbert Transform (MF-HT) Algorithm . 56

3 Quantifying Cooperation in Choir Singing: Respiratory and Cardiac Synchronisation 59

3.1 Introduction 59
3.2 Intrinsic Coherence (ICoh) 60
3.3 Data Acquisition and Pre-processing 61
3.4 Test for Wide-Sense Stationarity of the Respiratory and HRV signals 72
3.4.1 Means of the Respiratory and HRV signals 72
3.4.2 Variances of the Respiratory and HRV signals 72
3.5 Synchrony Analysis 78
3.6 Results of the Analysis 83
3.6.1 Phase Synchrony 83
3.6.2 Coherence analysis 84
3.7 Summary 86

4 Quantifying Team Cooperation Through Intrinsic Multi-scale Measures: Respiratory and Cardiac Synchronisation in Choir Singers and Surgical Teams 88

4.1 Introduction . . . 88

4.2 Algorithms and Background . . . 90

4.2.1 Intrinsic Synchrosqueezing Coherence (ISC) . . . 90

4.2.2 Nested Intrinsic Phase Synchrony (N-IPS) . . . 92

4.3 Applications . . . 94

4.3.1 Estimating Degrees of Synchrony in a Linear Bivariate Signal 94

4.3.2 Estimating Degrees of Synchrony in a Nonlinear Narrowband Bivariate Signal . . . 101

4.3.3 Highly-localised HRV- and Respiration-based Choral Synchrony Analysis . . . 105

4.3.4 Large Scale HRV- and Respiration-based Choral Synchrony Analysis . . . 110

4.3.5 Large Scale HRV-based Surgical Synchrony Analysis . . . 122

4.4 Summary . . . 127

5 Ear-EEG for Detecting Neuronal Synchrony in Continuous Cooperative Multi-person Scenarios 130

5.1 Introduction . . . 130

5.2 Methods . . . 132

5.2.1 Experimental Design . . . 132

5.2.2 Data Acquisition . . . 133

5.2.3 Neuronal Synchrony Estimation . . . 138

5.3 Results . . . 139

5.3.1 Time-frequency Representations of Neuronal Synchrony . . . 139

5.3.2 Frequency-averaged, Time-varying Neuronal Synchrony . . . 139

5.3.3 Correlation in Time-varying Neuronal Synchrony between the Modalities . . . 141

5.3.4 Proportions of Significant Neuronal Synchrony Detected . . . 142

5.3.5 Time-averaged Significant Neuronal Synchrony . . . 147

5.3.6 Power of EEG Activities in the Lower Theta Band 147

5.4 Summary 152

6 Adaptive-projection Intrinsically Transformed MEMD (APIT-MEMD) in Cooperative Brain-computer Interface Applications 153

6.1 Introduction 153

6.2 Algorithm 154

6.3 Simulation Results 159

6.3.1 Reconstructing Multivariate Data with Power Imbalances . . . 159

6.3.2 Noise-assisted Signal Decomposition 164

6.3.3 P300 reconstruction 164

6.4 Applications of NA-APIT-MEMD in the Intrinsic Multi-scale Analysis Framework 167

6.4.1 Application of Intrinsic Phase Synchrony to Cooperative SSVEP-based BCI 167

6.4.2 Application of Intrinsic Correlation to Cooperative P300-based BCI 170

6.5 Summary 175

7 Conclusions and Future Work 177

7.1 Conclusions 177

7.2 Future Work 181

References 182

Appendix A Areal Density 198

Appendix B Supportive Performance Evaluation of Ear-EEG 200

Appendix C Application of Intrinsic Phase Synchrony to Financial Signal Processing 201

List of Figures

1.1 A schematic diagram of the earpiece and its position inside the ear canal 30

1.2 An earpiece and two standard gold-cup electrodes for the ground and the reference connected to a conventional biosignal amplifier 31

1.3 Thesis structure 39

2.1 Sampling directions for multivariate extensions of EMD 45

2.2 Bivariate amplitude modulated signal with perfect phase locking between the channels and their PSIs 49

2.3 Software for R-peak extraction using the MF-HT algorithm 58

3.1 A custom-made respiration belt 62

3.2 Recording setup 63

3.3 Respiratory signals of the conductor and the subset of eight members of the choir 65

3.4 The ECG signals of the conductor and the subset of eight members of the choir recorded during the rehearsal 66

3.5 The ECG signals of the conductor and the subset of eight members of the choir recorded during the performance 67

3.6 The SNRs of the respiratory and ECG signals of the choir 68

3.7 The HRV signals of the conductor and the selected five members of the choir during the rehearsal 68

3.8 The HRV signals of the conductor and the selected five members of the choir during the performance 69

3.9 Respiratory signals of the five members of the audience 70

3.10 The ECG signals of the five members of the audience 70

3.11 The SNRs of the respiratory and ECG signals of the audience 71

3.12 The HRV signals of the five members of the audience 71

3.13 Means of the respiratory signals of the conductor and the selected five members of the choir 73

3.14 Means of the respiratory signals of the five members of the audience . 74

3.15 Means of the HRV signals of the conductor and the selected five members of the choir during the rehearsal 75

3.16 Means of the HRV signals of the conductor and the selected five members of the choir during the performance 76

3.17 Means of the HRV signals of the five members of the audience 77

3.18 Variances of the respiratory signals of the conductor and the selected five members of the choir 78

3.19 Variances of the respiratory signals of the five members of the audience 79

3.20 Variances of the HRV signals of the conductor and the selected five members of the choir during the rehearsal 80

3.21 Variances of the HRV signals of the conductor and the selected five members of the choir during the performance 81

3.22 Variances of the HRV signals of the five members of the audience . . 82

3.23 The PSI of the respiratory and HRV signals within the same subject group and between the subject groups 83

3.24 The COH values of the respiratory and HRV data 85

4.1 Standard TF spectrograms of the clean linear bivariate signal 97

4.2 The corrupted bivariate signal, the means and the variances of both the channels 97

4.3 TF representations of the degrees of synchrony in a synthetic linear bivariate signal estimated using four different combinations of algorithms 99

4.4 TF representations of the degrees of synchrony in a synthetic linear bivariate signal estimated using three different combinations of algorithms 100

4.5 TF representations of the degrees of synchrony in a synthetic nonlinear bivariate signal estimated using four different combinations of the considered algorithms 103

4.6 TF representations of the degrees of synchrony in a synthetic nonlinear bivariate signal estimated using three different combinations of the considered algorithms 104

4.7 Average SNRs of TF representations of signal dependence estimated using different algorithms . . . 105

4.8 Intrinsic synchrony in respiratory signals among the bass singers during the rehearsal and the performance estimated using IPS and STFT-based ISC . . . 108

4.9 Intrinsic synchrony in HRV signals among the bass singers during the rehearsal and the performance estimated using IPS and STFT-based ISC . . . 109

4.10 Intrinsic synchrony in respiratory and HRV signals among the bass singers during the rehearsal and performance estimated using CWT-based ISC . . . 111

4.11 Respiratory signals of the soprano and bass singers . . . 113

4.12 The ECG signals of the soprano and bass singers . . . 114

4.13 The SNRs of the respiratory and ECG signals of the soprano and bass singers . . . 115

4.14 The HRV signals of the soprano and bass singers . . . 116

4.15 Means of the respiratory signals of the soprano and bass singers . . . 117

4.16 Means of the HRV signals of the soprano and bass singers . . . 118

4.17 Variances of the respiratory signals of the soprano and bass singers . 119

4.18 Variances of the HRV signals of the soprano and bass singers . . . 120

4.19 Time-varying synchrony in the sopranos' and basses' respiratory and HRV signals . . . 121

4.20 The ECG and HRV signals of the cardiologists and physiologist . . . 125

4.21 The SNRs of the ECG signals of the cardiologists and physiologist . . 126

4.22 Means and variances of the HRV signals of the cardiologists and physiologist . . . 127

4.23 Trends in synchrony in the cardiologists' and physiologist' HRV data 128

5.1 Screenshot of the cooperative game and experimental setup . . . 134

5.2 Recording setup . . . 135

5.3 Ear-EEG signals of Couple 2, the means, and the variances . . . 136

5.4 On-scalp EEG signals of Couple 2 from CP4 electrodes, the means, and the variances . . . 137

5.5 Time-frequency neuronal synchrony between Couple 1 estimated from ear-EEG recordings . . . 140

5.6 Time-varying neuronal synchrony between Couple 1 . . . 142

5.7 Time-varying neuronal synchrony between Couple 2 . . . 143

5.8 Time-varying neuronal synchrony between Couple 3 . . . 144

5.9 Time-varying neuronal synchrony between Couple 4 . . . 144

5.10 Time-varying neuronal synchrony between Couple 5 . . . 145

5.11 Time-varying neuronal synchrony between Couple 6 . . . 145

5.12 Average correlation in neuronal synchrony between the recording modalities averaged over the six couples . . . 146

5.13 Correlation in neuronal synchrony between the recording modalities of each couple . . . 146

5.14 Average proportion of the number of significant SCI values detected in each level from ear-EEG and on-scalp EEG recordings averaged over the six couples . . . 147

5.15 Proportion of the number of significant SCI values detected in each level from ear-EEG and on-scalp EEG recordings of each couple . . . 148

5.16 Average significant SCI values in the easy and hard tasks estimated from each subband of ear-EEG and on-scalp EEG recordings averaged over the six couples . . . 149

5.17 Average significant SCI values in the easy and hard tasks estimated from each subband of ear-EEG and on-scalp EEG recordings of each couple . . . 150

5.18 Average power of EEG activities in the lower theta band of both the recording modalities of each couple during the cooperative trial compared to the power of instrumentation noise . . . 151

6.1 Uniform and nonuniform projection vectors . . . 154

6.2 Input signal to the first sifting operation . . . 157

6.3 Input signal to a sifting operation . . . 158

6.4 Performance comparison between APIT-MEMD and MEMD in reconstructing the f_1 sinusoid using different α values . . . 161

6.5 Performance comparison between APIT-MEMD and MEMD in reconstructing the f_2 sinusoid using different α values . . . 162

6.6 Suggested α value and the number of direction vectors for different degrees of power imbalances . . . 163

6.7 Performance comparison between APIT-MEMD and MEMD in reconstructing signal with the assistance of noise. 165

6.8 P300 ground truth generated by performing APIT-MEMD and MEMD on EEG data recorded from two subjects at different electrode positions 166

6.9 Mean square error of P300 responses of two subjects at different electrode positions 166

6.10 The PSD and time-frequency spectrogram of SSVEP stimuli and brain responses 168

6.11 Estimated PSI between SSVEP stimuli and brain responses 169

6.12 Examples of EEG signals with and without the P300 present 170

A.1 Areal densities of trends in synchrony 199

B.1 Game screenshot and correlation in neuronal synchrony between the recording modalities 200

C.1 Intrinsic synchrony between individual stock indices 203

List of Tables

1.1 Tasks performed in hyperscanning studies and synchronised areas of the brains [1]. 28

6.1 Average MSEs of the NA-APIT-MEMD and NA-MEMD algorithms for the two subjects at different electrodes. 167

6.2 Performance of the proposed two-person single-shot P300 detection algorithm. 174

Statement of Originality

I declare that the work presented in this thesis is the outcome of my research under the supervision of Prof. Danilo P. Mandic. Ideas and results from the work of others are appropriately acknowledged with the standard referencing practices employed in this discipline. The material in this thesis has not been submitted for any degree at any other academic or professional institution.

Copyright Declaration

The copyright of this thesis rests with the author and is made available under a Creative Commons Attribution Non-Commercial No Derivatives licence. Researchers are free to copy, distribute or transmit the thesis on the condition that they attribute it, that they do not use it for commercial purposes and that they do not alter, transform or build upon it. For any reuse or redistribution, researchers must make clear to others the licence terms of this work

List of Principal Symbols

N	number of samples
P and R	number of data channels
K	number of IMFs
M	number of frequency bins
Q	number of direction vectors
W	window length
C and D	number of white Gaussian noise channels
H	Shannon entropy
Ω	instantaneous frequency
A	instantaneous amplitude
ϕ	instantaneous phase
T	synchrosqueezing transform coefficient
$\mathbf{C}$	covariance matrix
$\mathbf{V}$	eigenvector matrix
$\mathbf{\Lambda}$	eigenvalue matrix
$\mathbf{T}$	multivariate synchrosqueezing transform coefficient
$\mathbf{\Omega}$	multivariate instantaneous phase
$\mathbf{A}$	multivariate instantaneous amplitude
$E\{\cdot\}$	statistical expectation operator
$(\cdot)^T$	transpose operator
$\delta(\cdot)$	Dirac delta function
$Re(\cdot)$	real part
σ	standard deviation
λ	eigenvalue
ρ	correlation coefficient
τ	time lag
g	sliding window
γ	phase synchrony
c	IMF

d	detail
m	local mean
x and y	univariate signal
$\tilde{x}$	proto-IMF
$\mathbf{x}$	multivariate signal
$\mathbf{s}$	multivariate sifting input
$\mathbf{c}$	multivariate IMF
$\mathbf{v}$	eigenvector
$\mathbf{d}$	multivariate detail
$\mathbf{m}$	multivariate local mean
$\tilde{\mathbf{x}}$	multivariate proto-IMF
$S_{ii}(f)$	power spectral density of channel i
$S_{ij}(f)$	cross-spectral power density between channels i and j
ψ	wavelet
$U(f,t)$	STFT coefficient for each frequency-time pair
$W(a,b)$	wavelet coefficient for each scale-time pair (a,b)
f	frequency
t	time
k	IMF index
p, i and j	channel index
pr	probability
$\Re$	real number
q	realisation number
u	spectral component index
var	variance
cov	covariance
n	time index
z	analytic signal
RP	R-peak

List of Abbreviations

AM	amplitude modulated
ANS	autonomic nervous system
APIT-MEMD	adaptive-projection intrinsically transformed multivariate empirical mode decomposition
BCI	brain-computer interface
BEMD	bivariate empirical mode decomposition
COH	coherence
CSPD	cross-spectral power density
CWT	continuous wavelet transform
ECG	electrocardiogram and electrocardiography
EEG	electroencephalogram and electroencephalography
EEMD	ensemble empirical mode decomposition
EMD	empirical mode decomposition
ERD	event-related desynchronisation
ERP	even-related potential
DS-BEMD	dynamically sampled bivariate empirical mode decomposition
FM	frequency modulated
FSST	short-time Fourier transform (STFT)-based synchrosqueezing transform
F-MSST	short-time Fourier transform (STFT)-based multivariate synchrosqueezing transform
HF	high frequency
HRV	heart rate variability
HT	Hilbert transform
ICoh	intrinsic coherence
IMF	intrinsic mode function
IPS	intrinsic phase synchrony
ISC	intrinsic synchrosqueezing coherence
ITE	in the ear
ITR	information transfer rate
LF	low frequency

MEMD	multivariate empirical mode decomposition
MSE	mean square error
MSST and W-MSST	continuous wavelet transform (CWT)-based multivariate synchrosqueezing transform
MVAR	multivariate autoregressive
NA-APIT-MEMD	noise-assisted adaptive-projection intrinsically transformed multivariate empirical mode decomposition
NA-MEMD	noise-assisted multivariate empirical mode decomposition
NA-NS-TEMD	noise-assisted nonuniformly sampled trivariate empirical mode decomposition
N-IPS	nested intrinsic phase synchrony
NS-BEMD	nonuniformly sampled bivariate empirical mode decomposition
NS-TEMD	nonuniformly sampled trivariate empirical mode decomposition
PNS	parasympathetic nervous system
PS	phase synchrony
PSD	power spectral density
PSI	phase synchronisation index
RSA	respiratory sinus arrhythmia
SCI	synchrosqueezing coherence index
SNR	signal-to-noise ratio
SNS	sympathetic nervous system
SSS	Strict-Sense Stationary
SST and WSST	continuous wavelet transform (CWT)-based synchrosqueezing transform
SSVEP	steady-state visual evoked potential
STFT	short-time Fourier transform
TF	time frequency
TEMD	trivariate empirical mode decomposition
WGN	white Gaussian noise
WSS	Wide-Sense Stationary

Publications

The following publications support the material given in this thesis:

Submitted Conference Paper

- **A. Hemakom**, V. Goverdovsky, and D. P. Mandic, "Ear-EEG for detecting neuronal synchrony in continuous cooperative multi-person scenarios," *Int. Conf. on Acoustics, Speech and Signal Processing (ICASSP 2018)*, in review, 2018.

Published Peer-Reviewed Journals

- **A. Hemakom**, K. Powezka, V. Goverdovsky, U. Jaffer, and D. P. Mandic, "Quantifying team cooperation through intrinsic multi-scale measures: Respiratory and cardiac synchronisation in choir singers and surgical teams," *Royal Society Open Science*, vol. 4, no. 1, pp. 170853-1–170853-23, 2017.

- **A. Hemakom**, V. Goverdovsky, D. Looney, and D. P. Mandic, "Adaptive-projection intrinsically transformed multivariate empirical mode decomposition in cooperative brain-computer interface applications," *Philosophical Transactions of Royal Society A*, vol. 374, no. 2065, pp. 20150199-1–20150199-15, 2016.

- **A. Hemakom**, T. Chanwimalueang, A. C. Garciá, L. Aufegger, A. G. Constantinides, and D. P. Mandic, "Financial stress through complexity science," *IEEE Journal of Selected Topics in Signal Processing*, vol. 10, no. 6, pp. 1112–1126, 2016.

- D. Looney, **A. Hemakom**, and D. P. Mandic, "Intrinsic multi-scale analysis: A multi-variate empirical mode decomposition framework," *Proceedings of the Royal Society A*, vol. 471, no. 2173, pp. 20140709-1–20140709-28, 2015.

Published Peer-Reviewed Conference Proceedings

- **A. Hemakom**, V. Goverdovsky, L. Aufegger, and D. P. Mandic, "Quantifying cooperation in choir singing: Respiratory and cardiac synchronisation," *In Proceedings of IEEE Int. Conf. on Acoustics, Speech and Signal Processing (ICASSP 2016)*, pp. 719–723, 2016.

- **A. Hemakom**, A. Ahrabian, D. Looney, N. ur Rehman, and D. P. Mandic, "Nonuniformly sampled trivariate empirical mode decomposition," *In Proceedings of IEEE Int. Conf. on Acoustics, Speech and Signal Processing (ICASSP 2015)*, pp. 3691–3695, 2015.

Chapter 1

Introduction

Cooperative human activities require high degrees of mental and physical synchronisation among multiple participants, to the extent that synchrony underpins performance level in activities such as choir singing, playing music in ensemble, rowing, flying an air plane with a couple of pilots and performing surgical procedures. Physically meaningful data-association metrics of the levels of cooperation between the team members while performing such coopertive tasks will offer an insight for the team to observe how well they perform and will help them to improve their group performance. While performing cooperative activities, different types of physiological and neuronal couplings (synchrony) among the individuals have been observed, such as synchrony in respiration and heart rate variability (HRV) among the choir members [2, 3], synchrony in brain activities, through electroencephalography (EEG), among musicians playing in ensemble [4, 5] and among couples of pilots during flight simulation [6, 7]. Physiological and neuronal couplings in multichannel data, which often contain inter-channel correlation or power imbalances between the data channels due to adjacent locations of the electrodes and different electrode impedances, are typically exhibited at unique temporal and spatial scales. Successful data analysis for physiological and neuronal coupling is therefore dependent on the choice of data-scale representation, and its ability to provide reliable and robust data-association metrics for real-world data. To this end, it is necessary to consider scales which are: (i) physically meaningful – free from rigid mathematical constraints in order to accommodate a signal representation which matches closely our intuitive

understanding of signal-generating mechanisms; and (ii) data driven – in order to reflect the inherent fluctuations embedded in the data, without a priori knowledge. These requirements are desirable, for instance, when analysing heart rate variability (HRV) and neuronal systems via EEG, since it is well known that HRV and EEG are best represented at different temporal scales (low- and high-frequency bands for HRV, and delta, theta, alpha, beta and gamma bands for EEG), and a physically meaningful approach is required to cater for their inherently nonlinear statistics.

The aim of this thesis is therefore fourfold. First, to present novel intrinsic data-association measures which yield physically meaningful interpretation and span different aspects of the analysis of coupled (synchronised, dependent) multivariate signals. The proposed measures include intrinsic coherence (ICoh, see Chapter 3), intrinsic synchrosqueezing coherence (ISC, see Chapter 4) and nested intrinsic phase synchrony (N-IPS, see Chapter 4). The ICoh quantifies phase and amplitude relationships between intrinsic modes in the data as a function of frequency. The ISC generates highly localised time-frequency representations of intrinsic inter-channel dependence, and the N-IPS empirically quantifies intrinsic trends in synchrony which are straightforward to interpret. Second, to build upon the enhanced discrimination capability of the proposed data-association measures, together with intrinsic phase synchrony (IPS) [8], in order to identify physiological coupling between participants during different collaborative tasks. Next, to employ the proposed ISC algorithm to evaluate the performance of a novel EEG recording concept, termed ear-EEG, against on-scalp EEG as an alternative for simultaneous data acquisition from multiple brains in the task of identifying the unknown, most robust EEG subbands for neuronal synchrony detection for cooperative multi-person scenarios. Lastly, since cooperative brain-computer interface (BCI) applications can exploit joint and collective information embedded in multiple data channels of cerebral data, which typically contain power imbalances and are simultaneously acquired from multiple participants, to reduce the time required for data collection, the last aim is to extend the adaptive, data-driven algorithm for the analysis of nonlinear and non-stationary multivariate signals, referred to as multivariate empirical mode decomposition (MEMD) [9, 10], to introduce adaptive-projection intrinsically transformed MEMD (APIT-MEMD, see Chapter 6), which caters for power imbalances

between data channels and thus admits higher information transfer rate (ITR) in BCI applications.

Brief overview of relevant physiological and neuronal responses which are the subjects of the studies is next presented and followed by a review of a novel EEG recording concept. This chapter next describes relevant novel algorithms for the analysis of nonlinear and non-stationary signals, their applications to quantifying inter-channel dependence (coupling, synchrony), and their shortcomings. Original contributions of this thesis are subsequently summarised, and the organisation of this thesis is lastly described.

1.1 Respiration and Heart Rate Variability

Respiration is typically involuntarily controlled by the autonomic nervous system (ANS), which comprises the sympathetic (SNS) and parasympathetic (PNS) nervous subsystems. The SNS also accelerates other functions, such as the arterial blood pressure and heart rate [11, 12, 13], by dilating bronchioles in the lungs, and by regulating neuronal and hormonal responses to stimulate the body. The PNS, on the other hand, slows down physiological functions when the body is at rest. *For choir singing in particular, the respiration is also voluntarily controlled by the choir members in order to perform long or short inhalation or exhalation in unison as dictated by the tempo and demands of a musical score.*

The interplay between the SNS and PNS, among other factors, manifests itself in *variations of the timing of the cardiac cycle* – heart rate variability (HRV) – in response to both external and internal factors. Changes in HRV are commonly evaluated in two frequency bands: (i) the low frequency (LF) band, 0.04–0.15 Hz, which is linked to the interaction of the SNS and PNS, and (ii) the high frequency (HF) band, 0.15–0.4 Hz, which primarily reflects the activity of the PNS [14, 15]. In addition, it is well understood that breathing modulates HRV via a phenomenon referred to as the respiratory sinus arrhythmia (RSA), whereby the heart rate accelerates during inspiration and decelerates during expiration. The RSA is usually

attributed to the activity of the PNS, so that the HF component of HRV is dominated by the changes in heart rate induced by breathing.

1.2 Hyperscanning via EEG

While performing cooperative activities, neuronal synchrony between the participants' brains has been observed through the so-called hyperscanning method, whereby cerebral data from two participants is acquired simultaneously. An fMRI device was employed for data acquisition in the first hyperscanning study [16], but due to its several limitations, including the size and cost, hyperscanning studies nowadays typically measure neuronal activity by recording electroencephalography (EEG) [17, 6, 4, 18]. The electroencephalogram refers to an electrical response which can be non-invasively recorded from the scalp with multiple electrodes placed on different locations according to the 10–20 system [19]. It is commonly evaluated in five frequency bands: delta 0–3 Hz, theta 3–7 Hz, alpha (mu) 7–13 Hz, beta 13–30 Hz, and gamma 30–40 Hz [20].

Neuronal activities of multiple brains have been found to synchronise in different areas of the brains, varying from task to task. Table 1.1 shows tasks performed in different hyperscanning studies and different areas of the brains which synchronised while the participants performed the tasks [1].

Despite some difference in results, EEG hyperscanning studies in [24, 17, 20] have conclusively shown that the right hemispheres of participants, dominating in the right centroparietal regions, are most synchronised *between* the brains (inter-brain synchronisation) during social interaction, reflected in synchronised activities in the theta and alpha EEG bands (see Chapter 5). These regions have been suggested to play a pivotal role in social interaction and are considered as 'functional hubs' of the brains [17]. The work in [24] has revealed increases in power in the frequency range 12–13 Hz (the high alpha band) of EEG signals of eight pairs of subjects over the

Task instructions	**Synchronised brain areas**
Handy-Dandy: the sender sees one of two colours on the screen and sends one of two colours to the receiver. The receiver says if the colour sent by the sender corresponds to the colour the sender saw before or not[16]	Supplementary motor area
'Bridge-like' card game [21]	Prefrontal and anterior cingulated cortex
Button press minimising time difference [22]	Right superior frontal cortices
Music production synchronously with the aid of a metronome [23]	Prefrontal cortices
Follow the other's hand movements or propose the own hand movement to the other partner [17]	Right centroparietal scalp regions
Follow the other's finger movements or propose the own finger movement to the other partner [24]	Right centroparietal scalp regions

Table 1.1: Tasks performed in hyperscanning studies and synchronised areas of the brains [1].

right centroparietal regions only during synchronised behaviour, where each pair of subjects moved their index fingers in unison at their own preferred rate and amplitude. This is believed to be due to the enhancement of the mirror-neuron system[1] and/or the inhibition of intrinsic premotor activity. The work in [17] has revealed increases in phase synchrony in 11 pairs of subjects in: (i) the theta EEG band over the parietal regions while they were imitating hand movements of the partners, and (ii) the alpha EEG band over the right centroparietal regions while they were synchronising hand movements with the partners. Note that synchronisation of hand movements in [17] was defined as simultaneous start and stop of a hand movement within the pair, which included both similar and different movements, thus showing a coordinated rhythm. The increased phase synchrony in the theta band was considered to be due to the processing of other self-similarities in the matched hand movements, and the increased phase synchrony in the alpha band was hypothesized to be due to the alpha band acting as a neural correlate of the mirror neuron system functioning. The work in [20] has shown increases in power in the theta band in several areas of the brains of 26 pairs of subjects while they were

[1]Mirror neurons represent a distinctive class of neurons that discharge both when an individual executes a motor act and when he observes another individual performing the same or a similar motor act [25].

cooperating and defecting in the Prisoner's dilemma game[2]. In addition to these results, it should be noted that the theta and alpha EEG bands can be divided in two subbands – lower (3–5 Hz) and upper (5–7 Hz) theta bands, and lower (7–10 Hz) and upper (10–13 Hz) alpha bands – and these subbands have been found to be associated with different cognitive functions *within* each individual. Suppression in power (*power desynchronisation*) in the lower theta and alpha bands is believed to be associated with attention [26, 27], while power desynchronisation in the upper alpha band reflects semantic memory processes [28, 26]. Increased coherence in the theta band, particularly the upper portion, between hippocampal and rhinal cortices is correlated with successful encoding of new information into episodic (working) memory [28, 29, 30]

1.3 Ear-EEG Recording Concept

An apparatus and method for the measurement of EEG signals from inside the ear canal was first introduced in [31]. The work proposed a means to present an auditory stimulus into the ear canal to evoke brain activity and to subsequently measure EEG, electrooculography (EOG, a technique for measuring eye movement), and electromyography (EMG, a technique for measuring muscle response) with electrodes placed inside or in close proximity to the ear canal, in order to identify abnormalities related to brain function, eye movement and muscle response. The concept of recording EEG from inside the ear canal, i.e. in-the-ear (ITE) recording, is now referred to as 'ear-EEG' [32, 33, 34, 35]. The recording concept allows for the acquisition of EEG signals from inside the ear canal with only a few electrodes and requires relatively short setup time. Several forms of earplugs for the ITE recording system have been introduced in recent years, which include:

1. personalised, hard-shell earpieces with silver chloride (AgCl) electrodes [32, 33],

[2]In the Prisoner's dilemma game, two players act as convicted criminals, where: (i) both of them will serve only 1 year in prison if both of them cooperate (remain silent, do not confess to the crime), or (ii) one who remains silent will serve 20 years in prison, if the other one confesses to the crime (defect) – the one who confesses will be set free, or (iii) both of them will serve 5 years in prison if both of them confess (pure defect).



(a) *(b)*

Figure 1.1: **A schematic diagram of the earpiece and its position inside the ear canal**. *(a)* An earpiece made of medium-density memory foam and two flexible electrodes. *(b)* An earpiece inserted into the ear canal. Due to its small size and user-friendliness, an earpiece requires relatively short setup time.

2. generic earpieces made of silicone and conductive silicone electrodes [36],

3. carbon nanotube polydimethylsiloxane (CNT/PDMS)-based canal-type ear electrodes [37],

4. individualised two-component addition-curing silicone earpieces [38],

5. generic earpieces made of a medium-density memory foam and conductive cloth electrodes [39],

6. customised ear moulds designed for each individual subject from ear impressions taken by a trained audiologist [34],

7. silvered glass silicone based in-the-ear electrode [40].

These earpieces generally comprise one to three electrodes, depending on the design. Figure 1.1 *(a-b)* shows an example of the recently proposed form of earpieces in [39], made of medium-density memory foam and conductive cloth electrodes, and its position when inserted into the ear-canal. Figure 1.2 shows an earpiece and two standard gold-cup electrodes for the ground and the reference connected to a conventional biosignal amplifier for data recording. Note that studies on ear-EEG have been conducted in the laboratory environment and focus on the feasibilty of ear-EEG as an alternative for the conventional on-scalp EEG, therefore, a small, portable and complete ear-EEG recording system which includes a signal amplifier



Figure 1.2: **An earpiece and two standard gold-cup electrodes for the ground and the reference connected to a conventional biosignal amplifier**. A gtec g.USBamp, a 16-channel CE-certified and FDA-listed biosignal amplifier, is used for ear-EEG experiments conducted at the Communications and Signal Processing (CSP) research group, Imperial College London, and in this thesis. Two standard gold-cup electrodes are used as the ground and the reference, and are typically placed on the ear lobe and behind the ear respectively, or vice versa.

and a data logger or transmitter and can be 'wearable EEG' to enable prolonged monitoring of chronic conditions [41] is not yet available on the market.

Since the sizes of ITE earpieces are constrained by the small size of the ear canal, which is typically 26 mm long and is 7 mm in diameter [32], the distance between electrodes on each earpiece is typically only 1 centimetre. This to an extent hinders its spatial discrimination compared to on-scalp electrodes, where the distances between the electrodes are approximately 2 centimetres and are located on different areas of the brain. It has been shown that, however, novel ITE earpieces enable the recordings of EEG activities generated from different areas of the brain:

1. alpha activity of EEG (alpha attenuation) [32, 42, 40], which predominantly originates from the occipital lobe,

2. auditory steady-state response (ASSR) [43, 42, 39], which is generated from the brain stem and the auditory cortex in the temporal lobe,

3. steady-state visual evoked potential (SSVEP) [44, 39], which is generated from the visual cortex in the occipital lobe,

4. P300 response [38, 45], which predominately originates from the parietal lobe,

5. responses to discrete and continuous auditory events (the dichotic oddball and diotic speaker paradigms, respectively) [34], which predominately originates from the central and fronto-central regions,

6. EEG activities related to different stages of sleep, which predominately originates from the frontal, occipital and, in particular, central regions, for manual and automatic sleep scoring [46, 47, 48],

7. EEG activities generated while performing different cognitive tasks, breathing, and listening for the authentication purpose [49].

It has been observed that although the signal level of EEG acquired using the ITE system is lower in amplitude compared to the conventional on-scalp EEG, their signal-to-noise ratios (SNRs), and thus the signal quality, are similar [32, 33, 36, 38]. *Despite a range of research on ear-EEG, its capability as an alternative, practical data acquisition approach to the hyperscanning technique has not been explored.*

1.4 Empirical Mode Decomposition and Its Variants

Physiological signals exhibit nonlinear and non-stationary characteristics, and therefore require signal processing schemes which can provide physically meaningful signal representation; one of such techniques is the empirical mode decomposition (EMD) [50]. Empirical mode decomposition is an adaptive, data-driven algorithm for the analysis of nonlinear and non-stationary time series. It employs a sifting process to decompose the signal into its multiple narrowband amplitude/frequency modulated (AM/FM) components in a deflation-type fashion. These components are referred to as intrinsic mode functions (IMFs, see Section 2.3 for more detail) and are used

as a basis for the representation of the signal. Unlike conventional projection-based time-frequency algorithms, such as the short-time Fourier transform and the discrete wavelet transform, the basis functions within EMD enable physically meaningful interpretation of instantaneous frequency and phase. Moreover, they also allow for a highly localised time-frequency representation of the signal via the Hilbert transform [51]. The effectiveness of EMD was demonstrated in a number of application areas, including bio-signal analysis [52], seismology [53] and paleoclimatology [54]. See Section 2.3 for more detail on the EMD algorithm.

Due to its empirical nature, EMD exhibits two types of artefacts: (i) mode mixing and (ii) mode misalignment. Mode-mixing refers to the existence of different oscillatory components in a single IMF. To alleviate mode mixing, a noise-assisted extension of EMD, called ensemble EMD (EEMD)[55], has been proposed, which adds white Gaussian noise (WGN) directly to the input signal, thus enforcing a dyadic filterbank structure. A large number of noise realisations with subsequent application of EEMD are therefore required to negate the effects of added noise and obtain ensemble means which are treated as true IMFs. Due to the empirical nature of EMD, its direct component-wise application to multivariate signals may result in multivariate IMFs with different centre frequencies and bandwidths across channels – a phenomenon known as mode misalignment. To mitigate this problem, multivariate extensions of EMD have been developed, including bivariate EMD (BEMD) [56], trivariate EMD (TEMD) [57] and multivariate EMD (MEMD) [9]. They estimate the local mean via the projections of the input signal along uniformly sampled direction vectors on a circle (BEMD), 3-dimensional sphere (TEMD) and multidimensional sphere (hypersphere, MEMD), respectively. For certain multivariate cases where a pre-defined structure within the IMFs is required, noise-assisted MEMD (NA-MEMD) [58] was proposed, which adds white Gaussian noise (WGN) channels adjacent to the input signal, thus enforcing the dyadic filterbank structure and at the same time reducing mode mixing in multivariate cases. Applications of MEMD include neural signal processing [59], brain-computer interfaces [60], image processing [61] and artefact removal [62]. See Section 2.4 for more detail on the MEMD algorithm.

Physiological signals often contain power imbalances or inter-channel correlation due to different electrode impedances and adjacent locations of the electrodes. Uniformly sampled direction vectors used in BEMD, TEMD and MEMD, may not be optimal for capturing the dynamics of multivariate data, unless a very high (greater than 127) number of projection vectors is used, which can dramatically increase computational complexity. For a low (8–31) to moderate (32–63) number of projections and unbalanced (power mismatched) and/or correlated data channels these algorithms provide suboptimal estimates of the local mean. To mitigate this problem in bivariate cases, nonuniformly sampled BEMD (NS-BEMD) [63] was proposed, which generates a set of projection vectors representing the direction of highest curvature. Another solution for bivariate cases – dynamically sampled BEMD (DS-BEMD) [64] – employs Menger curvature[3] to quantify local signal dynamics of bivariate signals to generate projection vectors which align with the highest local dynamics. To overcome the problem in trivariate cases, nonuniformly sampled TEMD (NS-TEMD) was proposed in [65]. In order to generate direction vectors which match the dynamics of trivariate signals, it performs the eigendecomposition of the covariance matrix of a trivariate input signal, in order to determine the directions of principal importance, defined in terms of inter-channel power imbalances and correlation, and relocates uniformly sampled direction vectors on a sphere, generated using the Hammersley sequence[4] [9], to their new positions on an ellipsoid parameterised by the eigenvectors and eigenvalues of the covariance matrix. *Despite these recent solutions for bivariate and trivariate cases, a solution for general multivariate cases was still lacking.*

[3]The curvature of a function measures its local deviation from a straight line, and is a natural choice to quantify local signal dynamics, since intuitively, the larger the deviation from straight line, the higher the dynamics (variations) of a signal (function). A convenient means of estimating curvature for real world signals is through the Menger curvature, which defines the curvature radius as the limit of the radius of a circle containing three points of a curve, i.e. it is the reciprocal of the radius of the circle that passes through three points of a curve.

[4]The Hammerley sequence is a convenient method for generating multidimensional low-discrepancy sequences. It has been shown to improve error bounds, compared to standard Monte Carlo methods [66], and the set of direction vectors generated by the Hammersley sequence also yields improved generalized discrepancy estimates as compared with other sampling methods, and hence are uniformly distributed on a sphere [67].

1.5 Quantifying Inter-channel Dependence

Inter-channel dependence can be quantified using standard data-association measures, such as correlation, coherence, bicoherence and phase synchrony. Correlation and coherence are measures of linear synchronisation between the two signals, and they account for both the amplitude and phase information. Coherence yields a data association metric which is a function of frequency, and *can be further extended to quantify phase and amplitude relationships between intrinsic modes in the data via the IMFs* (see Section 3.2 for more detail on the proposed intrinsic coherence measure). Bicoherence and phase synchrony are measures of nonlinear phase synchronisation between two signals. While correlation, coherence, and bicoherence take both amplitude and phase information into account, phase synchrony quantifies only the phase relationship without accounting for amplitude information. Phase synchrony is defined in terms of the deviation from perfect synchrony via the phase synchronisation index (PSI) [8]. Phase synchrony and two other standard data-association measures, correlation and sample entropy, are combined with NA-MEMD in the intrinsic multiscale analysis framework [8], in order to quantify intra- and inter-component dependence of a complex system, such as multiple synchronies and causalities.

Intrinsic phase synchrony (IPS) is a combination of NA-MEMD and phase synchrony proposed in this framework. It generalises standard phase synchrony by equipping it with the ability to operate at the intrinsic scale level. It employs NA-MEMD to decompose a given multivariate signal into narrowband intrinsic oscillations (IMFs), which makes it possible to quantify the temporal locking of the phase information in IMFs using the PSI (see Section 2.6 for more detail on the IPS algorithm). *Time-frequency representations of PSIs obtained using Hilbert transform, however, have lower frequency and time localisation, compared to synchrosqueezing transform* (see Sections 1.6, 2.7 & 4.2.1 for more detail on synchrosqueezing transform and the proposed intrinsic synchrosqueezing coherence measure). Also, for certain scenarios where synchrony takes place over a long period of time and prior knowledge on periods of trends for physically meaningful and straightforward interpretation is unavailable, *it is imperative to have a data-driven, data-association measure which*

empirically quantifies intrinsic trends in synchrony, whereby only those components which contain physically meaningful and straightforward interpretation can be combined (see Section 4.2.2 for more detail on the proposed nested IPS measure).

1.6 Synchrosqueezing Transform

In spite of the undoubted usefulness of the EMD algorithm and its variants, a rigorous theoretical description for the underlying algorithms is still lacking. To this end, the synchrosqueezing transform (SST or WSST) was proposed in [68]. It is a post-processing technique, originally based on the continuous wavelet transform (CWT), for the generation of highly localised time-frequency (TF) representations of nonlinear and non-stationary signals. It reassigns the wavelet coefficients in scale or frequency by combining the coefficients that contain the same instantaneous frequencies, such that the resulting energy is concentrated around the instantaneous frequency curves of the modulated oscillations. The CWT, however, has a limited time-frequency resolution, and since the CWT and STFT are both extensively used to analyse and process multicomponent signals, a natural extension of the univariate CWT-based SST (WSST) to the short-time Fourier transform (STFT) setting was proposed in [69] and is referred to as STFT-based SST (FSST). In order to identify oscillations common to multiple data channels, an extension of the univariate WSST to multivariate cases was proposed in [70], the so-called multivariate synchrosqueezing transform (MSST or W-MSST). It employs the WSST channel-wise to obtain the concentrated coefficients, and then estimates the multivariate instantaneous frequency by combining, for each frequency band, the instantaneous frequencies across all the channels using the joint instantaneous frequency (see [68, 70, 71, 72] for more detail). However, the performance of the W-MSST degrades with noise power (noticeable spurious harmonics are produced as the noise power increases), because: (i) the joint instantaneous frequency estimator is sensitive to noise, and (ii) wavelet functions are time limited – when performing time convolution (i.e. spectral windowing), accurate localisation of both time and frequency by the CWT cannot be achieved at the same time, the CWT thus produces mathematical artefacts (additional noise), that is, wavelet coefficients which correspond to undesired frequency

components. The additional noise (artefacts) generated by the W-MSST can be reduced by STFT-based MSST (F-MSST). See Sections 2.7 & 2.8 for more detail on the SST and MSST algorithms.

1.7 Original Contributions

- A measure of intrinsic inter-channel dependence as a function of frequency, termed **intrinsic coherence (ICoh)**. It quantifies phase and amplitude relationships between intrinsic modes in the data via the IMFs. This measure was proposed in an IEEE conference publication [2] and is outlined in **Chapter 3**.

- An intrinsic data association measure which exhibits precise time and frequency localisation, that is, accurate representation of frequency at each time instant (instantaneous frequency), for the analysis of coupled (synchronised, dependent) nonlinear and non-stationary multivariate signals, referred to as **intrinsic synchrosqueezing coherence (ISC)**. It employs NA-MEMD to generate a set of physically meaningful narrowband intrinsic oscillations, and then employs FSST and F-MSST algorithms to respectively generate univariate and multivariate TF planes with high time and frequency localisation. This algorithm was introduced in a Royal Society Open Science journal publication [73] and is elaborated in **Chapter 4**. It was also applied to evaluate the performance of ear-EEG as an alternative for practical data acquisition approach for the hyperscanning method, and presented in an IEEE conference publication [74], which shall be discussed in **Chapter 5**.

- A procedure for the empirical quantification of physically meaningful and straightforward to interpret trends in phase synchrony, referred to as **nested intrinsic phase synchrony (N-IPS)**. It further decomposes the time series of intrinsic phase synchrony into multiple scales, whereby only certain scales which contain physically meaningful and straightforward to interpret information are then combined. This contribution was proposed in [73] and is elaborated in **Chapter 4**.

- An adaptive, data-driven algorithm for the analysis of unbalanced multivariate signals, referred to as **adaptive-projection intrinsically transformed multivariate empirical mode decomposition (APIT-MEMD)**. Unlike the NS-TEMD, where the trivariate *input signal* is projected along the direction vectors which are aligned with the *global* directions of principal importance, the APIT-MEMD projects each multivariate *sifting input* along the direction vectors which are adaptively (*locally*) determined by the first principal component, reflecting the direction of the largest power imbalance, of each sifting input. This algorithm was presented in a Philosophical Transactions of the Royal Society A journal publication [75] and shall be discussed in **Chapter 6**.

- A two-person single-shot P300 detection algorithm. It employs intrinsic correlation to detect single-shot P300 from a pair of individuals to reduce the time and number of trials normally required to establish an average P300. This approach is based on an assumption that P300 responses of two people simultaneously engaging in the same oddball paradigm are intrinsically cross-correlated. This algorithm was presented in [75] and is outlined in **Chapter 6**.

1.8 Thesis Organisation

- **Chapter 2: Algorithms and Background.**

  The aim of this chapter is to provide necessary details of the adaptive, data-driven algorithms for the analysis of nonlinear and non-stationary univariate and multivariate signals, which include empirical mode decomposition (EMD), multivariate EMD (MEMD), noise-assisted MEMD (NA-MEMD), synchrosqueezing transform (SST) and multivariate SST (MSST). Furthermore, a novel data-association measure, termed intrinsic phase synchrony (IPS), is elaborated. These algorithms are instrumental in developing intrinsic coherence (ICoh) presented in Chapter 3, intrinsic synchrosqueezing coherence (ISC) and nested intrinsic phase synchrony (N-IPS) presented in Chapter 4.

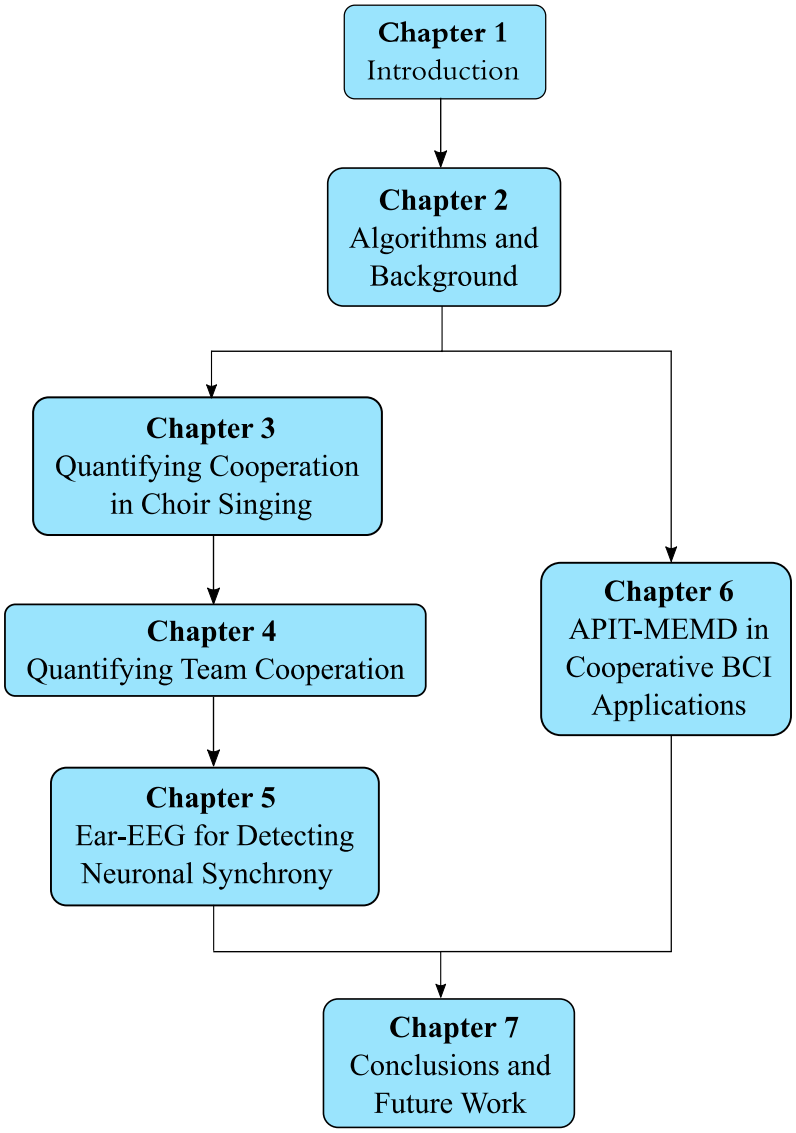


Figure 1.3: **Thesis structure.** Three new data-association measures and their applications are the focuses of Chapters 3–5, while Chapter 6 focuses on an extension of MEMD and its applications.

Remarks: Chapters 3–5 focus on introducing new data-association measures and presenting their applications to quantifying physiological and neuronal couplings in various collaborative tasks. Chapter 6, on the other hand, focuses on introducing an extension of MEMD for dealing with power imbalances between physiological data channels and proposing its applications to cooperative brain-computer interface (BCI) and financial signal processing.

- **Chapter 3: Quantifying Cooperation in Choir Singing: Respiratory and Cardiac Synchronisation.**

  In this chapter, a data-association measure, termed intrinsic coherence (ICoh),

is presented and is used along with intrinsic phase synchrony (IPS) in quantifying couplings in HRV and respiratory signals of a subset of choir members, the conductor and a subset of audience, while performing a 4-minute and 40-second piece of music.

- **Chapter 4: Quantifying Team Cooperation Through Intrinsic Multi-scale Measures: Respiratory and Cardiac Synchronisation in Choir Singers and Surgical Teams.**

  This chapter introduces two data-association measures: (i) intrinsic synchrosqueezing coherence (ISC), and (ii) nested intrinsic phase synchrony (N-IPS). The former is employed to identify precise physiological couplings in both time and frequency between a subset of bass singers of the same choir as in Chapter 3, while the latter is used to empirically identify trends in synchrony, i.e. the level of cooperation, between subsets of soprano and bass singers of another choir while performing a 1-hour evensong, and between pairs of surgeons while performing a 2-hour surgical procedure.

- **Chapter 5: Ear-EEG for Detecting Neuronal Synchrony in Continuous Cooperative Multi-person Scenarios.**

  The proposed ISC algorithm is employed in this chapter to evaluate the performance of ear-EEG against on-scalp EEG as an alternative data acquisition approach for the hyperscanning method in the task of identifying the most robust EEG subbands for neuronal synchrony detection for cooperative multiplayer gaming.

- **Chapter 6: Adaptive-projection Intrinsically Transformed MEMD (APIT-MEMD) in Cooperative Brain-computer Interface Applications**

  The main focus of this chapter is on an extension of the MEMD algorithm for dealing with power imbalances between physiological data channels. This is referred to as adaptive-projection intrinsically transformed MEMD (APIT-MEMD). We proceed to show its applications in the intrinsic multi-scale analysis framework to cooperative steady-state visual evoked potential (SSVEP) and P300-based brain-computer interface (BCI)

- **Chapter 7: Conclusions and Future Work.**
  Concluding remarks drawn from the thesis and ideas for future works are outlined in this chapter.

- **Appendix A: Areal Density.**
  This appendix provides further simplification of the trends in synchrony obtained using the N-IPS algorithm in Chapter 4 by calculating the areal density (AD).

- **Appendix B: Supportive Performance Evaluation of Ear-EEG.**
  The performance of ear-EEG against on-scalp EEG in another cooperative multi-player game is evaluated in this appendix to support the results in Chapter 5.

- **Appendix C: Application of Intrinsic Phase Synchrony to Financial Signal Processing.**
  This appendix shows an application of the APIT-MEMD algorithm in the intrinsic multi-scale analysis framework to financial signal processing, whereby the stress in the financial system is considered analogous to human physiological stress.

Chapter 2

Algorithms and Background

This chapters provides the required background on the concepts of stationarity of a random process and phase response of a filter, and algorithms extensively used in this thesis for the analysis of coupled nonlinear and non-stationary physiological signals. This includes a brief introduction to empirical mode decomposition (EMD), multivariate EMD (MEMD), noise-assisted MEMD (NA-MEMD), and intrinsic phase synchrony (IPS). This chapter also reviews novel algorithms for generating highly localised time-frequency representations (i.e. accurate representation of instantaneous frequency), termed synchrosqueezing transform (SST) and multivariate SST (MSST). This chapter next reviews the notions of bias and variance of an estimator, and it finally provides background on matched filtering, Hilbert transform, and the matched filtering and Hilbert transform (MF-HT) algorithm for the extraction of HRV from ECG signals, extensively used in this thesis..

2.1 Stationarity of a Random Process

A random process $x(t)$ is *Strict-Sense Stationary (SSS)* if for all n the joint distribution $p(x(t_1), \ldots, x(t_n))$ is invariant under time shifts, that is,

$$p(x(t_1 + t_0), \ldots, x(t_n + t_0)) = p(x(t_1), \ldots, x(t_n)), \forall t_0 \tag{2.1}$$

The SSS, however, is too strict for practical applications, the more 'relaxed' stationary condition is considered; a random process $x(t)$ is *Wide-Sense Stationary (WSS)* if its mean and autocorrelation functions are time invariant, that is,

- the expected value (mean) $E\{x(t_1)\} = E\{x(t_1 + t_2)\}$,
- the covariance $cov(t_1, t_2)$ is a function only of the time difference $t_1 - t_2$, i.e. $cov(t_1, t_2) = cov(t_1 - t_2, 0) = cov(t_1 - t_2)$,
- the expected value $E\{x(t)^2\} < \infty$.

2.2 Phase Response of a Filter

There are three types of phase response that a filter can have: zero phase, linear phase, and nonlinear phase. A filter with a zero-phase response introduces no delay in the output signal. However, it requires the use of negative numbered samples, which can be impractical in real-world applications. Linear phase is a property of a filter, where the phase response of a filter is a linear function of frequency (i.e. the slope of a plot of the phase response of the filter as a function of frequency is a straight line), resulting in all frequency components of the input signal experiencing the same delay. This property is achieved with a finite impulse response (FIR) filter, where the impulse response is symmetrical around a positive numbered sample. On the other hand, since the impulse response of an infinite impulse response (IIR) filter is not symmetrical, such a filter introduces a nonlinear phase response, that is, different frequency components of the input signal experience different delays.

2.3 Empirical Mode Decomposition (EMD)

Unlike conventional projection-based schemes, such as Fourier and wavelet transforms, which trade time localisation for frequency localisation, or vice versa, the Hilbert transform can obtain a physically meaningful estimate of frequency at each

time instant (instantaneous frequency) if the input signal satisfies monocomponent criteria [76]. In other words, the signal can be modelled by a single amplitude/frequency component changing slowly over time. A precise definition of the term 'monocomponent', however, does not exist, and a widely used approximation is the so-called narrow-band criteria [77]. These criteria primarily concern the global properties of the signal, that is, the number of extrema and the number of zero crossings should differ by at most one. In [50] an additional local criterion was proposed – the mean of the two envelopes that interpolate the local maxima and local minima must be approximately zero. Signals which satisfy both the local and global criteria are called *intrinsic mode functions* (IMFs), and enable a precise estimate of both instantaneous frequency and amplitude via the Hilbert transform. The univariate EMD [50] (see Algorithm 2.3) embarks upon these criteria to decompose a single-channel input $x(t)$ into a set of narrowband intrinsic oscillations (IMFs), that is,

$$x(t) = \sum_{k=1}^{K} c_k(t) \tag{2.2}$$

where $\{c_k(t)\}$, $k = 1, 2, \ldots, K$, denotes the set of IMFs.

Algorithm 2.1: Empirical mode decomposition (EMD).

---

1. Given a univariate signal $x(t)$, let proto-IMF $\tilde{x}(t) = x(t)$ and $k = 1$.
2. Identify all local minima and maxima of $\tilde{x}(t)$.
3. Interpolate all the minima and maxima to respectively obtain the lower envelope, $e_{\min}(t)$, and the upper envelope, $e_{\max}(t)$.
4. Compute the local mean $m(t)$, given by $m(t) = (e_{\min}(t) + e_{\max}(t))/2$.
5. Extract the detail $d(t)$, given by $d(t) = \tilde{x}(t) - m(t)$.
6. If $d(t)$ does not satisfy IMF stoppage criteria, let $\tilde{x}(t) = d(t)$ and go to Step (2). However, if $d(t)$ satisfies the IMF criteria,
   - $d(t)$ becomes an IMF, $c_k(t)$;
   - $\tilde{x}(t) = \tilde{x}(t) - c_k(t)$;

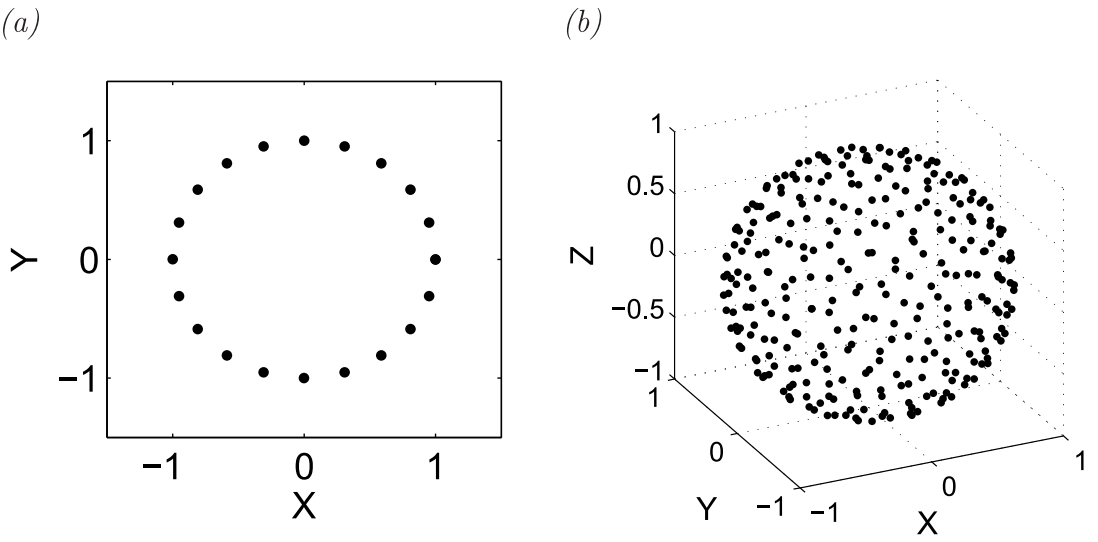


Figure 2.1: **Sampling directions for multivariate extensions of EMD**. *(a)* Projection set (Q) for bivariate EMD based on uniform angular sampling. *(b)* Projection set (Q) for multivariate EMD based on a low-discrepancy Hammersley sequence.

- increment k;
- repeat Steps (2)–(6) until $\tilde{x}(t)$ is a monotonic residue or trend.

The sifting process (Steps (2)–(5)) in Algorithm 2.3 is stopped once the signal detail $d(t)$ satisfies the IMF stoppage criteria: (i) the number of extrema is equal to the number of zero crossings for around 3 to 5 successive sifting operations [51]; and (ii) the difference between two consecutive sifting results is below a certain threshold [50]. In general, the more sifting operations that are performed, the more narrow-band the IMF spectra become. Too many sifting operations, however, should not be performed because this can produce a large number of IMFs with uniform amplitudes, that is, components which approximate a Fourier basis, which contradict the data-driven nature of the analysis.

2.4 Multivariate Extensions of Empirical Mode Decomposition

Bivariate [56] and multivariate [9] extensions of the EMD algorithm have been proposed in order to extend its operation for any number of data channels, so that IMFs in different channels are 'aligned', containing similar centre frequencies and

bandwidths. A key concept in creating these extensions has been the definition of the local mean for multivariate data. The bivariate EMD algorithm (BEMD) [56] proposed a solution for bivariate data wherein the data are projected in Q directions, with each direction vector defined based on equidistant points along the unit circle (uniform angular sampling), see Figure 2.1 *(a)*. Univariate estimates of the envelope in each direction are averaged to give a bivariate envelope, the centre of which is the local mean. This concept was extended further in [9] for multivariate data of dimension P – multivariate EMD (MEMD) – wherein the projection of the data is performed for Q direction vectors, based on a pointset on a hypersphere generated using a low-discrepancy Hammersley sequence, see Figure 2.1 *(b)*. Algorithm 2.4 describes the MEMD operation for a P-variate time series, with a pointset of size Q, giving the set of IMF components $c_k^p(t)$, where k denotes the IMF index ($k = 1, 2, \ldots, K$) and p the data channel index ($p = 1, 2, \ldots, P$).

Algorithm 2.2: Multivariate empirical mode decomposition (MEMD).

---

1. Given a multivariate signal $\mathbf{x}(t)$, let multivariate proto-IMF $\tilde{\mathbf{x}}(t) = \mathbf{x}(t)$.

2. Choose a weighting scheme based on a suitable pointset for sampling on a P-hypersphere, $\mathbf{w}_q = \{w_{\{q,1\}}, w_{\{q,2\}}, \ldots, w_{\{q,P\}}\}_{q=1}^{Q}$.

3. Calculate a projection, denoted by $\Upsilon\left(\tilde{\mathbf{x}}(t)\right)_{\mathbf{w}_q}$, of the proto-IMF $\tilde{\mathbf{x}}(\mathbf{t})$ along the direction vector $\mathbf{w}_q$, for all q (the whole set of direction vectors), giving $\{\Upsilon\left(\tilde{\mathbf{x}}(t)\right)_{\mathbf{w}_q}\}_{q=1}^{Q}$ as the set of projections.

4. Find the $j = 1, 2, \ldots, J$ time instants $\{t_{j,\min}^{\mathbf{w}_q}\}$ and $\{t_{j,\max}^{\mathbf{w}_q}\}$ corresponding respectively to the minima and maxima of the set of projected signals $\{\Upsilon\left(\tilde{\mathbf{x}}(t)\right)_{\mathbf{w}_q}\}_{q=1}^{Q}$.

5. Interpolate $\tilde{\mathbf{x}}(t_{j,\min}^{\mathbf{w}_q})$ and $\tilde{\mathbf{x}}(t_{j,\max}^{\mathbf{w}_q})$ to obtain respectively multivariate minima and maxima envelope curves $\{\mathbf{e}_{\min}^{\mathbf{w}_q}(t)\}_{q=1}^{Q}$ and $\{\mathbf{e}_{\max}^{\mathbf{w}_q}(t)\}_{q=1}^{Q}$.

6. For a set of Q direction vectors, the mean $\mathbf{m}(t)$ of the envelope curves is calculated as:
$$\mathbf{m}(t) = \frac{1}{2Q}\sum_{q=1}^{Q}\mathbf{e}_{\min}^{\mathbf{w}_q}(t) + \mathbf{e}_{\max}^{\mathbf{w}_q}(t) \tag{2.3}$$

7. Extract the detail $\mathbf{d}(t)$ using $\mathbf{d}(t) = \tilde{\mathbf{x}}(t) - \mathbf{m}(t)$.

8. If the detail $\mathbf{d}(t)$ fulfills the stoppage criterion for a multivariate IMF (the difference between two consecutive sifting results is below a certain threshold), $\mathbf{d}(t)$ becomes a multivariate IMF, $\mathbf{c}_k(t)$, and $\tilde{\mathbf{x}}(t) = \tilde{\mathbf{x}}(t) - \mathbf{c}_k(t)$. Otherwise, $\tilde{\mathbf{x}}(t) = \mathbf{d}(t)$. Go to Step (3).

9. Repeat Steps (3)–(8) until $\tilde{\mathbf{x}}(t)$ is a multivariate monotonic residue or trend.

2.5 Noise-assisted Multivariate Empirical Mode Decomposition (NA-MEMD)

It has been shown in [78, 79] that EMD acts essentially as a dyadic filter when decomposing WGN, enforcing the dyadic filterbank structure onto IMFs – Fourier spectra of the IMFs are all identical and cover the same area on a semi-logarithmic period scale. Therefore, the aim of simultaneously decomposing added separate artificial WGN channels and the input signal using noise-assisted MEMD (NA-MEMD) is to enforce the dyadic filterbank structure within the IMFs by using WGN as a decomposition reference and to reduce mode mixing. *While this may hinder the data-driven operation of MEMD, it is essential in multi-channel operations where the requirement is to compare IMFs with similar centre frequencies and bandwidths in order to preserve the physical meaning of the analysis.* It should also be noted that the most important aspect of an MEMD approach, via either standard MEMD or NA-MEMD, is that even if mode mixing occurs it is likely to happen simultaneously in every channel. In this way, multi-component comparisons at the IMF level are matched and physically meaningful. The work in [8] has shown that using NA-MEMD to decompose WGN using 10 *different* artificial noise channels reduced the degree of overlap between power spectral densities of the resulting IMFs, compared to using NA-MEMD to decompose the same WGN using 10 *identical* artificial noise channels. It was therefore suggested that the number of WGN channels should be as large as possible – computation time permitting – in order to reduce the degree of overlap between IMF spectra, that is, imposes a more pronounced dyadic filterbank structure within the IMFs.

In terms of phase responses, NA-MEMD, which acts as a dyadic filterbank, can be deemed having a linear phase response. This is because of the computational time required by the sifting process to decompose a given input signal into a set of IMFs, thus introducing the same delay to all frequency componentns of the input signal

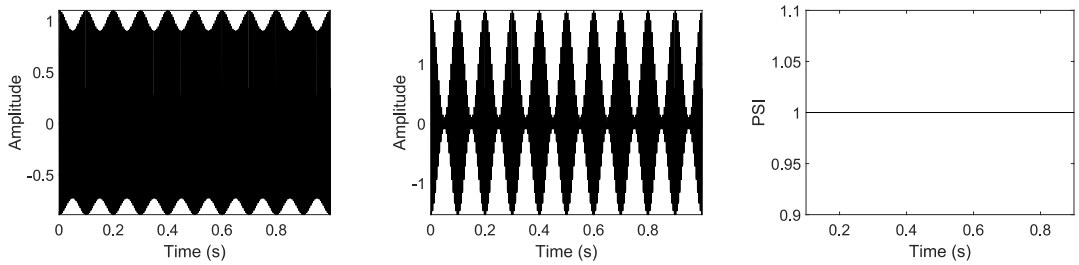
2.6 Intrinsic Phase Synchrony (IPS)

The degree of phase synchronisation between data channels can be measured through phase synchrony, which quantifies only the phase relationship between two signals without accounting for amplitude information. It is defined in terms of the deviation from perfect synchrony via the phase synchronisation index (PSI). The PSI values range from 0 to 1, with 1 indicating the perfect phase locking and 0 non-phase-synchronous relationship.

To show the principal difference between the correlation and phase synchrony measures, where the former accounts for both amplitude and phase information while the latter takes only phase information into account, Figure 2.2 *(a-b)* shows a bivariate amplitude modulated signal with perfect phase locking between the channels, given by

$$\begin{aligned} x_1(t) &= (1 + M_{AM,1}\cos(2\pi f_m t)) \cdot \cos(2\pi f_c t), \\ x_2(t) &= (1 + M_{AM,2}\cos(2\pi f_m t)) \cdot \cos(2\pi f_c t), \end{aligned} \tag{2.4}$$

where M_{AM} denotes amplitude modulation index, f_m baseband frequency, and f_c carrier frequency. In this example, $M_{AM,1} = 0.1$, $M_{AM,2} = 0.9$, f_m=10 Hz, and f_c=200 Hz, with a sampling frequency of 1 kHz. The phases of the two channels are perfectly synchronised, but they exhibited different patterns of the varying amplitudes – envelopes – due to the different values of the amplitude modulation indices, $M_{AM,1}$ and $M_{AM,2}$. The correlation measure was thus affected by the amplitude difference, resulting in a correlation coefficient of only 0.879. The phase synchrony measure, on the other hand, quantified only the phase relationship between the channels, resulting in PSI values of 1, as shown in Figure 2.2 *(c)*. See Algorithm



(a) *(b)* *(c)*

Figure 2.2: **Bivariate amplitude modulated signal with perfect phase locking between the channels and their PSIs.** *(a)* $x_1(t)$. *(b)* $x_2(t)$. *(c)* PSI values. Although the amplitudes of the two channels are different due to different amplitude modulation indices, their phases perfectly synchronised, resulting in PSI values of 1.

2.3 below for the calculation of PSI values. Note that for this example PSI values were calculated directly from the bivariate signal – NA-MEMD was not applied to decompose it into IMFs.

Intrinsic phase synchrony (IPS) was originally proposed in the so-called intrinsic multiscale analysis framework [8], and generalises standard phase synchrony by equipping it with the ability to operate at the intrinsic scale level. It employs NA-MEMD to decompose a given multivariate signal into its narrowband intrinsic oscillations (IMFs), which makes it possible to quantify the temporal locking of the phase information in IMFs using the standard phase synchronisation index (PSI), as outlined in Algorithm 2.3.

Algorithm 2.3: Intrinsic phase synchrony (IPS).

---

1. Given a P-variate signal $\mathbf{x}(t)$, obtain multivariate IMFs via NA-MEMD, $\mathbf{c}_k(t)$, where $k = 1, 2, \ldots, K$, and K denotes the number of IMFs.

2. For each channel p, calculate the instantaneous phases $\phi_p(t)$ for the IMFs through the analytic signals generated using the Hilbert transform.

3. Calculate phase difference between the instantaneous phases for the IMFs of channels i and j, $\Delta\phi_{i,j}(t)$, where $i = 1, 2, \ldots, P$, $j = 1, 2, \ldots, P$, and $i \neq j$.

4. Phase synchrony between channels i and j is then defined in terms of the deviation from perfect synchrony via the phase synchronisation index (PSI) [80],

given by

$$\gamma_{i,j}(t) = \frac{H_{max} - H}{H_{max}}, \tag{2.5}$$

where $H = -\sum_{m=1}^{M} pr_m \ln pr_m$ is the Shannon entropy of the distribution of phase differences $\Delta\phi_{i,j}(t - \frac{W}{2} : t + \frac{W}{2})$ within a window of length W, M is the number of bins within the distribution of phase differences, and pr_m is the probability of $\Delta\phi_{i,j}(t - \frac{W}{2} : t + \frac{W}{2})$ within the mth bin. The maximum entropy H_{max} is given by

$$H_{max} = 0.626 + 0.4 \ln(W - 1). \tag{2.6}$$

2.7 Synchrosqueezing Transform (SST)

The synchrosqueezing transform (SST or WSST) [68] is a post-processing technique originally applied to the continuous wavelet transform (CWT) in order to generate highly localised time-frequency representations of non-stationary signals. The CWT is a projection based algorithm that identifies oscillatory components of interest through a series of time-frequency filters known as wavelets. A wavelet $\psi(t)$ is a finite oscillatory function, which when convolved with a signal $x(t)$, in the form

$$W(a, b) = \int x(t) a^{(-1/2)} \psi(\frac{t - b}{a}) dt \tag{2.7}$$

gives the wavelet coefficients $W(a, b)$, for each scale-time pair (a, b). In this way, the wavelet coefficients can be seen as the outputs of a set of scaled bandpass filters. The scale factor a shifts the bandpass filters in the frequency domain, and also changes the bandwidth of the bandpass filters. Therefore, while the energy of a sinusoid at a frequency ω_s is spread across the scale factor a_s, the energy of the wavelet transform of a sinusoid at a frequency ω_s will spread out around the scale factor $a_x = \omega_\psi / \omega_s$, where ω_ψ is the centre frequency of a wavelet. Thus, the estimated frequency present in those scales is equal to the original frequency ω_s. Consequently, the instantaneous frequency $\Omega(a, b)$ of the wavelet coefficients $W(a, b)$ can be estimated as

$$\Omega(a,b) = -i(W(a,b))^{-1}\frac{\partial}{\partial b}W(a,b). \tag{2.8}$$

The wavelet coefficients that contain the same instantaneous frequencies can then be combined using a procedure referred to as synchrosqueezing (SST). For a set of wavelet coefficients $W(a,b)$ [68], the CWT-based synchrosqueezing transform coefficient is given by

$$T_{\mathrm{CWT}}(\omega_m, b) = (\Delta\omega)^{(-1)} \sum_{a_l:|\Omega(a_l,b)-\omega_m|\leq\Delta\omega/2} W(a_l,b)a_l^{-3/2}\Delta a_l, \tag{2.9}$$

where ω_m are the frequency bins with a resolution of $\Delta\omega$. A summary of the SST is outlined in Algorithm 2.4.

Algorithm 2.4: Synchrosqueezing transform (SST or WSST).

---

1. Given a univariate signal $x(t)$, convolve a wavelet $\psi(t)$ with the signal in order to obtain the wavelet coefficients $W(a,b)$, given by Eq. 2.7.

2. Estimate the instantaneous frequency $\Omega(a,b)$ of the wavelet coefficients $W(a,b)$, given by Eq. 2.8.

3. Combine the wavelet coefficients which contain the same instantaneous frequency in order to obtain the CWT-based synchrosqueezing transform coefficients $T_{\mathrm{CWT}}(\omega_m, b)$, given by Eq. 2.9.

The synchrosqueezing transform has been extended to the short-time Fourier transform (STFT) setting in [69], and is referred to as STFT-based SST (FSST). It performs STFT, instead of CWT, on a given univariate signal $x(t)$ to obtain STFT coefficients $U(\eta,t)$, given by

$$U(\eta,t) = \int_{\Re} x(\tau)g(\tau-t)e^{-2i\pi\eta(\tau-t)}d\tau, \tag{2.10}$$

where g is a sliding window, and τ time lag. The STFT coefficients, $U(\eta, t)$, are next relocated to the instantaneous frequency, Ω, according to the map $(\eta, t) \mapsto (\Omega(\eta, t))$, where Ω is defined by

$$\Omega(\eta, t) = \frac{1}{2\pi}\partial_t \text{arg}U(\eta, t) = Re(\frac{1}{2i\pi}\frac{\partial_t U(\eta, t)}{U(\eta, t)}). \tag{2.11}$$

The STFT-based synchrosqueezing transform coefficient is then given by

$$T_{\text{STFT}}(f, t) = \frac{1}{g(0)}\int_{\Re} U(\eta, t)\delta(f - \Omega(\eta, t))d\eta. \tag{2.12}$$

The FSST has been shown to exhibit better localisation, that is, sharper representation of instantaneous frequencies in low frequencies of linear, exponential and hyperbolic chirps, compared to the SST [69]. A summary of the FSST is outlined in Algorithm 2.5.

Algorithm 2.5: STFT-based synchrosqueezing transform (FSST).

---

1. Given a univariate signal $x(t)$, perform STFT on the signal in order to obtain the STFT coefficients $U(\eta, t)$, given by Eq. 2.10.

2. Estimate the instantaneous frequency $\Omega(\eta, t)$ of the STFT coefficients $U(\eta, t)$, given by Eq. 2.11.

3. Combine the STFT coefficients in order to obtain the STFT-based synchrosqueezing transform coefficients $T_{\text{STFT}}(f, t)$ given by Eq. 2.12.

2.8 Multivariate Synchrosqueezing Transform (MSST)

The multivariate synchrosqueezing transform (MSST or WMSST) [70] is an extension of the CWT-based SST to multivariate cases. It was proposed in order to

identify oscillations common to multiple data channels. It first partitions the time-frequency domain into M frequency bands $\{\omega_m\}_{m=1,2,\ldots,M}$. This makes it possible to identify a set of matched monocomponent signals from a given multivariate signal. The instantaneous amplitudes and frequencies present within those frequency bands can then be determined.

For a multivariate signal $\mathbf{x}(t)$ with the corresponding CWT-based SST coefficients of each channel p, $T^p_{\mathrm{CWT}}(\omega, b)$, and a set of frequency bands $\{\omega_m\}_{m=1,2,\ldots,M}$, the instantaneous frequency $\Omega(\omega_m, b)$ for each channel p and frequency band m is given by

$$\Omega(\omega_m, b) = \frac{\sum_{\omega\in\omega_m} |T^p_{\mathrm{CWT}}(\omega, b)|^2 \omega}{\sum_{\omega\in\omega_m} |T^p_{\mathrm{CWT}}(\omega, b)|^2} \tag{2.13}$$

and the instantaneous amplitude $A(\omega_m, b)$ for each channel and frequency band as

$$A(\omega_m, b) = \sqrt{\sum_{\omega\in\omega_m} |T^p_{\mathrm{CWT}}(\omega, b)|^2}. \tag{2.14}$$

In order to estimate the multivariate instantaneous frequency $\mathbf{\Omega}(\omega_m, b)$ for a given frequency band m, the instantaneous frequencies across the P channels are then combined using

$$\mathbf{\Omega}(\omega_m, b) = \frac{\sum_{p=1}^{P} (A(\omega_m, b))^2 \Omega(\omega_m, b)}{\sum_{p=1}^{P} (A(\omega_m, b))^2}, \tag{2.15}$$

while the multivariate instantaneous amplitude $\mathbf{A}(\omega_m, b)$ for each frequency band is given by

$$\mathbf{A}(\omega_m, b) = \sqrt{\sum_{p=1}^{P} (A(\omega_m, b))^2}. \tag{2.16}$$

The multivariate CWT-based synchrosqueezing transform coefficient $\mathbf{T}_{\mathrm{CWT}}(\omega_m, b)$ for each frequency band m is given by

$$\mathbf{T}_{\mathrm{CWT}}(\omega_m, b) = \mathbf{A}(\omega_m, b)\delta(\omega - \mathbf{\Omega}(\omega_m, b)) \tag{2.17}$$

where $\delta(\cdot)$ is the Dirac delta function. The multivariate CWT-based synchrosqueezing transforms for all frequency bands are then given by $\mathbf{T}_{\mathrm{CWT}}(\omega, b) = \mathbf{T}_{\mathrm{CWT}}(\omega_m, b)|_{m=1,2,\ldots,M}$.

A summary of the MSST is outlined in Algorithm 2.6.

Algorithm 2.6: Multivariate synchrosqueezing transform (MSST or W-MSST).

---

1. Given a P-variate signal $\mathbf{x}(t)$, apply the SST channel-wise in order to obtain the univariate SST coefficients $T^{p}_{\mathrm{CWT}}(\omega, b)$.

2. Determine a set of partitions along the frequency axis for the time-frequency domain, and calculate the instantaneous frequency $\Omega(\omega_m, b)$ and amplitude $A(\omega_m, b)$ for each frequency band m and channel p, given by Eqs. 2.13 and 2.14 respectively.

3. Calculate the multivariate instantaneous frequency $\mathbf{\Omega}(\omega_m, b)$ and amplitude $\mathbf{A}(\omega_m, b)$ for each channel m, using the Eqs. 2.15 and 2.16 respectively.

4. Determine the multivariate CWT-based synchrosqueezing coefficients $\mathbf{T}_{\mathrm{CWT}}(\omega, b)$.

2.9 Bias and Variance of an Estimator

The bias of an estimator $\hat{\theta}$, $bias[\hat{\theta}]$, is the difference between the expected value of the estimator $E\{\hat{\theta}\}$ and the true value of the parameter being estimated θ_0, that is, $bias[\hat{\theta}] = E\{\hat{\theta}\} - \hat{\theta}$. An estimator with zero bias is called *unbiased*. Estimators with small bias, however, can be used in practice, since for an unbiased estimator to be practical further assumptions about the considered population have to be made.

An unbiased estimator is considered having *minimum variance*, the so-called minimum variance unbiased estimator (MVUE) [81], if is has lower variance than any other unbiased estimator for all possible values of the parameter being estimated. Furthermore, if an estimator is unbiased and estimates the quantity of interest in some 'best possible' manner, it is the MVUE, where the notion of 'best possible' relies upon the choice of a particular loss function – the function which quantifies the relative degree of undesirability of estimation errors of different magnitudes; mean

square error (MSE) of an estimator, $MSE(\hat{\theta})$, is the most common loss function. In other words, among unbiased estimators the MVUE minimises MSE, whereby $MSE(\hat{\theta}) = var(\hat{\theta}) + (bias[\hat{\theta}])^2$. In some cases, however, biased estimators have lower MSE, because they have a smaller variance than any unbiased estimator [82].

2.10 Matched Filtering

A matched filter is obtained by correlating a known signal or template with an unknown signal to detect the presence of the template in the unknown signal [83, 84]. The idea of matched filtering is to start from a defined waveform or function and to search for a similar pattern in a time series. This is performed by taking the convolution between the conjugate of the defined mother pattern $h(\tau)$ and the original signal $x(t)$ with length V as shown in Eq. 2.18.

$$y(t) = \int_{\tau=0}^{V-\tau} h(\tau)x(t-\tau)d\tau, \tag{2.18}$$

where τ is time lag. The result of the convolution results in a high amplitude at times when the time series resembles the mother pattern and a low amplitude elsewhere. This technique is useful for locating the QRS complex in the ECG because the R-peak usually exhibits a high amplitude and the shape of QRS is unique even in noisy intervals.

2.11 Hilbert Transform

The Hilbert transform is a tool used to extend a real function $x(t)$ into the complex domain. The transform is shown in Eq. 2.19, where $x_h(t)$ is the complex output of the transform.

$$x_h(t) = HT[x(t)] = \frac{1}{\pi}\int_{\Re} x(\tau)\frac{1}{1-\tau}d\tau \tag{2.19}$$

The analytic version of $x(t)$, $z(t)$, can be written as in Eq. 2.20, and the instantaneous amplitude (i.e. a positive envelope), phase and frequency of $x(t)$ can be calculated using Eq. 2.21–2.23 respectively.

$$z(t) = x(t) + jx_h(t) \tag{2.20}$$

$$A(t) = \sqrt{x^2(t) + x_h^2(t)} \tag{2.21}$$

$$\phi(t) = \arctan\left(\frac{x_h(t)}{x(t)}\right) \tag{2.22}$$

$$\Omega(t) = \frac{d\phi(t)}{dt} \tag{2.23}$$

2.12 The Matched Filtering and Hilbert Transform (MF-HT) Algorithm

An algorithm to extract R-peaks from ECG using a combination of matched filtering and Hilbert transform (MF-HT) was proposed in [85]. The approach is semi-automatic with the user required to select a QRS waveform mother pattern from the recorded ECG. To locate R-peaks in noisy ECG, the user is provided with several R-peak estimates when an abnormal QRS waveform or heart rate is detected. This is achieved through a user friendly graphical interface facilitating straightforward data processing. After detecting the R-peaks, the HRV is constructed from the R-R intervals, the temporal difference between two subsequent R-peaks, yielding an unevenly sampled time series. The HRV is next resampled to create a regularly spaced time series using cubic spline interpolation with a sampling frequency of 4 Hz [86]. A summary of the MF-HT is outlined in Algorithm 2.7, and a screenshot of the graphical interface is shown in Figure 2.3.

Algorithm 2.7: Matched filtering and Hilbert transform (MF-HT).

1. Apply a Butterworth IIR band-pass filter (BPF) of order 6 with the passband set to 8–30 Hz to a given ECG signal.
2. Manually locate the first R-peak.
3. Create a window beginning at the previous R-peak and ending at the longest realistic heart beat interval.
4. Remove local trend by taking the difference between consecutive sample points.
5. Apply a matched filter between the mother QRS and the window, resulting in a degree of correlation ρ_{mf}.
6. Apply the Hilbert transform to ρ_{mf} to identify candidate R-peaks RP_j.
7. Locate the correct R-peak by selecting the peak RP_j with the highest cross-correlation with the mother QRS.
8. Repeat steps (3)–(7) for each window.
9. Construct heart rate variability (HRV) from the time difference between subsequent R-peaks using cubic spline interpolation with a sampling frequency of 4 Hz.

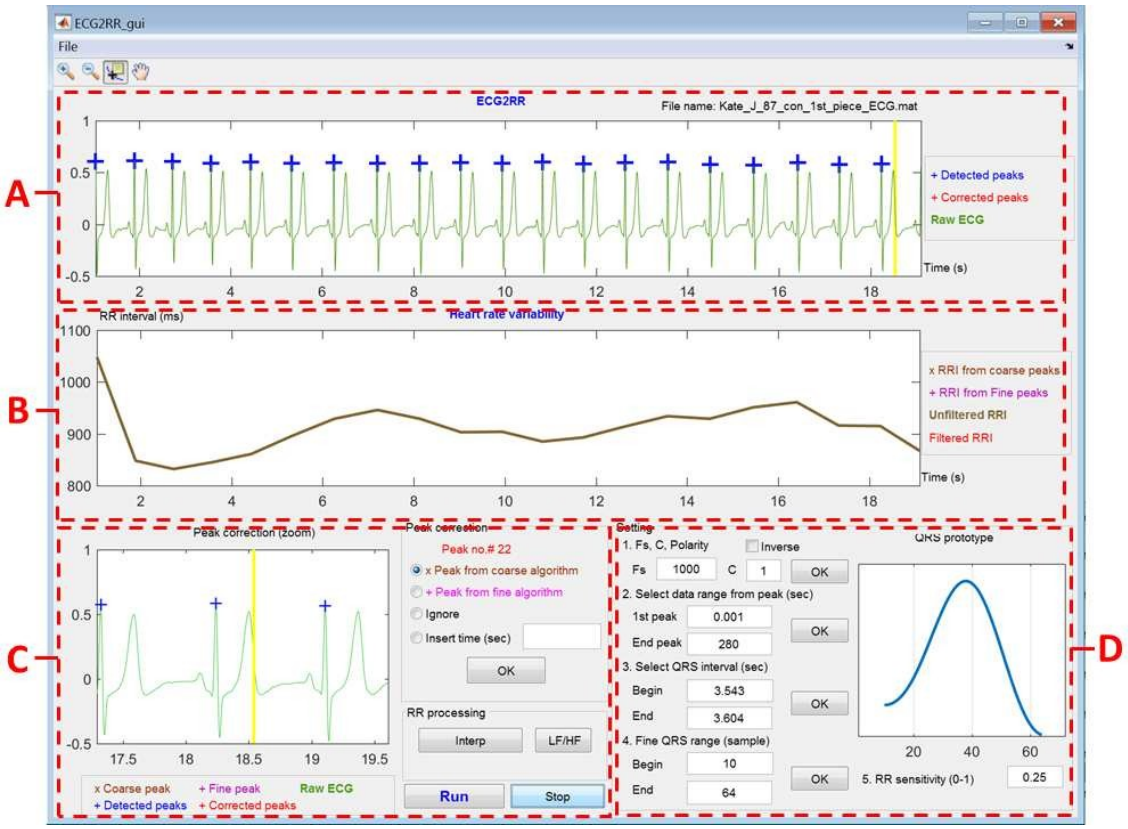


Figure 2.3: **Software for R-peak extraction using the MF-HT algorithm.** Four windows are designed to visualise: ECG and identified R-peaks (see panel A), the RR-intervals (see panel B), a close-up R-peak examination with suggested choices (see panel C), and the QRS pattern selection and settings (see panel D).

Chapter 3

Quantifying Cooperation in Choir Singing: Respiratory and Cardiac Synchronisation

3.1 Introduction

Cooperative tasks require coordinated joint actions among the participants, to the extent that a failure in an individual's action may have catastrophic consequences on the task of the group as a whole. One such activity is choir singing, where highly synchronised performance of the individual singers is a prerequisite to successful performance. It is particularly interesting as participants do not use any tools; it can be performed with or without musical instruments, whereby the conductor, essentially, plays 'human instruments' – the soprano, alto, tenor and bass. The normal respiratory rate in adults varies between 12 and 15 breaths per minute [87], yet despite this natural variation, breathing in unison among individuals is a prerequisite in choir singing, where the singers' breathing rhythm is dictated by the tempo and demands of a musical score. These demands and physical constraints give rise to both direct and indirect synchrony and causality in cardiac and respiratory activity at multiple levels.

A challenge in quantifying synchrony among choir members is that, depending on

the score and tempo, breathing rhythms of singers can be either: (i) voluntarily controlled by themselves, in order to perform long or short inhalation or exhalation; or (ii) involuntarily controlled by the autonomic nervous system (ANS) as described in Section 1.1.

The aim of this study is to build upon the enhanced discrimination capability of the intrinsic phase synchrony and intrinsic coherence data association metrics, in order to characterise the scale-wise dependence in the respiratory and HRV (variations of the timing of the cardiac cycle as a result of the interplay between the SNS and PNS nervous subsystems) signals of: (i) the same members of choir during a rehearsal and a real performance; (ii) the conductor in both of these situations; (iii) a subset of audience during the real performance. The so-enabled investigation of the manifold couplings in human physiological responses during a performance promises new, objective measures of the degree of human cooperation.

3.2 Intrinsic Coherence (ICoh)

Inter-channel dependence can be quantified using standard data-association measures, such as correlation and coherence. Similar to correlation, coherence is a measure of linear synchronisation between two signals. It accounts for both the amplitude and phase information, and yields a data association metric which is a function of frequency, f, with the coherence values ranging from 0 to 1 (0 indicating a non-coherent relationship and 1 the perfect coherence [88, 89]). This measure can be further extended to quantify phase and amplitude relationships between intrinsic modes in the data via the IMFs (as a function of scale), a procedure referred to as the *intrinsic coherence* (ICoh), as outlined in Algorithm 3.1.

Algorithm 3.1: Intrinsic coherence (ICoh)

---

1. Given a P-variate signal $\mathbf{x}(t)$, obtain multivariate IMFs via NA-MEMD, $\mathbf{c}_k(t)$, where $k = 1, 2, \ldots, K$, and K the number of IMFs.

2. For each channel i, calculate power spectral density of the IMF of interest $S_{ii}(f)$, where $i = 1, 2, \ldots, P$.

3. Calculate cross-spectral power densities between the IMFs of interest of channels i and j, $S_{ij}(f)$, where $i = 1, 2, \ldots, P$, $j = 1, 2, \ldots, P$, and $i \neq j$.

4. Coherence between the IMFs of interest of channels i and j, $COH_{ij}(f)$, is then given by

$$COH_{ij}(f) = \left| \frac{S_{ij}(f)}{\sqrt{S_{ii}(f)S_{jj}(f)}} \right|^2 . \tag{3.1}$$

   The COH[1] values range from 0 to 1, with 0 indicating a non-coherent relationship and 1 the perfect coherence [88, 89].

3.3 Data Acquisition and Pre-processing

The ECG and respiratory data recordings were conducted at Union Chapel, London, in March 2015 under the ethics approval ICREC_12_1_1, Joint Research Office at Imperial College London. Written consents of the subjects who participated in this study were obtained, and they were not paid for the participation. A male conductor, a subset of eight members (four males and four females) of the Eric Whitacre's choir participated in the recordings of their physiological signals during a 4-minute and 40-second rehearsal of a music piece called 'Lux Nova'. All the same nine subjects also participated in the recordings during a public performance of the same music piece. Three female and two male members of the audience also participated in the data recordings during the performance. During both the rehearsal and the performance, ECG signals were recorded with three Ag/AgCl ECG monitoring electrodes placed on the skin, just below the collar bone; one electrode on the left hand side for the signal and the other two electrodes on the right hand side for the ground and the reference. Respiratory signals were recorded using a custom-made

[1] COH is calculated from the intrinsic coherence (ICoh) procedure.

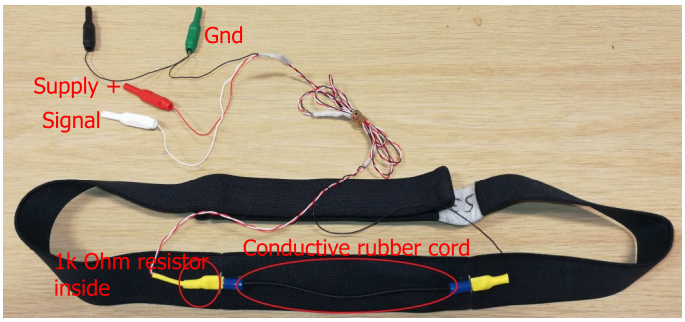
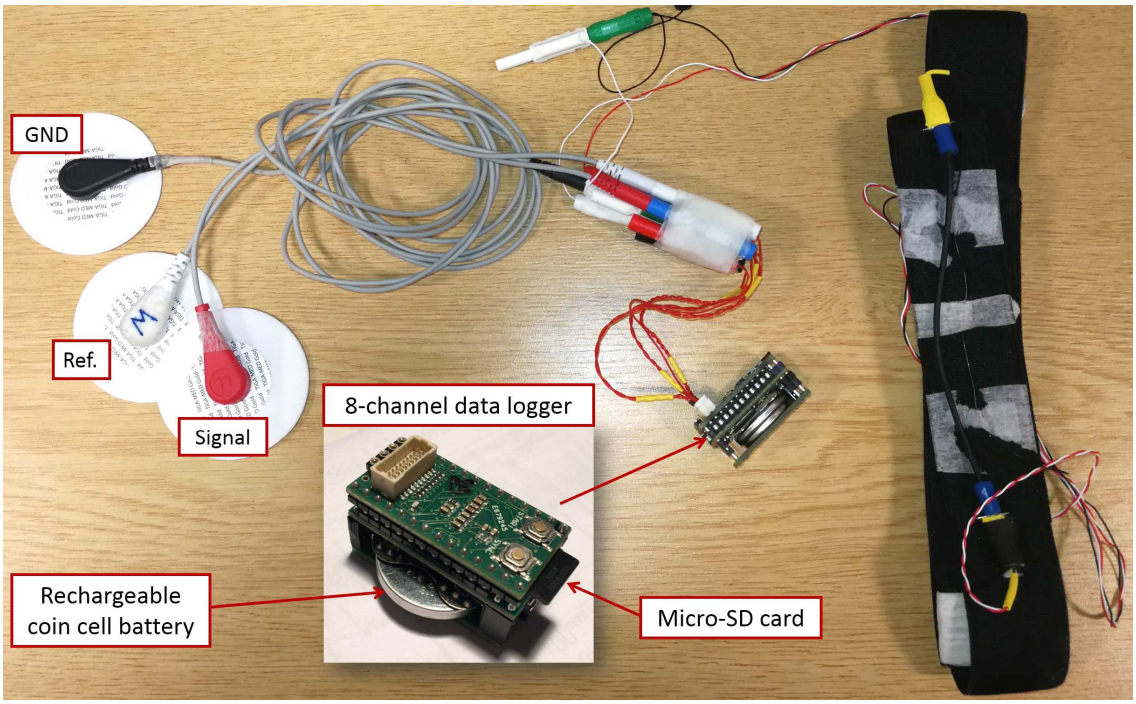


Figure 3.1: **A custom-made respiration belt**. A conductive rubber cord was attached to the belt. A 1kΩ potential divider was connected to the conductive rubber cord such that the voltage measured across the cord was suitable for our data loggers.

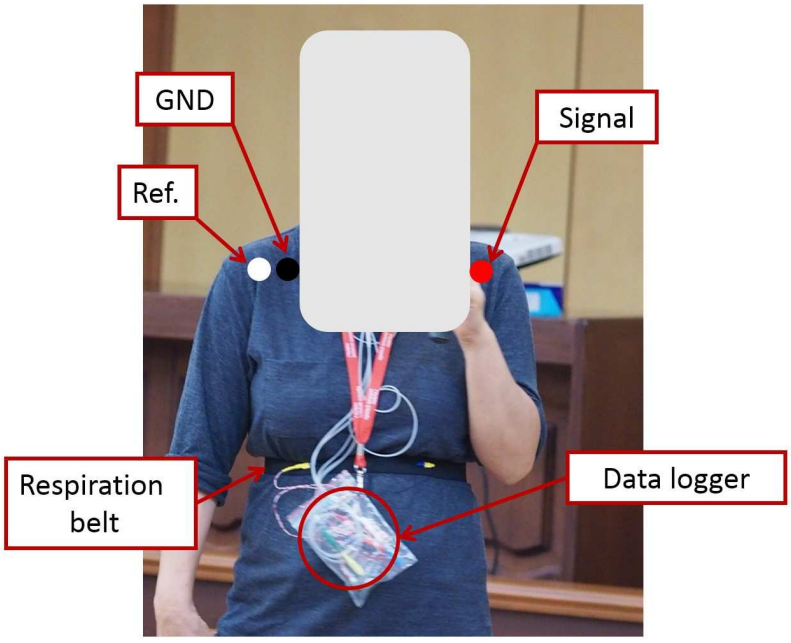
respiration belt placed around the chest. Figure 3.1 shows a custom-made respiration belt. A conductive rubber cord (https://www.adafruit.com/product/519) was attached to an elastic belt, whereby the resistance of the conductive rubber cord changed according to its length. When a participant inhaled, both the belt and the conductive rubber cord were, therefore, stretched, thus increasing the impedance and changing the voltage measured across the conductive rubber cord. The supply voltage for the cord was 3.3V, and a 1kΩ potential divider was connected to the cord so that the voltage range was suitable for our data loggers. Figure 3.2 shows the recording setup.

The respiration belt and the electrodes were connected to an 8-channel portable biosignal data logger powered by a rechargeable coin cell battery. The data logger sampled the signals at 1 kHz with 24-bit resolution and saved the respiratory and ECG data onto a micro-SD card. The data logger also recorded timestamps onto the micro-SD card in order to guarantee the synchronisation between the devices during both the rehearsal and the performance. The respiratory signals were then downsampled to 10 Hz using the 'resample' function in Matlab which includes an anti-aliasing filter, whereby the 'P' and 'Q' values for the resample function were set to 1 and 100 respectively (new sampling frequency = original sampling frequency * P / Q). [2] The HRV was estimated from the ECG data using the MF-HT algorithm.

[2]By using the resample function to perform the downsampling, the respiratory signals were first low-pass filtered using an FIR low-pass filter of order 10 (the default value) with the cut-off frequency set to 10 Hz (cut-off frequency = original sampling frequency / max(P,Q)), to prevent anti-aliasing, and the low-pass filtered respiratory signals were next downsampled from 1 kHz to 10 Hz by performing decimation by a factor of Q (100).



(a)



(b)

Figure 3.2: **Recording setup**. *(a)* An 8-channel data logger connected to three Ag/AgCl ECG monitoring electrodes and a custom-made respiration belt. *(b)* Positions of the three ECG electrodes and the respiration belt on a participant. The 8-channel portable biosignal data logger was powered by a rechargeable coin cell battery. The respiratory and ECG data were saved onto a micro-SD card.The respiration of each participant was recorded using the respiration belt placed around the chest. The ECG was recorded with the three Ag/AgCl ECG monitoring electrodes placed on the skin, just below the collar bone. The circles in *(b)* show the positions of the three electrodes on a participant, and their colours correspond to the colours of the cables in *(a)*.

Figures 3.3–3.5 shows respiratory and ECG signals of the conductor and the subset of eight members of the choir recorded during the rehearsal and the performance. Observe slow oscillations in the respiratory signals of the members of the choir in both the situations, which is due to their long exhalation while singing the music piece. Note that both the respiratory and ECG signals of M6 during the rehearsal was respectively corrupted and saturated, and the ECG signal of M8 during the performance saturated. Since the aim of this study is to quantify synchrony in respiration and HRV during both the rehearsal and the performance between the same members of the choir, all the recordings of M6 and M8 were excluded from this study.

In order to determine signal-to-noise ratio (SNR) of the respiratory signals, respiratory signals with frequencies lower than 1 Hz were deemed 'signal', and respiratory signals with frequencies over 1 Hz were deemed 'noise'. This is because the normal breathing rate in adults varies between 12 and 15 breathes per minutes (0.2–0.25 Hz) [87], and the breathing rate of members of the choirs were presumably markedly lower than 0.2 Hz due to their long exhalation while singing. To determine SNR of the ECG signals, ECG signals with frequencies between 1–30 Hz were deemed 'signal', and ECG signals with frequencies over 30 Hz were deemed 'noise' [90, 91]. Figure 3.6 shows SNRs of the respiratory and ECG signals of the conductor and the members of the choir. Note that respiratory and ECG data of M6 and M8 were excluded from this study. Observe high SNRs ($>$ 12 dB) of the respiratory signals of the conductor and M1–M5, moderate SNRs ($>$ 4 dB) of the ECG signals of the conductor and M1–M5 during both the situations, and very low SNR (2 dB, see the circle) of the ECG signal of M7 during the performance. As a consequence, HRV signals of the conductor and M1–M5 during both the situations were successfully extracted from their ECG, while HRV signal of M7 during the performance could not be obtained. Thus, all the data of M7 were also excluded from this study. Figures 3.7 & 3.8 show HRV signals of the conductor and the selected five members of the choir during respectively the rehearsal and the performance. Observe distinct variations in the HRV of the conductor and the selected five members of the choir during both the situations.

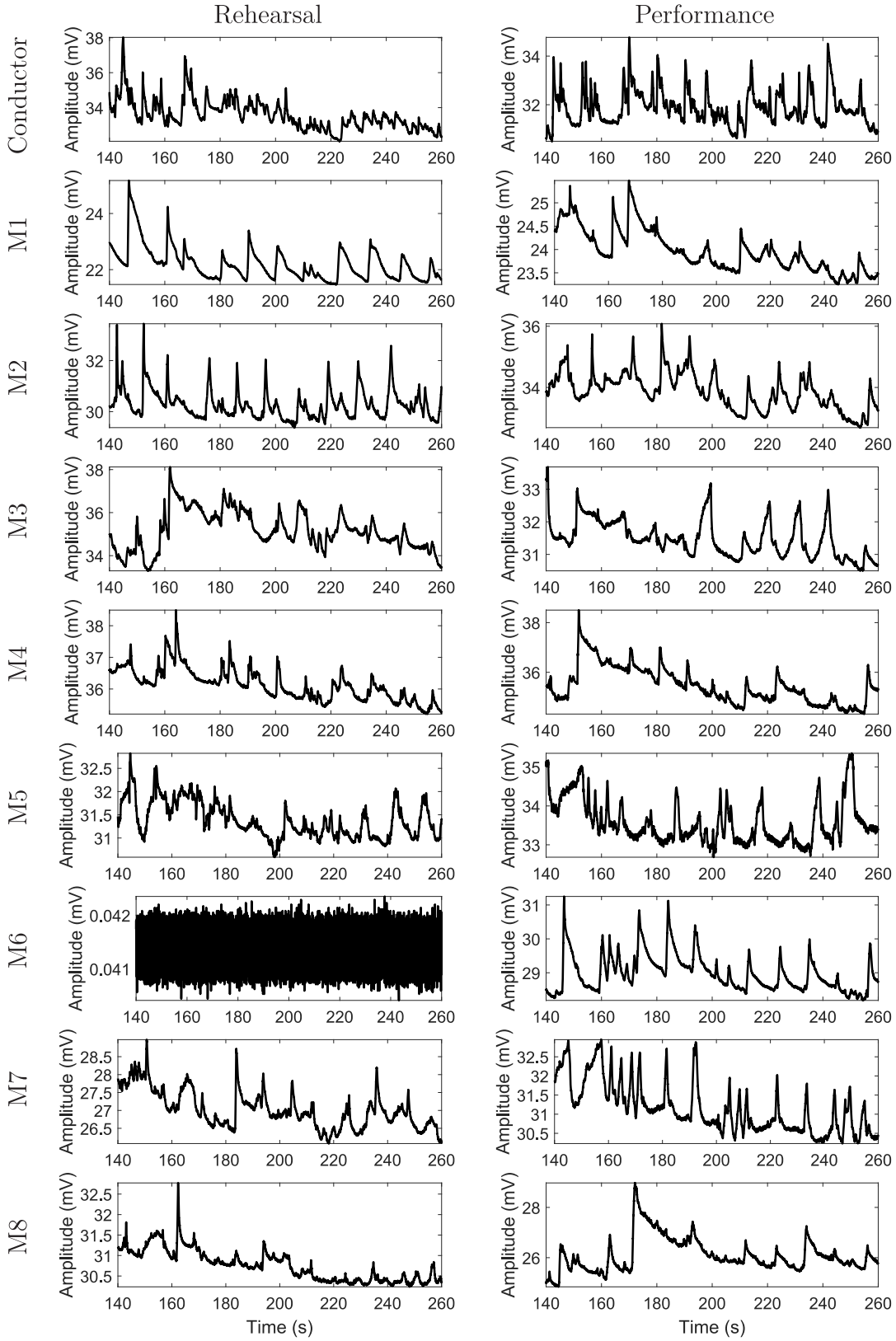


Figure 3.3: **Respiratory signals of the conductor and the subset of eight members of the choir**. For brevity each member of the choir is denoted Mx, with x denoting the member number. Respiratory signal of M6 recorded during the rehearsal was corrupted (left panel, seventh row).

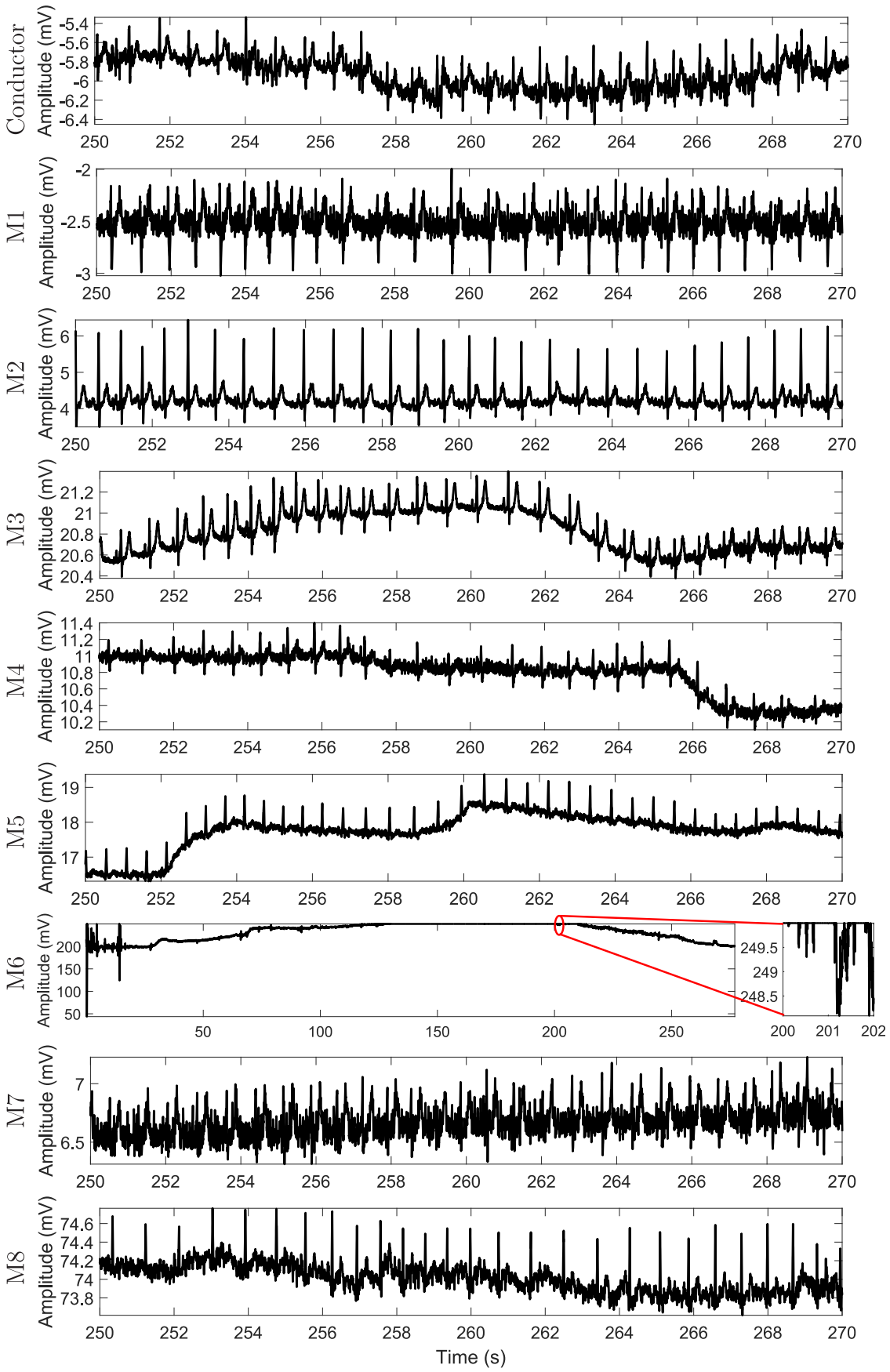


Figure 3.4: **The ECG signals of the conductor and the subset of eight members of the choir recorded during the rehearsal**. For brevity each member of the choir is denoted Mx, with x denoting the member number. The ECG signal of M6 saturated (seventh row).

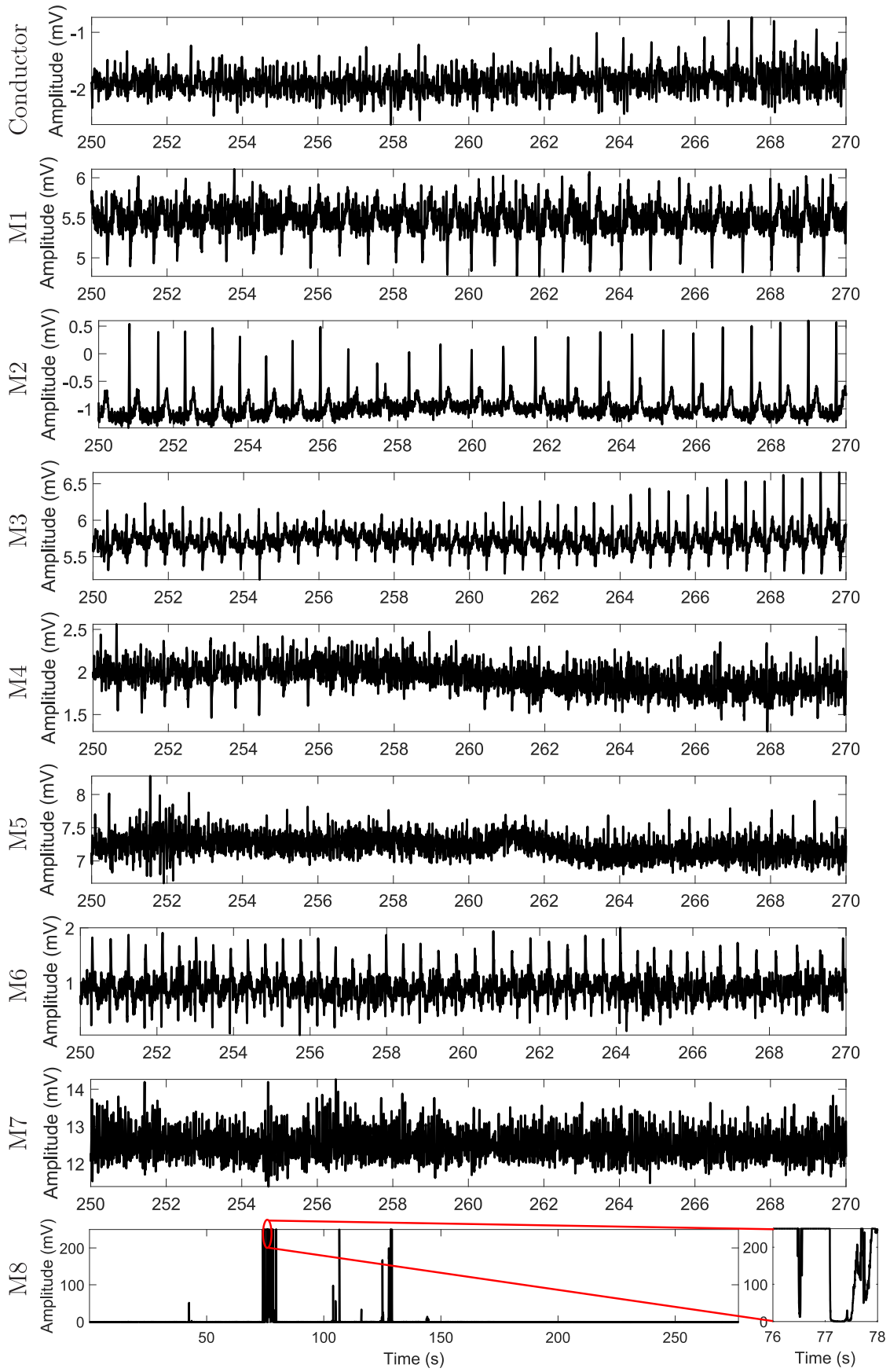


Figure 3.5: **The ECG signals of the conductor and the subset of eight members of the choir recorded during the performance**. For brevity each member of the choir is denoted Mx, with x denoting the member number. The ECG signal of M8 saturated (last row).

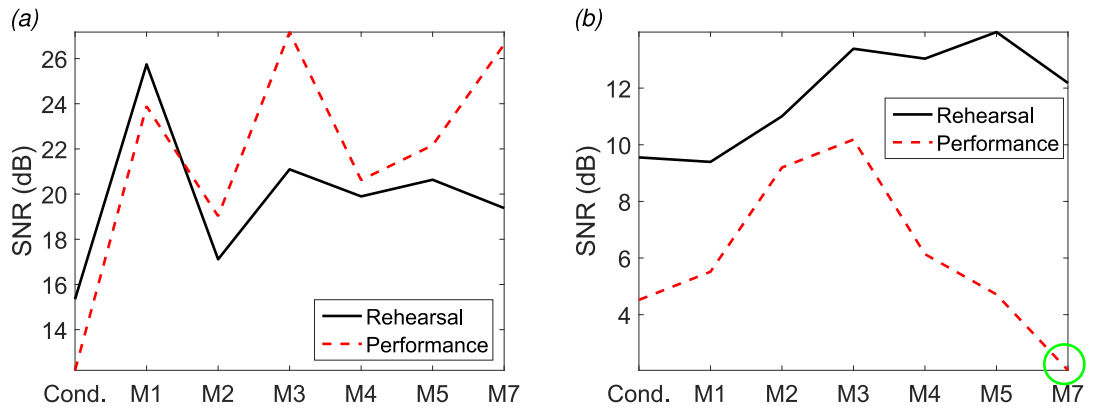


Figure 3.6: **The SNRs of the respiratory and ECG signals of the choir**. *(a)* The SNRs of the respiratory signals of the choir during the rehearsal and the performance. *(b)* The SNRs of the ECG signals of the choir during the rehearsal and the performance. For brevity the conductor is denoted Cond., each member of the choir is denoted Mx, with x denoting the member number. Observe that SNR of M7 during the performance was very low (2 dB).

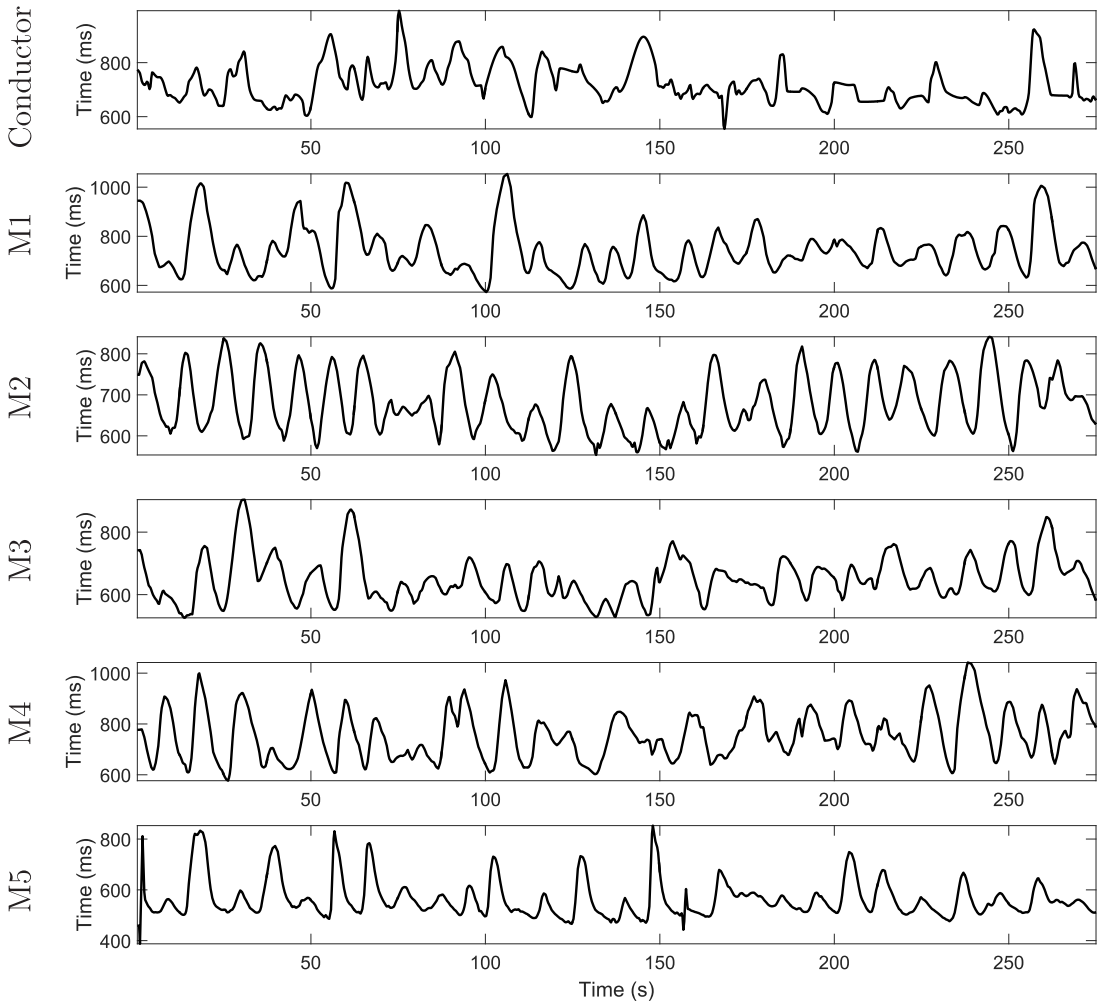


Figure 3.7: **The HRV signals of the conductor and the selected five members of the choir during the rehearsal**. For brevity each member of the choir is denoted Mx, with x denoting the member number. Observe high variations in the HRV signals of the conductor and the five members of the choir.

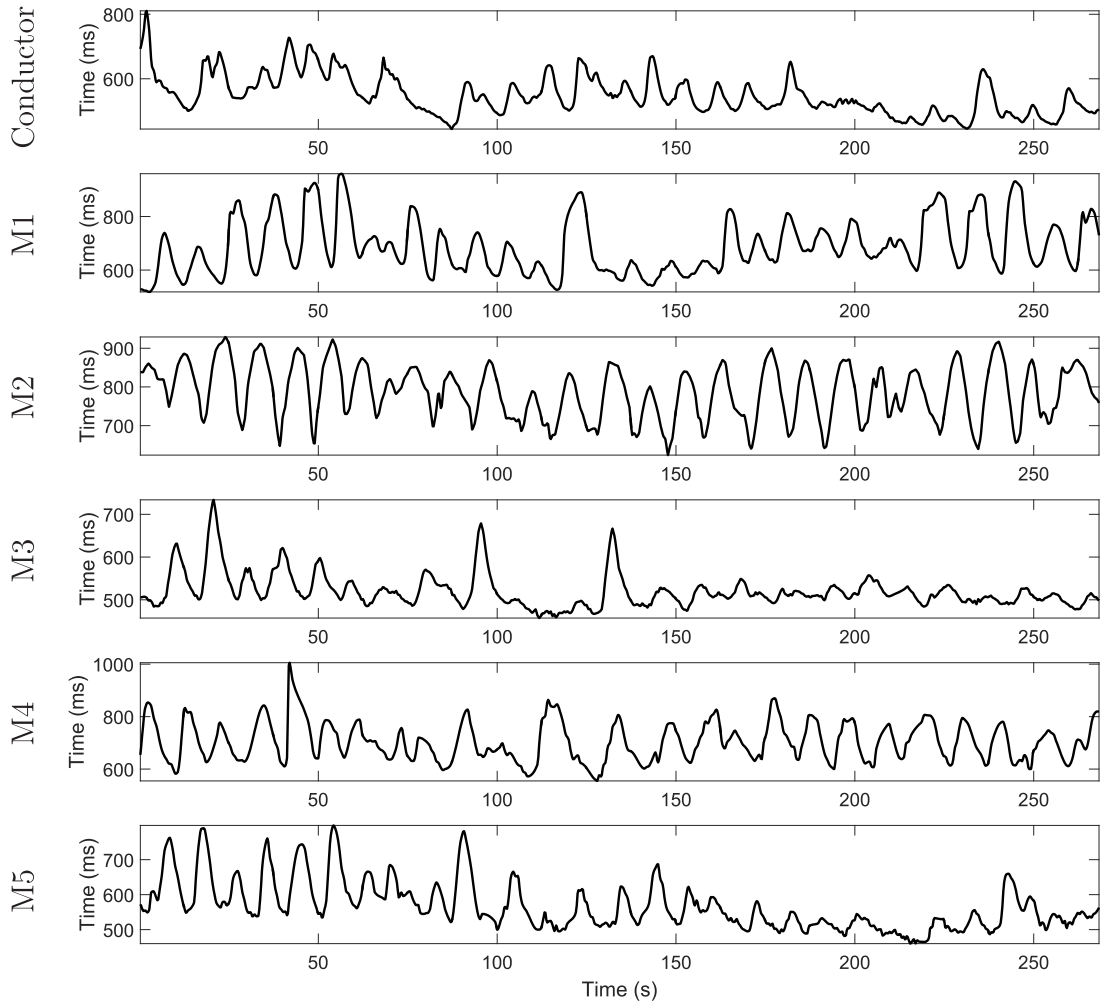


Figure 3.8: **The HRV signals of the conductor and the selected five members of the choir during the performance**. For brevity each member of the choir is denoted Mx, with x denoting the member number. Observe high variations in the HRV signals of the conductor and the five members of the choir.

Figures 3.9&3.10 show respectively respiratory and ECG signals of the five members of the audience, and Figure 3.11 shows SNRs of the respiratory and ECG signals of the five member of the audience. Observe high (> 13 dB) and moderate (> 5 dB) SNRs of respectively the respiratory and ECG signals. The HRV signals of the five members were successfully extracted from their ECG, as a result of the moderate SNRs, as shown in Figure 3.12. Observe subtle variations in the HRV of the five members of the audience.

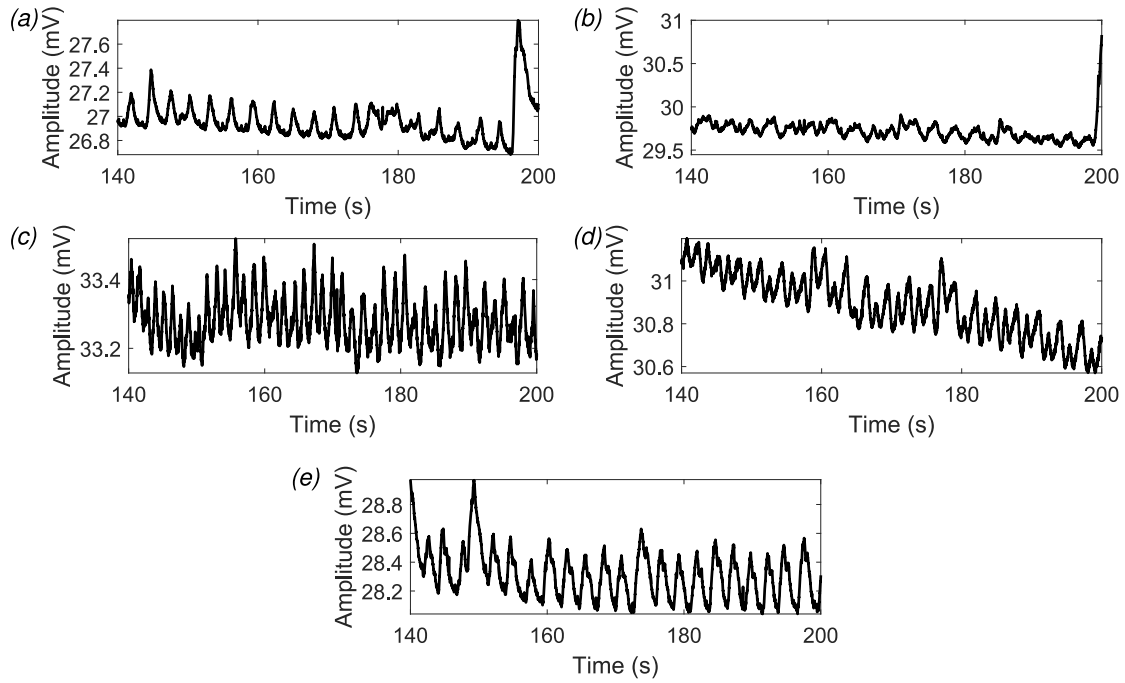


Figure 3.9: **Respiratory signals of the five members of the audience**. *(a–e)* Members 1–5 of the audience.

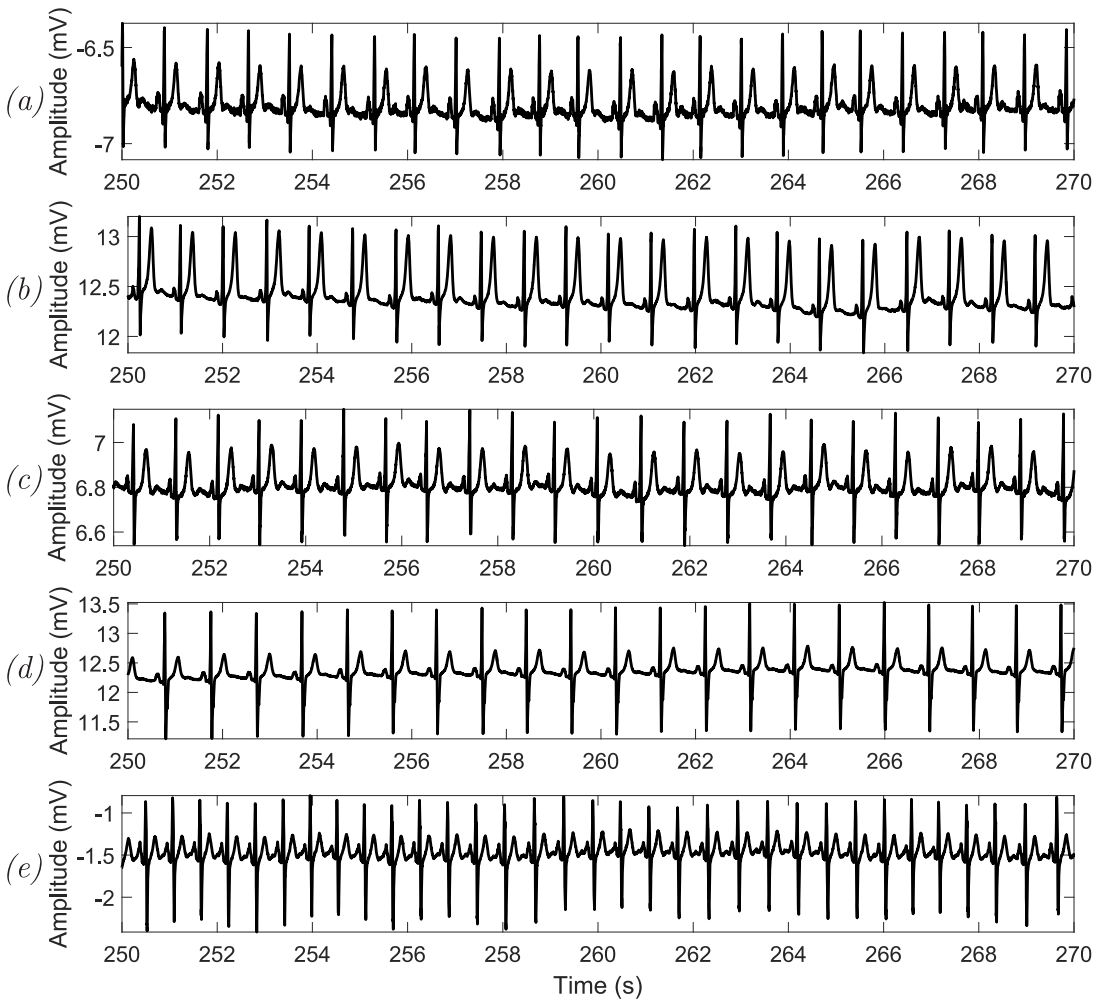


Figure 3.10: **The ECG signals of the five members of the audience**. *(a–e)* Members 1–5 of the audience.

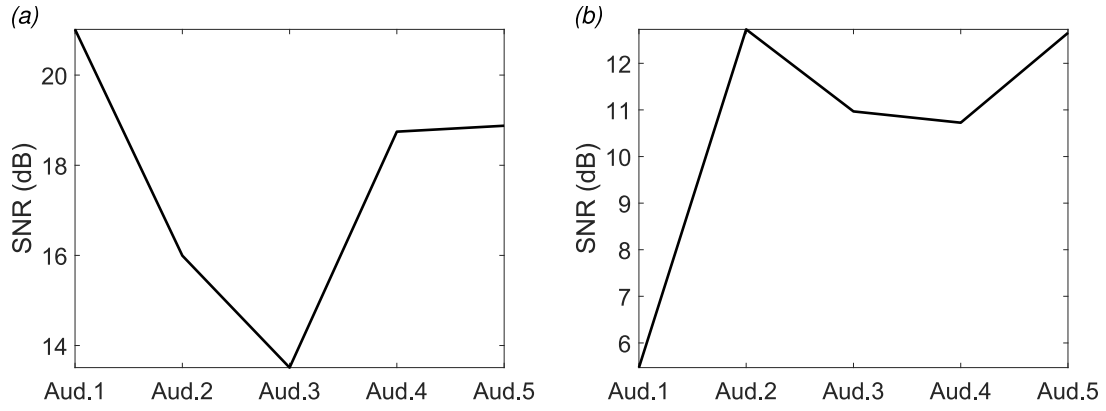


Figure 3.11: **The SNRs of the respiratory and ECG signals of the audience**. *(a)* The SNRs of the respiratory signals of the audience. *(b)* The SNRs of the ECG signals of the audience. For brevity each member of the audience is denoted Aud.y, with y denoting the member number. Observe high (> 13 dB) and moderate (> 5 dB) SNRs of respectively the respiratory and ECG signals.

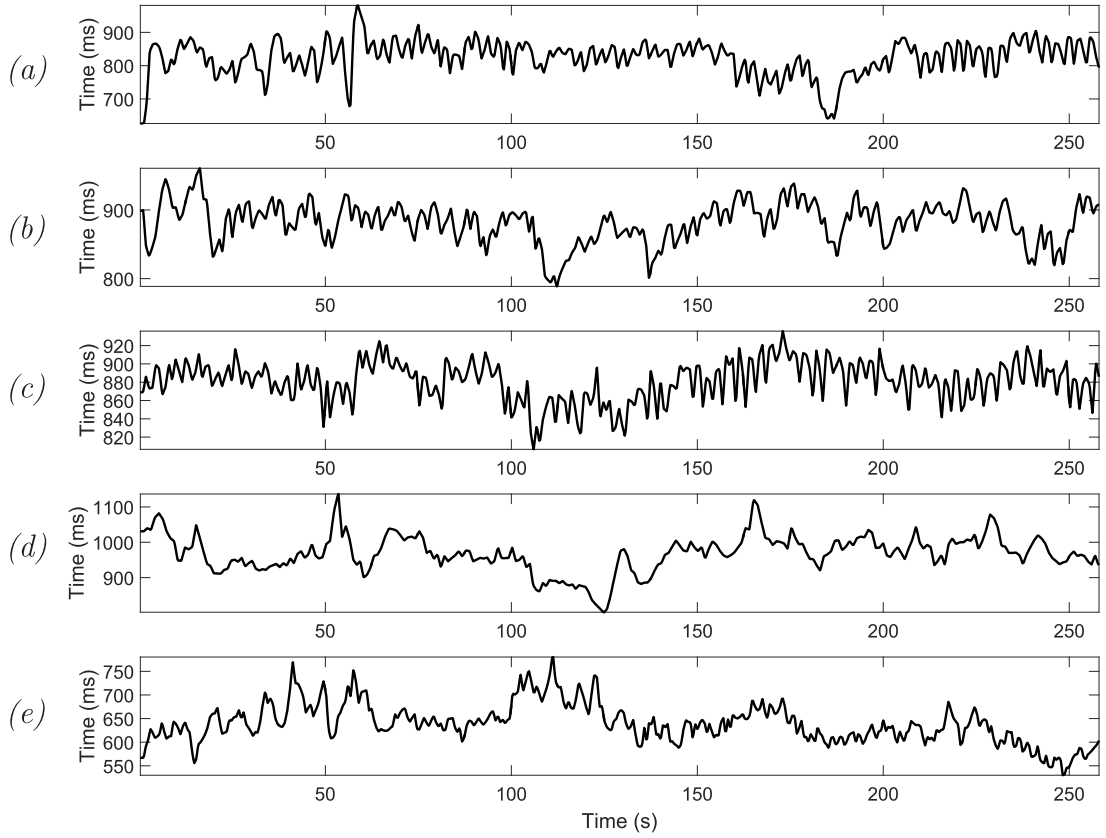


Figure 3.12: **The HRV signals of the five members of the audience**. *(a–e)* Members 1–5 of the audience. Observe subtle variations in the HRV signals of the five members of the audience.

3.4 Test for Wide-Sense Stationarity of the Respiratory and HRV signals

In order to test whether the respiratory and HRV signals are WSS and whether NA-MEMD should therefore be used for the data analysis, means and variances of all the signals were calculated using 10-second sliding windows with 5-second overlap (5-second increment).

3.4.1 Means of the Respiratory and HRV signals

Figures 3.13&3.14 show means of the respiratory signals of the choir during the rehearsal and the performance, and means of the respiratory signals of the audience during the performance, respectively. Figures 3.15–3.17 show means of the HRV signals of the choir during the rehearsal and the performance, and means of the respiratory signals of the audience during the performance, respectively. Variations of means over time indicate that the signals were not WSS and that NA-MEMD should be employed in the analysis.

3.4.2 Variances of the Respiratory and HRV signals

Figures 3.18&3.19 show variances of the respiratory signals of the choir during the rehearsal and the performance, and variances of the respiratory signals of the audience during the performance, respectively. Figures 3.20–3.22 show variances of the HRV signals of the choir during the rehearsal and the performance, and variances of the respiratory signals of the audience during the performance, respectively. The time-varying variances indicate that the signals were not WSS and that NA-MEMD should be employed in the analysis.

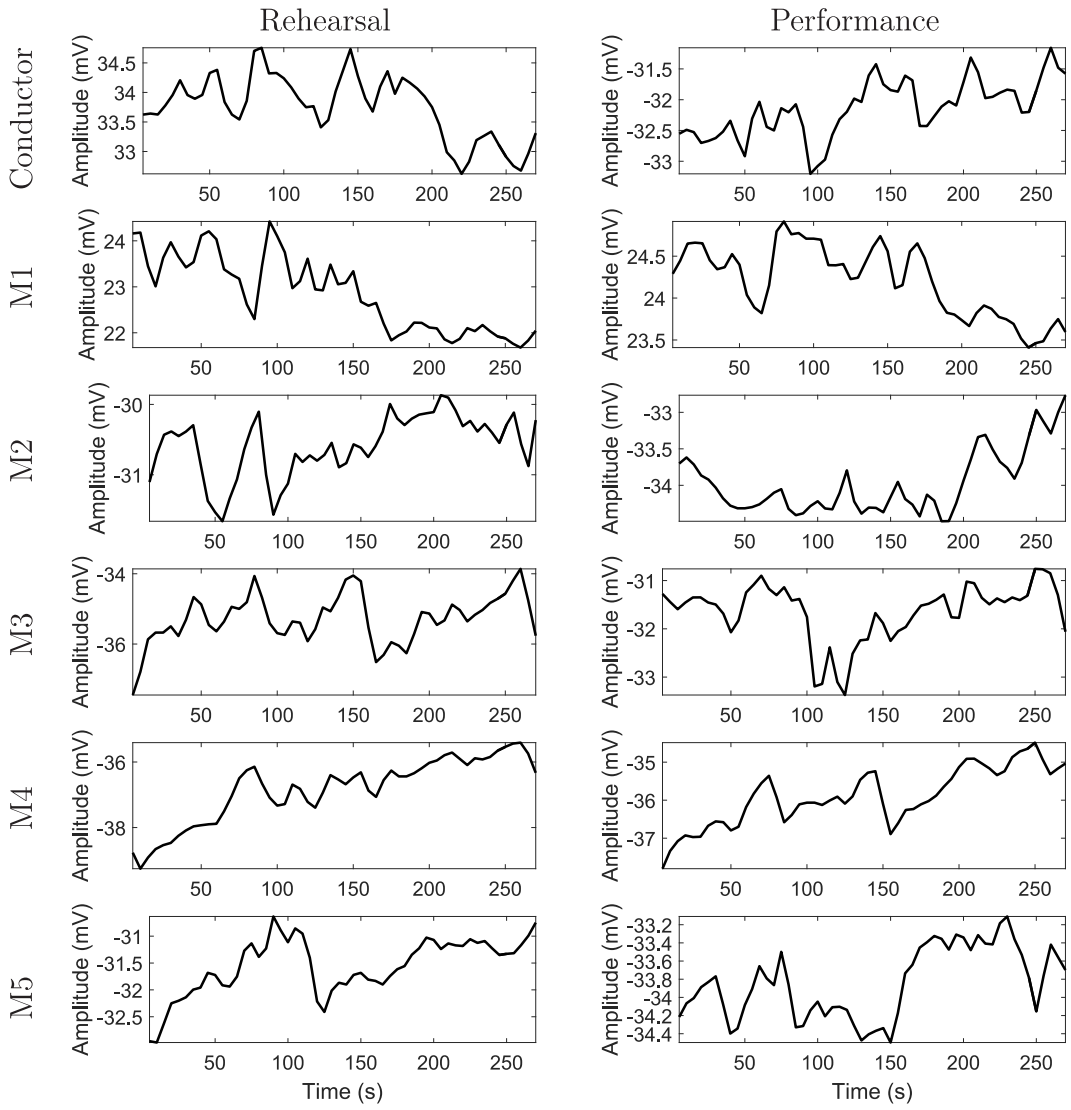


Figure 3.13: **Means of the respiratory signals of the conductor and the selected five members of the choir**. For brevity each member of the choir is denoted Mx, with x denoting the member number. The means were calculated using 10-second sliding windows with 5-second overlap (5-second increment).

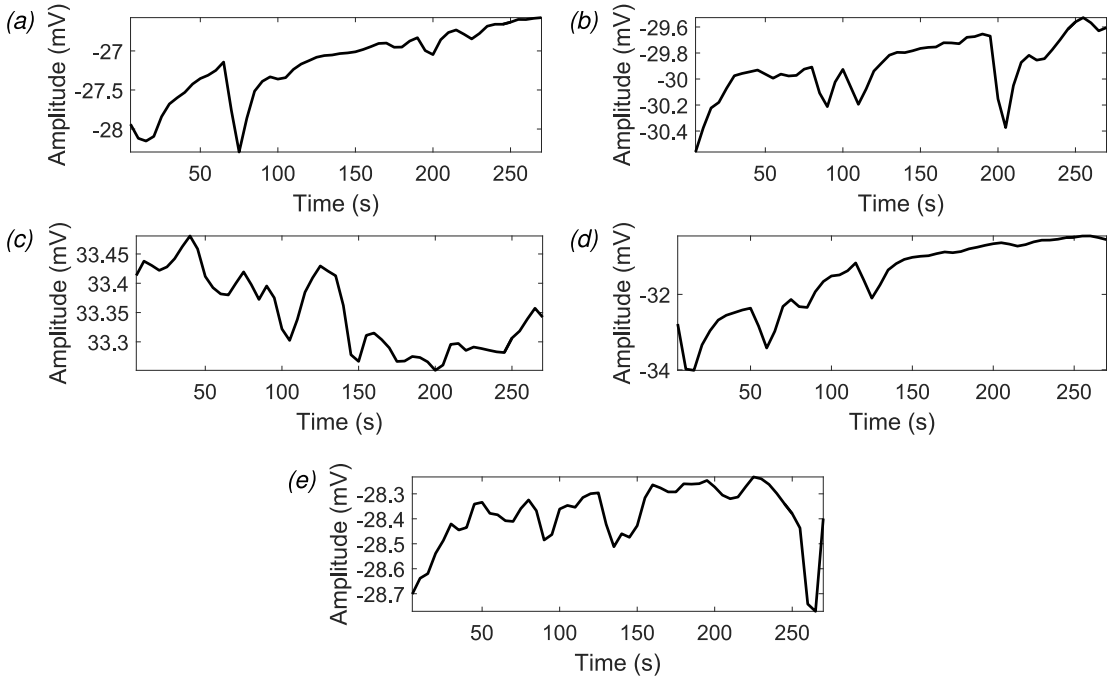


Figure 3.14: **Means of the respiratory signals of the five members of the audience**. *(a–e)* Members 1–5 of the audience. The means were calculated using 10-second sliding windows with 5-second overlap (5-second increment).

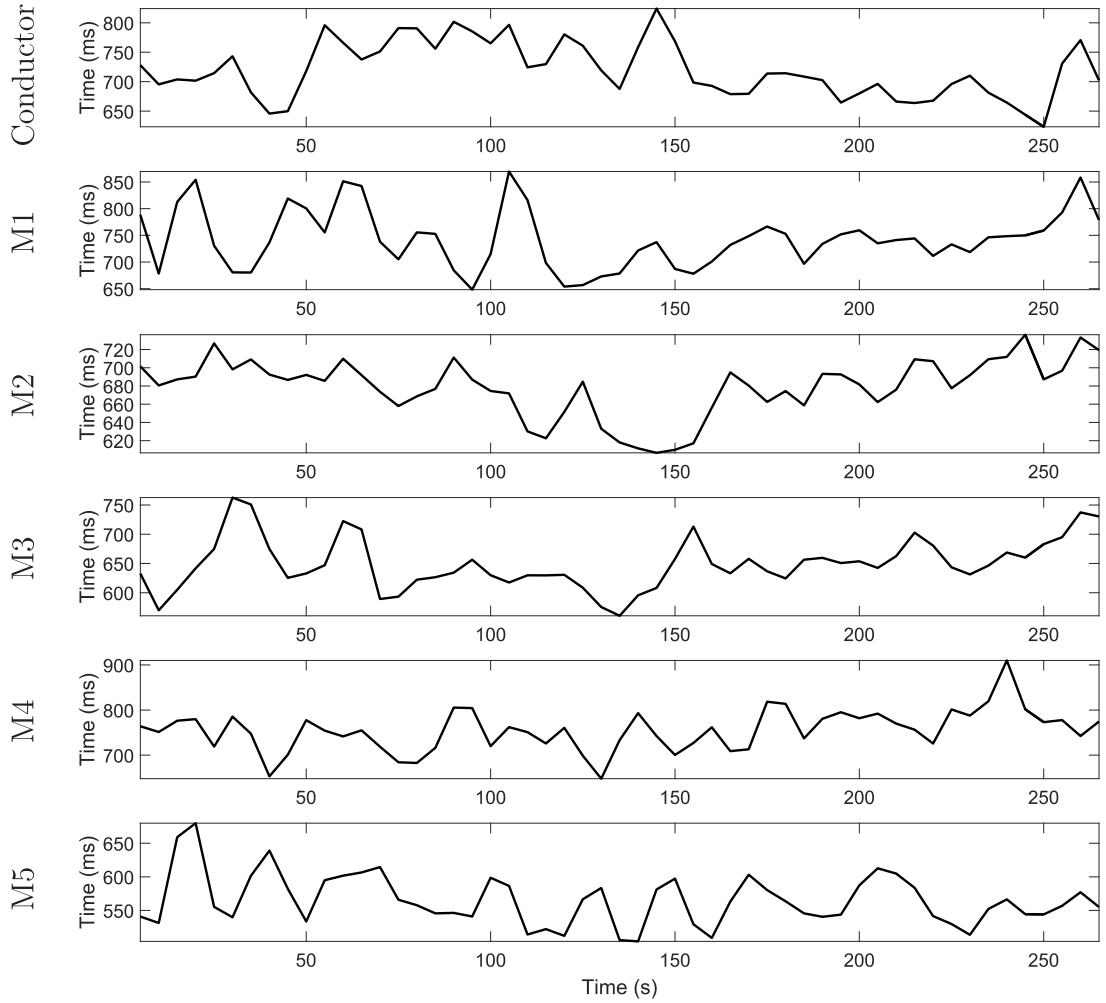


Figure 3.15: **Means of the HRV signals of the conductor and the selected five members of the choir during the rehearsal**. For brevity each member of the choir is denoted Mx, with x denoting the member number. The means were calculated using 10-second sliding windows with 5-second overlap (5-second increment).

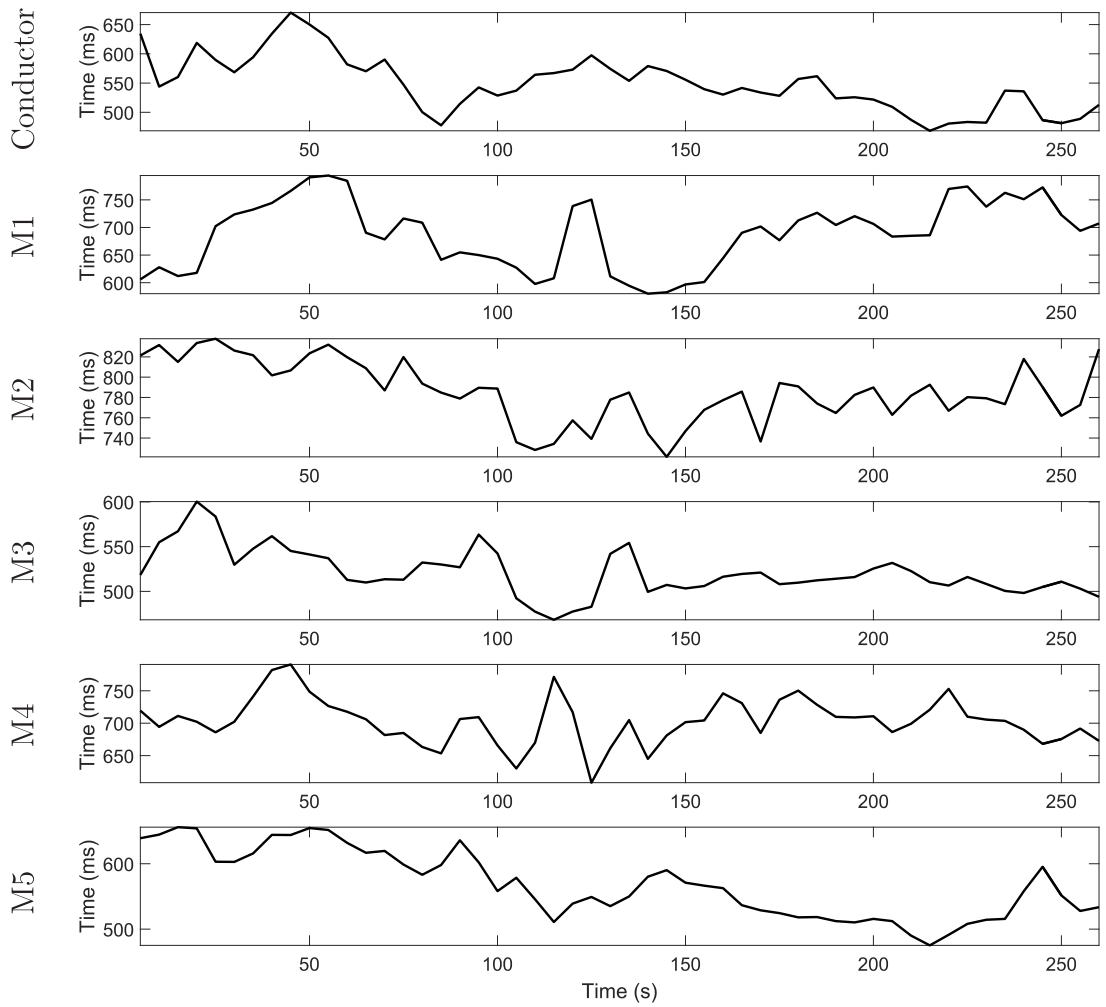


Figure 3.16: **Means of the HRV signals of the conductor and the selected five members of the choir during the performance**. For brevity each member of the choir is denoted Mx, with x denoting the member number. The means were calculated using 10-second sliding windows with 5-second overlap (5-second increment).

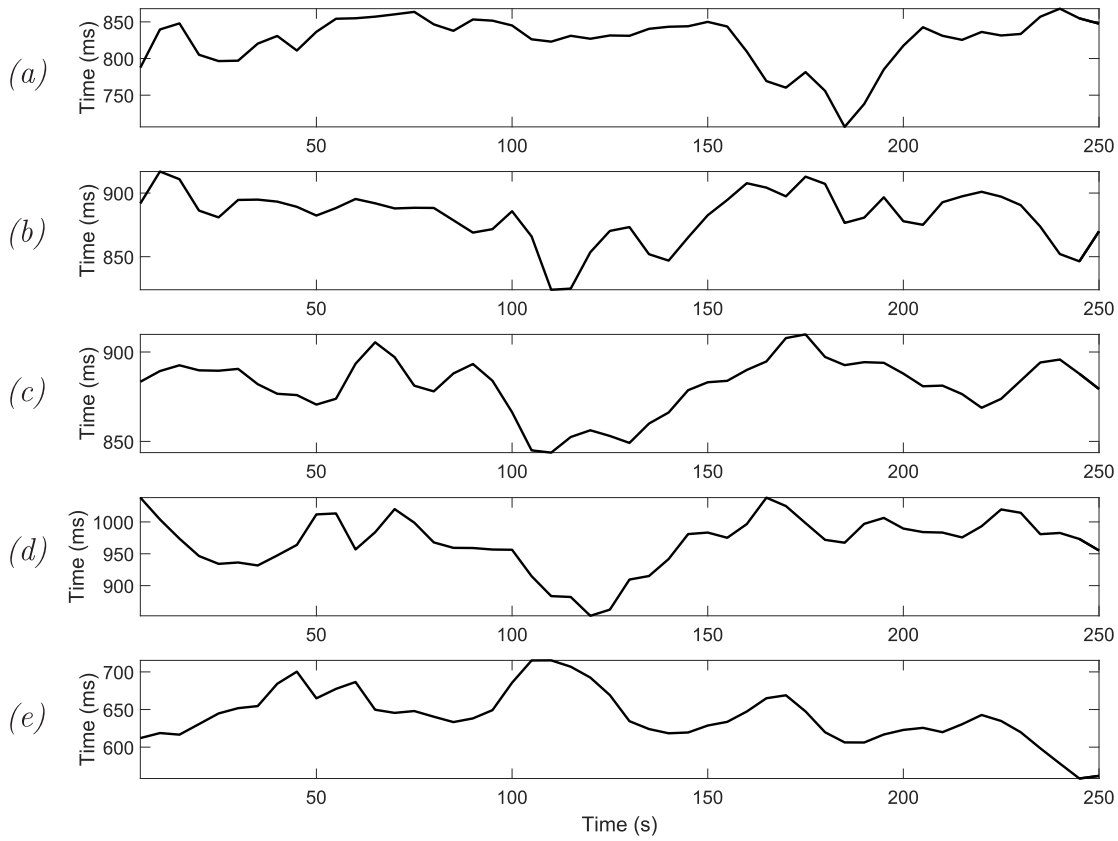


Figure 3.17: **Means of the HRV signals of the five members of the audience**. *(a–e)* Members 1–5 of the audience. The means were calculated using 10-second sliding windows with 5-second overlap (5-second increment).

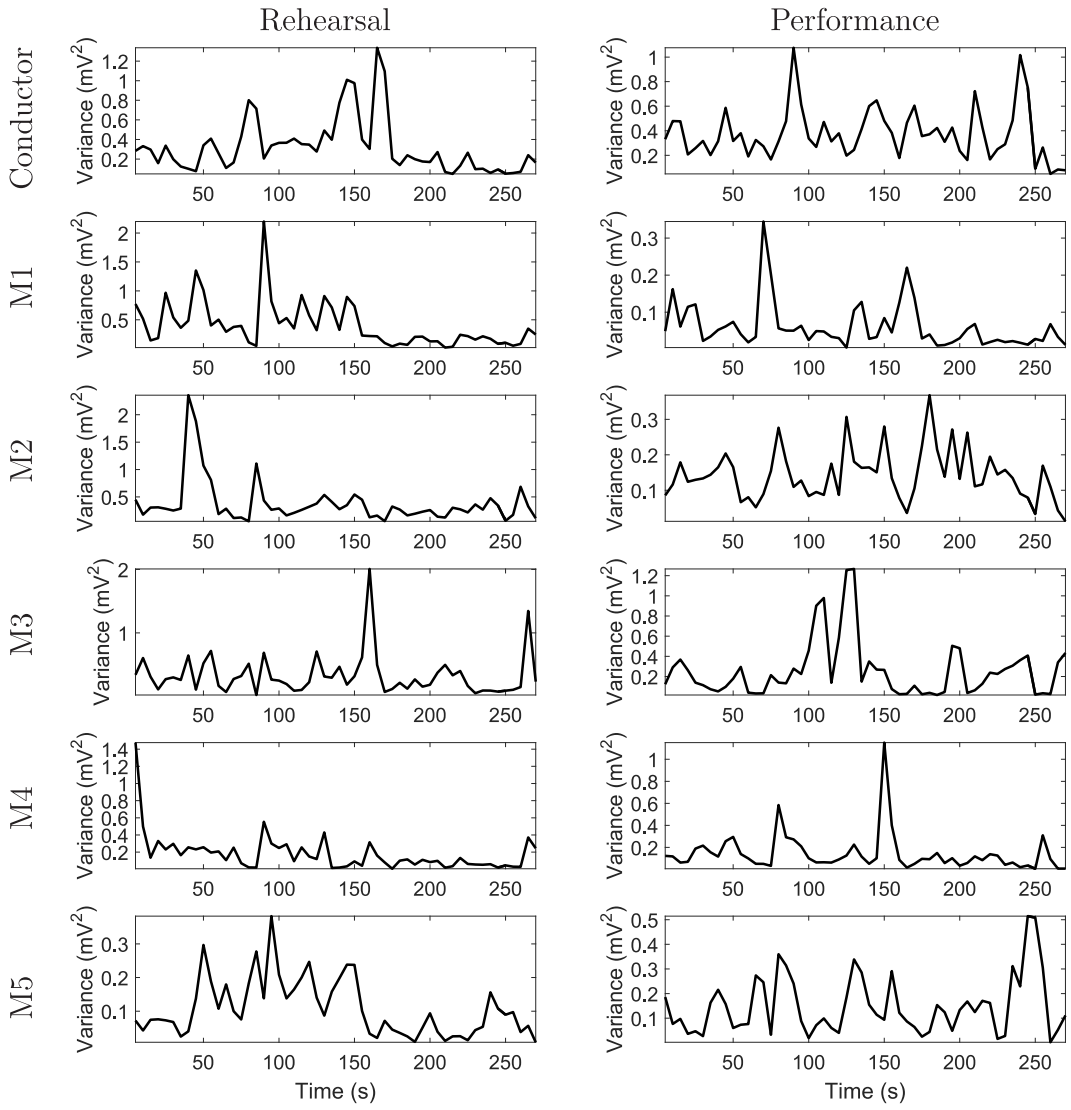


Figure 3.18: **Variances of the respiratory signals of the conductor and the selected five members of the choir**. For brevity each member of the choir is denoted Mx, with x denoting the member number. The means were calculated using 10-second sliding windows with 5-second overlap (5-second increment).

3.5 Synchrony Analysis

The PSI and COH indices of the respiratory and HRV signals were estimated in six categories as follows:

1. Among the selected five members of the choir (M1–5) during the rehearsal – within-group estimation.
2. Between the conductor and the selected five members of the choir (M1–5) during the rehearsal – between-group estimation.
3. Among the selected five members of the choir (M1–5) during the performance

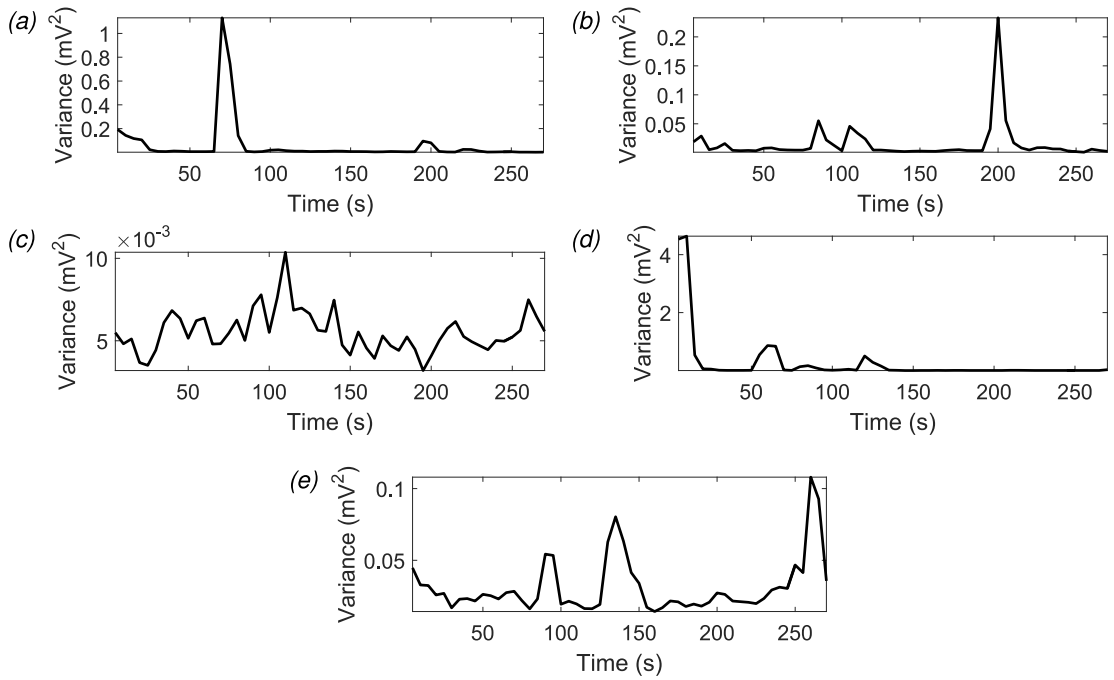


Figure 3.19: **Variances of the respiratory signals of the five members of the audience**. *(a–e)* Members 1–5 of the audience. The variances were calculated using 10-second sliding windows with 5-second overlap (5-second increment).

– within-group estimation.

4. Between the conductor and the selected five members of the choir (M1–5) during the performance – between-group estimation.
5. Among the five members of the audience during the performance – within-group estimation.
6. Between the conductor and the five members of the audience during the performance – between-group estimation.

For the categories (1)–(4), the respiratory (or HRV) signals of the conductor (channel 1) and the five members of the choir (channels 2–6) during both the rehearsal and the performance were used to form 6-channel data which was decomposed using NA-MEMD with 10 separate artificial WGN channels. For the categories (5) and (6), channels 2–6 contained data recorded from the five members of the audience, and the decomposition was carried out in the same manner as for the categories (1)–(4). It should be noted that in all the categories NA-MEMD was applied to 6-channel respiratory data and 6-channel HRV data separately.

The IMFs produced by the NA-MEMD with indices 3–7 of the 6-channel multivariate HRV signal of choir members contained the physically meaningful frequency range

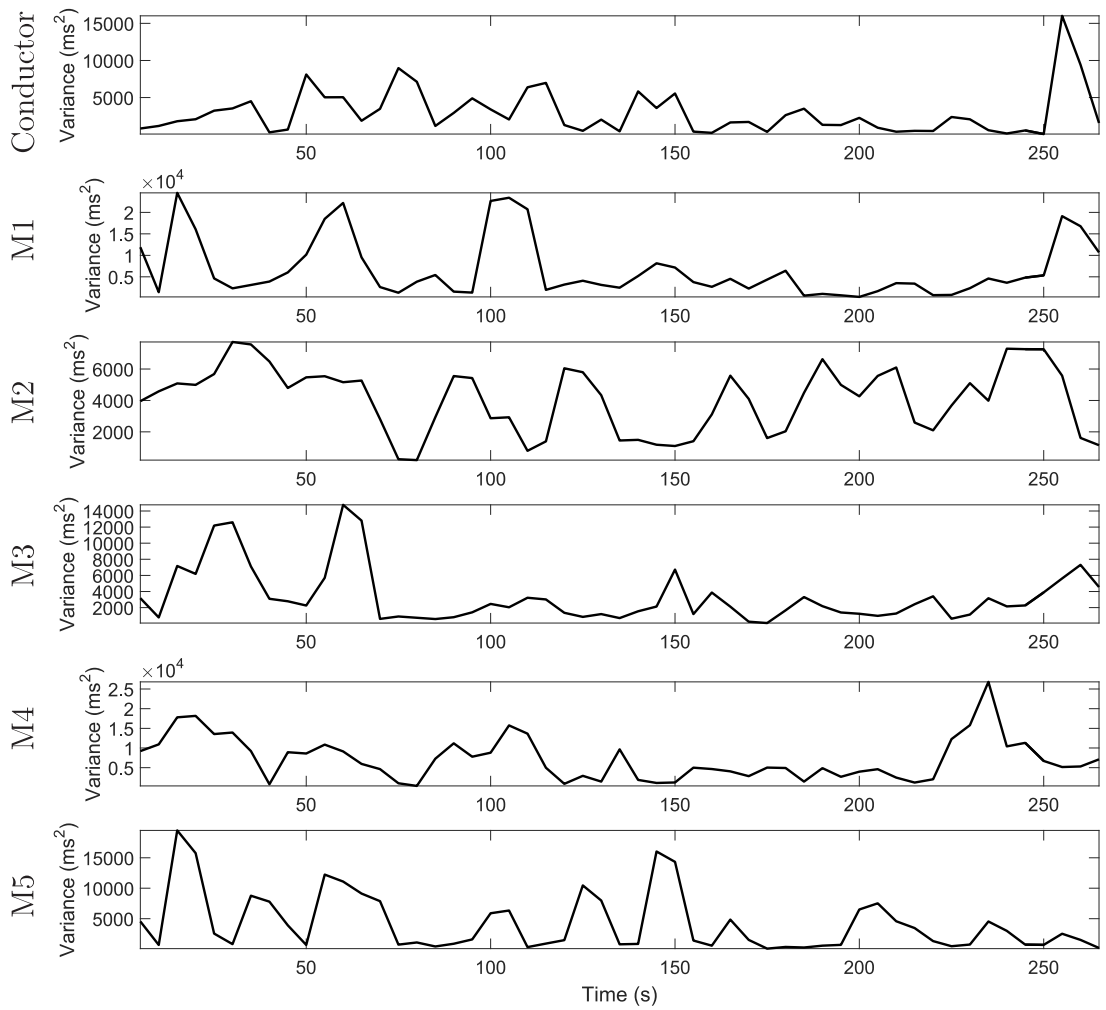


Figure 3.20: **Variances of the HRV signals of the conductor and the selected five members of the choir during the rehearsal**. For brevity each member of the choir is denoted Mx, with x denoting the member number. The variances were calculated using 10-second sliding windows with 5-second overlap (5-second increment).

0.04–0.4 Hz, that is, exactly the LF/HF frequency band of HRV. For convenience the same band in IMF indices 5–9 of respiration has been identified and used. The full band of interest in both the HRV and respiration data was produced by summing up the corresponding IMFs, in order to obtain the desired scale in data. The PSI and COH among the members of the choir (and the audience) were obtained by averaging PSI and COH values calculated from every combined-IMF pair of the data channels 2–6 (choir only), while PSI and COH between the conductor and each member of the choir (and the audience) were obtained by averaging the PSI and COH values between the combined-IMF of channel 1 (conductor) and combined-IMF of channels 2–6 (choir). The PSI indices between the combined-IMFs of the noise channels were also estimated in order to provide the PSI of random signals (i.e. noise) as a

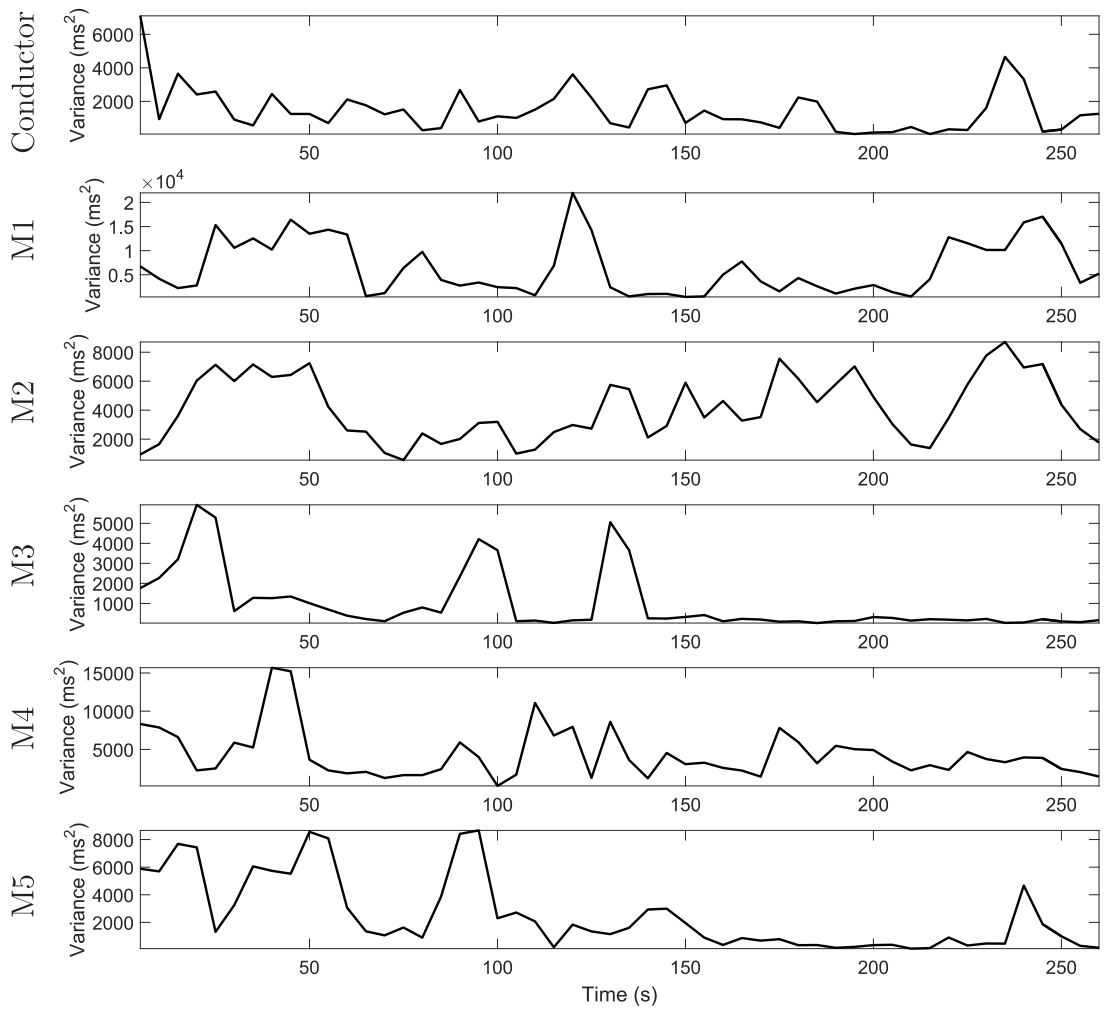


Figure 3.21: **Variances of the HRV signals of the conductor and the selected five members of the choir during the performance**. For brevity each member of the choir is denoted Mx, with x denoting the member number. The variances were calculated using 10-second sliding windows with 5-second overlap (5-second increment).

benchmark. For the coherence analysis, the power spectral densities were estimated using the MVAR model of order 3 for the combined IMF of the HRV signals of both the choir and the audience, and of orders 1 and 2 respectively for the combined IMF of the respiratory signals of the choir and the audience. These orders of the MVAR models were employed, because the power spectral densities estimated using the MVAR models with the chosen orders exhibited physically meaningful peaks in coherence in the LF/HF band in the IMFs of both the HRV and respiratory signals (see Section 3.6.2).

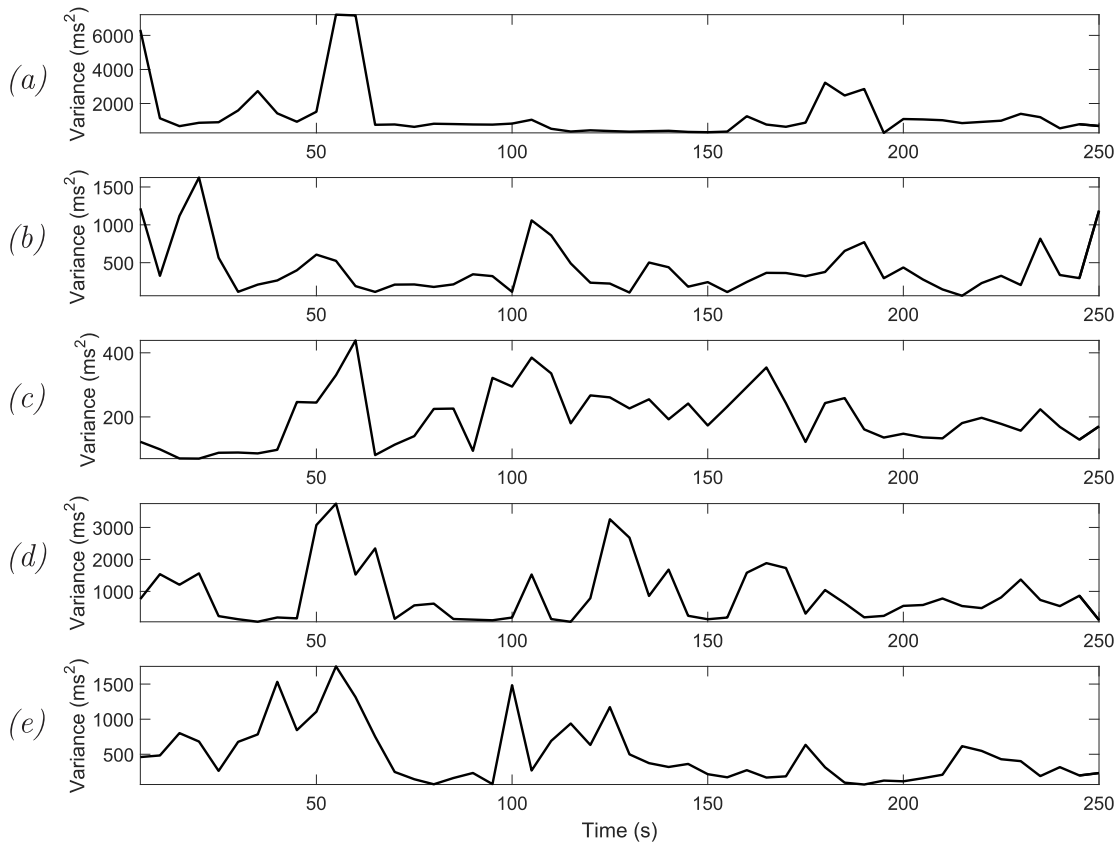


Figure 3.22: **Variances of the HRV signals of the five members of the audience**. *(a–e)* Members 1–5 of the audience. The variances were calculated using 10-second sliding windows with 5-second overlap (5-second increment).

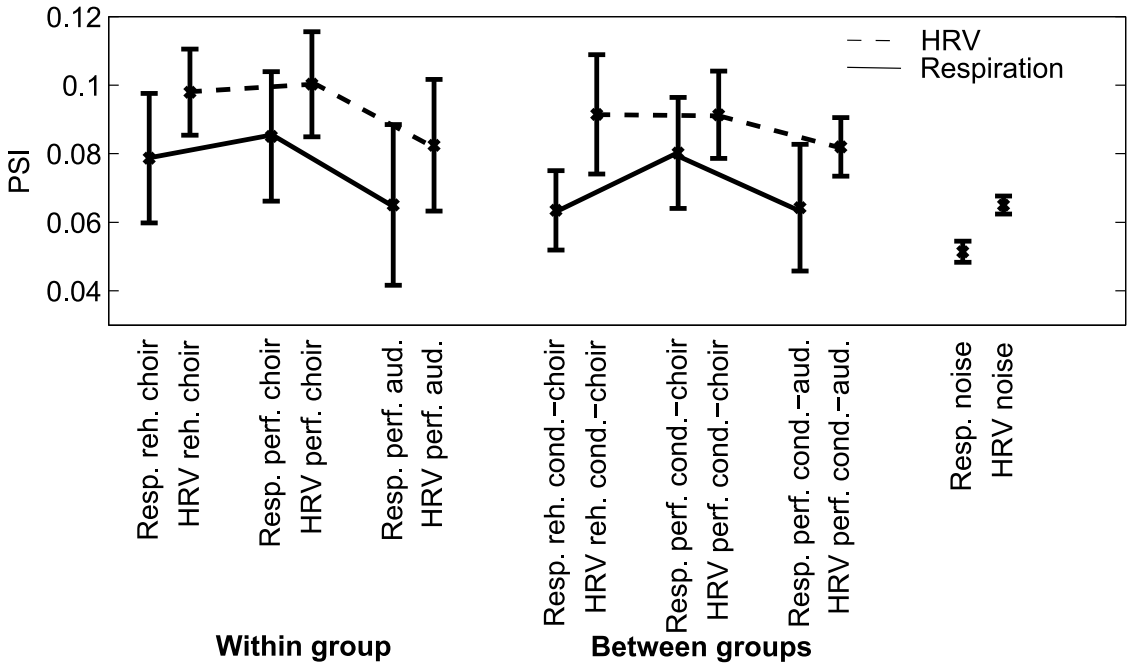


Figure 3.23: **The PSI of the respiratory and HRV signals within the same subject group and between the subject groups**. For brevity Resp.=Respiration, reh.=rehearsal, perf.=performance, aud.=audience and cond.=conductor. The PSI of noise was calculated from the combined-IMFs of the artificial noise channels.

3.6 Results of the Analysis

Inter-channel dependence in the respiratory and HRV signals were quantified using intrinsic phase synchrony and the proposed intrinsic coherence measure.

3.6.1 Phase Synchrony

Figure 3.23 shows the PSIs of the respiratory and HRV data for the 6 considered categories, estimated from 50 realisations of NA-MEMD. For each trial of NA-MEMD, the Z-test[3] [92] at a significance level of 0.05 was performed, in order to reveal statistical differences in the respiratory and HRV PSI values between the categories.

Observe that in the performance conditions, both the respiratory and HRV PSIs among the choir members significantly increased compared to the rehearsal. This indicates that the breathing rhythms, and by virtue of RSA the cardiac activities

[3]The Z-test assesses the probability that there is no effective difference between the means of two populations – the means of respiratory or HRV PSI values of the different categories.

too, of the choir members exhibited stronger dynamic coupling which was reflected in an increase in the synchrony of their physiological responses.
Hypothesis #1: The intrinsic synchrony of physiological responses of choir members is a signature of increased coordination between performers and their enhanced mental awareness in various types of performance.

Observe that the values of PSI indices of the respiratory and HRV signals among the audience were lower than those of the choir, both during the rehearsal and the performance.

Figure 3.23 also shows that the respiratory and HRV PSIs between the conductor and the members of the choir were lower than PSIs among the members of the choir, in both the rehearsal and performance scenarios.
Hypothesis #2: The physiological responses of the conductor were modulated by both the piece of music performed (as indicated by a degree of coupling with the choir) and the physical activity involved in the act of conducting.

Figure 3.23 highlights that PSIs between human subjects were significantly higher than noise PSIs, thus indicating that human PSIs were not random; also the PSIs of HRV exhibited similar patterns to those present in the respiratory signal – a consequence of RSA.

3.6.2 Coherence analysis

Figure 3.24 illustrates the coherence analysis of respiration and HRV, estimated for the 6 categories considered. Figure 3.24 *(a)* shows respiratory coherence among the members of the choir during both the rehearsal and performance, together with those among the members of the audience.

Observe the peaks in the frequency range 0.2–0.35 Hz which indicate the coherence in breathing at normal rates. The members of the audience breathed faster than the choir, resulting in coherence at higher frequencies. Conversely, owing to long exhalation while singing, the choir exhibited high coherences in the low frequency

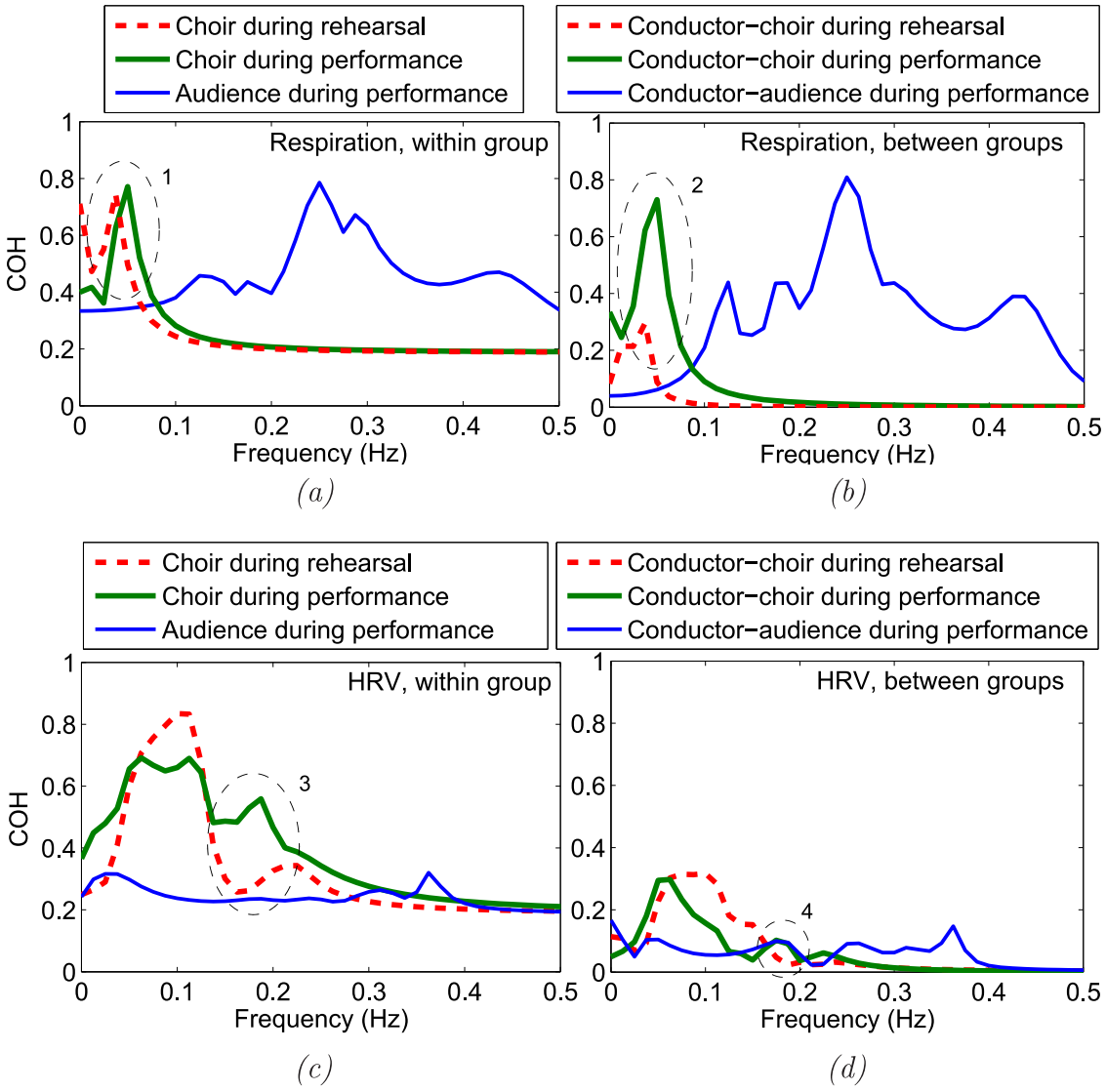


Figure 3.24: **The COH values of the respiratory and HRV data.** *(a)* Respiratory COH within the same group. *(b)* Respiratory COH between groups. *(c)* COH of HRV within the same group. *(d)* COH of HRV between groups.

region of 0.04–0.05 Hz (ellipse 1).

Remark #1: The coherence of the choir during the performance was similar to that during the rehearsal, while the coherence between between the conductor and the members of the choir was markedly higher (see Figure 3.24 *(b)*, ellipse 2). This indicates a higher degree of cooperation during the performance, when the stakes are high and both the conductor and the choir feel the pressure and thus the urge to work extra hard in order to produce a spot on performance.

Figure 3.24 *(c)* shows HRV coherences among the members of the choir during the rehearsal and performance, and those among the members of the audience during

the performance.

Remark #2: The higher COH values among the choir in the HF band (0.15–0.4 Hz) of HRV during the performance, compared to the rehearsal, can be attributed to the RSA (ellipses 3 & 4). This indicates a higher degree of cooperation mediated by the synchronised respiration, additionally notice how virtually no coherence is detected in the cardiac activity of the members of the audience.

3.7 Summary

This study has employed intrinsic phase synchrony and intrinsic coherence to quantify phase and amplitude relationships in the respiratory and cardiac signals of the choir, the conductor and the audience, in order to investigate degrees of cooperation during a social task. The results have shown that each group is represented by a distinctive degree of joint synchronisation of participants' physiological responses, caused by the act of performance. While the choir has demonstrated a marked increase in coordination from the rehearsal to the performance, less agreement has been observed between the subject groups (choir, conductor, audience), with the lowest coordination observed for the audience. This can be attributed to each group experiencing the performance in different physical and mental ways, as exemplified by the lower synchronisation between the groups. On the signal processing side, it has been shown that intrinsic phase synchrony has captured phase relationship of both physiological signals in all situations effectively, yielding a meaningful and straightforward to interpret data association metric. The coherence effects between the sympathetic and parasympathetic nervous systems in the participants, primarily mediated by respiration, has also been illuminated via the various degrees of coherence in the LF band of the HRV signals of the choir during both the scenarios and the increase in coherence in the HF band of HRV signals of the choir during the performance; these could not be found using intrinsic phase synchrony. Both the considered intrinsic measures have designated a quantitative approach to assessing joint endeavours, and have paved the way for mathematical characterisation of cooperative physiological systems across human activities. Note that this work provides time-averaged PSI and COH in order to investigate average degrees of physiologi-

cal coupling during the whole collaborative tasks. The next chapter focuses on the quantification of time-varying dependence of the respiratory and HRV signals.

Chapter 4

Quantifying Team Cooperation Through Intrinsic Multi-scale Measures: Respiratory and Cardiac Synchronisation in Choir Singers and Surgical Teams

4.1 Introduction

In an attempt to quantify the average degrees of synchronisation in the choir members' physiological responses (respiration and HRV), the quantification of the level of cooperation has been presented in the previous chapter. This is achieved via the assessment of phase and amplitude relationships between physiological responses of the singers using the intrinsic phase synchrony (IPS) and intrinsic coherence (ICoh) measures.

The IPS and ICoh are implemented through combination of the novel data-driven multivariate signal decomposition algorithm called *noise-assisted multivariate empirical mode decomposition* (NA-MEMD) [58, 10] and two standard data-association measures, phase synchrony and coherence. The IPS accounts only for phase infor-

mation between dependent signals, regardless of the differences in the magnitude of intrinsic oscillations between data channels obtained using NA-MEMD. The frequency aspect of synchrony which is estimated using this algorithm, however, is not highly localised using the Hilbert transform. Conversely, using ICoh, the degree of signal dependence can be quantified as a function of frequency, at a loss of the time aspect, because ICoh is computed over the whole data set.

To mitigate the aforementioned problems posed by both the intrinsic data association measures – poor frequency localisation in IPS and loss of time information in ICoh – a highly localised time-frequency data association measure is therefore proposed. It is achieved based on the combination of NA-MEMD, and STFT-based SST and MSST (F-M/-SST) algorithms. The NA-MEMD is first employed to obtain physically meaningful intrinsic oscillations of a given multivariate signal. Due to the resolution and noise problems in the CWT-based SST and MSST, the STFT-based SST and MSST algorithms are employed here to generate highly localised time-frequency representations of signal dependence between the intrinsic oscillations produced by the NA-MEMD. This procedure is referred to as the *intrinsic synchrosqueezing coherence* (ISC).

However, for certain scenarios, in the presence of

- collaborative tasks which take place over a long period of time,
- physically meaningful and straightforward to interpret trends in the level of cooperation during long and complex events being of interest,
- prior knowledge on periods of trends for physically meaningful and straightforward interpretation being unavailable,

it is imperative to have a data-driven, data-association measure which empirically quantifies *intrinsic trends*, whereby only those components which contain physically meaningful and straightforward interpretation can be combined. To this end, an extension to the standard IPS is proposed and is referred to as the *nested intrinsic phase synchrony* (N-IPS), which further decomposes time series of synchrony between data channels calculated using sliding windows in the standard IPS into multiple scales of synchrony; then only certain scales which admit straightforward

and meaningful physical interpretation are combined, without any prior knowledge on the frequencies of such scales.

The aim of this study is to build upon the enhanced discrimination capability of the intrinsic synchrosqueezing coherence and nested intrinsic phase synchrony data association metrics, in order to precisely identify physiological synchrony in frequency and time, using the ISC, and to empirically quantify physically meaningful intrinsic trends in the level of cooperation associated with *events* during the course of long cooperative tasks, using the N-IPS. The intrinsic synchrosqueezing coherence is employed to precisely reveal the synchronised respiratory and HRV frequencies among a subset of bass singers of the Eric Whitacre Choir during 4-minute and 40-second rehearsal and performance of the same musical score. The nested intrinsic phase synchrony is employed to empirically estimate physically meaningful trends in the levels of cooperation of: (i) subsets of soprano and bass singers of the Imperial College Chamber Choir during a 1-hour evensong performance through trends of synchrony in their respiratory and HRV signals, and (ii) three pairs of catheterisation laboratory team members (cardiology consultant, cardiology registrar and physiologist) during a 2-hour invasive coronary procedure through trends of synchrony in their HRV signals.

4.2 Algorithms and Background

The proposed intrinsic synchrosqueezing (ISC) and nested intrinsic phase synchrony (N-IPS) algorithms are described below.

4.2.1 Intrinsic Synchrosqueezing Coherence (ISC)

The proposed intrinsic synchrosqueezing coherence (ISC) is a data association measure which exhibits precise time and frequency localisation for the analysis of coupled nonlinear and non-stationary multivariate signals. This is achieved through the combination of NA-MEMD, FSST and F-MSST algorithms. The NA-MEMD is first employed to decompose a given multivariate signal into a set of physically

meaningful narrowband intrinsic oscillations (IMFs). The FSST is next employed channel-wise to generate multiple univariate multicomponent time-frequency (TF) planes with high localisation in both time and frequency. The F-MSST is then used to construct multivariate highly-localised TF representations. These univariate and multivariate TF representations are subsequently employed to generate TF representations of signal dependence (synchrony) in IMFs; see Algorithm 4.1 for detail of the proposed intrinsic synchrosqueezing coherence (ISC). The synchrosqueezing coherence index (SCI) ranges between 0 and 1, with 1 indicating perfect synchrony and 0 a non-synchronous state. For the implementation of F-MSST, FSST is employed instead of SST in Step (1) of Algorithm 2.6.

Algorithm 4.1: Intrinsic synchrosqueezing coherence (ISC)

---

1. Given a P-variate signal $\mathbf{x}(t)$, obtain multivariate IMFs via NA-MEMD, $\mathbf{c}_k(t)$, where $k = 1, 2, \ldots, K$, and K is the number of IMFs.

2. For each channel p, combine the IMFs corresponding to the frequency band of interest, IMF_p.

3. Apply FSST channel-wise to the combined IMFs, IMF_p, to generate P univariate STFT-based synchrosqueezing transform coefficients, $T^p_{\text{STFT}}(f,t)$, where $p = 1, 2, \ldots, P$.

4. Apply F-MSST to the combined IMFs between channels i and j, IMF_i and IMF_j, where $i = 1, 2, \ldots, P$, $j = 1, 2, \ldots, P$, and $i \neq j$, to generate multivariate STFT-based synchrosqueezing transform coefficients of the two channels, $T^{i,j}_{\text{STFT}}(f,t)$.

5. Time-frequency representation of the degree of signal dependence (synchrony) in frequency and time between channels i and j is then determined via the synchrosqueezing coherence index (SCI), given by

$$SCI_{i,j}(f,t) = \frac{\sqrt{\frac{|T^i_{\text{STFT}}(f,t)| \cdot |T^j_{\text{STFT}}(f,t)|}{|T^{i,j}_{\text{STFT}}(f,t)|}}}{\max\limits_{f,t}\left(\sqrt{\frac{|T^i_{\text{STFT}}(f,t)| \cdot |T^j_{\text{STFT}}(f,t)|}{|T^{i,j}_{\text{STFT}}(f,t)|}}\right)}; \forall f, \forall t \tag{4.1}$$

6. Perform 30 realisations of NA-MEMD[1], repeat steps (1)–(5) for each realisation, and average the 30 time-frequency representations of signal dependence between channels i and j, $SCI_{i,j}(f,t)$, in order to obtain a highly localised representation of synchrony.

The rationale behind Eq. 4.1 is as follows: the multiplication of univariate TF representations, that is, instantaneous amplitudes and frequencies, of channels i and j, which are respectively represented by $|T^i_{\text{STFT}}(f,t)|$ and $|T^j_{\text{STFT}}(f,t)|$, is performed in order to reveal instantaneous frequencies which exist in both the channels *at the same time instants*. However, if there exists smearing in both the univariate TF representations, the resulting multiplication also exhibits such smearing. This can be removed by dividing the resulting multiplication with the multivariate TF representation of both the channels, $|T^{i,j}_{\text{STFT}}(f,t)|$. If the resulting division is not a number (infinitiny) due to a value of zero of the denominator, $|T^{i,j}_{\text{STFT}}(f,t)|$, which indicates the non-existence of smearing, it must be replaced by zero. Finally, SCI values in the range 0 to 1 are obtained by dividing the numerator with its maximum value across the whole time and frequency considered.

4.2.2 Nested Intrinsic Phase Synchrony (N-IPS)

The intrinsic phase synchrony (IPS) was originally proposed in the so-called intrinsic multi-scale analysis framework in [8] and generalises standard phase synchrony by equipping it with the ability to operate at the intrinsic scale level. It employs NA-MEMD to decompose a given multivariate signal into its narrowband intrinsic

[1]In order to reduce the 'leakage' effect in the input channels, which is caused by artificial WGN channels while performing NA-MEMD, additional multiple realisations of WGN are recommened and must be averaged out across the realisations to obtain the 'true' IMFs [58]. This study has empirically found that performing 30 realisations of NA-MEMD is computationally time permitted and is sufficient to reduce the leakage effect. To exemplify computational time required to perform a single realisation of NA-MEMD, a single realisation of NA-MEMD was performed on a personal computer with an 8-core processor running at the speed of 3.4 GHz, with 32 GB of RAM, to decompose 2-channel 1-minute-long synthetic data with a sampling frequency of 1 kHz, where both the channels consisted of 100 Hz sinusoids, using 5 additional WGN channels. The computational time required for this NA-MEMD operation was 11 minutes. In general, computational time required for each realisation of NA-MEMD depends on the numbers of data channels and data points.

oscillations (IMFs), which makes it possible to quantify the temporal locking of the phase information in IMFs using the standard phase synchronisation index (PSI).

An extension of the IPS is introduced here and is referred to as nested intrinsic phase synchrony (N-IPS), for the empirical quantification of physically meaningful and straightforward to interpret trends in phase synchrony. The N-IPS first employs the conventional IPS to quantify intrinsic phase relationship in IMFs, and further decomposes the resulting time series of intrinsic phase synchrony into multiple scales, whereby only certain scales which contain physically meaningful and straightforward to interpret information are then combined, as outlined in Algorithm 4.2. Note that trends in synchrony obtained using the N-IPS algorithm can be negative, since IMFs of synchrony which contain a positive offset in the raw PSI values can be neglected. In such circumstances, the baseline for the trends in synchrony obtained using N-IPS is an imperative, since it is used to judge whether the trends in synchrony are significant or not – they are deemed significant if above the baseline.

Algorithm 4.2: Nested intrinsic phase synchrony (N-IPS)

---

1. Given a P-variate signal $\mathbf{x}(t)$, obtain multivariate IMFs via NA-MEMD, $\mathbf{c}_{k_x}(t)$, where $k_x = 1, 2, \ldots, K_x$, and K_x is the number of IMFs.

2. Calculate phase synchrony between channels i and j, $\gamma_{i,j}(t)$, using the IPS algorithm (see Algorithm 2.3), where $i = 1, 2, \ldots, P$, $j = 1, 2, \ldots, P$, and $i \neq j$.

3. Obtain IMFs of the phase synchrony between channels i and j, $\gamma_{i,j}(t)$, via NA-MEMD, $c_{\gamma_{i,j},k_\gamma}$, $k_\gamma = 1, 2, \ldots, K_\gamma$, and K_γ is the number of IMFs of the phase synchrony.

4. Combine certain IMFs of the phase synchrony, $c_{\gamma_{i,j},k_\gamma}$, which contain physically meaningful and straightforward interpretation.

4.3 Applications

Applications of the proposed ISC algorithm shall now be demonstrated, which include: (i) estimating degrees of synchrony in a linear bivariate signal; (ii) estimating degrees of synchrony in a nonlinear narrowband bivariate signal; and (iii) the precise identification of physiological synchrony among choir members. Applications of the N-IPS algorithm in large scale analyses for the empirical quantification of the levels of cooperation in (i) choir singing and (ii) performing a surgical procedure are also demonstrated.

4.3.1 Estimating Degrees of Synchrony in a Linear Bivariate Signal

The utility of the proposed ISC algorithm, a combination of NA-MEMD and STFT-based M/-SST (F-M/-SST) algorithms, is demonstrated over the task of estimating degrees of synchrony in a linear bivariate signal against the standard intrinsic phase synchrony (IPS) algorithm, which is a combination of NA-MEMD and phase synchrony, and other five combinations of algorithms for performing Steps (1)–(4) in Algorithm 4.1. These combinations are:

- FIR band-pass filter (BPF) & CWT-based M/-SST (W-M/-SST)
- FIR BPF & STFT-based M/-SST (F-M/-SST)
- IIR BPF & CWT-based M/-SST (W-M/-SST)
- IIR BPF & STFT-based M/-SST (F-M/-SST)
- NA-MEMD & CWT-based M/-SST (W-M/-ST)

To resemble real-world physiological signals, which typically contain 1/f noise and a low frequency trend [93], the linear bivariate signal consisted of sinusoidal oscil-

lations corrupted by additive 1/f noise[2] and a low-frequency trend of magnitude A oscillating at 0.01 Hz, $A_{0.01}$, given by

$$
\begin{aligned}
x_1(t) &= A_{0.01} + k\cos(2\pi f(t)t+\phi) + n_1(t),\\
f(t) &= \begin{cases} f_1; t = 0s, \ldots, 1.667s \\ f_2; t = 1.667s, \ldots, 3.334s \\ f_3; t = 3.334s, \ldots, 5s \end{cases}\\
k &= \begin{cases} k_1; t = 0s, \ldots, 1.667s \\ k_2; t = 1.667s, \ldots, 3.334s \\ k_3; t = 3.334s, \ldots, 5s \end{cases}\\
x_2(t) &= A_{0.01} + k\cos(2\pi f(t)t+\phi) + n_2(t),\\
f(t) &= \begin{cases} f_1; t = 0s, \ldots, 1.667s \\ f_3; t = 1.667s, \ldots, 5s \end{cases}\\
k &= \begin{cases} k_1; t = 0s, \ldots, 1.667s \\ k_4; t = 1.667s, \ldots, 5s \end{cases}
\end{aligned}
\tag{4.2}
$$

where $A_{0.01}$=5, f_1=5 Hz, f_2=11 Hz, f_3=18 Hz, k_1=1, k_2=0.5, k_3=2, k_4=0.1 and the sampling frequency f_s=200 Hz. The SNR of the first channel corrupted by additive 1/f noise n_1 was 10 dB, while the SNR of the second channel governed by 1/f noise n_2 was set at 0 dB, 5 dB and 10 dB. For each combination of the algorithms 30 realisations were performed, whereby different values of phase ϕ were set in different realisations, ranging from 0 to 2π, that is, $\phi = \frac{q-1}{30}(2\pi)$, where q is the realisation number. It must be noted that this simulation aimed to demonstrate straightforward comparisons between the combinations of algorithms in: (i) removing 1/f noise

[2]The 1/f noise was generated using the 'pinknoise' Matlab script downloaded from https://uk.mathworks.com/matlabcentral/fileexchange/42919-pink–red–blue-and-violet-noise-generation-with-matlab-implementation?focused=7825006&tab=function, whereby a time series of white Gaussian noise (WGN) is first generated, and the fast Fourier transform (FFT) is then applied to the artificial WGN. Next, to obtain the -3dB/octave characteristic of 1/f noise (the power is proportional to the frequency by a factor of 1/f, that is, the amplitudes are proportional to $\frac{1}{\sqrt{f}}$), each spectral component of the WGN in the real part is multiplied by $\frac{1}{\sqrt{u}}$, where u is the spectral component index. The imaginary part is then the symmetric copy of the real part. Inverse FFT is finally applied to all the modified spectral components to construct a time series of 1/f noise.

and trend, which typically govern physiological signals, using the standard filtering techniques and NAMEMD, essentially acting as a dyadic filterbank; and (ii) most importantly, estimating degrees of synchrony. This simulation, therefore, did not introduce other non-biological or physiological artefacts, such as electrical motor noise, mechanical ventilator noise, respiration, eye blinks, and muscle movement, which often overlap with physiological signals of interest in both spectral and temporal domains such that it becomes difficult to use a simple filtering technique for the removal [94]. Efficient detection and removal of such artefacts require further sophisticated signal processing schemes, such as independent component analysis (ICA) [95, 96, 97], artificial neural network (ANN) [98, 99, 100], and support vector machines (SVM) [101, 102, 103], which are beyond the scope of this thesis.

Figure 4.1 shows the spectrograms of the clean linear bivariate signal without the low-frequency trend estimated using the standard STFT. In this bivariate signal, there was strong synchrony between the two channels at 5 Hz from $0s$ to $1.667s$, and weak synchrony at 18 Hz from $3.334s$ to $5s$. Figure 4.2 shows the corrupted bivariate signal, the means and the variances of both the channels. The means and the variances were calculated using 0.2-second sliding windows with 0.1-second overlap (0.1-second increment). The time-varying means and variances indicate that the signal was not WSS. The bivariate signal was decomposed using NA-MEMD with 10 additional WGN channels. Three IMFs of each of the two channels which governed the frequency band of 4–19 Hz were combined and averaged over 30 realisations of NA-MEMD. Alternatively, the bivariate signal was band-pass filtered using an FIR BPF of order 50 with the passband set to 4–19 Hz, a bandwidth similar to the combined IMFs. A Butterworth IIR BPF of order 3 with the same passband was also applied to the bivariate signal. The different filtered bivariate signals obtained using the NA-MEMD, FIR BPF, and IIR BPF were then fed into the W-M/-SST and F-M/-SST algorithms to generate TF representations of signal dependence (synchrony) calculated using Eq. 4.1 in Algorithm 4.1. Phase synchrony estimation was also employed to estimate phase relationship in the filtered bivariate signal obtained using NA-MEMD, that is, intrinsic phase synchrony, and TF representations of phase synchrony were obtained using the Hilbert transform.

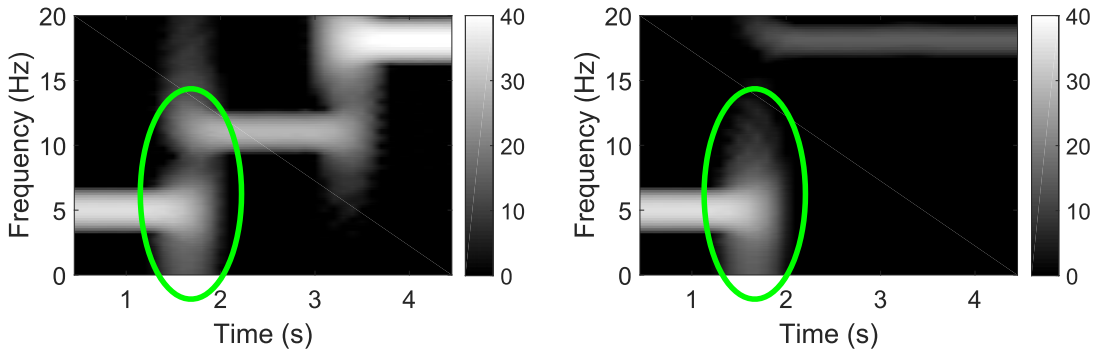


Figure 4.1: **Standard TF spectrograms of the clean linear bivariate signal**. *(a)* First channel consisted of 3 sinusoids of frequencies 5 Hz, 11 Hz, and 18 Hz. *(b)* Second channel consisted of 2 sinusoids of frequencies 5 Hz and 18 Hz. There were therefore both strong and weak signal dependence at 5 Hz and 18 Hz at different time instants. Observe smearing due to frequency swithches from 5 Hz to 11 Hz in the first channel, and from 5 Hz to 18 Hz in the second channel (see the ellipses).

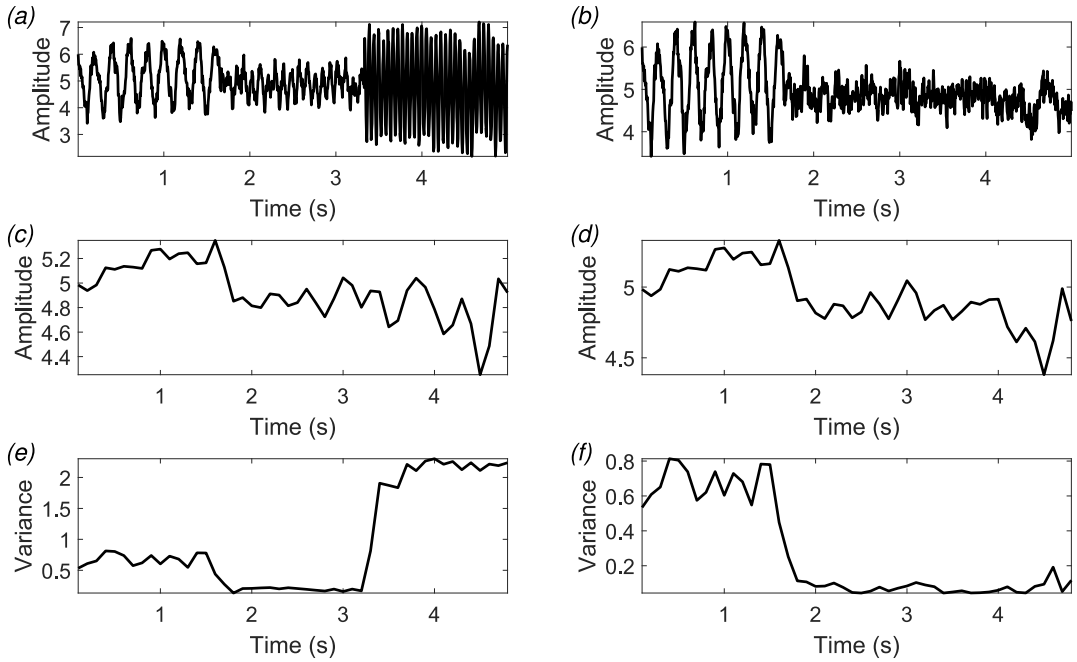


Figure 4.2: **The corrupted bivariate signal, the means and the variances of both the channels**. *(a)* The corrupted first channel. *(b)* The corrupted second channel. *(c)* Means of the corrupted first channel. *(d)* Means of the corrupted seconds channel. *(e)* Variances of the corrupted first channel. *(f)* Variances of the corrupted seconds channel. The means and the variances were calculated using 0.2-second sliding windows with 0.1-second overlap (0.1-second increment).

Figures 4.3 & 4.4 show TF representations of degrees of synchrony in the linear bivariate signal estimated by averaging over 30 realisations of the different combinations of algorithms considered. The W-M/-SST combined with either FIR BPF, IIR BPF, or NA-MEMD, produced noticeable spurious synchrony (see first and third rows in Figure 4.3, and first row in Figure 4.4), since CWT introduced mathematical artefacts (noise)[3], and consequently they were localised by the joint frequency estimator in W-MSST. Since the 0.01 Hz trend added to the signal was not filtered out completely using the FIR BPF and the remaining trend was localised by F-M/-MSST, the SCI values at this frequency consequently dominated the TF representations of degrees of synchrony (second row in Figure 4.3). Undesired synchrony at f_2 was produced by the combination of IIR BPF & F-M/-SST (see fourth row in Figure 4.3). This is because the IIR BPF introduced artefacts to the filtered second channel at f_2, thus resulting in undesired F-SST coefficients of the filtered second channel at f_2 and consequently undesired synchrony between the channels at f_2. Using IPS (last row in Figure 4.4), the degrees of synchrony estimated at f_1 were not highly localised, spreading around f_1, and the estimation of weak synchrony at f_3 was not achieved. The proposed ISC algorithm (NA-MEMD & F-M/-SST, second row in Figure 4.4) produced less spurious synchrony, yielded desired synchrony at f_1, and achieved the estimation of weak synchrony at f_3 at high SNR. Note that smeared synchrony produced by the ISC around the 2nd second (see the ellipse) was generated due to the frequency swithches from f_1 to f_2 in the first channel, and from f_1 to f_3 in the second channel.

[3]Mathematical artefacts (additional noise) are produced by CWT, because wavelet functions are time limited, thus when performing time convolution (i.e. spectral windowing), accurate localisation of both time and frequency by the CWT cannot be achieved at the same time.

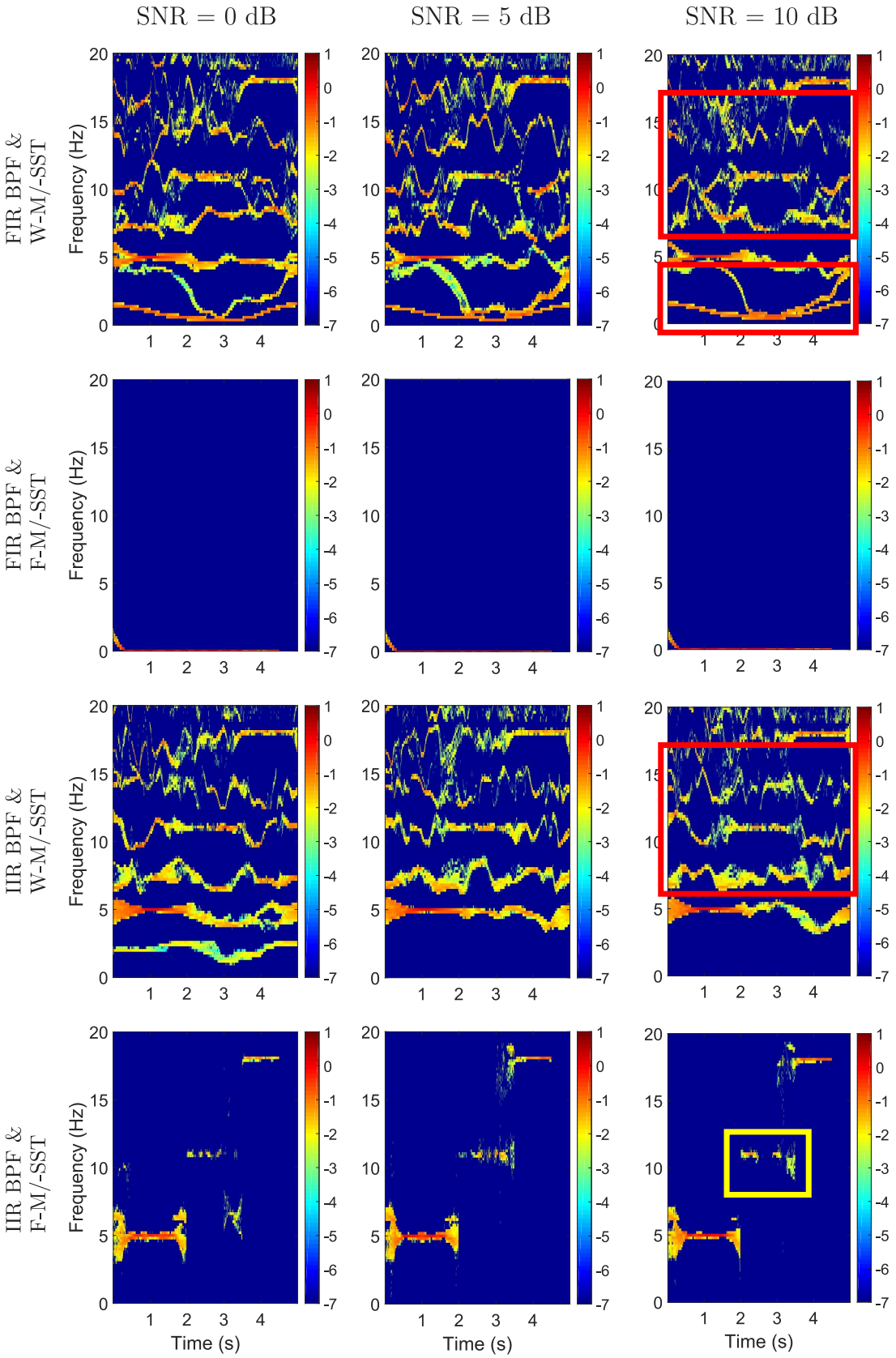


Figure 4.3: **TF representations of the degrees of synchrony in a synthetic linear bivariate signal in Figure 4.1 estimated using four different combinations of algorithms**. The TF representations are shown in logarithmic scale. The SNR of the second channel governed by 1/f noise was set to 0 dB, 5 dB and 10 dB (left, centre and right panels, respectively). Observed mathematical artefacts produced by CWT and exemplified in the red boxes.

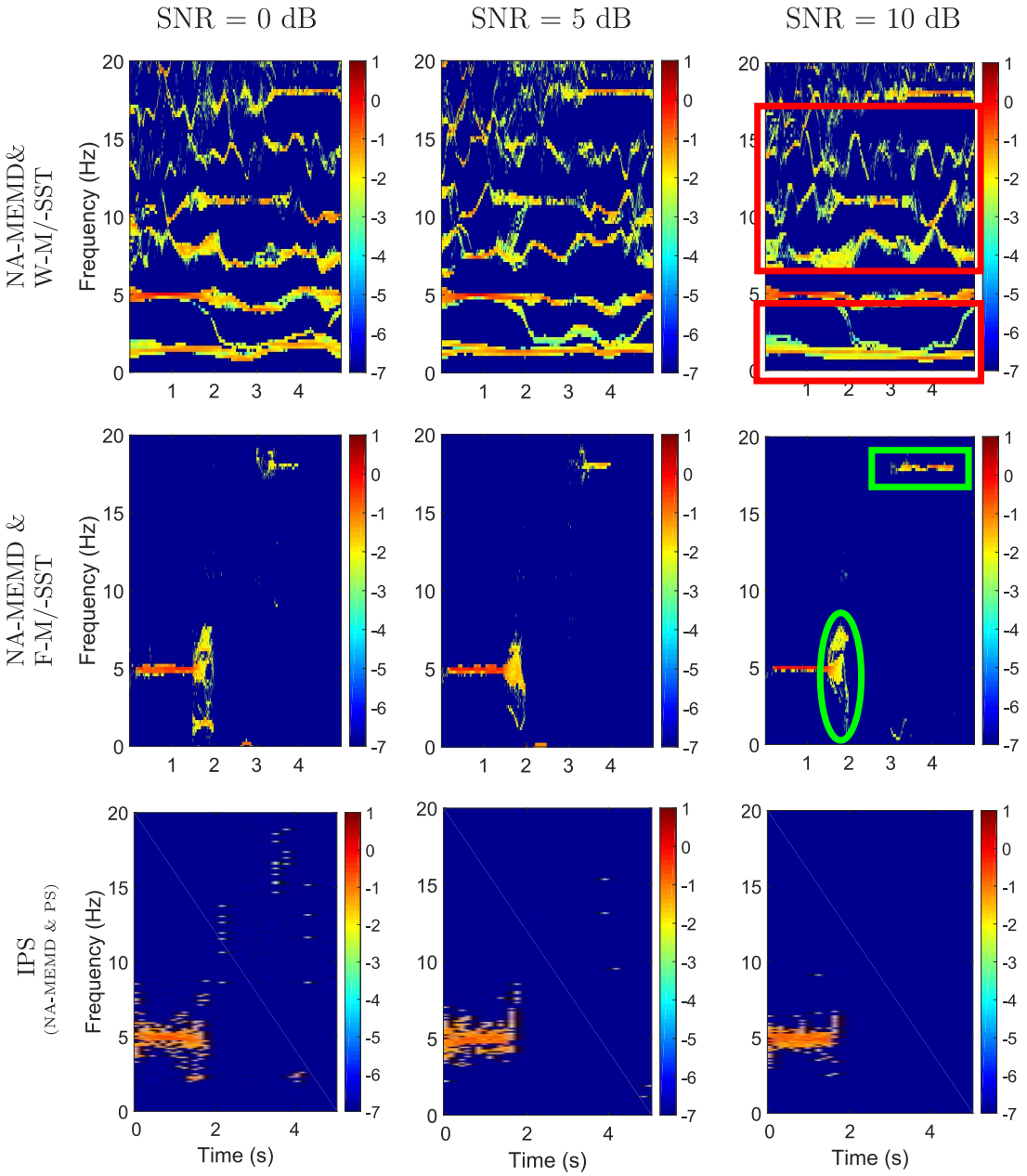


Figure 4.4: **TF representations of the degrees of synchrony in a synthetic linear bivariate signal in Figure 4.1 estimated using three different combinations of algorithms**. The TF representations are shown in logarithmic scale. Observed mathematical artefacts produced by CWT and exemplified in the red boxes. The ISC algorithm, NA-MEMD & F-M/-SST, performed the best due to no spurious synchrony and the identified weak synchrony at 18 Hz (see the synchrony in the green box). Smeared synchrony produced by the ISC around the 2nd second (see the ellipse) was generated due to the frequency swithches from f_1 to f_2 in the first channel, and from f_1 to f_3 in the second channel.

4.3.2 Estimating Degrees of Synchrony in a Nonlinear Narrowband Bivariate Signal

The performance of the seven combinations of algorithms was next evaluated in the task of estimating synchrony in a nonlinear narrowband bivariate signal extracted from a nonlinear wideband bivariate AM/FM signal corrupted by additive WGN, given by

$$\begin{aligned} x_1(t) &= ((1 + M_{AM}\cos(2\pi f_m t + \phi))A_1)\cdot \\ &\quad \sin(2\pi f_c t + (A_1 M_{FM}\sin(2\pi f_m t + \phi))) + n(t), \\ x_2(t) &= ((1 + M_{AM}\cos(2\pi f_m t + \phi))A_2)\cdot \\ &\quad \sin(2\pi f_c t + (A_2 M_{FM}\sin(2\pi f_m t + \phi))) + n(t), \end{aligned} \tag{4.3}$$

where M_{AM} denotes amplitude modulation index, M_{FM} frequency modulation index, f_c carrier frequency, f_m baseband frequency, A_1 and A_2 scalars which define signal magnitude, and $n(t)$ the added WGN. In this example, $M_{AM} = 0.5$, $M_{FM} = 20$, $f_c = 500$ Hz, $f_m = 11$ Hz, $A_1 = 1$, $A_2 = 0.5$, and the sampling frequency $f_s = 1$ kHz. The SNR of both the channels was set at 3 different values (0 dB, 5 dB and 10 dB). For each combination of the algorithms 30 realisations were performed, whereby different values of phase ϕ were set in different realisations, ranging from 0 to 2π, that is, $\phi = \frac{q-1}{30}(2\pi)$, where q is the realisation number. The NA-MEMD was employed to extract a narrowband bivariate signal of 7–15 Hz ($f_m \pm 4$ Hz) from the corrupted wideband bivariate signal. The corrupted signal was also alternatively band-pass filtered to 7–15 Hz by FIR and IIR BPFs with the same orders as in the previous example. The degrees of synchrony in the filtered narrowband bivariate signals were then estimated as previously described.

Figures 4.5&4.6 show TF representations of degrees of synchrony in the nonlinear narrowband bivariate signal estimated using the different combinations of algorithms. Using W-M/-SST combined with either FIR BPF, IIR BPF, or NA-MEMD, there exist noticeable spurious synchronies outside the band of interest (see first and third rows in Figure 4.5, and first row in Figure 4.6). This is because there still existed a considerable (FIR BPF) and a small (IIR BPF and NA-MEMD) amount

of noise – the nonlinear signal outside the band of interest – after applying the FIR BPF, IIR BPF and NA-MEMD, which were consequently localised by the joint frequency estimator in the CWT-based MSST, which is sensitive to noise [70]. Synchrony in the band of interest was not exhibited using the combination of FIR BPF & F-M/-SST (second row in Figure 4.5), and was poorly estimated using the combination of IIR BPF & F-M/-SST (see fourth row in Figure 4.5). The proposed ISC algorithm (NA-MEMD & F-M/-SST, second row in Figure 4.6) did not produce spurious synchrony outside the band of interest, and exhibited high concentration of synchrony around 11 Hz (f_m), outperforming IPS (last row in Figure 4.6).

Figure 4.7 shows average SNRs of the TF representations of synchrony produced by the seven combinations previously shown in Figures 4.3–4.6. The degrees of synchrony estimated at the frequencies f_1 & f_3 in the linear bivariate signal and those in the band of interest in the nonlinear bivariate signal were deemed 'signals', and the degrees of synchrony outside these were deemed 'noise'. The proposed ISC algorithm had respectively 4.33 dB and 5.71 dB higher SNRs than the second best combination, which is the IIR BPF & F-M/-SST, in estimating degrees of synchrony in the synthetic linear and nonlinear bivariate signals. The ISC algorithm outperformed the others in both of the tasks, because essentially it did not produce spurious synchrony, its performance increased with SNR, and it exhibited highly localised synchrony at the frequencies of interest, making it the most reliable among them. It should also be noted that: (i) both FIR and IIR filters generally introduce several problems, such as group delay and nonlinear phase response (see Section 2.2 Phase Response of a Filter); (ii) these filters are not data-driven and not designed specifically for nonlinear and nonstationary signals as opposed to NA-MEMD; and (iii) CWT produces mathematical artefacts which degrade the performance of W-MSST.

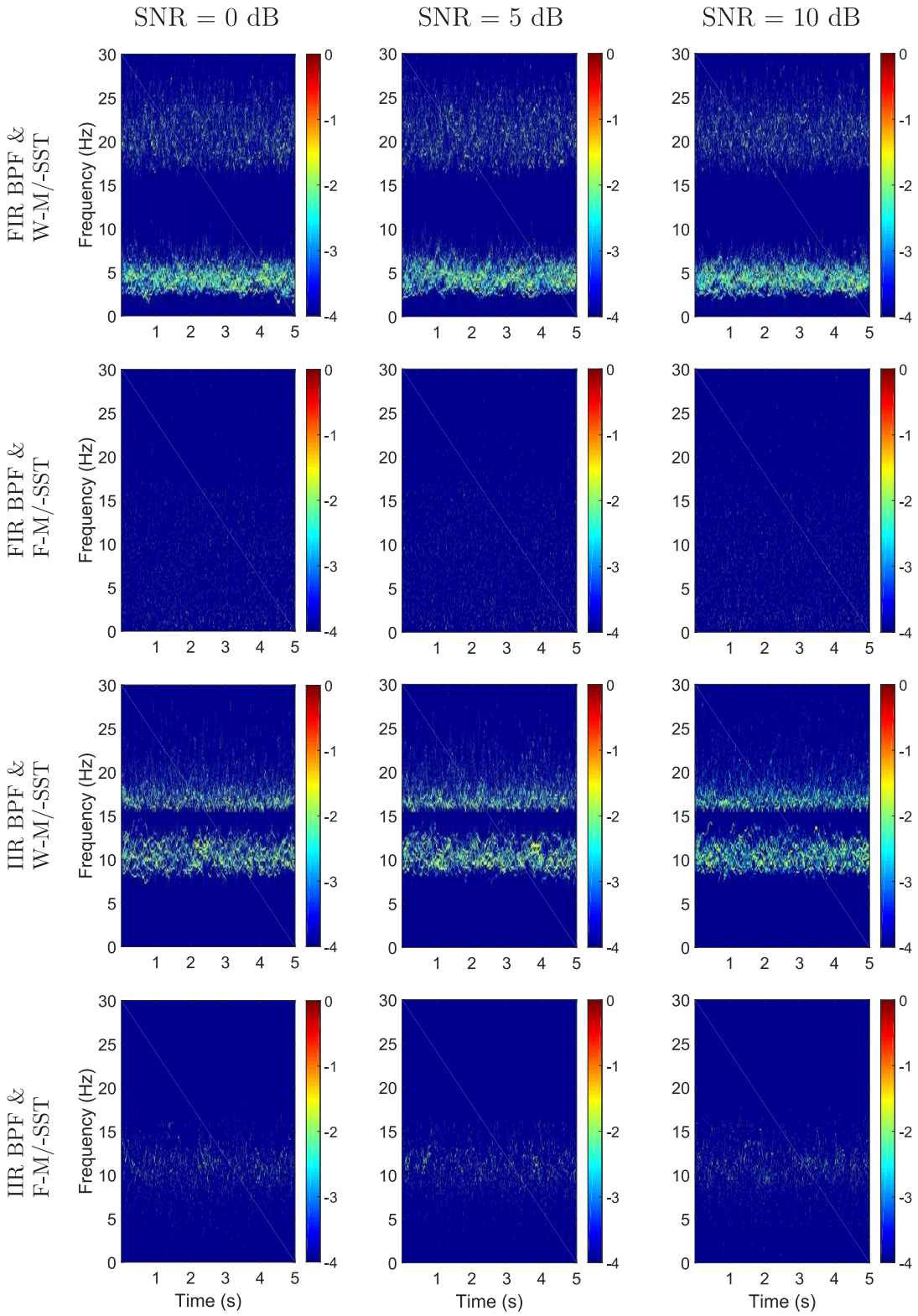


Figure 4.5: **TF representations of the degrees of synchrony in a synthetic nonlinear bivariate signal estimated using four different combinations of algorithms.** The TF representations are shown in logarithmic scale. The SNR of the second channel governed by WGN noise was set to 0 dB, 5 dB and 10 dB (left, centre and right panels, respectively).

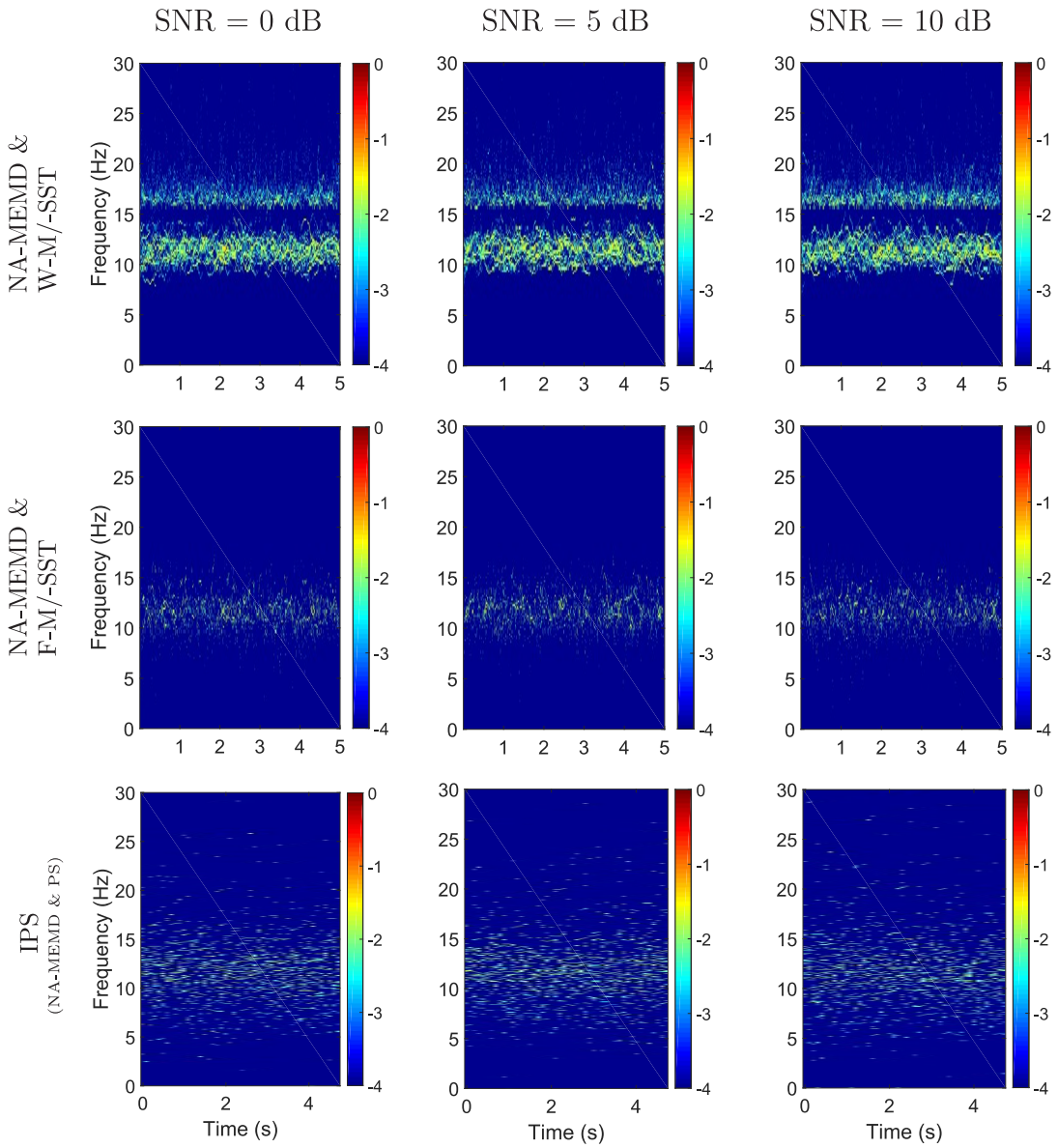


Figure 4.6: **TF representations of the degrees of synchrony in a synthetic nonlinear bivariate signal estimated using three different combinations of algorithms.** The TF representations are shown in logarithmic scale. The ISC algorithm, NA-MEMD & F-M/-SST, performed the best due to the identified synchrony in the band of interest and no spurious synchrony outside of this band.

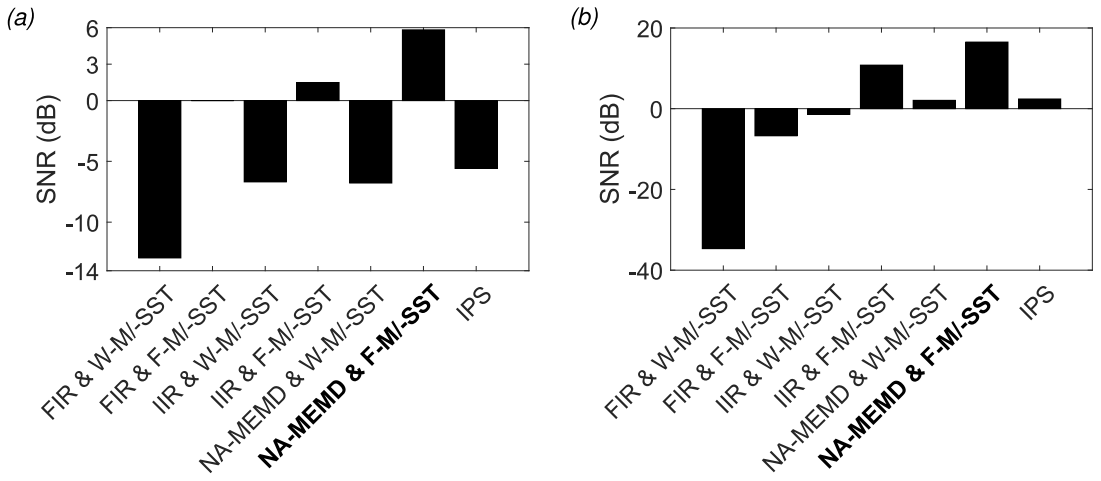


Figure 4.7: **Average SNRs of TF representations of signal dependence estimated using different algorithms**. *(a)* Average SNRs of TF representations of synchrony in the synthetic linear bivariate signal. *(b)* Average SNRs of TF representations of synchrony in the synthetic nonlinear bivariate signal.

4.3.3 Highly-localised HRV- and Respiration-based Choral Synchrony Analysis

Heart rate variability (HRV) represents variations of the cardic cycle caused by the interplay between the sympathetic (SNS) and parasympathetic (PNS) nervous systems. The low frequency (LF) band of the HRV, 0.04–0.15 Hz, is linked to the interaction of the SNS and PNS, while the high frequency (HF) band, 0.15–0.4 Hz, primarily reflects the activity of PNS. The previous chapter has shown that during choral singing, HRV and respiration of a subset of five singers synchronised during both the rehearsal and the performance. That study, however, examined the average level of cooperation by averaging the PSI of the respiratory and HRV signals of 3 different voices (1 tenor, 1 soprano and 3 bass singers) over time. This did not allow for the quantification of the level of cooperation of specific voices and at different time instants where the tempo of the musical score varied. In addition, a highly localised TF representation of synchrony in the respiration and HRV signals was not available.

To this end, IPS was employed to reveal the degrees of time-varying synchrony in HRV and respiration among only the 3 bass singers, since as the same voice they performed long- or short- inhalation or exhalation almost exactly at the same time

over the course of the 4-minute and 40-second rehearsal and performance. This time-varying synchrony estimated using IPS was next used to verify patterns of temporal dynamics and time localisation of the TF representations of synchrony in the bass singers' HRV and respiration, obtained using the proposed ISC algorithm.

This study included respiratory and ECG signals of 3 bass singers (Members 1, 3 & 4, see Chapter 3) of the Eric Whitacre's Choir during 4-minute and 40-second periods of a rehearsal and a public performance at Union Chapel, London, UK. (The same scenarios as in the previous chapter.) The respiratory and ECG signals were recorded as described in the previous chapter. The respiratory signals were downsampled to 4 Hz using the 'resample' function in Matlab, whereby the 'P' and 'Q' values for the resample function were set to 1 and 250 respectively (new sampling frequency = original sampling frequency * P / Q). The HRV was estimated from the ECG data using the MF-HT algorithm.

The respiratory (or HRV) signals of the 3 bass singers during both the rehearsal and performance were used to form 3-channel data which was decomposed using NA-MEMD with 10 adjacent WGN channels. The IMFs with indices 3–6 produced by the NA-MEMD of the 3-channel multivariate HRV (or respiratory) signal of the bass singers contained the physically meaningful frequency range 0.04 Hz to 0.4 Hz, that is, exactly the LF/HF frequency band of HRV. The full band of interest in both the HRV and respiration data was produced by summing up the corresponding IMFs, in order to obtain the desired scale in data. The time-varying PSI values among the singers were obtained by averaging PSI values calculated from 3 combined-IMF pairs of the 3 data channels (pair 1: first and second bass singers, pair 2: first and third bass singers, pair 3: second and third bass singers), whereby the PSI values for each pair were computed using 20-second sliding windows with 18 seconds overlap (2-second increment) for the respiratory signals, and 40-second sliding windows with 36 seconds overlap (4-second increment) for the HRV signals. The PSI indices between the combined-IMFs of the noise channels were also estimated in order to provide the PSI of random signals as a baseline.

The ISC was performed on each of the same 3 combined-IMF pairs of the 3 data channels of the respiratory (or HRV) signals to obtain 3 TF representations of syn-

chrony in each of the signals for all the pairs. The 3 TF representations were next averaged in order to obtain a TF representation of synchrony in the respiratory (or HRV) signals among the bass singers.

Figures 4.8*(a)* & 4.9*(a)* show the timings of long or short exhalation of the bass singers when they performed in unison, and when they remained silent or inhaled. Figures 4.8*(b)* & 4.9*(b)* show degrees of synchrony in respectively the respiratory and HRV signals during the rehearsal and the performance, estimated using IPS with 30 realisations of NA-MEMD. Observe that the respiratory synchrony in both situations (see Figure 4.8*(b)*) reached their peaks approximately during a series of long exhalation, while the HRV synchrony during the performance (see the broken line in Figure 4.9*(b)*) reached its first and last peaks during a series of relatively long inhalation (approximately at the 50th and 220th seconds). The increased synchrony in HRV was presumably due to synchronised acceleration of heart rates of the singers. Figures 4.8*(e-f)* & 4.9*(e-f)* show TF representations of respectively respiratory and HRV synchrony during the rehearsal and the performance estimated using the proposed STFT-based ISC. In both situations, the respiratory synchrony (see Figure 4.8*(e-f)*) was highly localised at 0.1 Hz due to a series of long exhalations they had to perform in unison. This exemplifies that the singers were heavily demanded by the musical score to breath in unison at a very slow rate of 6 breaths per minute (breaths per minute = 60 * breathing frequency). This rate is slower than the normal breathing rate in adults which varies between 12 and 15 breaths per minutes (0.2–0.25 Hz) [87]. The HRV synchrony (see Figure 4.9*(e-f)*) was dominant in the LF band of HRV, 0.04–0.15 Hz. This conforms with the finding in the previous chapter, where ICoh revealed a large proportion of coherence in the HRV signals in the LF band.

The sums of SCI values across frequencies as a function of time of the respiratory and HRV signals during both the rehearsal and the performance are respectively shown in Figures 4.8*(c-d)* & 4.9*(c-d)* (see thin dotted lines). Observe that the sums of SCI values of both the signals varied dramatically during both situations, indicating that the proposed ISC algorithm effectively yielded highly localised time-varying respiratory and HRV synchrony. To perform straightforward verification of patterns of

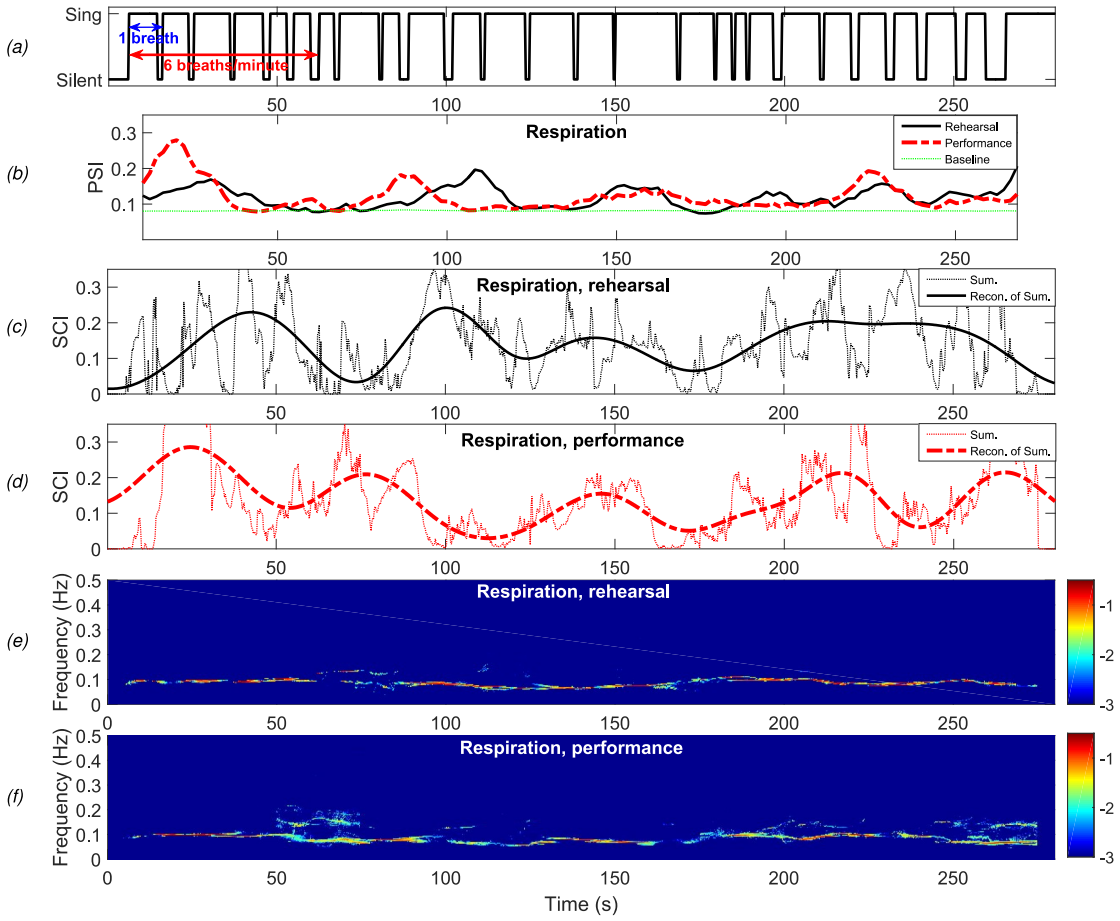


Figure 4.8: **Intrinsic synchrony in respiratory signals among the bass singers during the rehearsal and the performance estimated using IPS and STFT-based ISC**. *(a)* Singing timing of the bass singers. *(b)* The PSI of the respiratory signals. *(c)* The sum of SCI values across frequencies of the respiratory signals during the rehearsal, and its reconstruction from IMFs with indices 8–13. *(d)* The sum of SCI values across frequencies of the respiratory signals during the performance, and its reconstruction from IMFs with indices 8–13. *(e)* The SCI of the respiratory signals during the rehearsal, shown in logarithmic scale. *(f)* The SCI of the respiratory signals during the performance, shown in logarithmic scale. For brevity, the sum of SCI values are denoted by Sum., and the reconstruction of the sum of SCI values from IMFs with indices 8–13 by Recon. of Sum. Observe: (i) similar patterns of temporal dynamics between the Recon. of Sum. and the corresponding PSIs; and (ii) time instants of peaks in the Recon. of Sum. are close to those of the peaks in the corresponding PSIs.

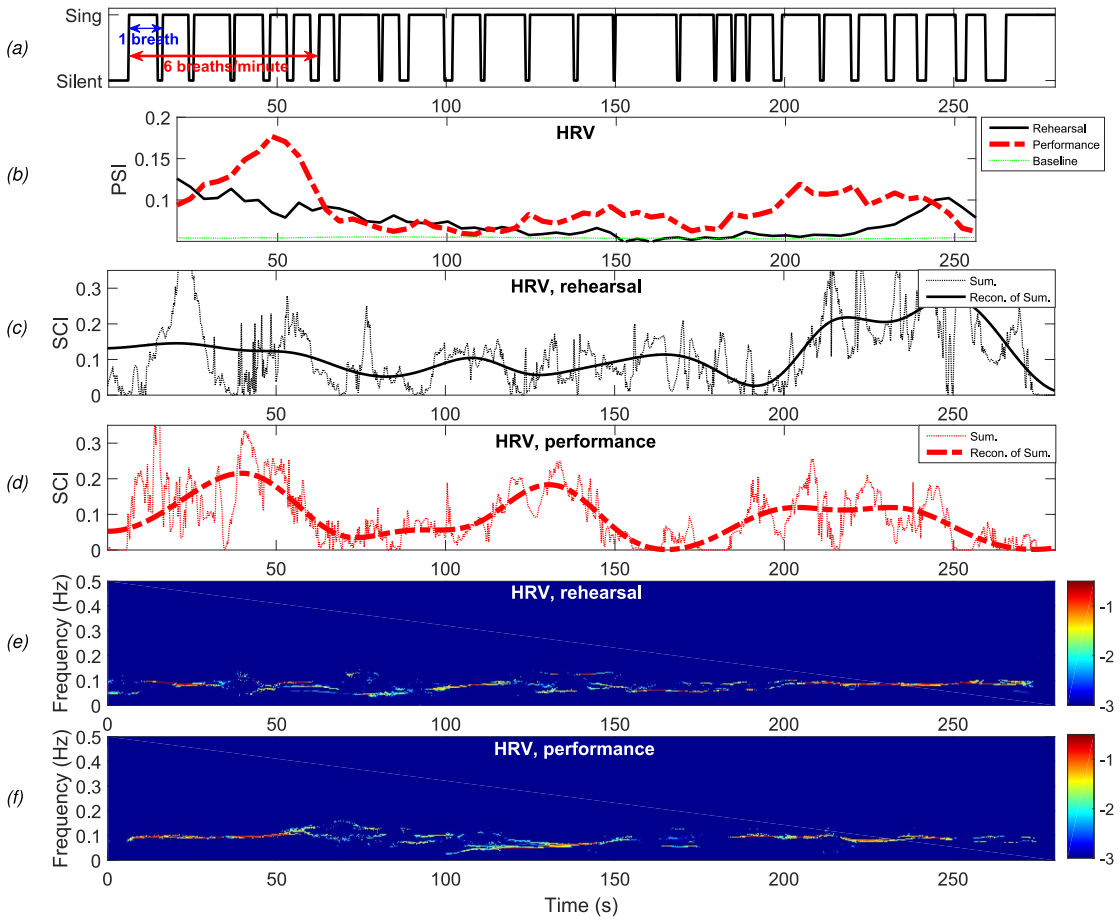


Figure 4.9: **Intrinsic synchrony in HRV signals among the bass singers during the rehearsal and the performance estimated using IPS and STFT-based ISC**. *(a)* Singing timing of the bass singers. *(b)* The PSI of the HRV signals. *(c)* The sum of SCI values across frequencies of the HRV signals during the rehearsal, and its reconstruction from IMFs with indices 8–13. *(d)* The sum of SCI values across frequencies of the HRV signals during the performance, and its reconstruction from IMFs with inidices 8–13. *(e)* The SCI of the HRV signals during the rehearsal, shown in logarithmic scale. *(f)* The SCI of the HRV signals during the performance, shown in logarithmic scale. For brevity, the sum of SCI values are denoted by Sum., and the reconstruction of the sum of SCI values from IMFs with indices 8–13 by Recon. of Sum. Observe: (i) similar patterns of temporal dynamics between the Recon. of Sum. and the corresponding PSIs; and (ii) time instants of the peaks in the Recon. of Sum. are close to those of the peaks in the corresponding PSIs.

temporal dynamics and time localisation of the relatively 'faster' temporal dynamics of the sums of SCI values against the 'slow' temporal dynamics of the corresponding PSIs shown in Figures 4.8*(b)* & 4.9*(b)*, the sums of SCI values of both the signals during both situations were used to form 4-channel data which was decomposed using MEMD. It was empirically found that the multivariate IMFs with indices 1–7 of the 4-channel data could be deemed 'fast oscillatory components', while the multivarite IMFs with indices 8–11 'slow oscillatory components', and that the combinations of the multivariate IMFs in the latter set yielded the reconstructions of the sums of SCI values which exhibited: (i) 'slow' temporal dynamics similar to the 'slow' temporal dynamics of the corresponding PSIs for both the signals and in both situations; and (ii) time instants of peaks in the reconstructions of the sums of SCI values of both the signals and in both situations being close to those of the peaks in the corresponding PSI in Figures 4.8*(b)* & 4.9*(b)*. Observe similar patterns of temporal dynamics and close positions of the peaks between: (i) the solid lines in Figures 4.8*(b)* & 4.8*(c)*; (ii) the thick broken lines in Figure 4.8*(b)* & 4.8*(d)*; (iii) the solid lines in Figures 4.9*(b)* & 4.9*(c)*; and (iv) the thick broken lines in Figures 4.9*(b)* & 4.9*(d)*.

The degrees of synchrony in the bass singers' respiratory and HRV signals during both the situations using CWT-based ISC, which combines the conventional CWT-based SST and MSST algorithms, was also examined, as shown in Figure 4.10 *(a-d)*. Since the joint frequency estimator in the CWT-based MSST is sensitive to noise [70] and CWT produced mathematical artefacts (additional noise), the TF representations produced by the CWT-based ISC exhibited noticeable spurious synchrony at several frequencies.

4.3.4 Large Scale HRV- and Respiration-based Choral Synchrony Analysis

In addition to Section 4.3.3 where the degrees of synchronisation in the respiratory and HRV signals were highly localised in frequency and time using the proposed ISC algorithm, it is equally important to establish a measure which provides physically

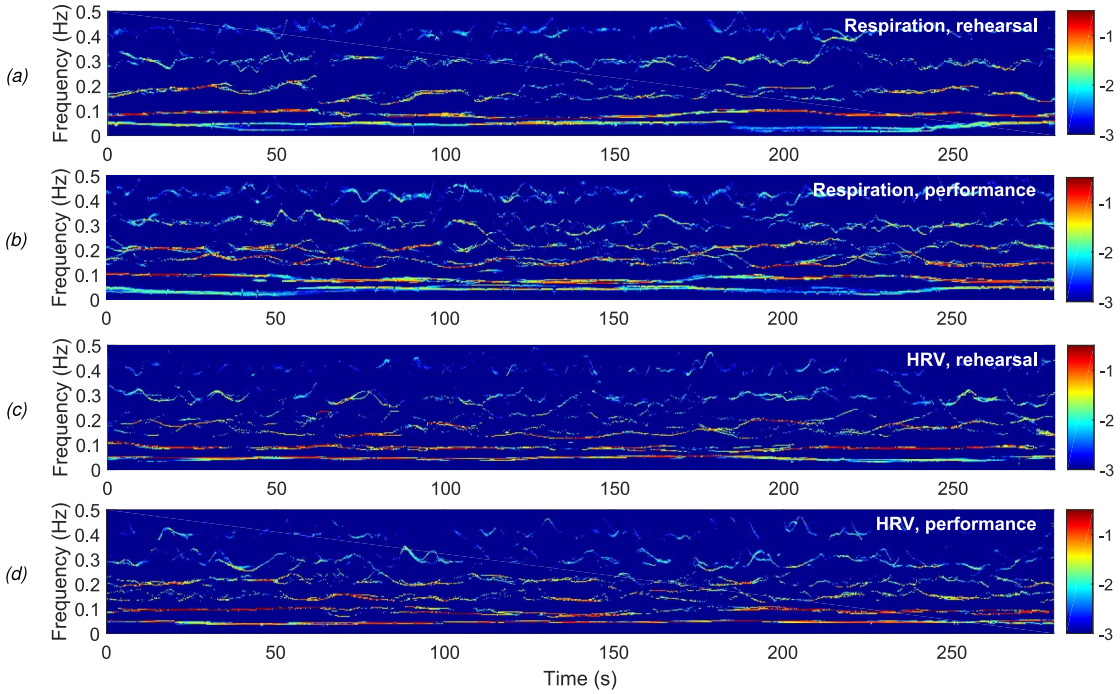


Figure 4.10: **Intrinsic synchrony in respiratory and HRV signals among the bass singers during the rehearsal and performance estimated using CWT-based ISC**. The TF representations are shown in logarithmic scale. *(a)* The SCI of the respiratory signals during the rehearsal. *(b)* The SCI of the respiratory signals during the performance. *(c)* The SCI of the HRV signals during the rehearsal. *(d)* The SCI of the HRV signals during the performance. Observe mathematical artefacts shown in the red boxes. They are introduced by the CWT.

meaningful and straightforward interpretation of the level of cooperation in the scenarios where physiological responses are acquired from a long period of time. To this end, the proposed N-IPS algorithm was employed to empirically quantify physically meaningful and straightforward to interpret trends in the degrees of synchronisation in physiological signals of choir singers while performing an evensong.

The ECG and respiratory data recordings were conducted at St Martin-in-the-Fields church, London, UK, in July 2016 under the ethics approval ICREC_12_1_1, Joint Research Office at Imperial College London. Written consents of the subjects who participated in these studies were obtained, and they were not paid for the participation. Five soprano choir singers and four bass choir singers of the Imperial College Chamber Choir participated in the recordings of their physiological signals during 10 minutes before an evensong performance, 1 hour of an evensong performance, and 10 minutes after the performance. The data were acquired in the same manner as in Section 3.3

The respiratory signals were downsampled to 4 Hz using the 'resample' function in Matlab, whereby the 'P' and 'Q' values for the resample function were set to 1 and 250 respectively (new sampling frequency = original sampling frequency * P / Q), and HRV was estimated from the ECG data using the MF-HT algorithm.

Figures 4.11–4.14 show respectively respiratory signals, ECG signals, SNRs of both the signals, and HRV signals of the subset of soprano and bass singers. Respiratory signals of soprano singer numbers 2 and 5, and bass singer number 2 (second, fifth and seventh rows in Figure 4.11) exhibited a number of spikes (see the ellipses) which were subsequently found to hamper NA-MEMD decomposition, producing same oscillatory components in several IMFs – mode splitting. These signals were thus excluded from this study, while SNRs of the respiratory signals of the other singers were high ($>$ 13 dB, see Figure 4.13 *(a)*), and were therefore included in this study. The ECG signals of all the singers exhibited high SNRs ($>$ 9.9 dB, see Figure 4.13 *(b)*), consequently resulting in successful extraction of HRV as shown in Figure 4.14. Figures 4.15–4.18 show means and variances of the included respiratory and HRV signals. The means and the variances were calculated using 10-second sliding windows with 5-second overlap (5-second increment). The time-varying means and variances indicate the signals were not WSS and that NA-MEMD should be employed in the analysis.

The respiratory (or HRV) signals of the soprano and bass singers were used to form multi-channel data which was decomposed using NA-MEMD with 10 adjacent WGN channels. The IMFs which were produced by the NA-MEMD with indices 3–6 of the multivariate HRV (or respiratory) signal of the singers and contained the physically meaningful frequency range 0.04 Hz to 0.4 Hz (the LF/HF frequency band of HRV) were then summed up to obtain the desired scale in data. The PSI estimation was next performed in the same manner as in Section 4.3.3. The time-varying PSI indices between the combined-IMFs of the signal and noise channels (baseline) were next used to form multi-channel data which were further decomposed using NA-MEMD with 10 adjacent WGN channels. Certain IMFs of the multivariate synchrony produced by the NA-MEMD which exhibited physically meaningful and interpretable trends in synchrony were then combined.

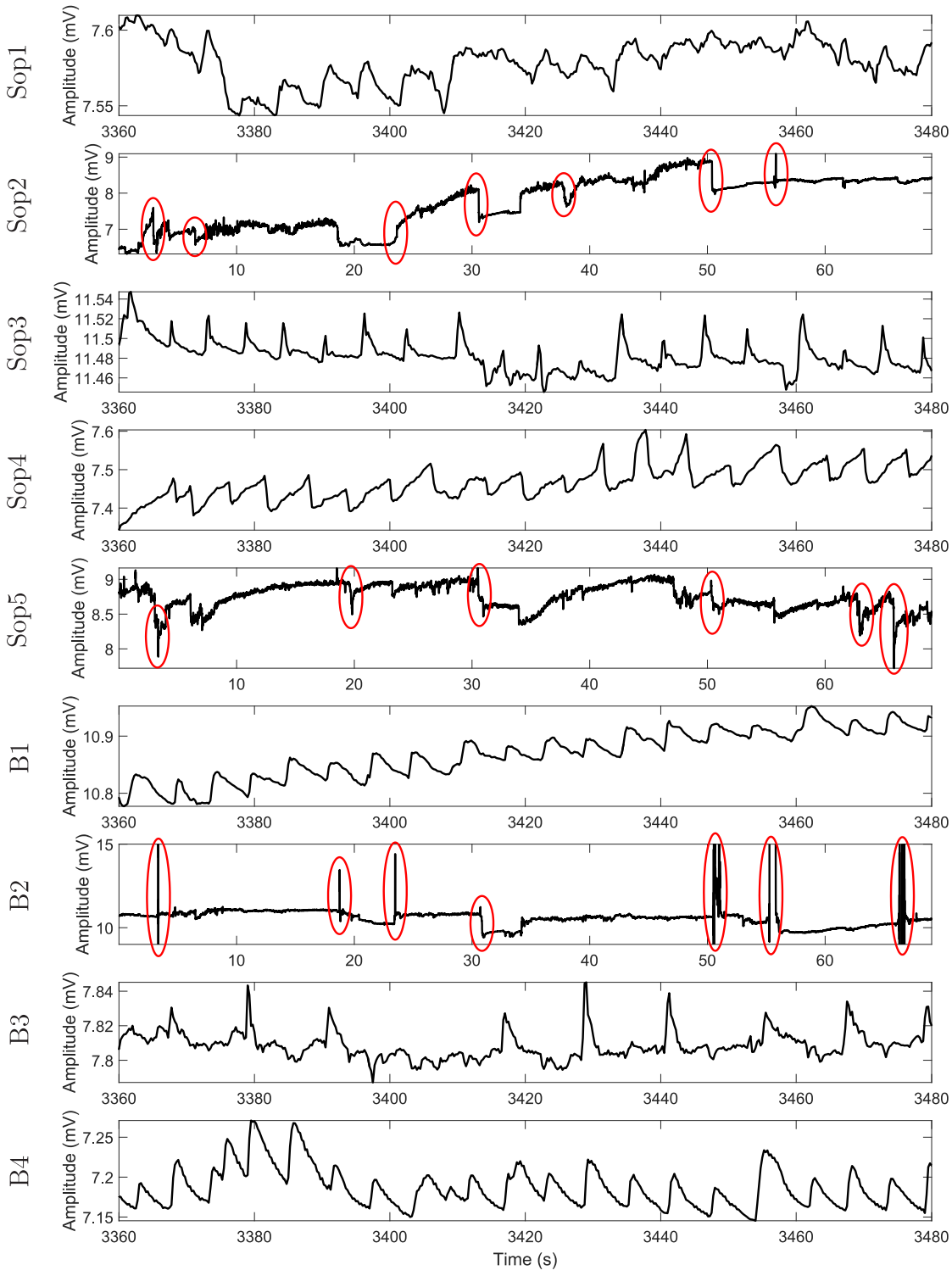


Figure 4.11: **Respiratory signals of the soprano and bass singers**. For brevity each soprano singer is denoted Sopx, with x denoting the singer number, and each bass singer is denoted By, with y denoting the singer number. Respiratory signals of Sop2, Sop5, and B2 exhibited a number of spikes (see the ellipses), severely affecting the NA-MEMD decomposition.

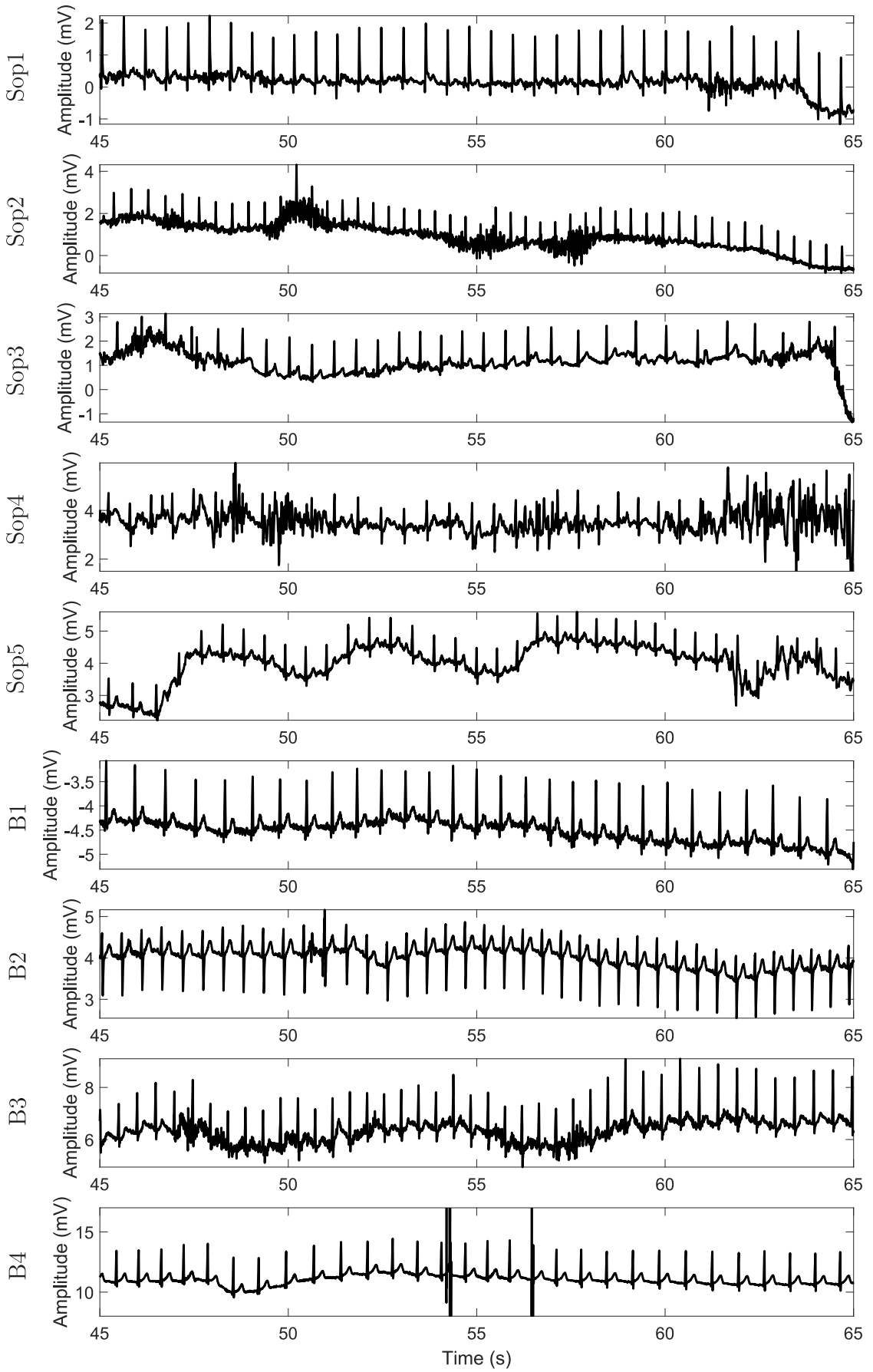


Figure 4.12: **The ECG signals of the soprano and bass singers**. For brevity each soprano singer is denoted Sopx, with x denoting the singer number, and each bass singer is denoted By, with y denoting the singer number.

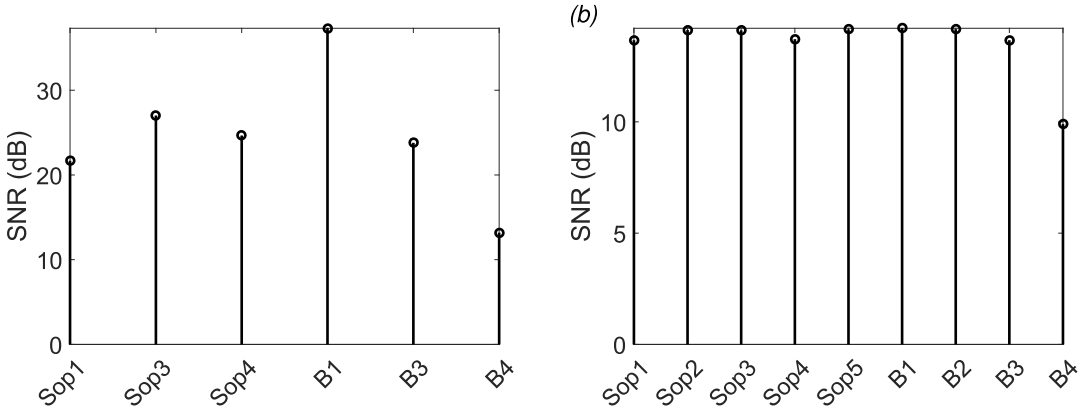


Figure 4.13: **The SNRs of the respiratory and ECG signals of the soprano and bass singers**. *(a)* The SNRs of the respiratory signals. *(b)* The SNRs of the ECG signals. For brevity each soprano singer is denoted Sopx, with x denoting the singer number, and each bass singer is denoted By, with y denoting the singer number. Note that the respiratory signals of Sop2, Sop5, and B2 were excluded from this study.

Figure 4.19 *(a-d)* shows physically meaningful trends in synchrony in the sopranos' and basses' respiratory and HRV signals, estimated from 30 realisations of NA-MEMD. Observe that all the 'raw' synchrony obtained using the standard IPS algorithm (solid thin lines) varied dramatically during the course of events (singing and pausing), thus being less amenable to physical interpretation. Trends in the synchrony obtained using the proposed N-IPS algorithm, on the other hand, exhibited smooth variations of synchrony during the events, and smooth transitions between them. This offers more physically meaningful and interpretable results, that is, the levels of cooperation markedly increased during most of the songs (depicted by the upward pointing arrows), and decreased during the long pauses (the downward pointing arrows). Variations in the degrees of synchrony (levels of cooperation) were because the breathing rhythms, and by virtue of RSA the cardiac activities too, of the singers were modulated by the pieces of music performed, thus exhibiting stronger dynamic coupling reflected in increases in the synchrony of their physiological responses. During the pauses, however, their breathing rhythms were not dictated by any piece of music, thus resulting in decreases in the synchrony. It must be emphasized that the empirical quantification of physically meaningful and straightforward to interpret trends in synchrony is focused on here, which is a first step towards prediction.

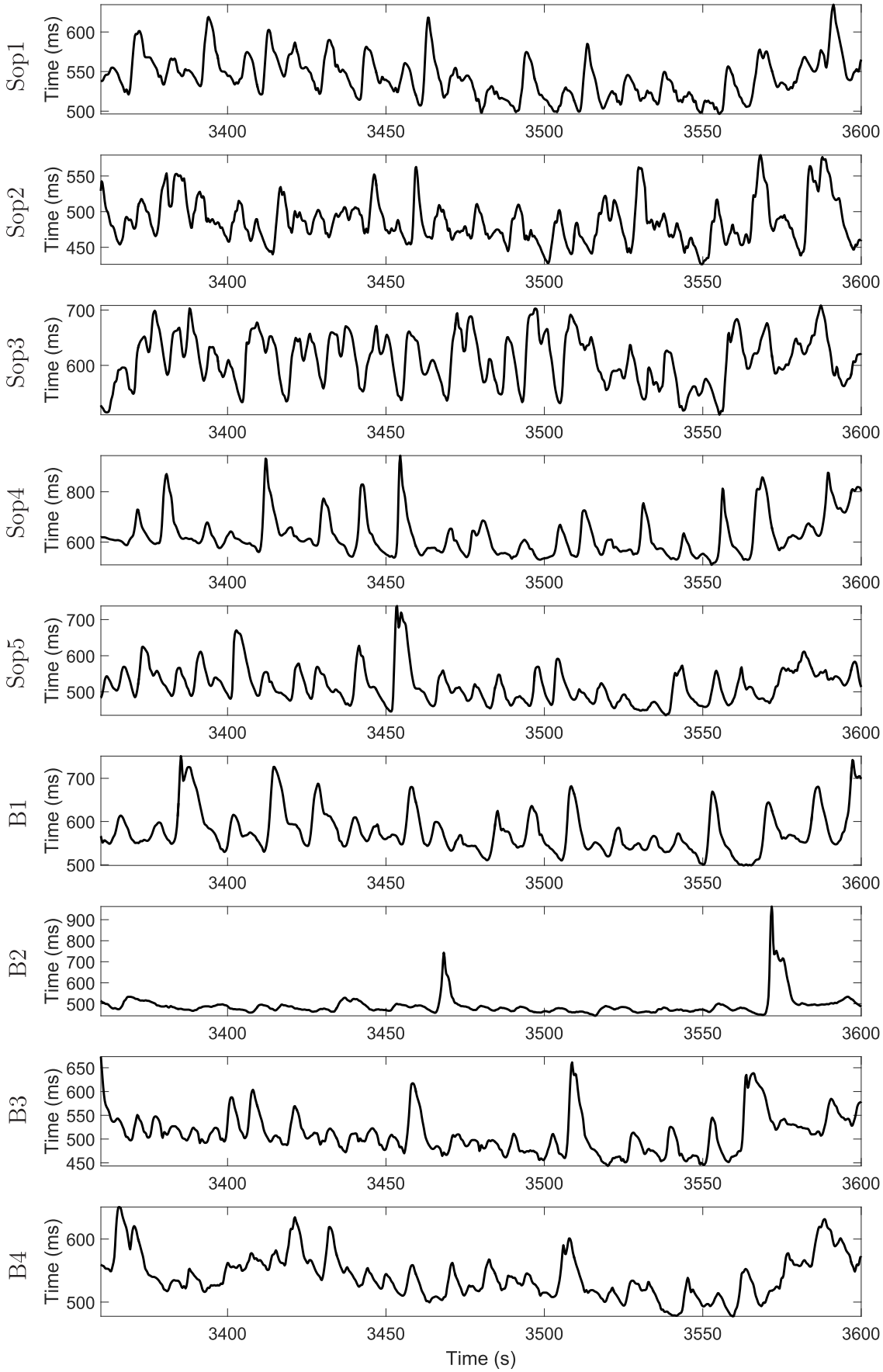


Figure 4.14: **The HRV signals of the soprano and bass singers**. For brevity each soprano singer is denoted Sopx, with x denoting the soprano singer number, and each bass singer is denoted By, with y denoting the bass singer number.

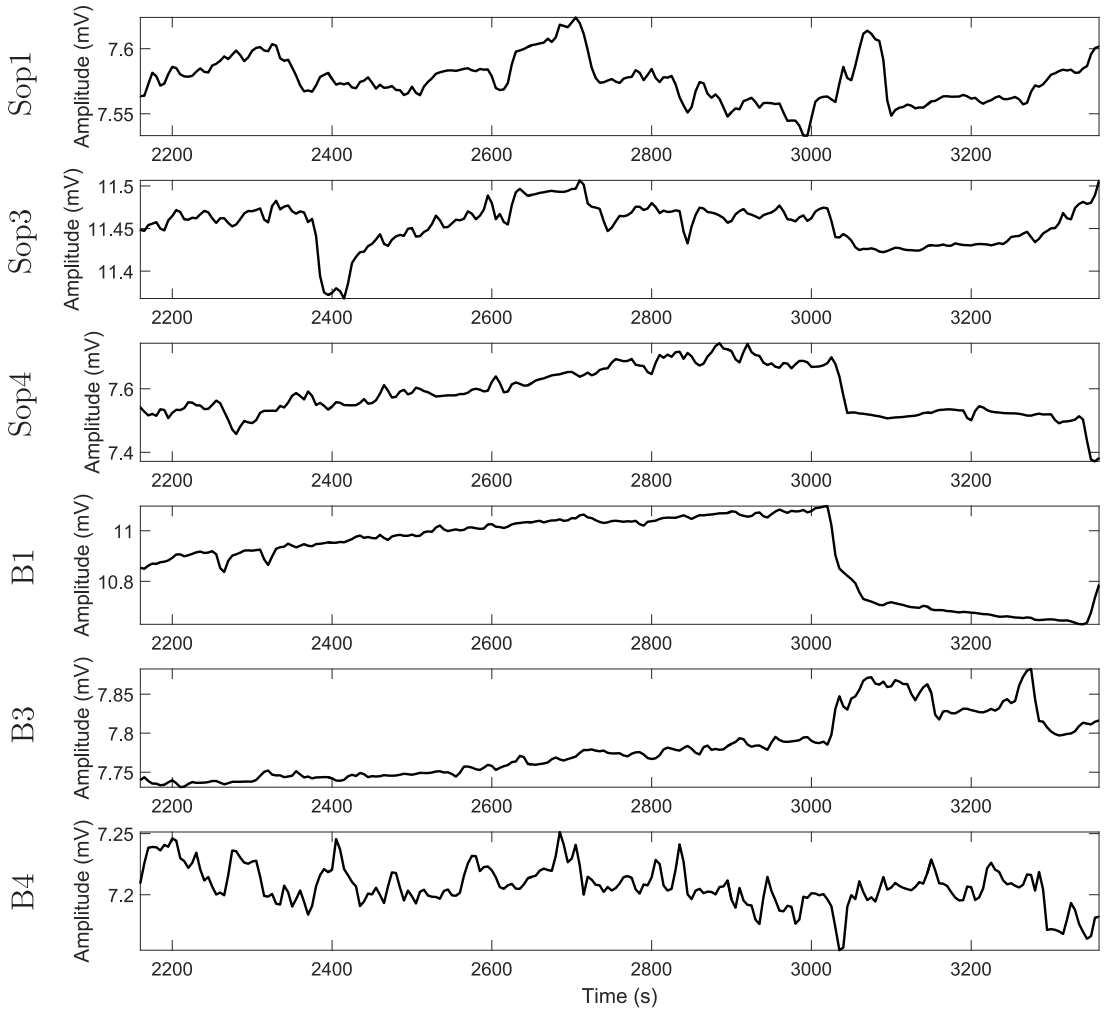


Figure 4.15: **Means of the respiratory signals of the soprano and bass singers**. For brevity each soprano singer is denoted Sopx, with x denoting the singer number, and each bass singer is denoted By, with y denoting the singer number. The means were calculated using 10-second sliding windows with 5-second overlap (5-second increment). Note that respiratrory signals of Sop2, Sop5, and B2 were excluded from this study.

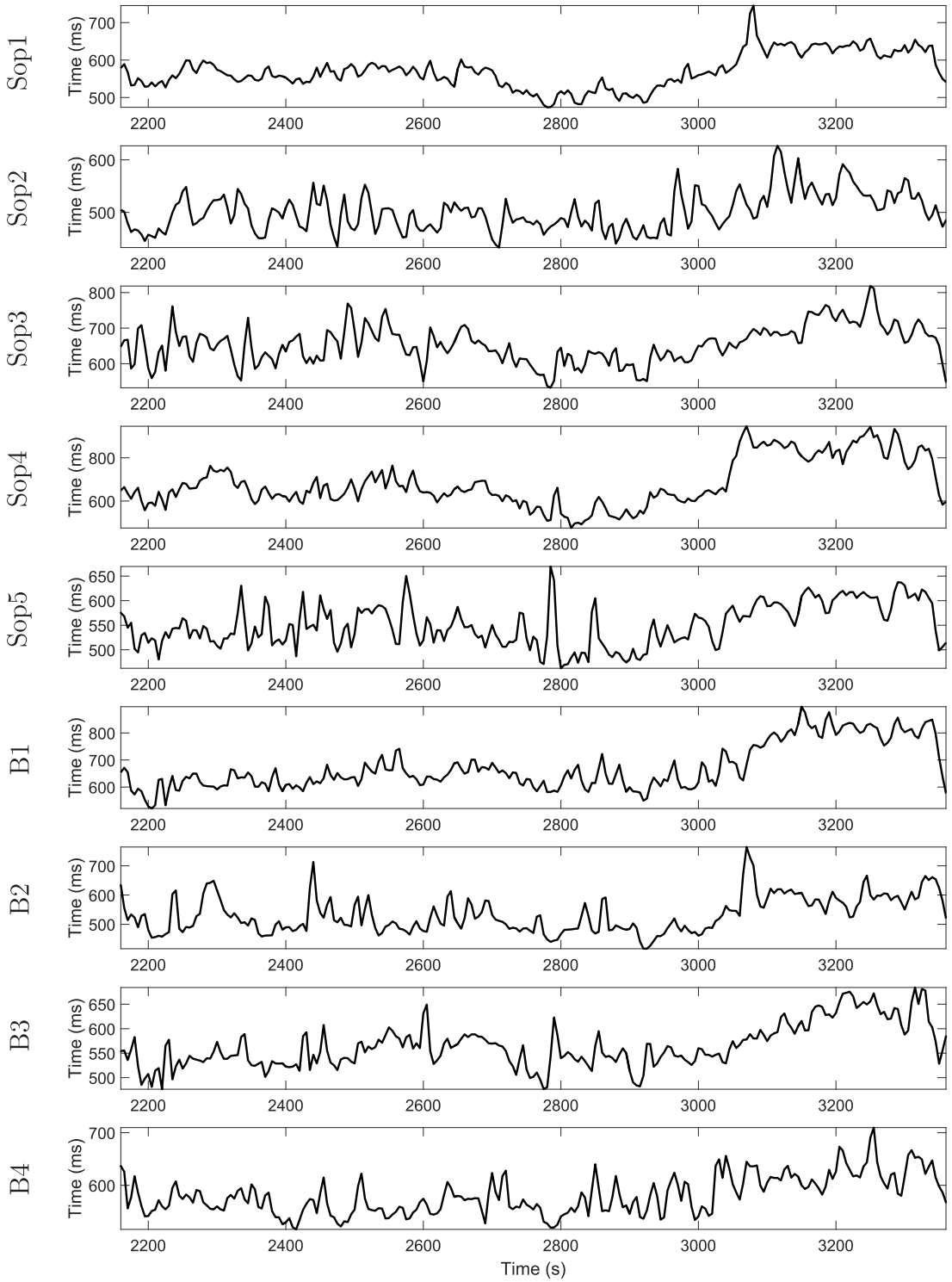


Figure 4.16: **Means of the HRV signals of the soprano and bass singers**. For brevity each soprano singer is denoted Sopx, with x denoting the singer number, and each bass singer is denoted By, with y denoting the singer number. The means were calculated using 10-second sliding windows with 5-second overlap (5-second increment).

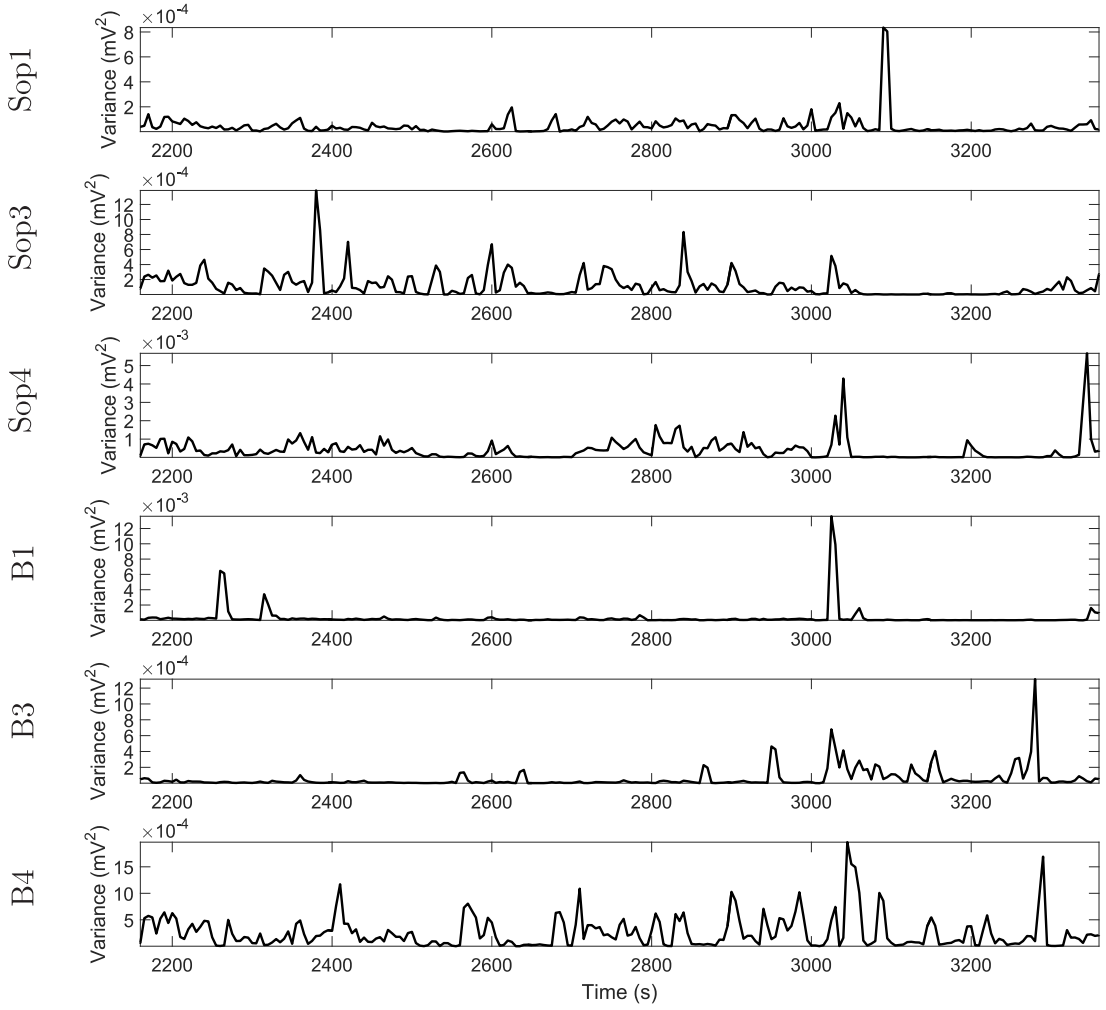


Figure 4.17: **Variances of the respiratory signals of the soprano and bass singers**. For brevity each soprano singer is denoted Sopx, with x denoting the singer number, and each bass singer is denoted By, with y denoting the singer number. The variances were calculated using 10-second sliding windows with 5-second overlap (5-second increment). Respiratrory signals of Sop2, Sop5, and B2 were excluded from this study.

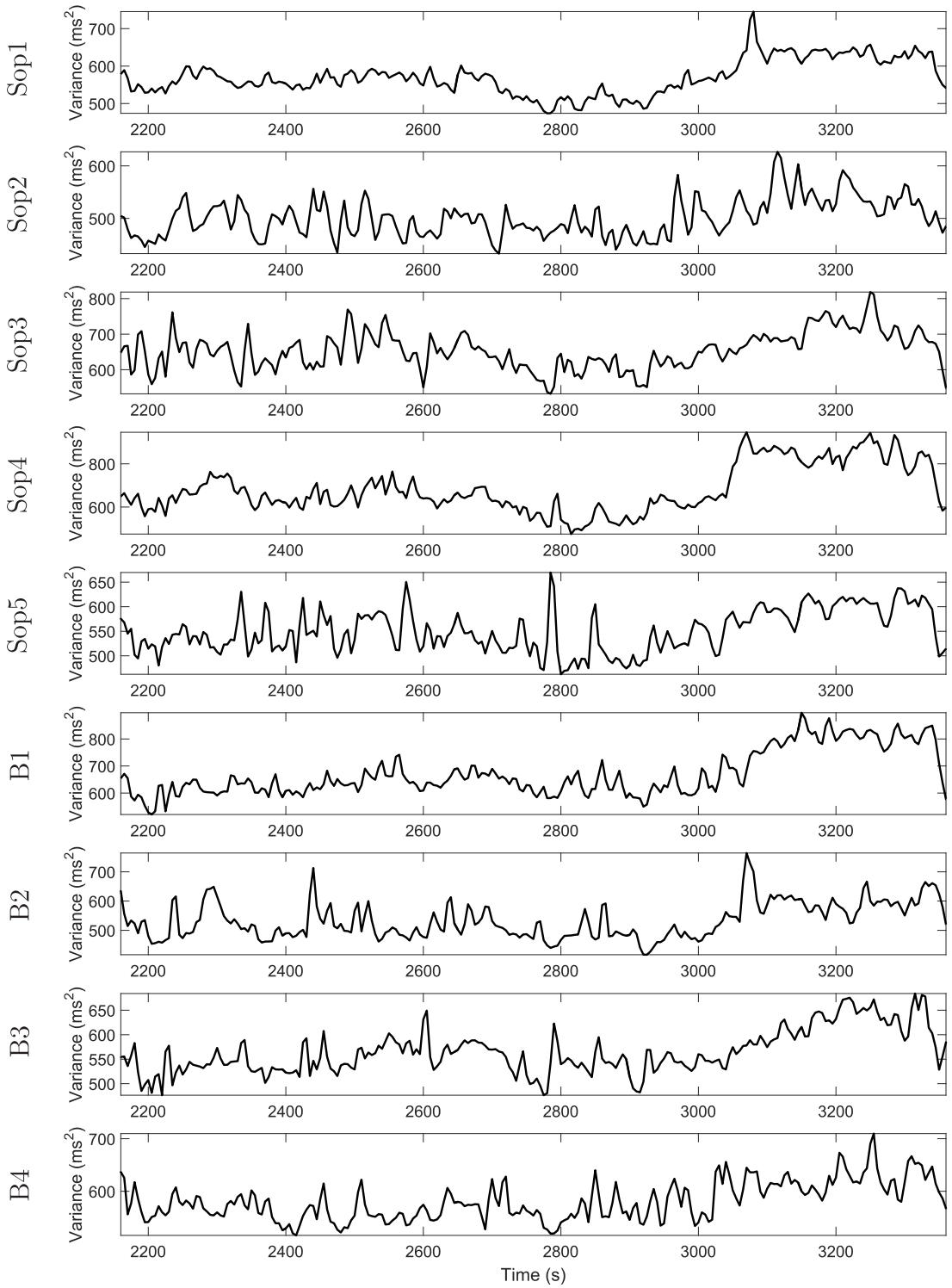


Figure 4.18: **Variances of the HRV signals of the soprano and bass singers**. For brevity each soprano singer is denoted Sopx, with x denoting the singer number, and each bass singer is denoted By, with y denoting the singer number. The variances were calculated using 10-second sliding windows with 5-second overlap (5-second increment).

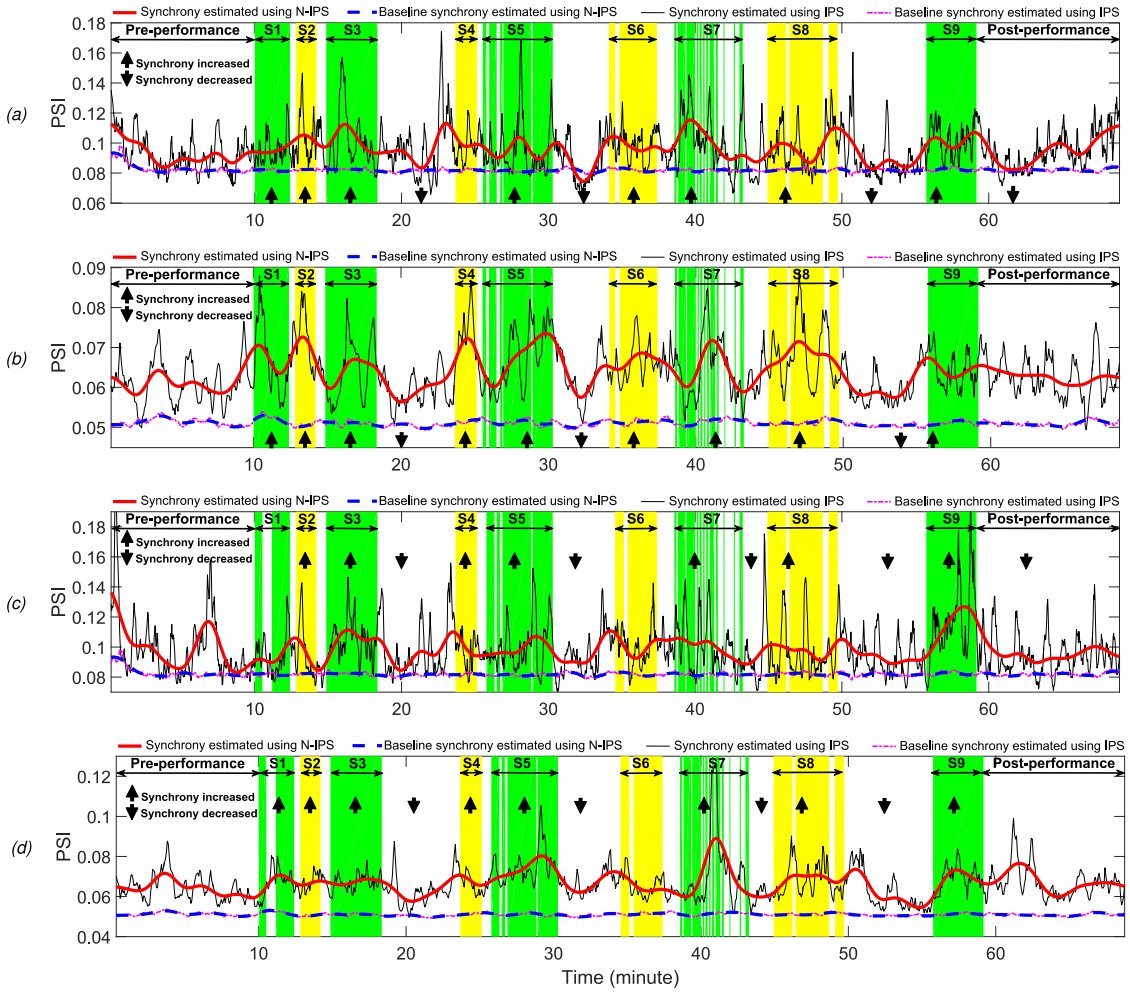


Figure 4.19: **Time-varying synchrony in the sopranos' and basses' respiratory and HRV signals**. *(a)* Respiratory PSI among the sopranos. *(b)* HRV PSI among the sopranos. *(c)* Respiratory PSI among the basses. *(d)* HRV PSI among the basses. Degrees of raw synchrony (thin solid lines) and the corresponding baselines (thin broken lines) were estimated using IPS. Trends of the raw synchrony (thick solid lines) and the corresponding baselines (thick broken lines) were estimated using N-IPS. Time instants when the singers sang during the 9 songs (S1–S9) are depicted by the shaded areas. Observe increases in the synchrony of their physiological responses during most of the songs depicted by the upward pointing arrows. These are due to their breathing rhythms and HRV being modulated by the demands of pieces of music.

4.3.5 Large Scale HRV-based Surgical Synchrony Analysis

The performance of interventional cardiology is dependent on seamless collaboration, as well as on effective teamwork as well as technical skills. These non-technical skills rely on cooperation, leadership, problem solving and situation awareness. It has been widely recognised that effective teamwork is crucial to patient safety in the operating room. Suboptimal team performance is at the heart of adverse events and near misses [104, 105, 106]. Good teamwork relies on responsible leadership and communication. Breakdowns in communication and teamwork have been shown to underlie harmful events occurring during invasive procedures. It has been shown that pitfalls in the operating room are associated with significant morbidity. Up to 60% of all adverse effects take place in the operating room, with up to 33% of these resulting in permanent disability and up to 13% resulting in death [107]. Glitches are defined as problems and faults that may hinder, impede, or delay successful accomplishment of the procedure.

Understanding team dynamics in the operating room or interventional suite, how teams function, and the factors that facilitate or impede teamwork is critical to the achievement of high-quality care and patient safety. A large body of evidence in psychology and growing numbers of surgical studies suggest that excessively high levels of intraoperative stress are disadvantageous to performance, and, consequently, to patient care [108, 109, 110]. In technically challenging tasks, an appropriate level of stress is important for performance, however, greater levels of stress and mental strain may impair both nontechnical skills and operative performance, potentially leading to an adverse impact on patient safety and outcomes [104, 111]. Multi-disciplinary interventional cardiology catheterization laboratory (Cath Lab) teams are composed of an interventional cardiology consultant, a cardiology registrar, a nurse, a physiologist and a radiographer, each with different background in terms of training and competencies. These team members are expected to work and function together to achieve an optimal outcome. Close cooperation between physicians performing the procedure (cardiology consultant and cardiology registrar) and physiologist outside the suite recording and monitoring pressures during coronary intervention is essential.

The ECG signals were recorded from a Cath Lab team starting 10 minutes before and during a percutaneous coronary intervention (PCI) procedure, which was 1 hour and 56 minutes long, and was carried out in the Cath Lab at Hammersmith Hospital, Imperial College Healthcare NHS Trust, London, in August 2016 under the ethics approval ICREC_12_1_1, Joint Research Office at Imperial College London. Written consents of the subjects who participated in these studies were obtained, and they were not paid for the participation. During the procedure, team members were closely observed by an independent observer, who noted times and types of any glitches that occurred. Based on the published literature, possible glitches have been divided into 15 categories [112] as follows:

1. Absence – absence of theatre staff member when required (e.g. circulating nurse not available to obtain equipment)

2. Communication – difficulties in communication among team members (e.g. repeat requests, incorrect terminology, and misinterpretations)

3. Distractions – anything causing distraction from the task (e.g. phone calls or bleeps and loud music requiring to be turned down)

4. Environment – aspects of the working environment causing difficulties (e.g. low lighting or variable temperature causing difficulties)

5. Equipment design – issues arising from equipment design that would not otherwise be corrected with training or maintenance (e.g. compatibility problems with different implant system and equipment blockage)

6. Maintenance – faulty or poorly maintained equipment (e.g. battery depleted during use and blunt equipment)

7. Health and safety – any observed risk to the personnel (e.g. mask violations and food or drink in the theatre)

8. Planning and preparations – instances that may have otherwise been avoided with appropriate prior planning and preparation (e.g. insufficient equipment resources and staffing levels and planning)

9. Patient related – issues related to the physiological status of the patient (e.g. difficulty in extracting previous implants and unexpected anatomically related surgical difficulty and anaphylaxis)

10. Process deviation – incomplete or reordered completion of standard task (e.g. unnecessary equipment opened)

11. Slips – psychomotor errors (e.g. dropped instrument)

12. Training – repetition or delay of operative steps due to training (e.g. consultant corrects assistant operating technique)

13. Workplace – equipment or theatre layout issues (e.g. de-sterilising of equipment and scrubbed staff on environment)

14. Change of the personnel during procedure

15. All staff present during WHO check (yes/no).

The electrode placement for ECG recordings, data acquisition, HRV estimation, and PSI estimation were carried out in the same manner as in Section 3.3. Figures 4.20 and 4.21 show respectively the ECG and HRV signals, and SNRs of the ECG signals. Observe that the ECG signals exhibited high SNRs ($>$ 13 dB). Figure 4.22 shows means and variances of the HRV signals. The means and the variances were calculated using 10-second sliding windows with 5-second overlap (5-second increment). The time-varying means and variances indicate that the signals were not WSS and that NA-MEMD should be employed in the data analysis. After applying IPS to quantify degrees of synchrony in the HRV signals, the time varying PSI indices between IMFs of the HRVs and noise channels (baseline) were used to form multi-channel data, which was further decomposed using NA-MEMD with 10 additional WGN channels. The IMFs produced by the NA-MEMD with indices 10–12 of the multivariate PSI values were combined to produce trends in the synchrony, since these combinations best represented changes in trends of the synchrony in response to gliches. Figure 4.23 shows trends in synchrony in HRV data during the recorded procedure, which exhibited cooperation and responses to glitches between the following pairs: (i) cardiology consultant – cardiology registrar, (ii) cardiology

consultant – physiologist, and (iii) cardiology registrar – physiologist. Note that no specific types of glitches were expected to be observed during the procedure. Recorded glitches during the procedure included the following groups: (i) group 3 – distractions – anything causing distraction from task (phone calls/bleeps, loud music, alarms), and (ii) group 5 – equipment design – issues arising from equipment design that would not otherwise be corrected with training or maintenance (e.g. compatibility problems with different implants or wires, or equipment failure).

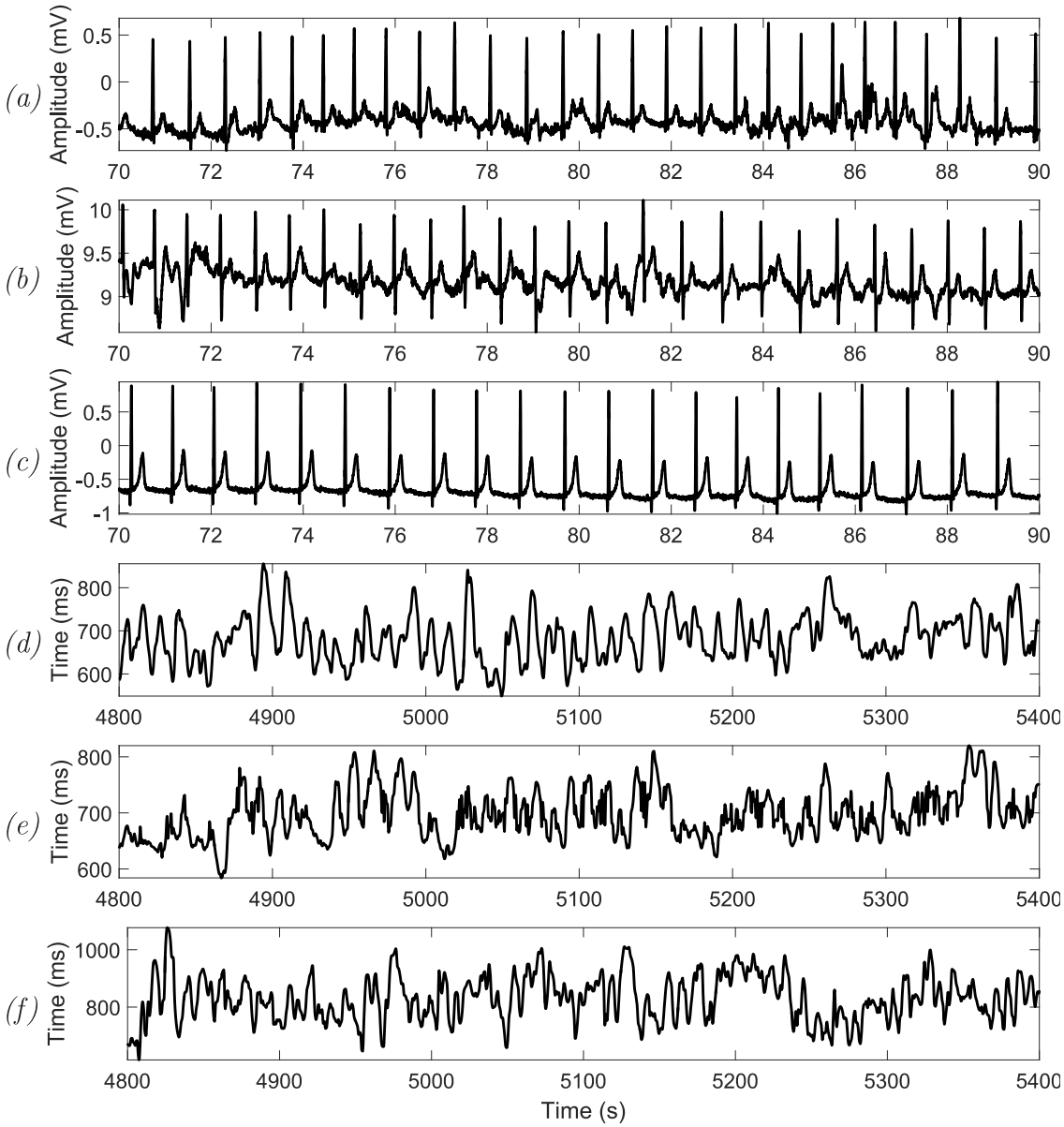


Figure 4.20: **The ECG and HRV signals of the cardiologists and physiologist**. *(a)* The ECG signal of the cardiology consultant. *(b)* The ECG signal of the cardiology registrar. *(c)* The ECG signal of the physiologist. *(d)* The HRV signal of the cardiology consultant. *(e)* The HRV signal of the cardiology registrar. *(f)* The HRV signal of the physiologist.

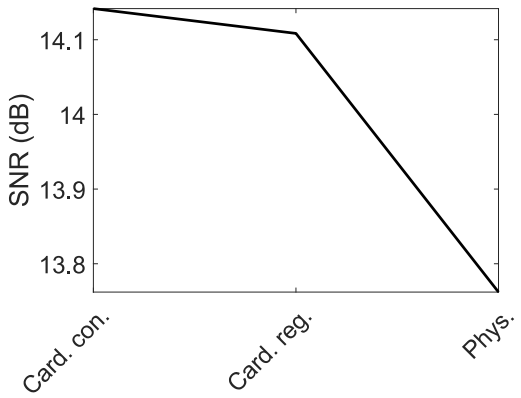


Figure 4.21: **The SNRs of the ECG signals of the cardiologists and physiologist**. For brevity Card. con. = cardiology consultant, Card. reg. = cardiology registrar, and Phys. = physiologist.

Figure 4.23 shows that physiological responses of pairs of professionals responded to the recorded glitches with increased synchrony in HRV. Observe that the first glitch at the 27th minute caused immediate negative deflections (increases) in trends of HRV synchrony between (i) the cardiology consultant and the physiologist (thin solid line) and (ii) the cardiology consultant and the cardiology registrar (thick broken line). Also, the third glitch at the 72nd minute caused another immediate negative deflection (increase) in a trend of HRV synchrony between the cardiology registrar and the physiologist (thick solid line). These findings suggest these glitches were impeding the procedure and may affect procedural duration as well as outcome.

A growing body of literature suggests that shared knowledge and understanding of each others roles and objectives during the invasive and high risk procedures in turn facilitates team cooperation and coordination. For a team to function efficiently, its members should share a 'mental model' of the team's tasks, objectives, means and environment [113, 114, 115]. It is hoped that this prospective research will help to facilitate better training programme across UK hospitals in order to deliver better care to the patients.

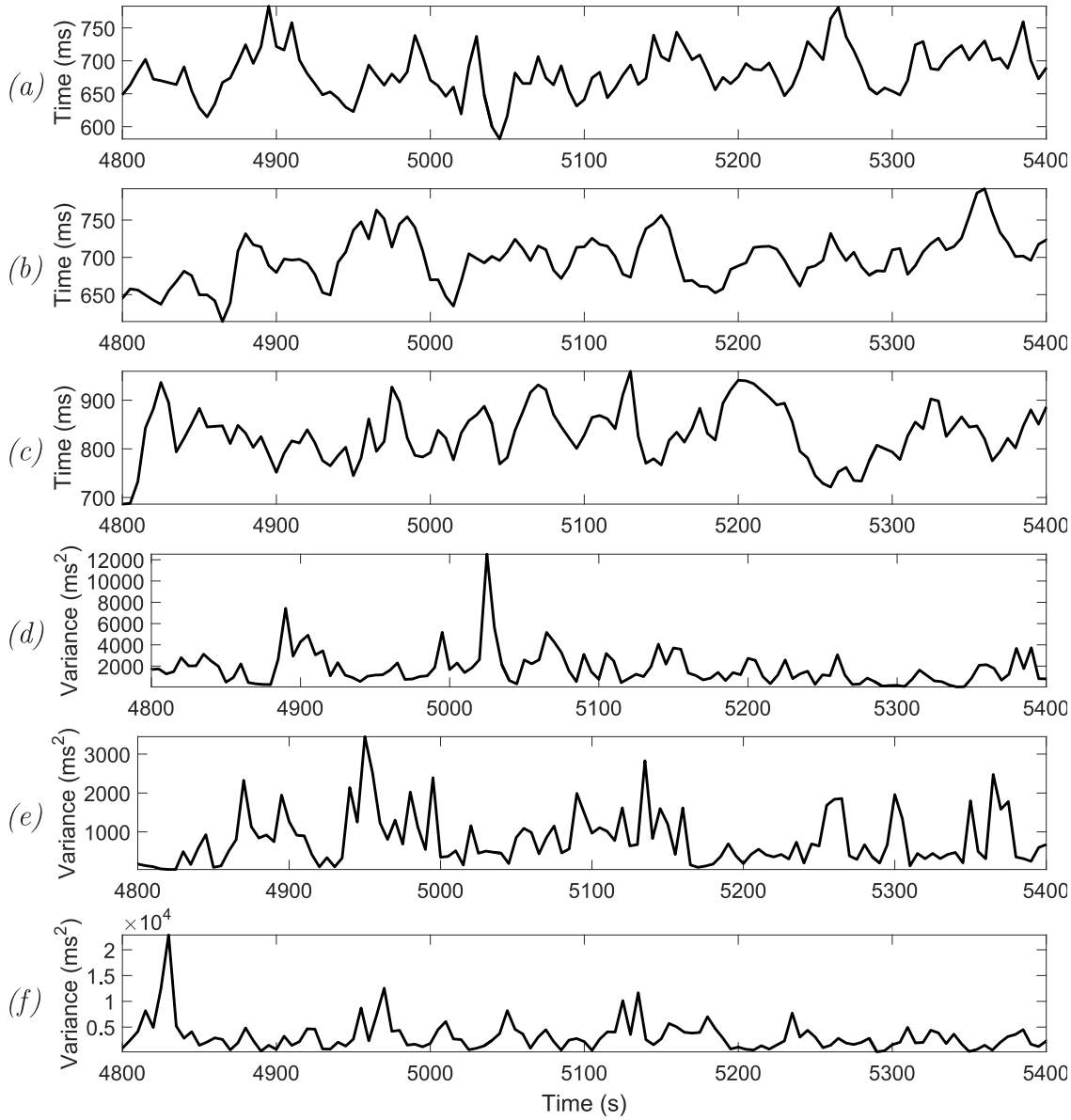


Figure 4.22: **Means and variances of the HRV signals of the cardiologists and physiologist**. *(a)* Means of the HRV signal of the cardiology consultant. *(b)* Means of the HRV signal of the cardiology registrar. *(c)* Means of the HRV signal of the physiologist. *(d)* Variances of the HRV signal of the cardiology consultant. *(e)* Variances of the HRV signal of the cardiology registrar. *(f)* Variances of the HRV signal of the physiologist. The means and variances were calculated using 10-second sliding windows with 5-second overlap (5-second increment).

4.4 Summary

A data association measure with high frequency and time localisation, termed intrinsic synchrosqueezing coherence (ISC), has been introduced for the analysis of coupled nonlinear and non-stationary multivariate signals. This has been achieved through the combination of multivariate signal analysis using NA-MEMD and the

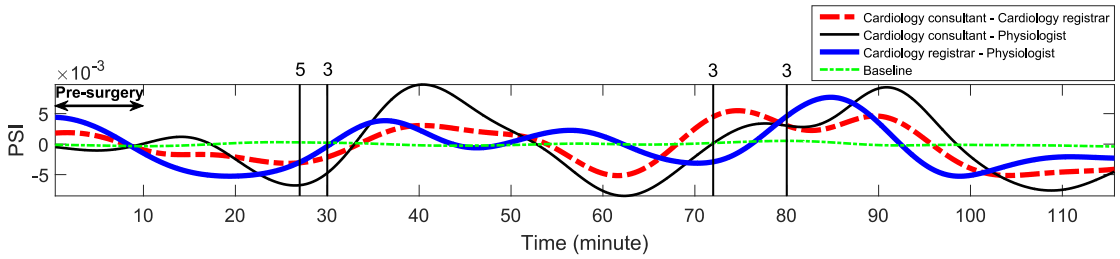


Figure 4.23: **Trends in synchrony in the cardiologists' and physiologist' HRV data**. Baseline of the degree of synchrony (broken thin line). Trend in the degree of synchrony between a cardio-consultant and a cardio-registrar (broken thick line), a cardio-consultant and a physiologist (solid thin line), and a cardio-registrar and a physiologist (solid thick line). The trends were estimated using the N-IPS algorithm, whereby 40-second sliding windows with 36 seconds overlap (4 second increment) were used in the PSI estimation. Two groups of glitches were recorded during the procedure: group 3 (distractions) and group 5 (equipment design). The recording was 116 minutes long.

generation of highly localised time-frequency univariate and multivariate representations of the multivariate intrinsic oscillations using the STFT-based SST and MSST algorithms. The proposed measure has enabled precise identification of physiological dependence in both frequency and time. The performance of the proposed ISC algorithm has been evaluated against other combinations of algorithms in the tasks of estimating synchrony in linear and nonlinear bivariate signals. The proposed ISC algorithm has been shown to outperform the other combinations of algorithms and exhibit higher average SNR of TF representations of signal dependence. An application of the ISC algorithm to the quantification of inter-channel dependence in respiratory and HRV signals has been demonstrated. The proposed algorithm has highly exhibited localised synchrony in the respiratory and HRV signals among a subset of 3 bass singers of a choir during both a rehearsal and a performance. The proposed STFT-based ISC algorithm has been shown to outperform CWT-based ISC, which was built upon CWT-based SST and MSST, in the localisation of synchronised frequencies in respiratory and HRV signals.

In addition to the ISC algorithm, an extension of IPS has been proposed and is referred to as nested intrinsic phase synchrony (N-IPS) as a meaningful and straightforward to interpret data association metric for trends in the level of cooperation. This is achieved by first employing the standard IPS to quantify intrinsic phase relationship between data channels, and then further decomposing time series of the

multivariate degrees of phase synchrony into multiple scales, whereby certain intrinsic scales which contain physically meaningful and straightforward interpretation are then combined. This algorithm allows for empirical quantification of physically meaningful and straightforward to interpret trends in phase synchrony. Two applications of the N-IPS algorithm to the empirical quantification of physically meaningful trends in the level of cooperation through the empirical estimation of trends in synchrony in respiratory and HRV signals have been demonstrated. The N-IPS algorithm has effectively quantified physically meaningful increases and decreases in trends in levels of cooperation among subsets of soprano and bass singers of a choir during a 1-hour evensong performance. It has also revealed significant increases in trends in levels of cooperation between pairs of cardiologists and physiologist when certain types of glitches occurred during a surgery. This is a first attempt to empirical quantification of intrinsic, physically meaningful and interpretable trends in the level of cooperation of long collaborative tasks.

Chapter 5

Ear-EEG for Detecting Neuronal Synchrony in Continuous Cooperative Multi-person Scenarios

5.1 Introduction

While performing cooperative activities, neuronal synchrony between the participants' brains has been observed through the so-called hyperscanning method, whereby cerebral data from two participants are acquired simultaneously. An fMRI device was employed for data acquisition in the first hyperscanning study [16], but due to its several limitations, including the size and cost, hyperscanning studies nowadays typically measure neuronal activity by recording electroencephalography (EEG) [17, 6, 4, 18].

The electroencephalogram refers to an electrical response which can be non-invasively recorded from the scalp with multiple electrodes placed on different locations according to the 10–20 system [19]. It is commonly evaluated in five frequency bands: delta 0–3 Hz, theta 3–7 Hz, alpha (mu) 7–13 Hz, beta 13–30 Hz, and gamma 30–40 Hz [20]. Recent EEG hyperscanning studies have shown that the theta and alpha

bands are synchronised *between* the brains (inter-brain synchronisation) during social interaction, and they can be recorded over the right hemispheres of participants, dominating in the right centroparietal regions [24, 17, 20].

Inter-brain synchronisation was also observed between other brain regions, and is typically identified through changes in power in EEG frequency bands common to the participants' brains [4, 5, 6] and phase synchrony [80, 17]. The right inferior frontal gyrus cortices is known to show common increases in power in the theta band during the Prisoner's Dilemma game [20]. Couples of pilots performing different phases of a flight reproduced in a flight simulator exhibited increases in power in the theta band over the frontal lobes and decreases in power in the alpha band over the parietal lobes during the takeoff and landing which were the most demanding phases [6].

The work in [17] revealed increases in phase synchrony in the alpha band between the right centroparietal regions during spontaneous imitation of hand movements. The identification of brain connectivities using the first approach (common power changes), however, loses time information. Using phase synchrony for brain connectivity estimation leads to ambiguous interpretation for the true underlying dynamics of EEG power, since it takes only phase information into account. For example, since the power of mu rhythm decreases while performing a motor task (event-related desynchronisation, ERD), the increased phase synchrony during the imitation of hand movements shown in [17] does not explicitly show whether the increased phase synchrony was in fact associated with a decrease in the power of mu rhythm (ERD) or a possible increase in the power of the alpha band as a result of social cognitive functions of the brains.

During social interaction, there also exist several cognitive functions *within* each participant, and they can be joint between the participants. Knowing the associations of such intra-brain cognitive functions with the dynamics of EEG frequency bands offers a better understanding on occurrences of inter-brain synchronisation. The theta and alpha bands, the most relevant bands to inter-brain synchronisation, comprise two subbands: lower (3–5 Hz) and upper (5–7 Hz) theta bands, and lower (7–10 Hz) and upper (10–13 Hz) alpha bands. Suppression in power (*power desyn-*

chronisation) in the lower theta and alpha bands is believed to be associated with attention [26, 27], while power desynchronisation in the upper alpha band reflects semantic memory processes [28, 26]. Increased coherence in the theta band, particularly the upper portion, between hippocampal and rhinal cortices is correlated with successful encoding of new information into episodic (working) memory [28, 29, 30].

As mentioned in Section 1.3, the capability of a novel EEG recording concept, termed ear-EEG, as an alternative, practical data acquisition approach to the hyperscanning technique has not been explored. The aim of this study is, therefore, to employ the enhanced discrimination capability of the intrinsic synchrosqueezing coherence data association metric, in order to evaluate the performance of ear-EEG against on-scalp EEG as an alternative. This provides a practical data acquisition approach for the hyperscanning method in the task of identifying the unknown, most robust EEG subbands for neuronal synchrony detection for cooperative multi-player gaming. For a full control over the experiment, a cooperative multi-player game has been developed. It was designed to encourage the participants to highly collaborate. While playing the game, the participants' EEG signals were simultaneously recorded with both on-scalp and in-the-ear (ITE) electrodes. Synchrony in their brain activities was then estimated using intrinsic synchrosqueezing coherence, and a comparison between the two EEG recording modalities was performed, a first step towards fully wearable EEG outside of a lab.

5.2 Methods

5.2.1 Experimental Design

A cooperative multi-player game – Bar Balancing – was developed in order for the brains of six couples of participants to synchronise as a result of their cooperation while playing the game. The couples' EEG signals were simultaneously recorded using on-scalp and ITE electrodes, and neuronal synchrony was estimated using the intrinsic synchrosqueezing coherence.

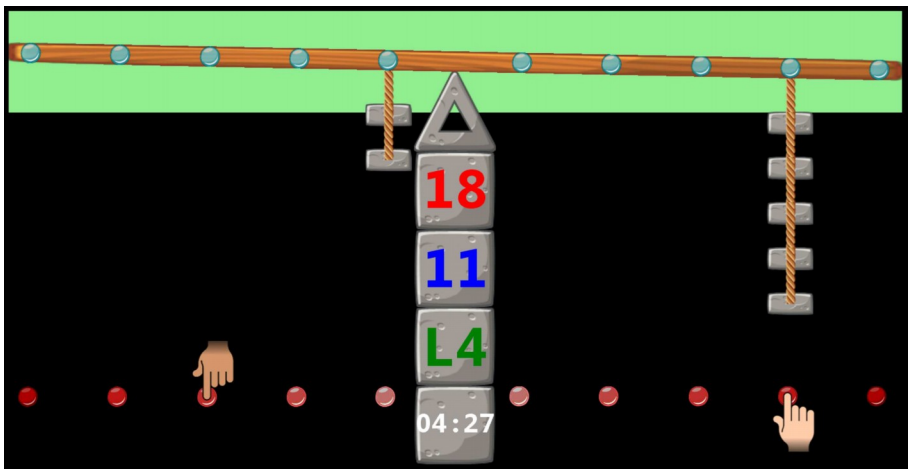
The experiment consisted of three 5-minute trials for the participants to play the

game, which comprised 5 levels of difficulty, ranging from 1 (easiest) to 5 (hardest). Before starting each level, the subjects were instructed to pause playing for 10 seconds. After a level started, the wooden bar was rotating around the pivot point, whereby its rotating speed was determined by the net *virtual* momentum calculated from the number of bricks hanging on both sides of the bar and their positions, that is, the more net virtual momentum, the faster the bar rotated. The amount of net virtual momentum increased from levels 1 to 5 – the wooden bar rotated faster in harder levels. Two separate keyboards were provided to each couple. To complete each level, the subjects were instructed to use pre-defined keys to move the hand further away from or closer to the centre, and to push the bar up or down in order to keep the bar inside the designated area for 20 seconds. For each trial, they were given 5 minutes to complete as many levels as they could. During the first trial, Subject 1 was instructed to play the game alone, while Subject 2 was resting, listening to relaxing music and wearing a blindfold to prevent the firing of mirror neurons[1], which causes undesired neuronal synchrony. The tasks were next swapped in the second trial. The purpose of these two trials was to establish a baseline in neuronal synchrony when no cooperative tasks were performed. During the third trial, a couple were instructed to cooperatively balance the bar and complete as many levels as they could together. Since the levels 4 and 5 were designed to be very difficult to accomplish by a single person, these were the situations in which a couple were expected to highly cooperate, thus resulting in synchrony in their brain activities. Figure 5.1 *(a)* shows a screenshot of the game.

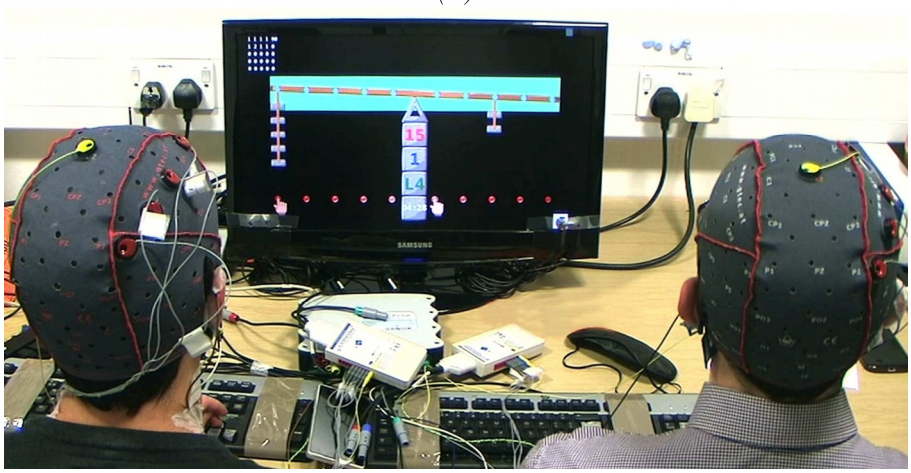
5.2.2 Data Acquisition

The EEG signals were recorded from six couples of subjects (11 males and 1 female) aged between 24 and 38 years old at Imperial College London in December 2016. Ethics approval was obtained from the Joint Research Office at Imperial College London, reference ICREC_12_1_1. Written consents of the subjects who participated in these studies were obtained, and they were paid for the participation. The EEG signals of each couple were simultaneously recorded with C4, CP4,

[1]Mirror neurons represent a distinctive class of neurons that discharge both when an individual executes a motor act and when he observes another individual performing the same or a similar motor act [25].



(a)



(b)

Figure 5.1: **Screenshot of the cooperative game and experimental setup.** *(a)* Screenshot. *(b)* Setup. The hand on the left was controlled by Subject 1, while the hand on the right was controlled by Subject 2. The red circle dots indicate the positions where the hands can be moved to. The bar was pushed harder if the hand was further away from the centre. The subjects had to repeatedly push the bar either up or down in order to balance it in the designated green area. The subjects sat in front of a computer screen and were given two separate keyboards for controlling the game. Their on-scalp EEG and ear-EEG were simultaneously recorded with electrodes placed over the right centroparietal regions and ITE electrodes inserted into the right ear canals. The electrodes were connected to a 16-channel medical grade biosignal amplifier.

P4 on-scalp g.LADYbird active ring electrodes, and ITE electrodes inserted into the right ear canals. The on-scalp active electrodes for each subject were powered by g.GAMMAbox, an active electrode driver box. These on-scalp electrode positions were chosen because they are located over the right centroparietal regions, which were expected to synchronise while the couples were cooperating and were the best possible ground truth for the evaluation. All the electrodes were connected to a gtec

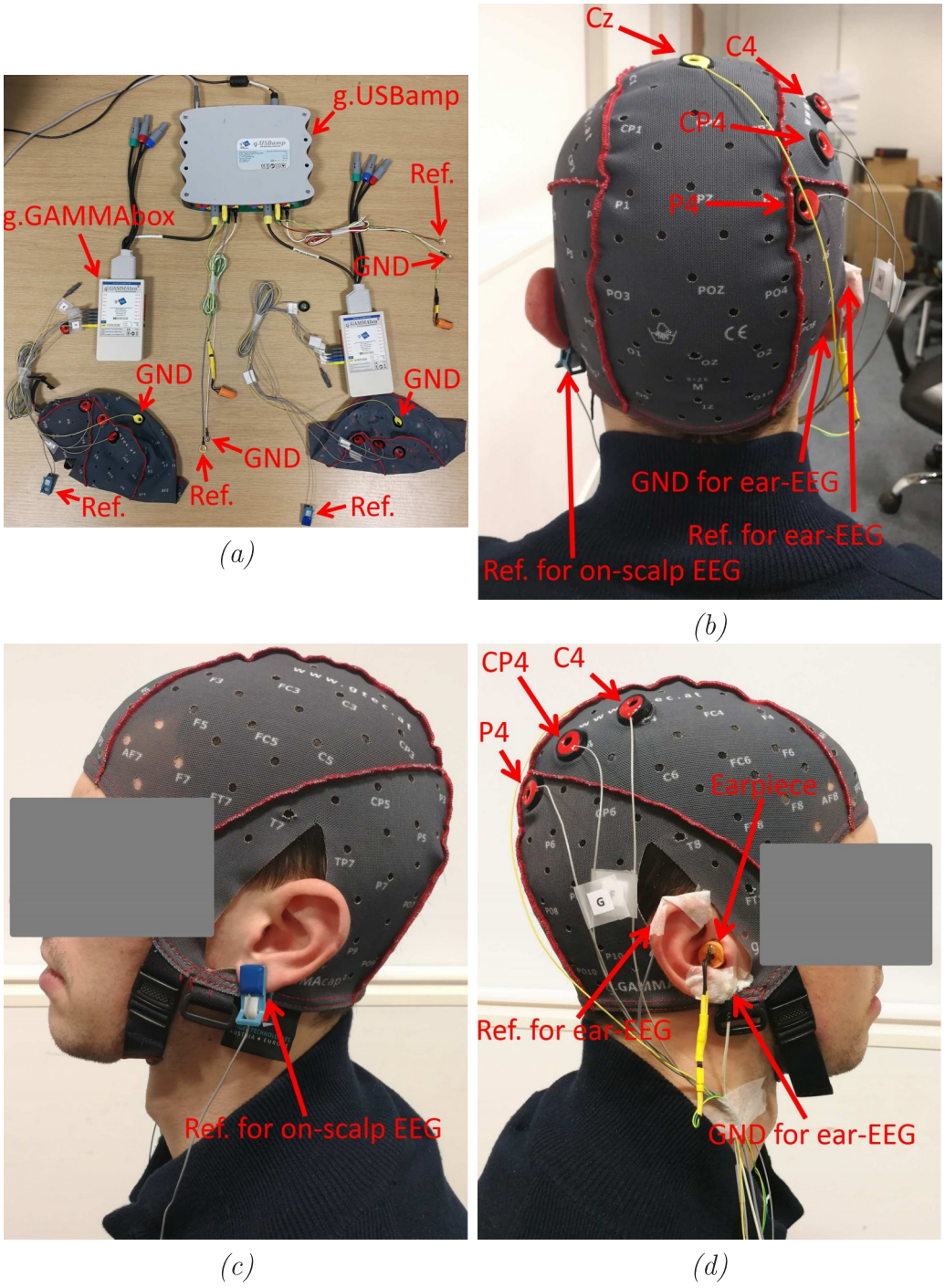


Figure 5.2: **Recording setup.** *(a)* Equipment used in the EEG recordings. *(b)* Positions of the electrodes viewed from the back. *(c)* Positions of the electrodes viewed from the left. *(d)* Positions of the electrodes viewed from the right. For each couple two sets of on-scalp and ITE electrodes were used. For on-scalp EEG recordings of each subject, three g.LADYbird active ring electrodes (the red ring electrodes) were placed on an EEG cap on the C4, CP4, and P4 positions, and were powered by g.GAMMAbox, an active electrode driver box. A yellow ring electrode, located on the Cz position, and a blue clip electrode, which would be attached to the subject's left earlobe (see *(c)*), were used respectively for the ground and the reference for on-scalp EEG recordings. For ear-EEG recordings of each subject, an earpiece was inserted into the right ear canal (see *(d)*), and two standard gold-cup electrodes which were placed on the right earlobe and behind the right ear were used respectively for the ground and the reference.

g.USBamp, a 16-channel CE-certified and FDA-listed biosignal amplifier. Generic earpieces used for the in-the-ear recording were made of a medium-density memory foam and conductive cloth electrodes [39]. Figure 5.1 *(b)* shows a couple playing the game while their EEG signals were simultaneously recorded, and Figure 5.2 shows the recording setup.

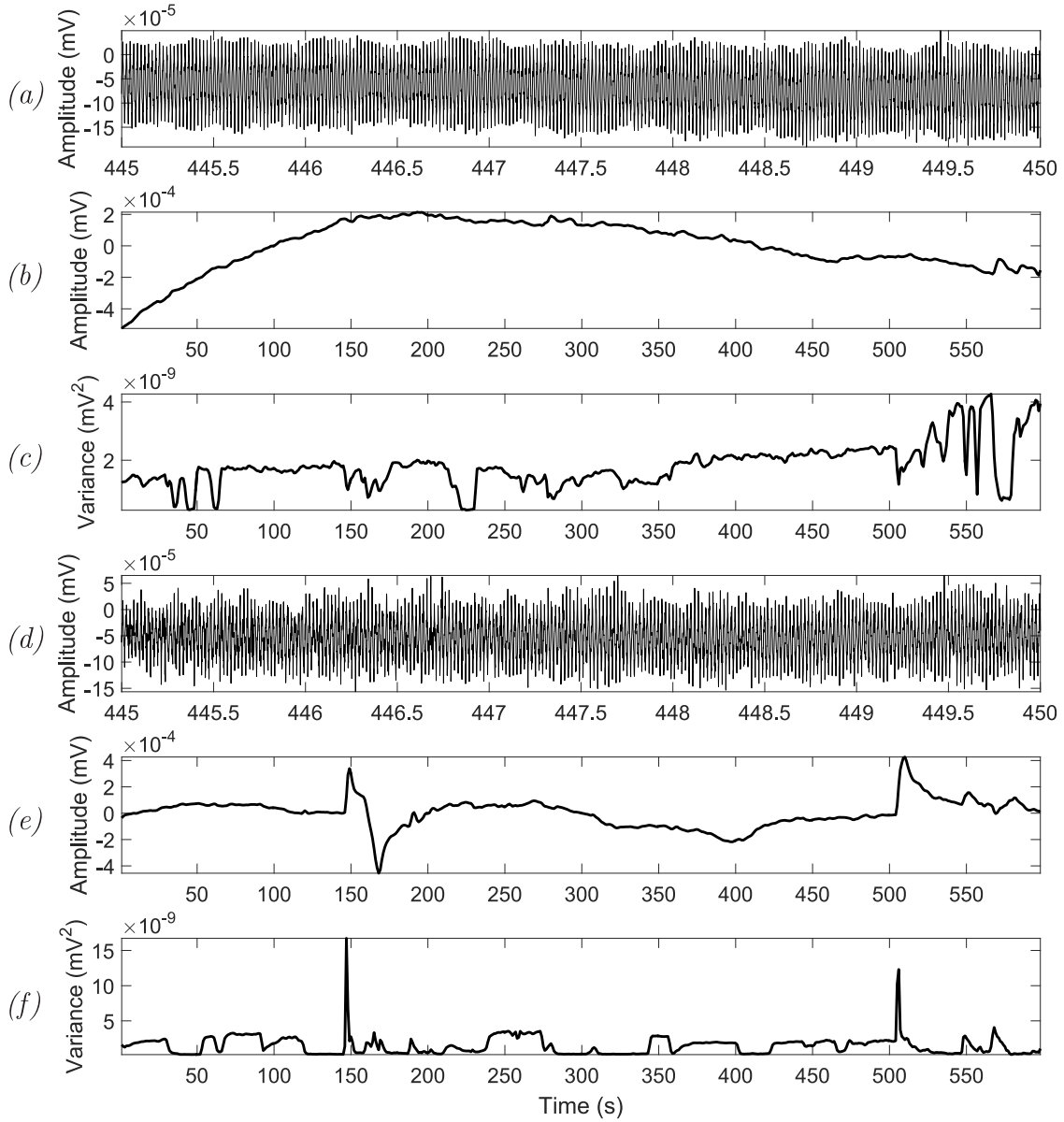


Figure 5.3: **Ear-EEG signals of Couple 2, the means, and the variances**. *(a)* Ear-EEG signal of Subject 1. *(b)* Means of the ear-EEG signal of Subject 1. *(c)* Variances of the ear-EEG signal of Subject 1. *(d)* Ear-EEG signal of Subject 2. *(e)* Means of the ear-EEG signal of Subject 2. *(f)* Variances of the ear-EEG signal of Subject 2. The means and the variances were calculated using 2-second sliding windows with 1-second overlap (1-second increment).

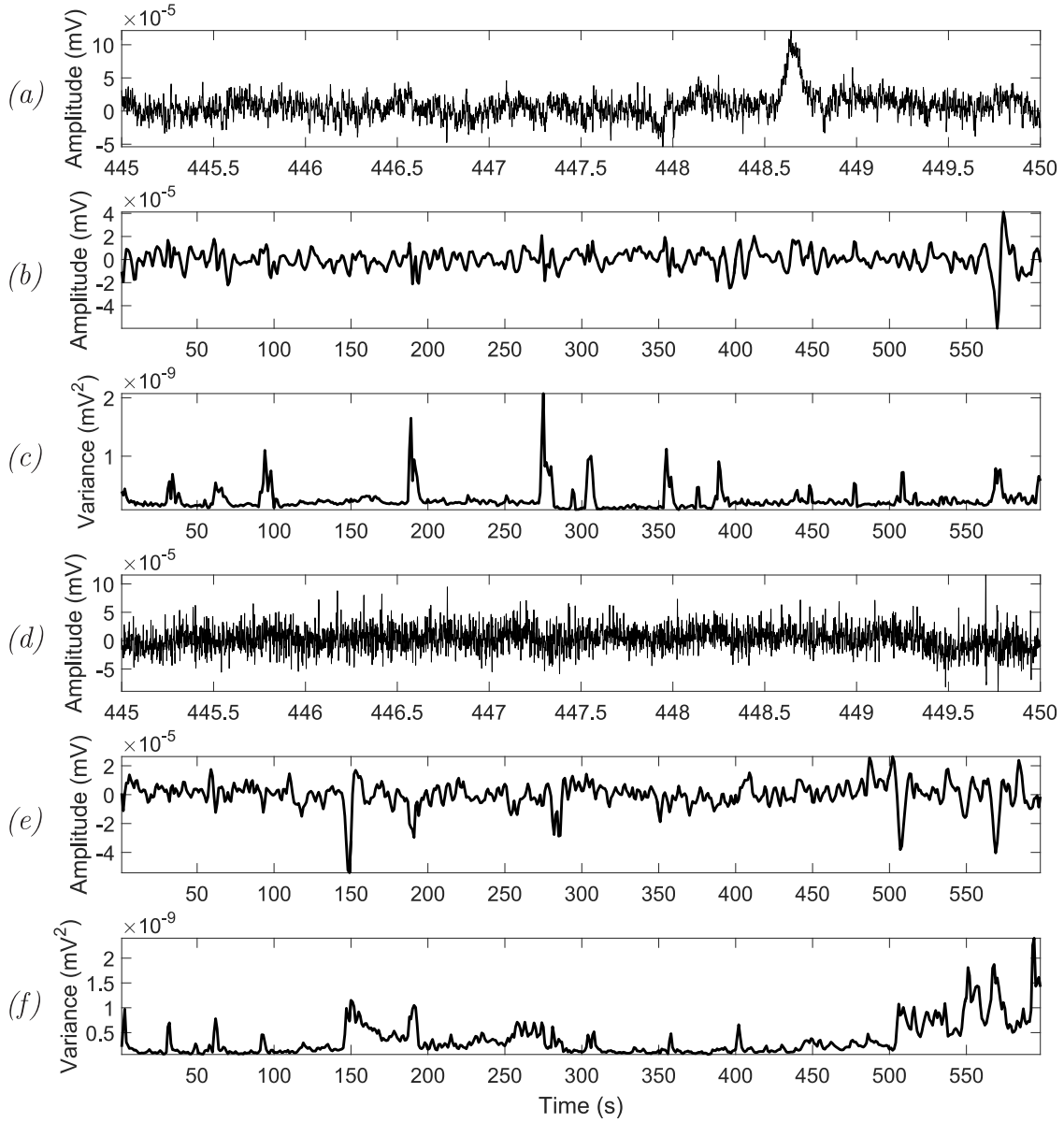


Figure 5.4: **On-scalp EEG signals of Couple 2 from CP4 electrodes, the means, and the variances**. *(a)* On-scalp EEG signal of Subject 1 from CP4 electrode. *(b)* Means of the on-scalp EEG signal of Subject 1. *(c)* Variances of the on-scalp EEG signal of Subject 1. *(d)* On-scalp EEG signal of Subject 2 from CP4 electrode. *(e)* Means of the on-scalp EEG signal of Subject 2. *(f)* Variances of the on-scalp EEG signal of Subject 2. The means and the variances were calculated using 2-second sliding windows with 1-second overlap (1-second increment). The time-varying means and variances indicate that the signals were not WSS.

5.2.3 Neuronal Synchrony Estimation

The EEG signals of each couple were downsampled from 1200 Hz to 120 Hz using the 'resample' function in Matlab, whereby the 'P' and 'Q' values for the resample function were set to 1 and 10 respectively (new sampling frequency = original sampling frequency * P / Q). Figures 5.3&5.4 show respectively ear-EEG and on-scalp EEG signals, together with the means and the variances, of Couple 2. The means and the variances were calculated using 2-second sliding windows with 1-second overlap (1-second increment). The time-varying means and variances indicate that both the ear-EEG and on-scalp EEG signals were not WSS. The EEG signals from all the considered electrodes were combined into 10-channel data which were decomposed using NA-MEMD with 10 additional WGN channels. The IMFs produced by the NA-MEMD with indices 2–5 of the 10-channel multivariate EEG signal contained the physically meaningful frequency range 3 to 13 Hz, that is, the theta and alpha bands of EEG. The full band of interest in the EEG data was produced by summing up these IMFs, in order to obtain the desired scale in data. For SCI estimation, frequency resolution of both the univariate and multivariate STFT-based synchrosqueezing transforms was set to 0.05 Hz instead of having its value determined by the data length as originally proposed in [68, 70], which makes both the univariate and multivariate synchrosqueezing transforms of long data computationally prohibitive. Since EEG signals typically exhibit $1/f$ frequency-domain characteristics, where a large amount of power is contained in lower frequencies, and the IMFs which contained both the theta and alpha bands were chosen, peaks in the theta band could be considerably larger than peaks in the alpha band, resulting in a biased SCI estimation (see Eq. 4.1, whereby the maximum value is used in the calculation). Therefore, in order to achieve un-biased, reliable SCI estimation, SCI values for the theta and alpha bands were estimated separately, and outliers – any values which were higher than 10 standard deviations[2] and could cause unreliable estimation – were also removed from the numerator and de-nominator in Eq. 4.1.

[2]The threshold of 10 standard deviations was employed since it was empirically found to reliably detect very large spurious peaks or spikes (i.e. artefacts) in the estimated SCI values of the EEG signals.

5.3 Results

5.3.1 Time-frequency Representations of Neuronal Synchrony

Figure 5.5 *(a-b)* respectively show SCI values for the single-player and cooperative trials between Couple 1 estimated from ear-EEG recordings, and Figure 5.5 *(c)* shows the timings of the levels played by Couple 1. Note that Couple 1 finished level 5 within the 5 minutes given, so they played levels 1 and 2 again. In the cooperative trial, observe two clusters (see the two solid ellipses) of decreased SCI values in the lower theta band in levels 4&5 (the hard tasks requiring cooperation). This was due to the suppression of power in the lower theta band in both the subjects (power desynchronisation, synchronous decreases in power), suggesting synchronous increases in the levels of attention between them when performing the cooperative tasks. Also, during level 4 a cluster of increased SCI values can be observed in the upper theta band (see the broken ellipse). This was presumably because working memory also played a role in cooperation, that is, each of the participants subconsciously memorised their actions – the timings of pressing the keys for moving the bar up or down – and adjust them so as to successfully cooperate with the other to keep the fast moving bar inside the designated area.

5.3.2 Frequency-averaged, Time-varying Neuronal Synchrony

In order to compare ear-EEG for detecting neuronal synchrony against on-scalp EEG, average SCI values were calculated from 10-second sliding windows with 5-second overlap (5-second increment) in each of the subbands (see the red rectangles in Figure 5.5 *(b)*) for both ear-EEG and on-scalp EEG recorded during the same *cooperative* trial. For each sliding window, the Z-test at a significance level of 0.01 was performed, in order to reveal statistical differences in the SCI values between that window and the *whole* corresponding subband in the single-player trial. Since the subjects must be more attentive while cooperating, power desynchronisation, i.e. synchronous decreases in power, in the lower alpha and theta bands, to a different extent, was expected. Therefore, *SCI values in the lower alpha and theta*

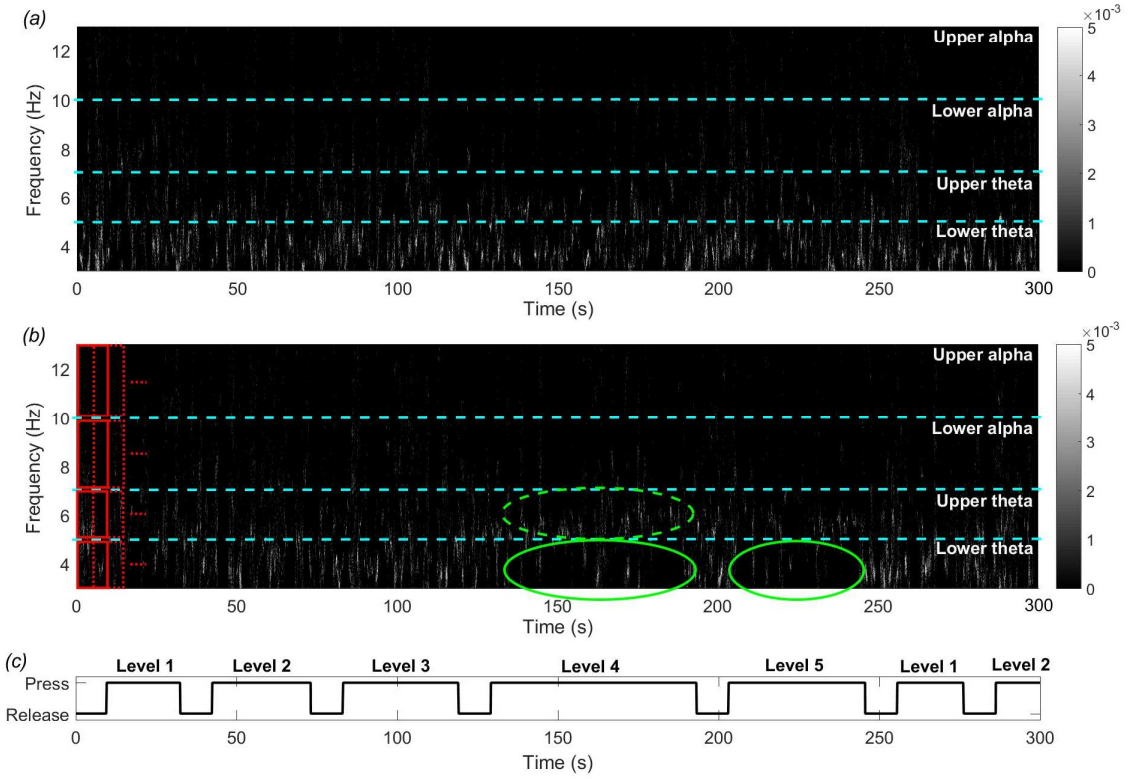


Figure 5.5: **Time-frequency neuronal synchrony between Couple 1 estimated from ear-EEG recordings**. *(a-b)* The SCI between Couple 1 respectively for the single-player and cooperative trials. *(c)* Time intervals for the 5 levels played in the cooperative trial. The couple finished level 5 within the 5 minutes given, so they played levels 1&2 again. Observe power desynchronisation, i.e. synchronous decreases in power, in the lower theta band during levels 4&5 in the cooperative trial (solid ellipses), and power synchronisation in the upper theta band during level 4 in the same trial (broken ellipse). Sliding windows of 10 seconds with 5-second overlap (5-second increment) were used to calculate average SCI values in each subband of the cooperative trial. These average SCI values were statistically tested against SCI values for the whole corresponding subband in the single-player trial.

bands for the cooperative trial were deemed statistically significant – significant SCI values – if they were statistically lower than the SCI values for the corresponding subbands in the single-player trial. Working memory to an extent was also related to the cooperation, increases in power and *SCI values in the upper theta bands were therefore deemed significant – significant SCI values – if they were they statistically higher than those for the same subband in the single-player trial.* Since verbal communication was prohibited during the experiment, semantic memory had no role in the cooperation and the significant SCI values in the upper alpha band – the ones that were statistically lower than those in the single-player trial – do not have any implication on the comparison between ear-EEG and on-scalp EEG.

Figure 5.6 shows average SCI values estimated from the 4 subbands of ear-EEG and on-scalp EEG recordings of Couple 1. Clusters of significant SCI values (black dots) for both the ear-EEG and on-scalp EEG recordings can be observed in levels 4&5 (the hard tasks requiring cooperation) in the lower theta band (see the two solid ellipses) and in level 4 in the upper theta band (see the broken ellipse). These conform with the visual observations on the clusters of decreased and increased SCI values for ear-EEG from Figure 5.5 *(b)*. Figure 5.7 shows average SCI values estimated from the 4 subbands in ear-EEG and on-scalp EEG recordings of Couple 2. Clustering in both the recording modalities can also be observed from this couple (see the 3 ellipses), and is similar to the clustering of SCI values in the hard tasks for Couple 1. For Couple 3 (see Figure 5.8), however, clusters of significant SCI values for both the modalities cannot be observed; significant SCI values were mostly detected through the ear-EEG recording only. Similar clustering for both recording modalities in the lower theta band can also be observed in Couples 4–6. Clustering of significant SCI values in the lower and upper theta bands in the hard tasks was presumably due to synchronous increases in the levels of attention and working memory of the couples while cooperatively playing the game.

5.3.3 Correlation in Time-varying Neuronal Synchrony between the Modalities

Figure 5.12 shows average correlation coefficient (ρ) in time-varying neuronal synchrony in the 4 subbands between the ear-EEG and on-scalp EEG recordings averaged over the six couples. The highest correlation in time-varying SCI values between the two recording modalities can be observed in the lower theta band, associated with attention, and the lowest correlation in the upper alpha band, associated with semantic memory. Both the recording modalities were most correlated in synchrony detection in the lower theta band. Figure 5.13 shows correlation coefficient in time-varying neuronal synchrony in the 4 subbands between the recording modalities of each couple. For most of the couples the lower theta band exhibited the most correlation between the recording modalities, except for Couple 4, where both the recording modalities were most correlated in the lower alpha band, the other EEG

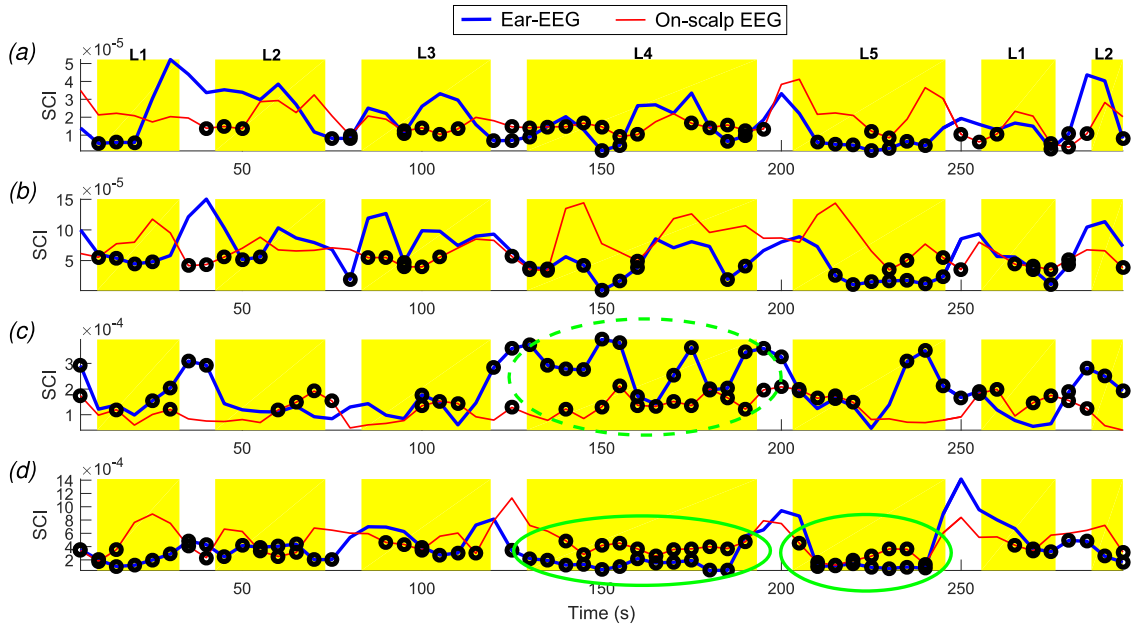


Figure 5.6: **Time-varying neuronal synchrony between Couple 1.** *(a)* The SCI of upper alpha band. *(b)* The SCI of lower alpha band. *(c)* The SCI of upper theta band. *(d)* The SCI of lower theta band. For brevity each level is denoted Lx, with x denoting the level number. Time instants when the couple played each level are depicted by the shaded areas. Significant SCI values are shown in dots. Observe clusters of significant SCI values in the lower theta band during levels 4&5 (solid ellipses) and in the upper theta band during level 4 (broken ellipse) for both the recording modalities. These conform with the visual observations from Figure 5.5 *(b)*

.

frequency band associated with attention. The highest correlations between the recording modalities in the lower theta band was presumably due to synchronous increases in the levels of attention of the couples while cooperatively playing the game, manifested itself in most similar patterns of time-varying neuronal synchrony in the lower theta band.

5.3.4 Proportions of Significant Neuronal Synchrony Detected

Figure 5.14 *(a-d)* respectively shows average proportion of the number of significant SCI values detected (i.e. observed) in each level in the lower theta, upper theta, lower alpha, and upper alpha bands of all the ear-EEG and on-scalp EEG recordings of the six couples. The proportion was calculated by dividing the number of *detected (i.e.*

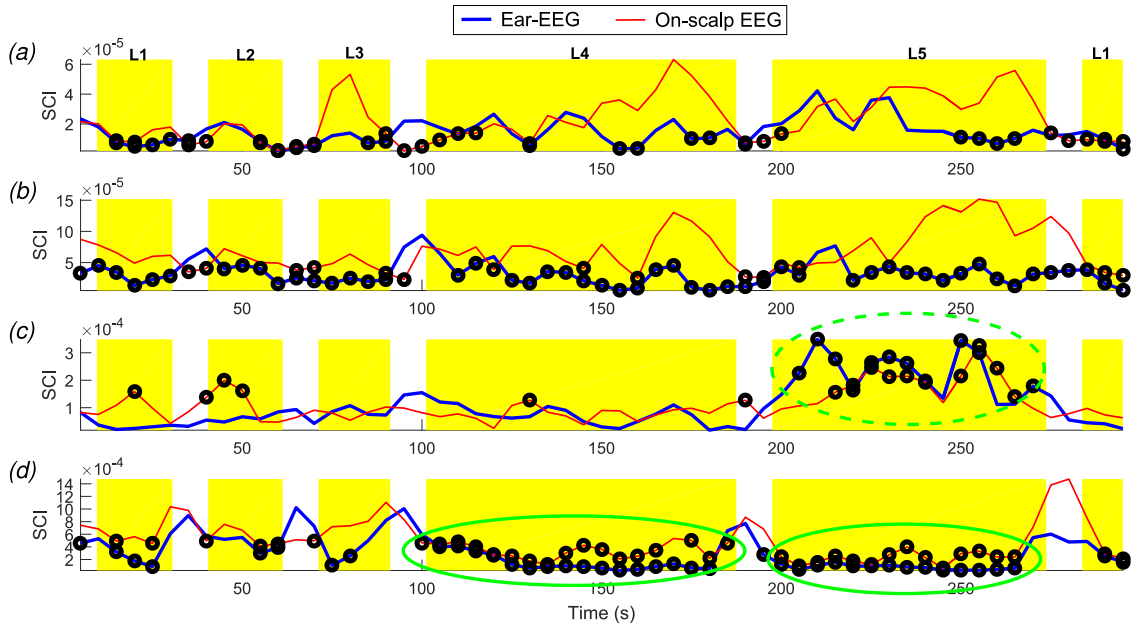


Figure 5.7: **Time-varying neuronal synchrony between Couple 2.** *(a)* Upper alpha band. *(b)* Lower alpha band. *(c)* Upper theta band. *(d)* Lower theta band. For brevity each level is denoted Lx, with x denoting the level number. Time instants when the couple played each level are depicted by the shaded areas. Significant SCI values are shown in dots. Observe clusters of significant SCI values in the lower theta band during levels 4&5 (solid ellipses) and in the upper theta band during level 5 (broken ellipse) for both the recording modalities. These are similar to the clusters in Figure 5.6, where the clusters can be observed in the hard tasks (levels 4&5).

observed) significant SCI values in that level[3] by the number of *possible* SCI values in that level[4], and the proportion was averaged over the six couples. In the lower theta band the proportion of significant SCI values detected was highest in levels 4&5 (the hard tasks) for both the ear-EEG and on-scalp recordings (approximately 64%–72%, see the solid ellipse) compared to only approximately 36%–51% in levels 1–3 (the easy tasks, see the broken ellipse). This distinct discrimination between the easy and hard tasks was exhibited by both the ear-EEG and on-scalp EEG recordings. For the other subbands, however, similar discrimination by both the recording modalities cannot be observed. Figure 5.15 shows proportion of the number of significant SCI values detected in each level of both the recording modalities of each couple. Due to low numbers of detected significant SCI values and possible SCI values in each

[3]The number of *detected* or *observed* significant SCI values in that level is the number of significant SCI values for each level in the cooperative trial which were found to be statistically lower, in the lower theta and alpha bands, or higher, in the upper theta band, than SCI values for the same subband in the single-player trial.

[4]The number of possible SCI values in that level is the number of SCI values calculated for each level in the cooperative trial. For example, by using 10-second sliding windows with 5-second overlap (5-second increment) to calculate the frequency-averaged, time-varying SCI values, 13 SCI values were obtained within a period of 65 seconds.

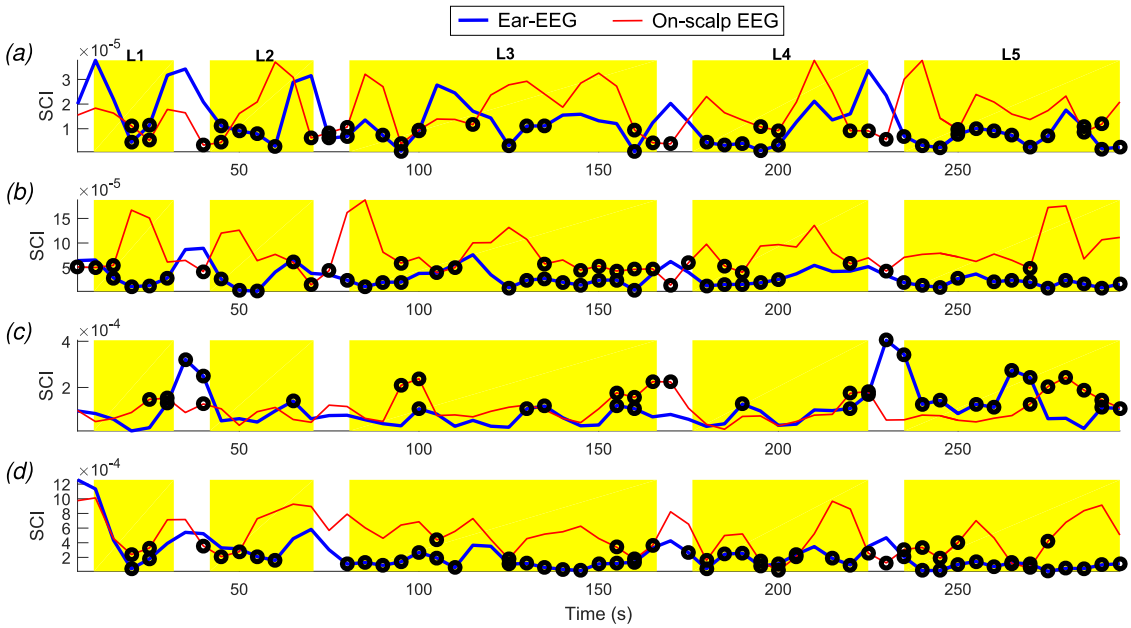


Figure 5.8: **Time-varying neuronal synchrony between Couple 3.** *(a)* Upper alpha band. *(b)* Lower alpha band. *(c)* Upper theta band. *(d)* Lower theta band. For brevity each level is denoted Lx, with x denoting the level number. Time instants when the couple played each level are depicted by the shaded areas. Significant SCI values are shown in dots. Clusters of significant SCI values for both the recording modalities in the hard tasks cannot be observed from this couple. Significant SCI values were mostly detected through ear-EEG only.

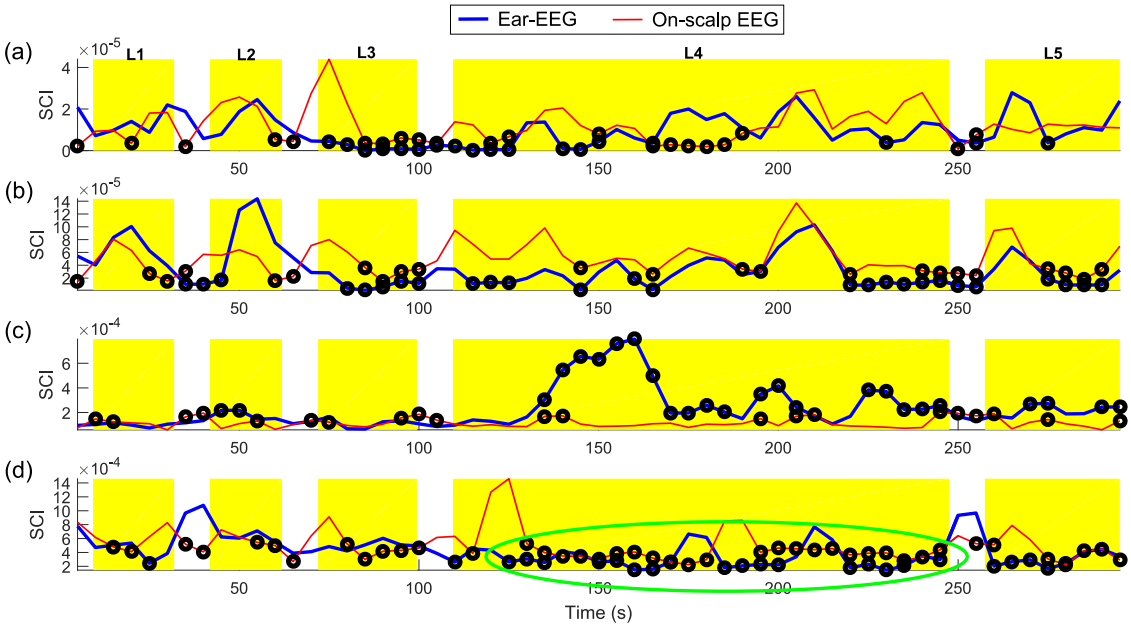


Figure 5.9: **Time-varying neuronal synchrony between Couple 4.** *(a)* The SCI of upper alpha band. *(b)* The SCI of lower alpha band. *(c)* The SCI of upper theta band. *(d)* The SCI of lower theta band. For brevity each level is denoted Lx, with x denoting the level number. Time instants when the couple played each level are depicted by the shaded areas. Significant SCI values are shown in dots. Observe clusters of significant SCI values in the lower theta band during level 4 (solid ellipse).

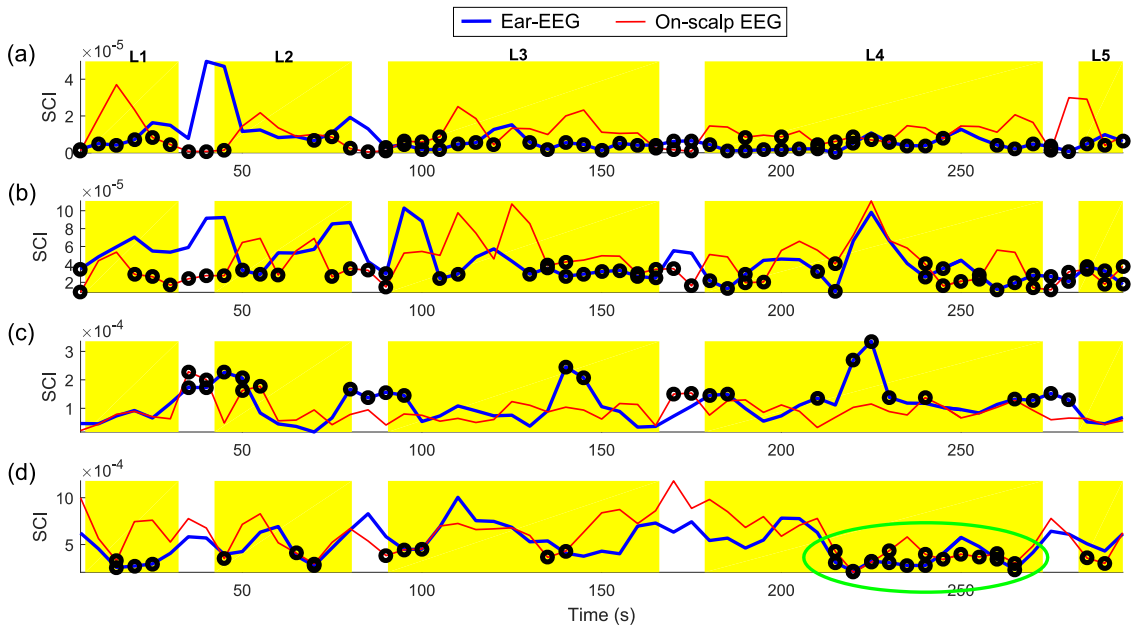


Figure 5.10: **Time-varying neuronal synchrony between Couple 5.** *(a)* The SCI of upper alpha band. *(b)* The SCI of lower alpha band. *(c)* The SCI of upper theta band. *(d)* The SCI of lower theta band. For brevity each level is denoted Lx, with x denoting the level number. Time instants when the couple played each level are depicted by the shaded areas. Significant SCI values are shown in dots. Observe clusters of significant SCI values in the lower theta band during level 4 (solid ellipse).

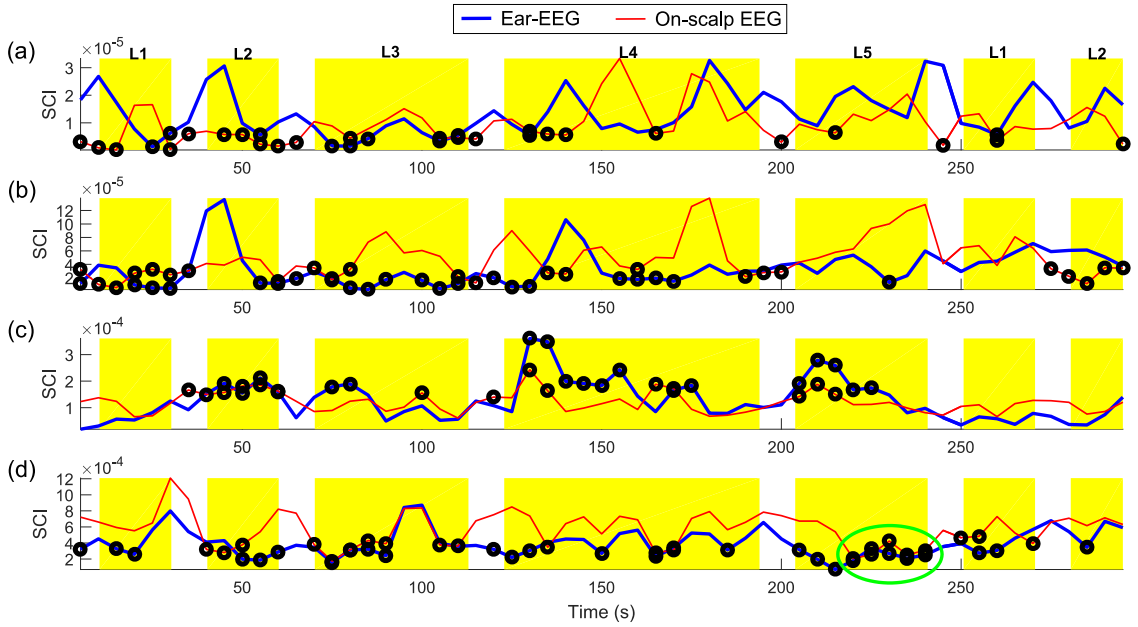


Figure 5.11: **Time-varying neuronal synchrony between Couple 6.** *(a)* The SCI of upper alpha band. *(b)* The SCI of lower alpha band. *(c)* The SCI of upper theta band. *(d)* The SCI of lower theta band. For brevity each level is denoted Lx, with x denoting the level number. Time instants when the couple played each level are depicted by the shaded areas. Significant SCI values are shown in dots. Observe clusters of significant SCI values in the lower theta band during level 5 (solid ellipse).

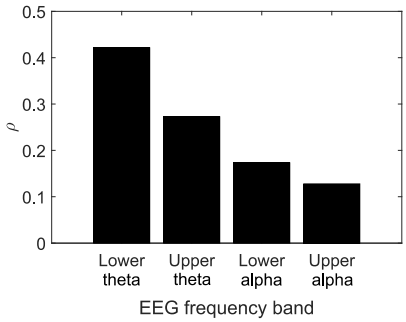


Figure 5.12: **Average correlation in neuronal synchrony between the recording modalities averaged over the six couples.** The ear-EEG and on-scalp EEG recordings were most correlated in the lower theta band, associated with attention, and least correlated in the upper alpha band, associated with semantic memory.

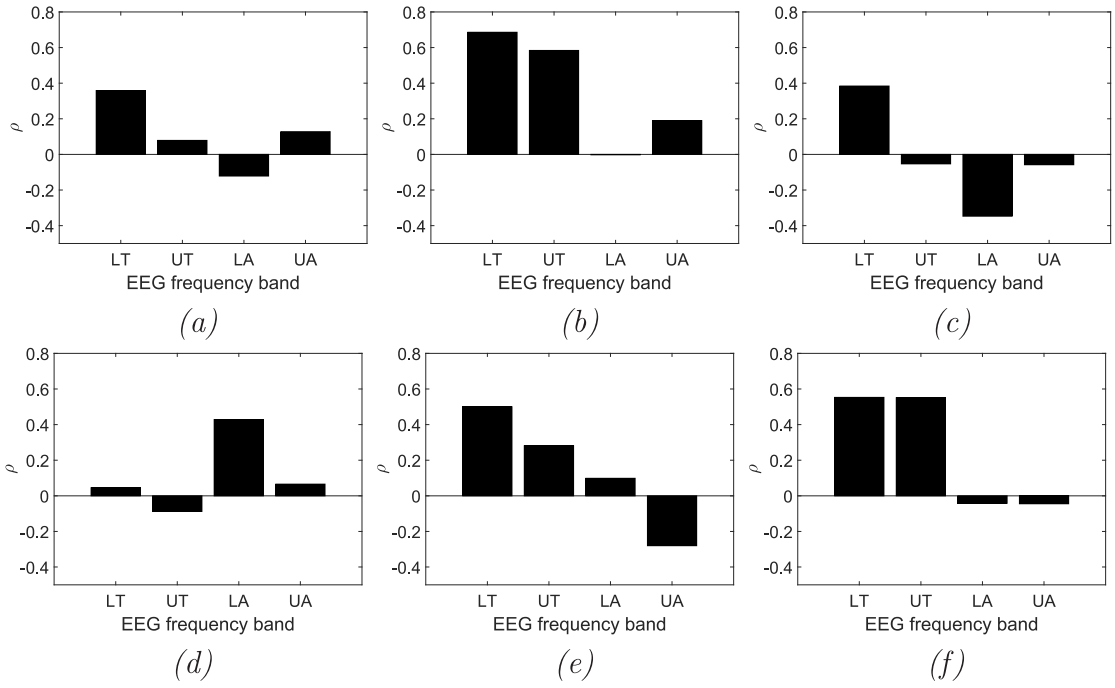


Figure 5.13: **Correlation in neuronal synchrony between the recording modalities of each couple.** *(a)* Couple 1. *(b)* Couple 2. *(c)* Couple 3. *(d)* Couple 4. *(e)* Couple 5. *(f)* Couple 6. For brevity LT=lower theta, UT=upper theta, LA=lower alpha, and UA=upper alpha. The ear-EEG and on-scalp EEG recordings were most correlated in the lower theta band for most of the couples, except for Couple 4.

level for each couple, distinct discrimination between the easy and hard tasks in the lower theta band in both the recording modalities can be distinctly observed in only Couples 2 and 4. The average proportion shown in Figure 5.14 obtained by taking all the couples into account, therefore, exhibited the more distinct discrimination.

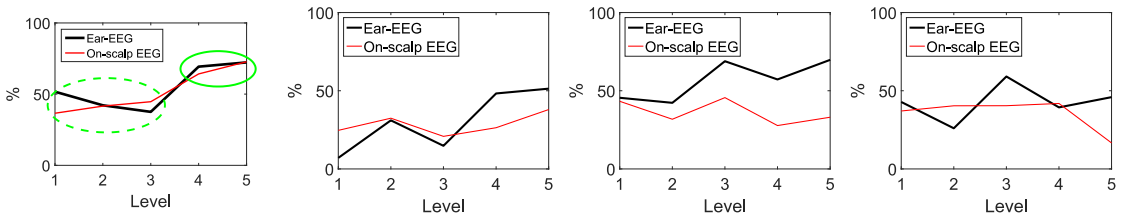


Figure 5.14: **Average proportion of the number of significant SCI values detected in each level from ear-EEG and on-scalp EEG recordings averaged over the six couples**. *(a)* Lower theta band. *(b)* Upper theta band. *(c)* Lower alpha band. *(d)* Upper alpha band. For both the recording modalities neuronal synchrony estimated from the lower theta band exhibited distinct discrimination between the easy and hard tasks.

5.3.5 Time-averaged Significant Neuronal Synchrony

In addition to considering the proportion of significant SCI values detected, time-average significant SCI values were calculated for the easy and hard tasks in each subband of both the recording modalities, as shown in Figure 5.16 *(a-b)*. For each subband and recording modality, the Z-test at a significance level of 0.05 was performed, in order to reveal statistical differences in the SCI values between the easy (levels 1–3) and hard (levels 4&5) tasks. For the lower and upper theta bands of both the recording modalities, the hard tasks respectively exhibited significantly lower and higher SCI values than the easy tasks (see the solid and broken ellipses). Figure 5.17 shows time-average significant SCI values of each couple. Observe lower and higher average SCI values in the hard task in the lower and upper theta bands respectively. Robust statistical relevance, however, cannot obtained due to the low numbers of significant SCI values.

5.3.6 Power of EEG Activities in the Lower Theta Band

In order to verify the occurrences of power desynchronisation, i.e. synchronous decreases in power, of EEG activities and, thus, lower SCI values, in the lower theta band, the average power of EEG activities of each couple in this subband during each pause and level in the cooperative trial (i.e. the desired activities) was calculated and was compared against the average power of instrumentation noise in the same subband. To obtain instrumentation noise, sensing electrodes were connected to the

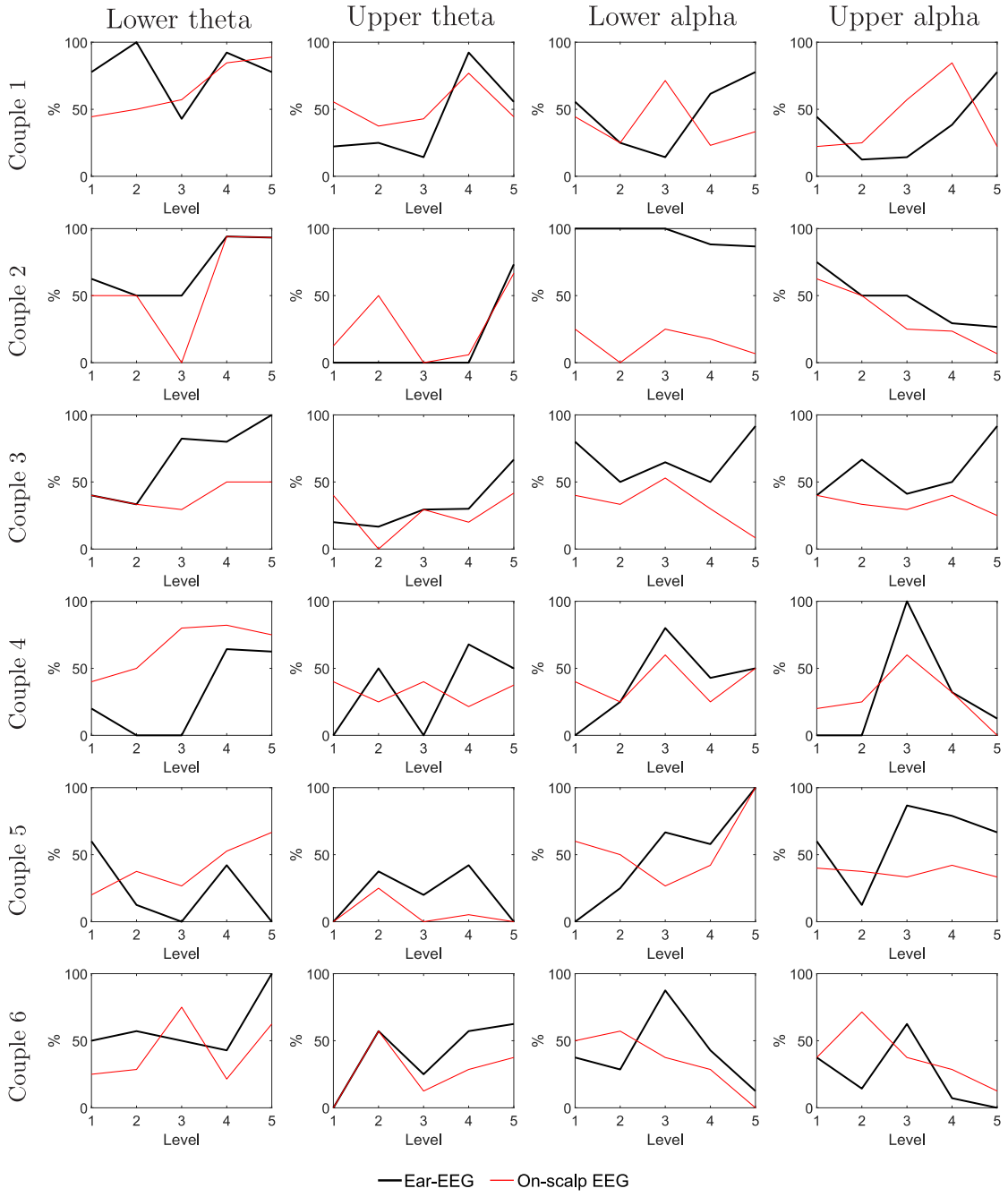


Figure 5.15: **Proportion of the number of significant SCI values detected in each level from ear-EEG and on-scalp EEG recordings of each couple**. Distinct discrimination between the easy and hard tasks in the lower theta band in both the recording modalities can be observed in only Couples 2 and 4 due to low numbers of observed and possible significant SCI values in each level for each couple.

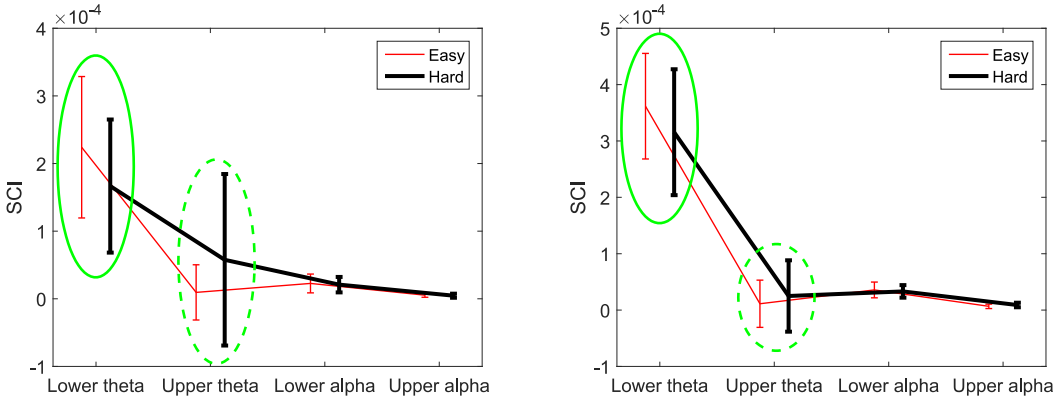


Figure 5.16: **Average significant SCI values in the easy and hard tasks estimated from each subband of ear-EEG and on-scalp EEG recordings averaged over the six couples.** *(a)* Ear-EEG. *(b)* On-scalp EEG. Neuronal synchrony in the lower theta band between the couples statistically decreased from the easy tasks to the hard tasks for both the recording modalities, while it statistically increased in the upper theta band for both the recording modalities.

corresponding grounds and references, and a 1-minute recording was performed using g.USBamp. Figure 5.18 shows the average power of EEG activities of each couple in the lower theta band for both the recording modalities during the cooperative trial, compared to the power of the instrumentation noise. Observe: (i) the powers of EEG activities during the cooperative trial of both the recording modalities typically exhibited similar patterns – increased during pauses and decreased during levels and (ii) the powers of ear-EEG and on-scalp EEG activities of all the couples were all higher than the corresponding powers of the instrumentation noise. Both the observations strongly suggest that the reduction in powers of both the ear-EEG and on-scalp EEG activities in the lower theta band while performing the cooperative tasks truly existed.

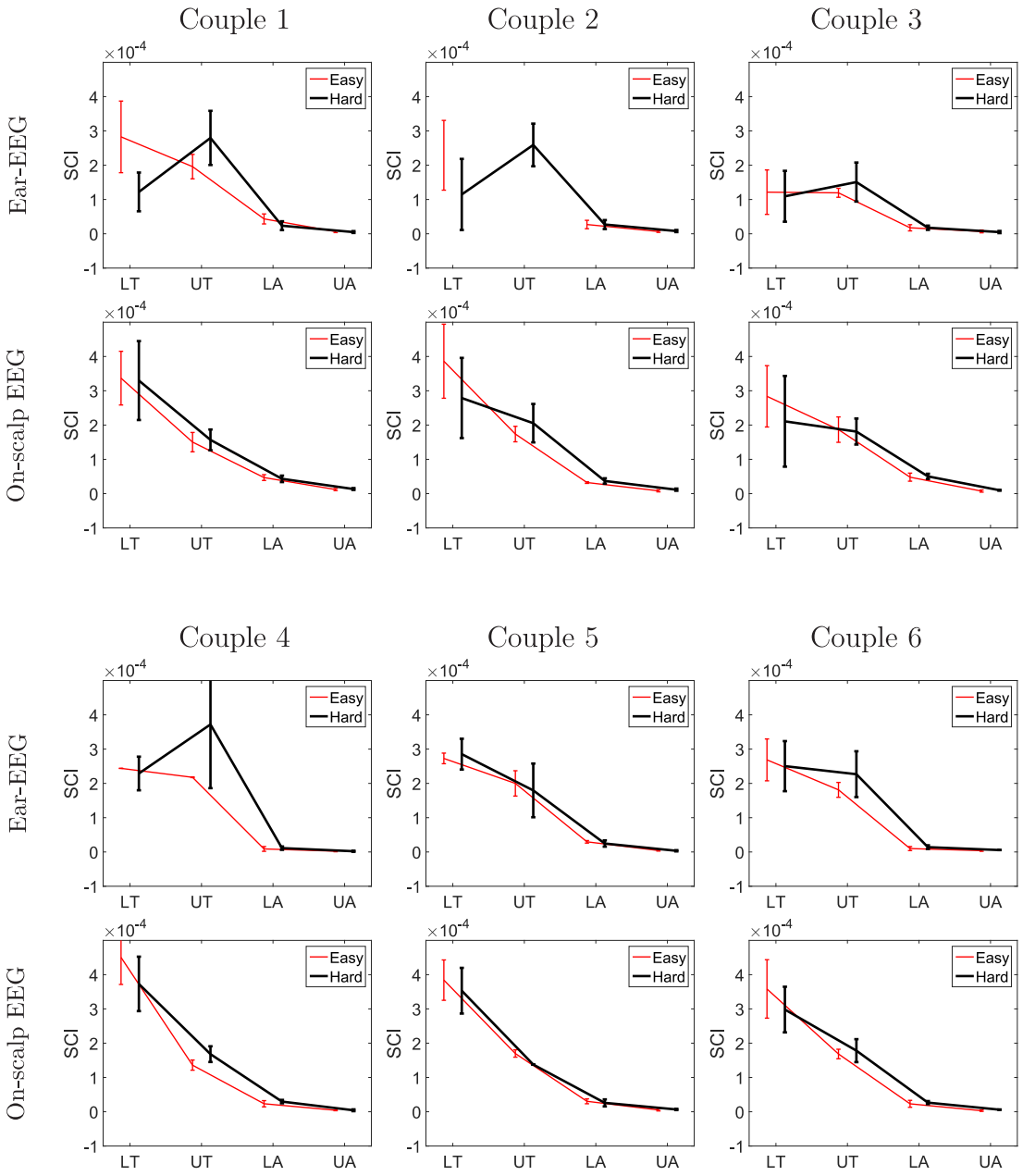


Figure 5.17: **Average significant SCI values in the easy and hard tasks estimated from each subband of ear-EEG and on-scalp EEG recordings of each couple.** For brevity LT=lower theta, UT=upper theta, LA=lower alpha, and UA=upper alpha. Note that average significant SCI values in the hard task for the upper theta band of on-scalp EEG recording of Couple 2 cannot be calculated, since there were no significant SCI values in this task and EEG frequency band of this recording modality of this couple. Observe lower and higher average SCI values in the hard task in the lower and upper theta bands respectively.

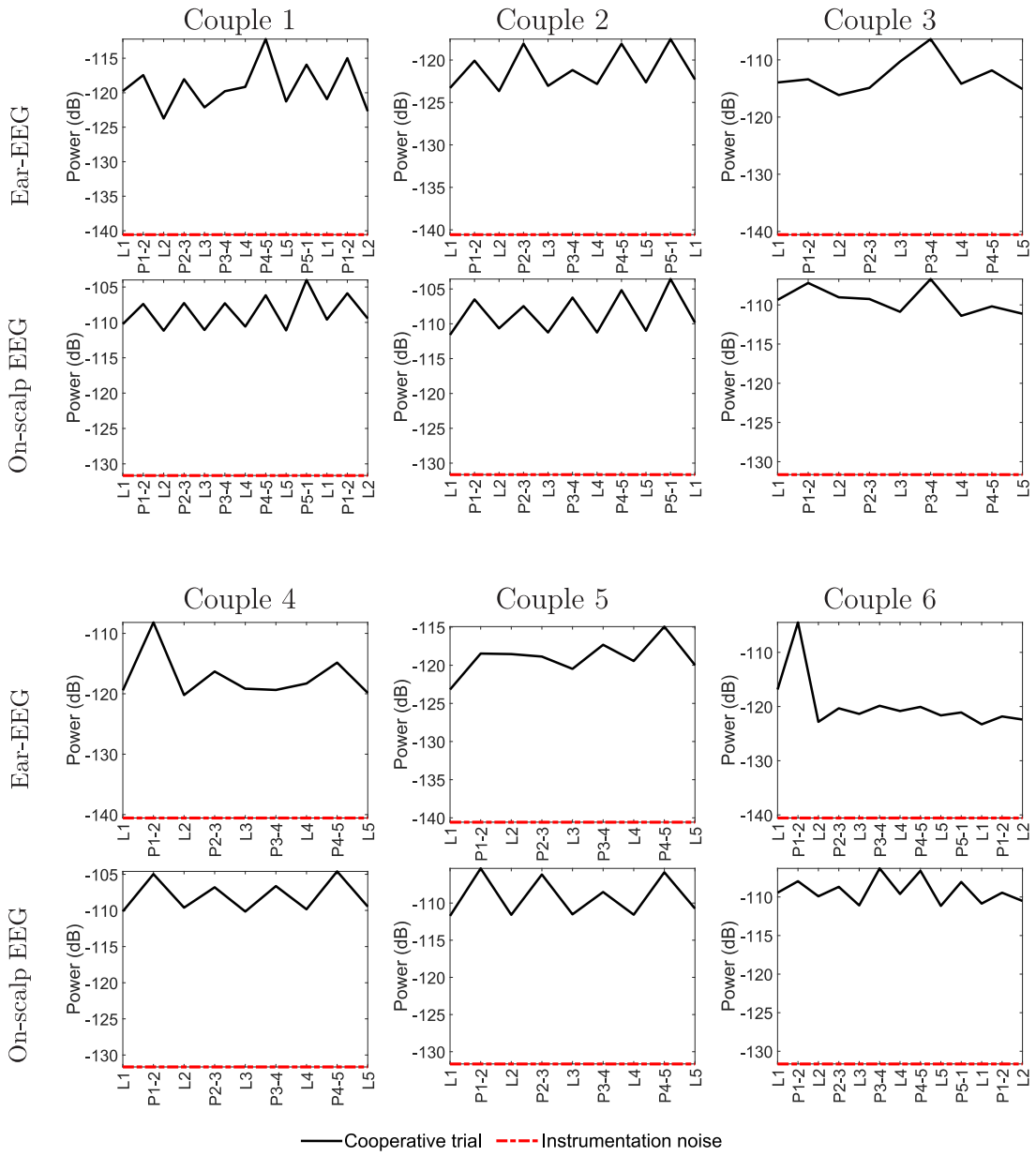


Figure 5.18: **Average power of EEG activities in the lower theta band of both the recording modalities of each couple during the cooperative trial compared to the power of instrumentation noise**. For brevity each level is denoted Lx, with x denoting the level number, and each pause between two levels is denoted Py-z, with y and z denoting two consecutive levels. Observe that both the recording modalities exhibit similar patterns, and that the powers of ear-EEG and on-scalp EEG activities of all the couples were all higher than the corresponding powers of the instrumentation noise.

5.4 Summary

A novel time-frequency data association measure, termed intrinsic synchrosqueezing coherence, has been employed in order to evaluate the performance of ear-EEG against on-scalp EEG as an alternative, practical real-world approach for the hyperscanning technique in the task of identifying the unknown, most robust EEG frequency band for neuronal synchrony detection for cooperative multi-player gaming.

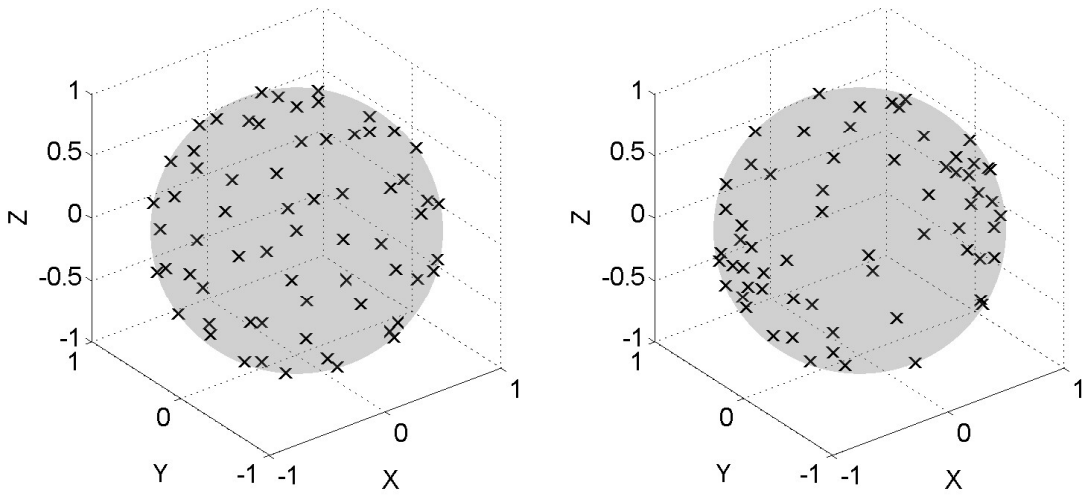
On-scalp EEG recordings were obtained with conventional EEG electrodes placed on the brain regions which were expected to synchronise during the cooperation of six couples of subjects. Ear-EEG signals were acquired at the same time, and intrinsic synchrosqueezing coherence (ISC) was then employed to estimate neuronal synchrony between the subjects through both the ear-EEG and on-scalp EEG recordings. Through unambiguous physical interpretation of neuronal synchrony produced by the ISC algorithm, both the recording modalities have effectively exhibited power desynchronisation (synchronous decreases in power) in the lower theta band of EEG which associates with attention. It should be noted that an EEG subband which exhibits distinct neural synchrony can vary from task to task, depending upon the cognitive demands. For the Bar Balancing game, the cooperation was presumably mediated by joint attention and, to an extent, adaptive working memory of the participants, reflected respectively by the synchronous decreases and increases in power and, thus, SCI values in the lower and upper theta bands for both the recording modalities. This study also has exhibited that through both the recording modalities the lower theta band was the most robust neuronal marker for brain synchronisation during such a cooperative task, since: (i) it exhibited the highest correlation in neuronal synchrony between the modalities, (ii) in this subband the average proportions of significant neuronal synchrony detected in the easy and hard tasks yield enhanced discrimination ability by both the modalities, and (iii) in this subband the average values of significant neuronal synchrony for both of the tasks were statistically different in both the modalities. It should be noted that the differences in performances of both the recording modalities in detecting neural synchrony could be caused by different sources of variation, such as different pairs of subjects and different days of recordings.

Chapter 6

Adaptive-projection Intrinsically Transformed MEMD (APIT-MEMD) in Cooperative Brain-computer Interface Applications

6.1 Introduction

Physiological signals often contain power imbalances or inter-channel correlation due to different electrode impedances and adjacent locations of the electrodes. Despite recent progress in computationally efficient MEMD for unbalanced data, a solution for the general multivariate case was still lacking. In addition, as cooperative brain-computer interfaces (BCIs) typically use a number of data channels of cerebral data to acquire 'coupled' information from multiple users to enhance information transfer rate (ITR), an analysis approach which would adapt to the dynamics of the multichannel data and would be capable of revealing 'intrinsic and correlated' inter-channel information with physically meaningful interpretation would be of great importance. To this end, this work extends NS-TEMD to introduce *adaptive-projection*



(a) *(b)*

Figure 6.1: **Uniform and nonuniform projection vectors**. *(a)* Uniform projection vectors based on a low-discrepancy Hammersley sequence. *(b)* Nonuniform projection vectors for NS-TEMD when accounting for inter-channel dependence.

intrinsically transformed MEMD (APIT-MEMD), which caters for power imbalances and correlations in multichannel data. Similarly to the standard MEMD, the proposed APIT-MEMD accommodates nonlinear and non-stationary signals. It is also capable of alleviating mode mixing for unbalanced data. This work also introduces applications of intrinsic multiscale analysis [8] using noise-assisted APIT-MEMD (NA-APIT-MEMD) to cooperative BCI applications based on SSVEP and P300 responses.

6.2 Algorithm

The NS-TEMD algorithm [65] enhances the performance of the conventional TEMD by relocating the direction vectors, pre-generated using the conventional uniform sampling scheme (see Figure 6.1 *(a)*), to their new positions on an ellipsoid (see Figure 6.1 *(b)*), with the directions and relative powers determined by all the eigenvectors and eigenvalues, representing the directions of principal importance, of the trivariate covariance matrix of the signal. In the case of multivariate signals, relocating the pre-generated n-dimensional uniform projection vectors to their new positions on an n-dimensional ellipsoid using the above scheme is an exceptionally complicated task, not least because the directions of *global* principal importance

of *the original input signal* may not always align with the direction of *local* first principal component of *each sifting input*, resulting in a suboptimal estimate of the local mean.

To address this problem, a projection scheme is proposed, whereby the direction of the first principal component reflecting the largest power imbalance and/or correlation in the channels of the multivariate signal, is determined adaptively. For a given multivariate sifting input, $\mathbf{s}(t)$, with covariance matrix $\mathbf{C} = E\{\mathbf{s}(t)\mathbf{s}^T(t)\}$, where $E\{\cdot\}$ is the statistical expectation operator and $(\cdot)^T$ is the transpose operator, the direction of the first principal component is determined via the eigendecomposition of the covariance matrix, $\mathbf{C} = \mathbf{V}\mathbf{\Lambda}\mathbf{V}^T$, where the matrix $\mathbf{V}$ corresponds to the matrix of eigenvectors and the entries of the diagonal matrix $\mathbf{\Lambda}$ are the corresponding eigenvalues. Subsequently, the first principal component, pointing in the direction of the highest power imbalance, is used to construct a vector pointing in the diametrically opposite direction. These two vectors are subsequently used to relocate the direction vectors pre-generated by the conventional uniform projection scheme. Each sifting operation then projects its multivariate sifting input along these adaptive direction vectors, so as to estimate the local mean; see Algorithm 6.1 for detail of the proposed adaptive-projection intrinsically transformed MEMD (APIT-MEMD).

Algorithm 6.1: Adaptive-projection intrinsically transformed MEMD (APIT-MEMD)

---

1. Given a P-variate input signal to each sifting operation $\mathbf{s}(t)$, perform the eigendecomposition of the covariance matrix, $\mathbf{C} = E\{\mathbf{s}\mathbf{s}^T\} = \mathbf{V}\mathbf{\Lambda}\mathbf{V}^T$, where $\mathbf{V} = [\mathbf{v}_1, \mathbf{v}_2, ..., \mathbf{v}_P]$ is the eigenvector matrix, and $\mathbf{\Lambda} = diag\{\lambda_1, \lambda_2, ..., \lambda_P\}$ is the eigenvalue matrix, with the largest eigenvalue λ_1 corresponding to eigenvector $\mathbf{v}_1$ (first principal component).

2. Construct a vector pointing in the diametrically opposite direction to the first principal component vector in P-dimensional space, $\mathbf{v}_{o1} = -\mathbf{v}_1$.

3. Uniformly sample a (P-1) sphere using the Hammerseley sequence to generate

a set of Q direction vectors $\{s^{\theta_q}\}_{q=1}^{Q}$.

4. Calculate the Euclidean distances from each of the uniform direction vectors to $\mathbf{v}_1$.

5. Half of all the uniform projection vectors, $\mathbf{z}_{\mathbf{v}_1}^{\theta_q}$, nearest to $\mathbf{v}_1$, are relocated using $\hat{\mathbf{z}}_{\mathbf{v}_1}^{\theta_q} = \frac{\mathbf{z}_{\mathbf{v}_1}^{\theta_q} + \alpha \mathbf{v}_1}{|\mathbf{z}_{\mathbf{v}_1}^{\theta_q} + \alpha \mathbf{v}_1|}$, where α is used to control the density of the relocated vectors. The α values can be determined through the degree of power imbalances between data channels, and a suggested range is from 0 (no power imbalance) to 1 (high power imbalances).

6. The other half of all the uniform projection vectors, $\mathbf{z}_{\mathbf{v}_{o1}}^{\theta_q}$, nearest to $\mathbf{v}_{o1}$, are relocated using $\hat{\mathbf{z}}_{\mathbf{v}_{o1}}^{\theta_q} = \frac{\mathbf{z}_{\mathbf{v}_{o1}}^{\theta_q} + \alpha \mathbf{v}_{o1}}{|\mathbf{z}_{\mathbf{v}_{o1}}^{\theta_q} + \alpha \mathbf{v}_{o1}|}$, where α is used to control the density of the relocated vectors.

7. Perform local mean estimation according to the conventional MEMD algorithm, using the adaptive direction vectors $\hat{\mathbf{z}}_{\mathbf{v}_1}^{\theta_q}$ and $\hat{\mathbf{z}}_{\mathbf{v}_{o1}}^{\theta_q}$.

The α values can be determined through the degree of power imbalances between data channels, and a suggested range is from 0 to 1. For $\alpha = 0$, when power imbalances do not exist or are not accounted for, the APIT-MEMD operates similarly to the standard MEMD – no adaptive projection is performed. Conversely, for $\alpha = 1$, the case with high power imbalances between data channels, the APIT-MEMD is perfectly well equipped to deal with the importance-sampling of the signal space.

To illustrate the principle of APIT-MEMD and the adaptive direction of the first principal component of the input to each sifing operation in a 3-dimensional space, which consequently determines the positions of the relocated projection vectors, Figure 6.2 *(a-c)* shows the first, second and third channels, respectively, of a trivariate signal, given by

$$\begin{aligned} x_1(t) &= k_1 \cos(2\pi f_1 t) + k_1 \cos(2\pi f_2 t) + n(t), \\ x_2(t) &= k_2 \sin(2\pi f_2 t), \\ x_3(tn &= k_1 \sin(2\pi f_1 t), \end{aligned} \tag{6.1}$$

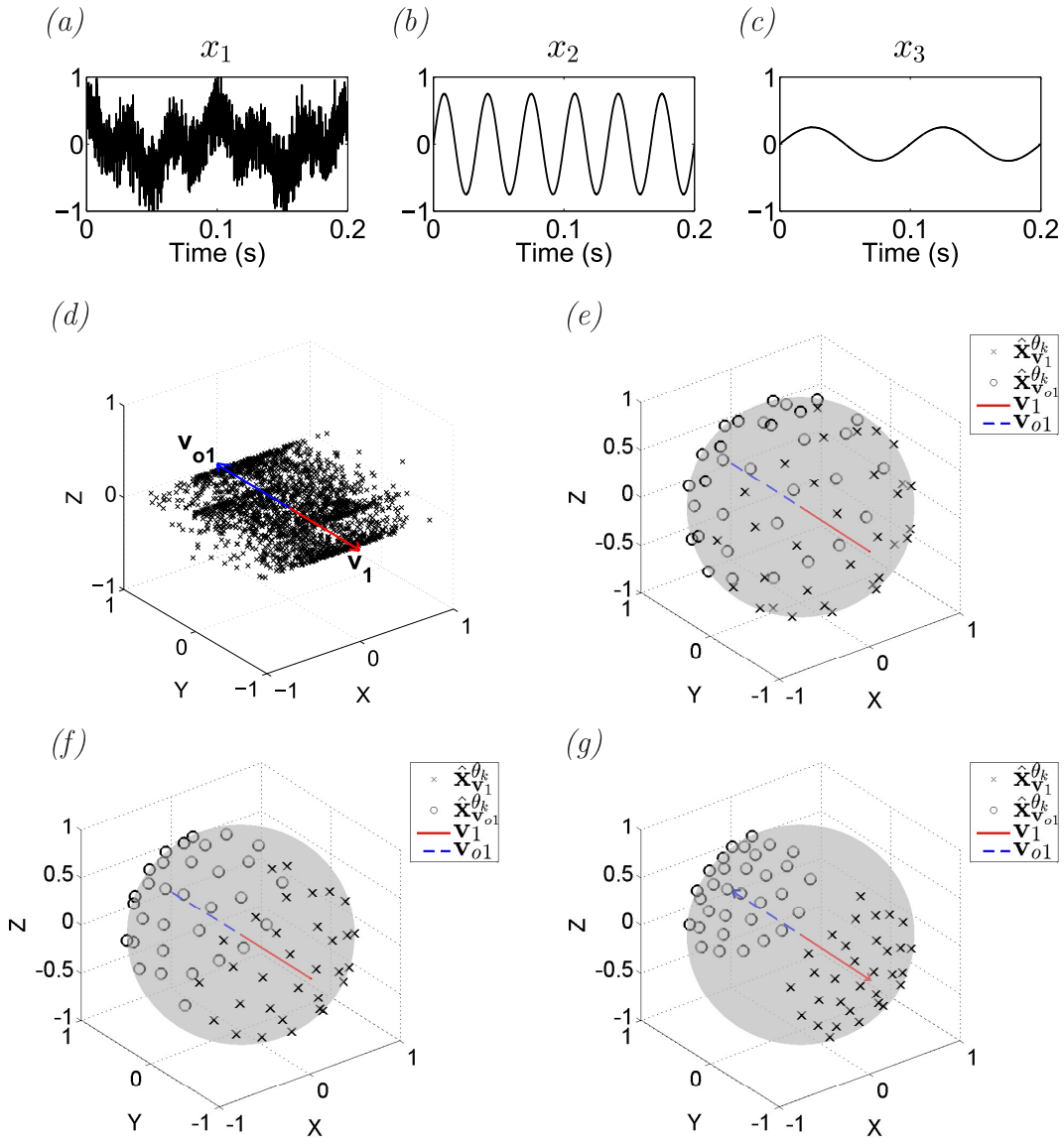


Figure 6.2: **Input signal to the first sifting operation**. *(a-c)* The three data channels considered. *(d)* Scatter plot of the trivariate data, first principal component and its diametrically opposite vector. *(e-g)* Projection vectors adapted according to the proposed scheme using different α values (0, 0.5 and 1, respectively).

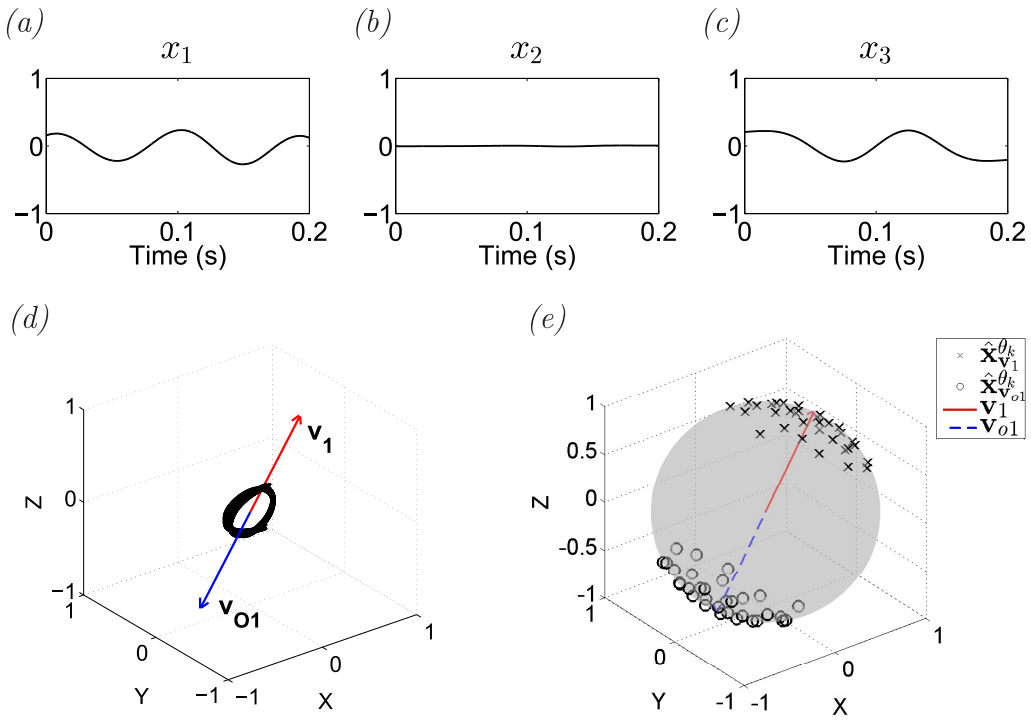


Figure 6.3: **Input signal to a sifting operation**. *(a-c)* 3-channel data. *(d)* Scatter plot of the 3-channel data, the first principal component and its opposite. *(e)* Projection vectors adapted to first principal component and the opposite vector.

where $n(t)$ denotes the added WGN and k_1 and k_2 are scalars which define the degrees of power imbalances between the data channels. In this example, the signal SNR of the first channel was 0 dB, $k_1 = 0.25$, $k_2 = 0.75$, f_1=10 Hz and f_2=30 Hz, with a sampling frequency of 10 kHz. Figure 6.2 *(d)* shows the scatter plot of the input signal in a 3-dimensional space, together with the first principal component, $\mathbf{v}_1$, and the diametrically opposite vector, $\mathbf{v}_{o1}$. Figure 6.2 *(e-g)* shows the projection vectors adapted to the direction of highest power imbalance, $\hat{\mathbf{z}}^{\theta_k}_{\mathbf{v}_1}$ and $\hat{\mathbf{z}}^{\theta_k}_{\mathbf{v}_{o1}}$, of the input. The densities of the projection vectors were controlled by different α values (0, 0.5 and 1). Observe that the relocated direction vectors, $\hat{\mathbf{z}}^{\theta_k}_{\mathbf{v}_1}$ and $\hat{\mathbf{z}}^{\theta_k}_{\mathbf{v}_{o1}}$, were clustered around the corresponding 'centroids', $\mathbf{v}_1$ and $\mathbf{v}_{o1}$, and that the density of the direction vectors increased with the α values. For the trivariate signal considered, $\alpha = 1$ was used in order for the APIT-MEMD to capture the directions of highest power imbalances. The input data to the first sifting operation was then projected along all the resulting adaptive projection vectors generated, to estimate the local mean within the sifting algorithm.

After a number of sifting operations, several IMFs containing decomposed WGN and

the higher frequency component in x_1 and x_2, that is f_2, were obtained, resulting in the remaining lower frequency component in x_1 and x_3, that is f_1, as shown in Figure 6.3 *(a-c)*; the remaining 3-channel data was then fed into the next sifting operation. Figure 6.3 *(d)* shows the scatter plot of the remaining signal, together with the $\mathbf{v}_1$ and $\mathbf{v}_{o1}$, and Figure 6.3 *(e)* shows projection vectors adapted to the dynamics of the remaining signal.

6.3 Simulation Results

Performance of the proposed APIT-MEMD algorithm was evaluated using simulations on multivariate signals with different channel powers with and without the assistance of WGN, and real-world P300 responses measured via EEG.

6.3.1 Reconstructing Multivariate Data with Power Imbalances

To examine the effect of power imbalances, which in this simulation were introduced to the channels containing the same sinusoidal oscillations as in the channels with fixed powers, on the performances of APIT-MEMD and MEMD, both the algorithms were employed to reconstruct sinusoidal oscillations in a 6-channel signal corrupted by additive WGN, given by

$$\begin{aligned} x_1(t) &= \cos(2\pi f_1 t) + \cos(2\pi f_2 t) + n_1(t), & x_4(t) &= x_1(t) - n_1(t) + n_4(t), \\ x_2(t) &= \sin(2\pi f_2 t) + n_2(t), & x_5(t) &= x_2(t) - n_2(t) + n_5(t), \\ x_3(t) &= \sin(2\pi f_1 t) + n_3(t), & x_6(t) &= x_3(t) - n_3(t) + n_6(t), \end{aligned} \tag{6.2}$$

where f_1=10 Hz, f_2=30 Hz, and the sampling frequency f_s =1 kHz. The SNRs of the first, second and third channels corrupted by independent additive WGN processes, n_1, n_2 and n_3, were fixed at 20 dB, while the SNRs of the fourth, fifth and sixth channels governed by n_4, n_5 and n_6, were varied between 0 dB and 20 dB. The performance was measured using the mean square error (MSE) in the task of reconstructing the f_1 and f_2 sinusoids in channel 4. The number of direction vectors

for MEMD and APIT-MEMD was varied from 8 to 128 (low to high). The α value for the APIT-MEMD was varied from 0.1 to 1. To evaluate the performance of the APIT-MEMD and MEMD algorithms in alleviating the mode-mixing problem, a novel performance measure is introduced, termed the Mode-Mixing Ratio (MMR), given by

$$MMR = \frac{\sum_{i=1:K}^{i \neq j} \rho_i}{\rho_j}, \tag{6.3}$$

where $\sum_{i=1:K}^{i \neq j} \rho_i$ (K is the total number of IMFs) is the sum of the all the correlation values between IMF index i, where $i \neq j$, which should not contain the desired oscillations (f_1 or f_2), and the clean original oscillation (f_1 or f_2), while ρ_j denotes the correlation value between the IMF index j containing the desired oscillation (f_1 or f_2) and the corresponding clean original oscillation (f_1 or f_2). If mode mixing is not present, there is correlation only between the information-bearing IMF and the corresponding clean original oscillation, resulting in $MMR = 0$. However, if mode mixing is present, besides the non-zero correlation between the information-bearing IMF and the clean original oscillation, there are also non-zero correlations between other IMFs and the clean original signal, resulting in $MMR > 0$.

Blue areas in Figures 6.4 & 6.5 illustrate the degrees of power imbalances where the APIT-MEMD algorithm outperformed the MEMD algorithm – APIT-MEMD exhibited lower MSE and/or MMR – in the tasks of reconstructing respectively the f_1 and f_2 sinusoids in channel 4. The degree of power imbalances ranging from 0 dB (no power imbalance) to 20 dB (very high power imbalance) inversely corresponds to the SNR of the fourth channel varying from 20 dB to 0 dB. Observe that when the degree of power imbalances was approximately 5–10 dB, the APIT-MEMD algorithm outperformed the MEMD algorithm by using approximately only 8–40 (low to moderate) direction vectors, and as the degree of power imbalances increased, ranging approximately between 10 dB to 14 dB, the APIT-MEMD consistently outperformed the MEMD by using the number of direction vectors as low as 40 and as high as 128. However, MEMD gradually outperformed APIT-MEMD, as the α value increased, at very high degrees of power imbalances between 15 dB to 20 dB, as shown by the red areas. This suggests that the APIT-MEMD algorithm shall be used with precaution, and the degree of power imbalances between data channels

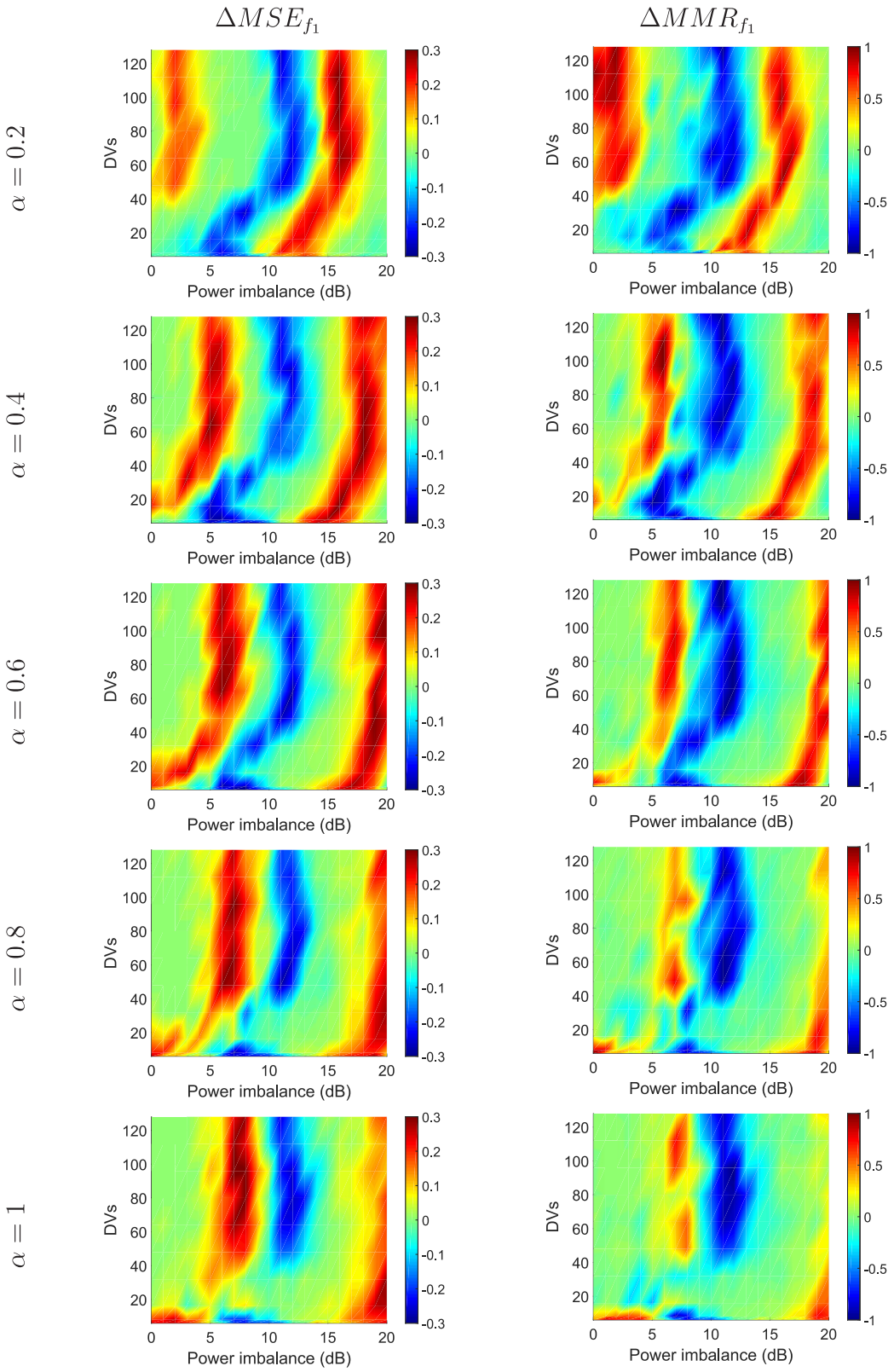


Figure 6.4: **Performance comparison between APIT-MEMD and MEMD in reconstructing the f_1 sinusoid using different α values**. All performance measures follow the format: 'APIT-MEMD – MEMD'. Left panel: Mean square error (MSE). Right panel: Mode mixing ratio (MMR). First row: $\alpha = 0.2$. Second row: $\alpha = 0.4$. Third row: $\alpha = 0.6$. Fourth row: $\alpha = 0.8$. Fifth row: $\alpha = 1$.

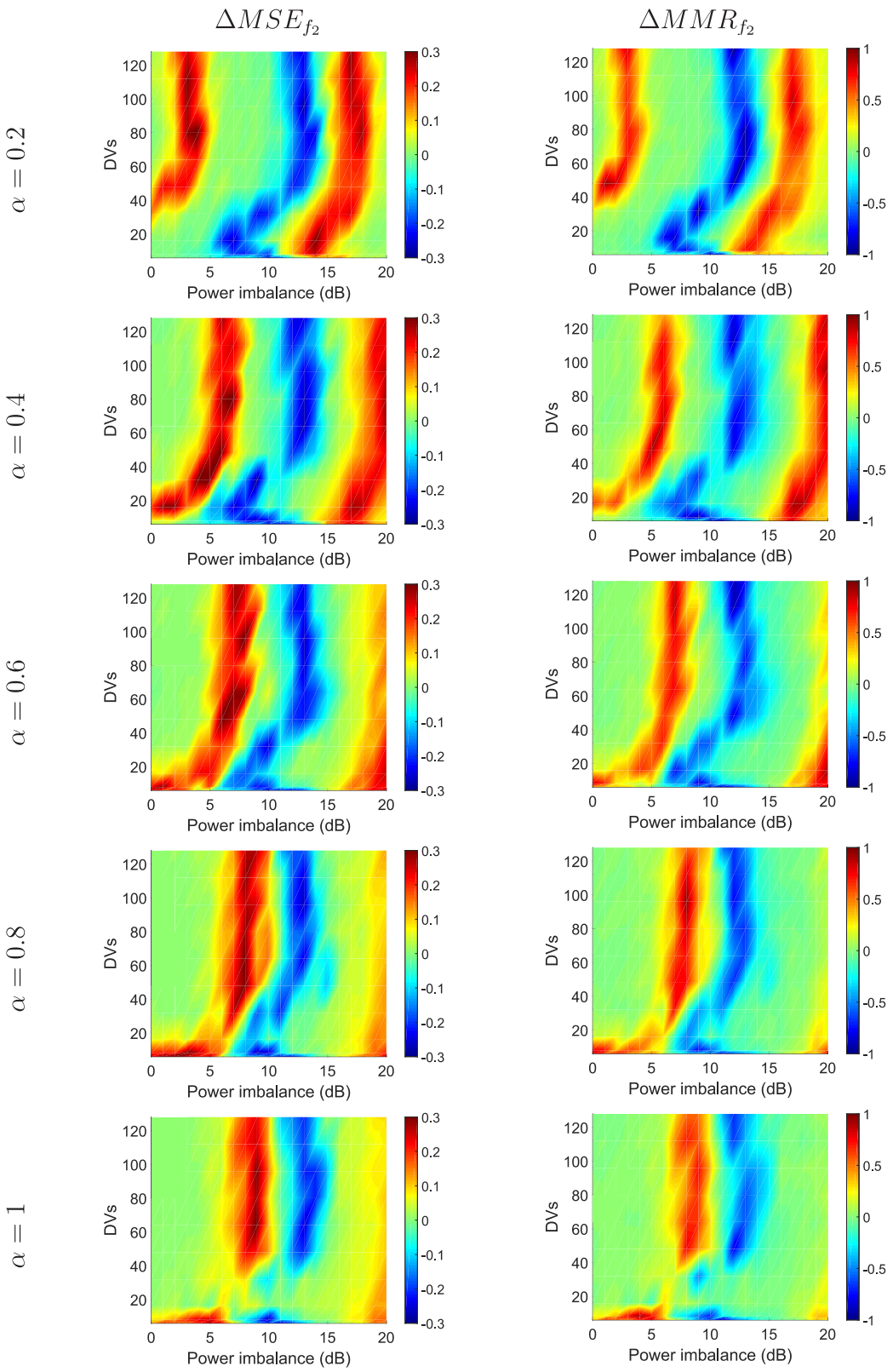


Figure 6.5: **Performance comparison between APIT-MEMD and MEMD in reconstructing the f_2 sinusoid using different α values**. All performance measures follow the format: 'APIT-MEMD – MEMD'. Left panel: Mean square error (MSE). Right panel: Mode mixing ratio (MMR). First row: $\alpha = 0.2$. Second row: $\alpha = 0.4$. Third row: $\alpha = 0.6$. Fourth row: $\alpha = 0.8$. Fifth row: $\alpha = 1$.

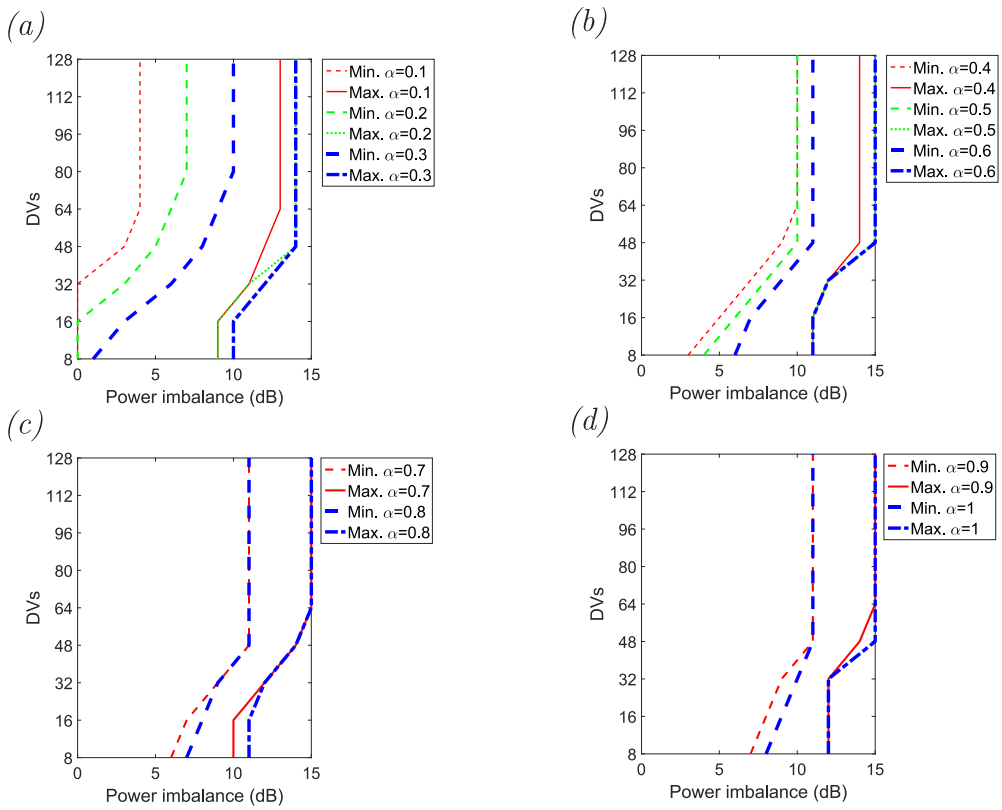


Figure 6.6: **Suggested α value and the number of direction vectors for different degrees of power imbalances**. *(a)* Minimum (Min.) and maximum (Max.) degrees of power imbalance for $\alpha = 0.1, 0.2, 0.3$. *(b)* Minimum (Min.) and maximum (Max.) degrees of power imbalance for $\alpha = 0.4, 0.5, 0.6$. *(c)* Minimum (Min.) and maximum (Max.) degrees of power imbalance for $\alpha = 0.7, 0.8$. *(d)* Minimum (Min.) and maximum (Max.) degrees of power imbalance for $\alpha = 0.9, 1$. Higher α values are suggested for higher degrees of power imbalances.

must be taken into account for choosing an α value. Figure 6.6*(a-d)* shows an α value and the number of direction vectors that shall be used for APIT-MEMD at different degrees of power imbalances. From Figure 6.6*(a)*, for example, $\alpha = 0.1$ and 8 direction vectors are recommended for a degree of power imbalances in the range 0–9 dB (minimum (Min.) to maximum (Max.) power imbalances), and $\alpha = 0.2$ and 80 direction vectors are recommended for a degree of power imbalances in the range 7–14 dB. Observe that the increasing degrees of power imbalances require the higher α values, that is, in principal, at a higher degree of power imbalances the adaptive projection vectors shall be more clustered around the first principal component, $\mathbf{v}_1$, and the diametrically opposite vector, $\mathbf{v}_{o1}$.

6.3.2 Noise-assisted Signal Decomposition

The performance of the proposed APIT-MEMD algorithm in a noise-assisted mode of operation was evaluated against MEMD. Both algorithms were employed to decompose 3-channel data, augmented with 5 adjacent WGN channels, where the 3-channel data were composed of sinusoids given by

$$\begin{aligned} x_1(t) &= \cos(2\pi f_1 t) + \cos(2\pi f_2 t), \\ x_2(t) &= \sin(2\pi f_2 t), \\ x_3(t) &= \sin(2\pi f_1 t), \end{aligned} \tag{6.4}$$

where f_1=10 Hz, f_2=30 Hz, the sampling frequency f_s=10 kHz, while the channels 4 to 8 were WGN processes with constant power. The SNRs of the 3-channel data relative to the noise channels were varied from 0 to 20 dB. The α value for the NA-APIT-MEMD was 1. Figure 6.7 *(a-b)* shows the differences in MSE in reconstructing the f_1 and f_2 sinusoids using NA-APIT-MEMD and NA-MEMD. Figure 6.7 *(c-d)* shows the differences in MMR in reconstructing the f_1 and f_2 sinusoids using NA-APIT-MEMD and NA-MEMD. All the results were obtained by averaging over 30 independent realisations. It can be seen that the performance of the proposed algorithm in terms of the MSE was comparable to that of NA-MEMD. The proposed algorithm, however, yielded lower MMR than NA-MEMD in the presence of power imbalances between the signal and noise channels (relative SNR $>$ 5 dB).

6.3.3 P300 reconstruction

Power imbalances and inter-channel correlation are typically found in multichannel EEG due to different electrode impedances and adjacent locations – a perfect scenario for APIT-MEMD to reconstruct multichannel real-world EEG data. The P300 response is a positive deflection in the EEG signal, elicited approximately 250–500 ms after the brain is exposed to an unexpected visual and/or auditory stimulus

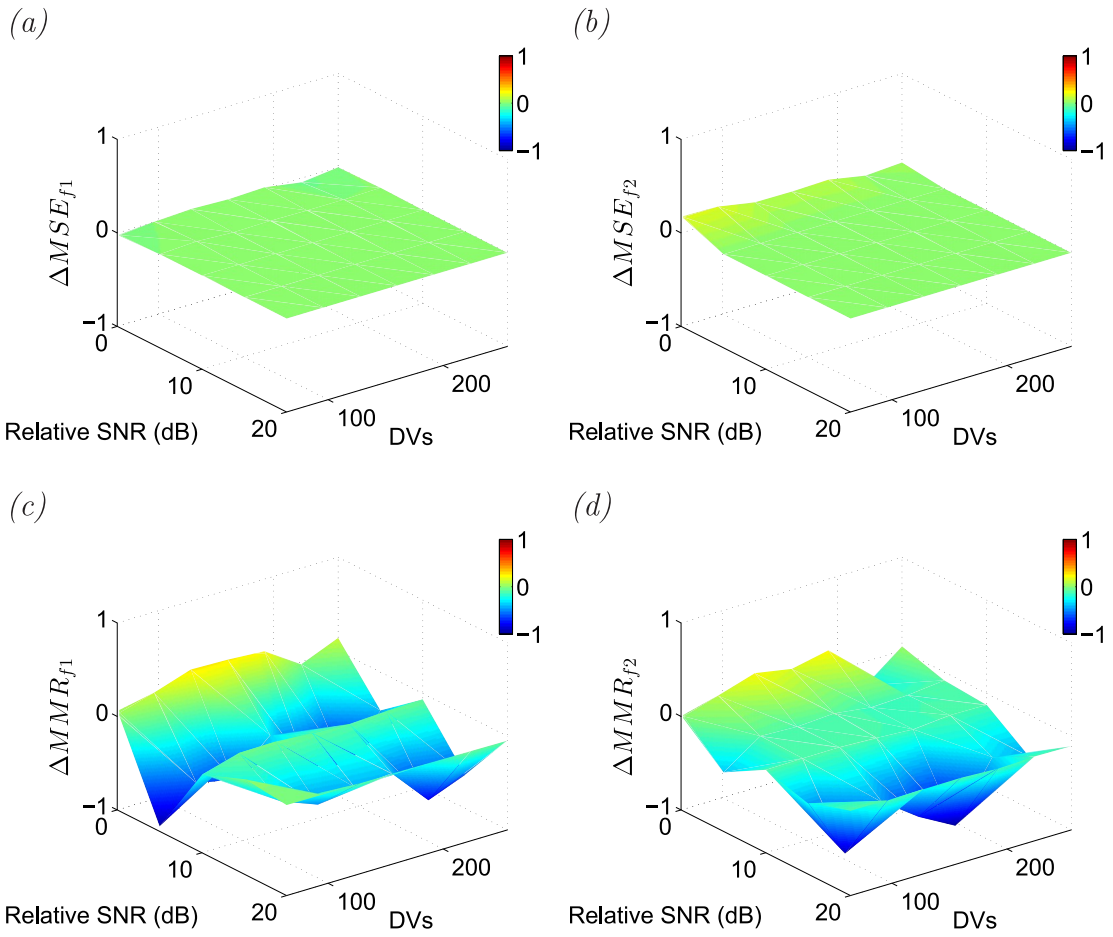


Figure 6.7: **Performance comparison between APIT-MEMD and MEMD in reconstructing signal with the assistance of noise.** All performance measures follow the format: "APIT-MEMD – MEMD". *(a)* Difference in MSE in reconstructing the f_1 sinusoid. *(b)* Difference in MSE in reconstructing the f_2 sinusoid. *(c)* Difference in MMR in reconstructing the f_1 sinusoid. *(d)* Difference in MMR in reconstructing the f_2 sinusoid.

[116], the so-called oddball paradigm. Two male subjects participated in the experiment and were exposed to randomly coloured boxes (non-target) and a box with white background and red foreground (target) presented on an LCD screen, where the time intervals between each of the target stimuli were randomised. The EEG signals were recorded from the Fz, Cz and Pz electrodes of Subject 1 and from the Fz, POz and Oz electrodes of Subject 2. The recorded signals were then band-pass filtered to the 1–40 Hz range, averaged over 10 trials and combined to construct a multichannel signal. Channels 1–3 contained the responses of Subject 1, channels 4–6 contained the responses of Subject 2, while channel 7 contained WGN to facilitate the noise-assisted mode of operation of both the APIT-MEMD and MEMD. Due to low power imbalances (3 dB on the average) between the data channels, the α value

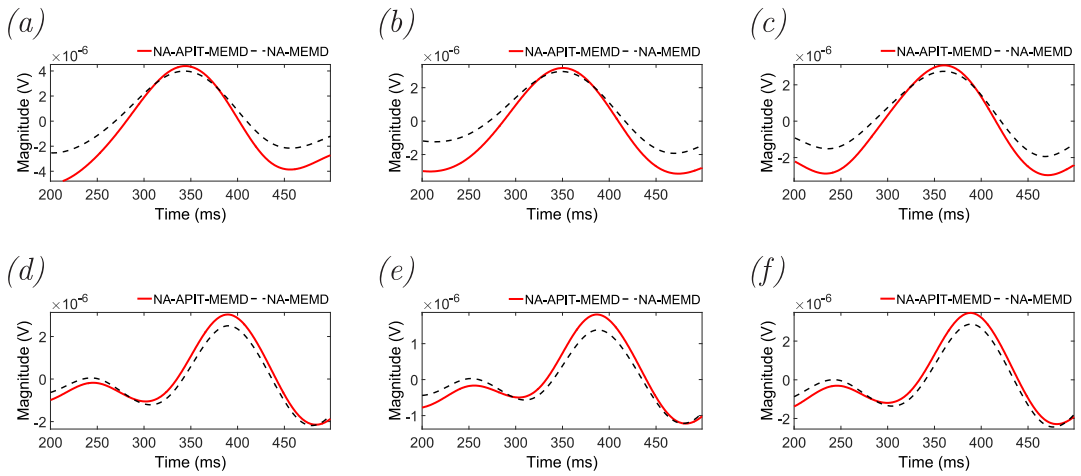


Figure 6.8: **P300 ground truth generated by performing APIT-MEMD and MEMD on EEG data recorded from two subjects at different electrode positions**. *(a)* Subject 1, Fz electrode. *(b)* Subject 1, Cz electrode. *(c)* Subject 1, Pz electrode. *(d)* Subject 2, Fz electrode. *(e)* Subject 2, POz electrode. *(f)* Subject 2, Oz electrode.

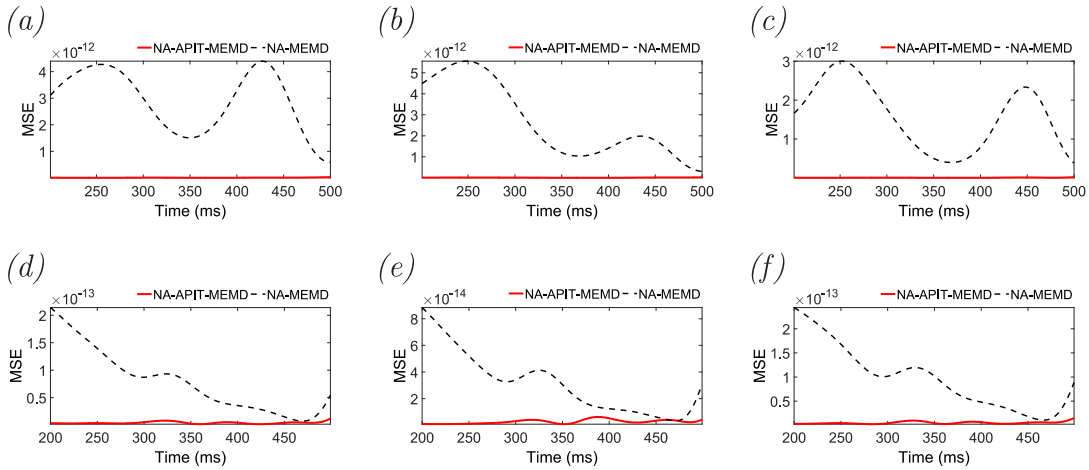


Figure 6.9: **Mean square error of P300 responses of two subjects at different electrode positions**. *(a)* Subject 1, Fz electrode. *(b)* Subject 1, Cz electrode. *(c)* Subject 1, Pz electrode. *(d)* Subject 2, Fz electrode. *(e)* Subject 2, POz electrode. *(f)* Subject 2, Oz electrode.

of 0.1 and 32 direction vectors were used for NA-APIT-MEMD. The P300 ground truths for each of the 6 electrodes were then constructed by averaging 1,000 P300-IMFs (IMFs containing the maximum power were treated as IMFs containing P300) obtained by applying 1,000 realisations of the NA-APIT-MEMD and NA-MEMD to the multichannel data (see Figure 6.8 *(a-f)*).

The performance of both the algorithms for P300 reconstruction was examined as described in [65]. By performing another 100 realisations (a small fraction of the 1,000 realisations of NA-MEMD applied to generate the P300 ground truths), the

Table 6.1: Average MSEs of the NA-APIT-MEMD and NA-MEMD algorithms for the two subjects at different electrodes.

	Subject 1			Subject 2		
	Fz	Cz	Pz	Fz	POz	Oz
NA-APIT-MEMD	9.36×10^{-15}	1.14×10^{-14}	5.21×10^{-15}	4.22×10^{-15}	2.71×10^{-15}	5.04×10^{-15}
NA-MEMD	2.91×10^{-12}	2.66×10^{-13}	1.59×10^{-12}	7.79×10^{-14}	3.08×10^{-14}	9.64×10^{-13}

performance of both algorithms was evaluated in terms of MSE in reconstructing the P300 response with respect to the P300 ground truth of each electrode. Observe from Figure 6.9 *(a-f)* and Table 6.1 that the proposed NA-APIT-MEMD algorithm yielded significantly lower MSE compared to the NA-MEMD for every electrode position of both subjects. Note that the differences were three orders of magnitude for Fz and Pz electrodes of Subject 1.

6.4 Applications of NA-APIT-MEMD in the Intrinsic Multi-scale Analysis Framework

Intrinsic multiscale analysis framework [8] incorporates NA-MEMD with standard data-association measures, such as phase synchrony, sample entropy and correlation, in order to quantify intra- and inter-component dependence of a complex system such as multiple synchronies and causalities. This work proposed to use NA-APIT-MEMD for signal decomposition in the framework to optimally capture dynamics of (i) unbalanced EEG data in order to enhance information transfer rate (ITR) for cooperative brain-computer interface (BCI), and (ii) unbalanced financial data to reveal systemic risk during financial crises.

6.4.1 Application of Intrinsic Phase Synchrony to Cooperative SSVEP-based BCI

Information transfer rate (ITR) is an essential measure which indicates the performance of a BCI system. In cooperative BCI systems, EEG data acquired from multiple users simultaneously engaging in the same paradigm can provide joint and

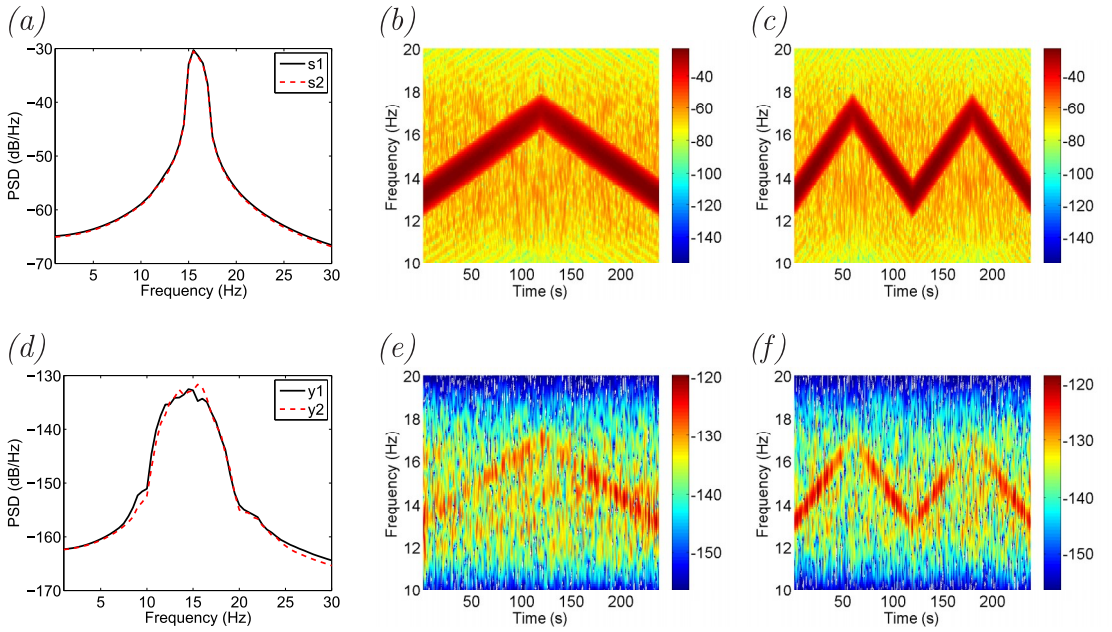


Figure 6.10: **The PSD and time-frequency spectrogram of SSVEP stimuli and brain responses**. *(a)* The PSD of SSVEP stimuli presented to subjects 1 and 2 (s1 and s2). *(b)* Time-frequency spectrogram of s1. *(c)* Time-frequency spectrogram of s2. *(d)* The PSD of SSVEP responses of subjects 1 and 2 (y1 and y2). *(e)* Time-frequency spectrogram of y1. *(f)* Time-frequency spectrogram of y2.

collective information, which can effectively reduce the time required for data collection, thus increasing the ITR.

Steady-state visual evoked potential (SSVEP) is a natural response of the brain to the visual stimuli operating in the frequency range of 5–60 Hz [117]. The SSVEP responses are typically discriminated based on their frequencies, resulting in a limited ITR. Integrating phase information in SSVEP-based BCI systems promises a higher number of possible targets and thus a higher ITR [118].

In this section, intrinsic phase synchrony was applied to differentiate between SSVEP responses of two subjects simultaneously participating in an experiment. The 4-minute SSVEP responses were recorded from two subjects seated next to each other and attending two different SSVEP stimuli with similar power spectral densities (PSDs), occupying the range 13–17 Hz (see Figure 6.10 *(a)*), but different phases and generated with two separate LEDs. Subject 1 (y1) attended a chirp signal (s1) with frequencies increasing from 13 Hz to 17 Hz over 2 minutes and decreasing from 17 Hz to 13 Hz over the following 2 minutes (see Figure 6.10 *(b)*), while Subject 2 (y2) attended a chirp signal (s2) with frequencies varying from 13 Hz to 17 Hz at

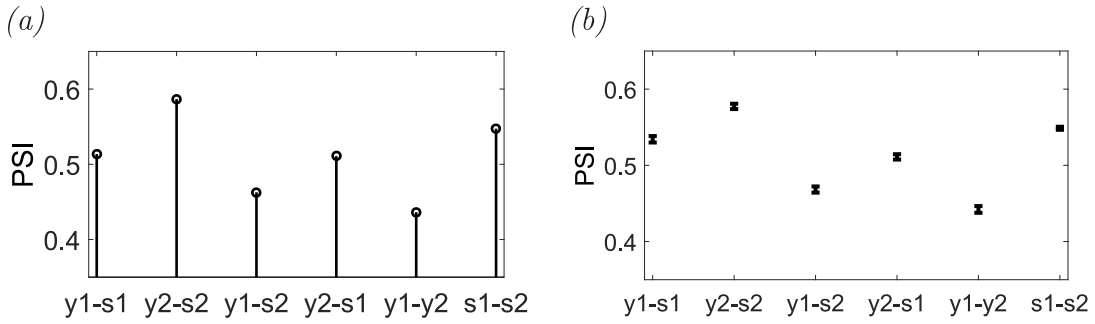


Figure 6.11: **Estimated PSI between SSVEP stimuli and brain responses**. *(a)* The PSI estimated using the standard approach. *(b)* The PSI estimated using the intrinsic multiscale analysis.

twice the speed of s1 (see Figure 6.10 *(c)*). The recorded signals were then band-pass filtered to the range 10–20 Hz. The PSD and spectrograms of SSVEP responses of the two subjects (y1 and y2), exposed to the corresponding stimuli, are shown in Figure 6.10 *(d-f)*. Observe from Figure 6.10 *(d)* that PSD of SSVEP response of subject 1 (y1) was similar to that of subject 2 (y2).

Following the standard approach to phase synchrony estimation, PSI between each of the two stimuli (s1 and s2), and each of the responses (y1 and y2) was estimated and is shown in Figure 6.11 *(a)*. Next, within our intrinsic multiscale analysis framework, the stimuli and responses (s1, s2, y1 and y2) were used to form 4-channel data which was decomposed using NA-APIT-MEMD with 10 adjacent WGN channels. The number of direction vectors was 64 and α was 1 for the NA-APIT-MEMD due to acute power imbalances (over 90 dB) between the stimuli and responses. The IMF with maximum power was treated as the information-bearing IMF (IMF containing the required 13 Hz or 15 Hz oscillation). The PSIs between each of the information-bearing IMFs of the stimuli and responses were then calculated from 30 realisations of NA-APIT-MEMD as shown in Figure 6.11 *(b)*.

Figure 6.11 *(a)* demonstrates a subtle difference in the PSI values between y1-s1 (0.5136) and y2-s1 (0.5109), implying that the standard approach could not effectively discriminate between the phases of the SSVEP responses and stimuli, while the results obtained using the proposed intrinsic multiscale approach in Figure 6.11 *(b)*, indicate successful separation of the responses of the subjects, determined by the Z-test at the significance level of 0.01.

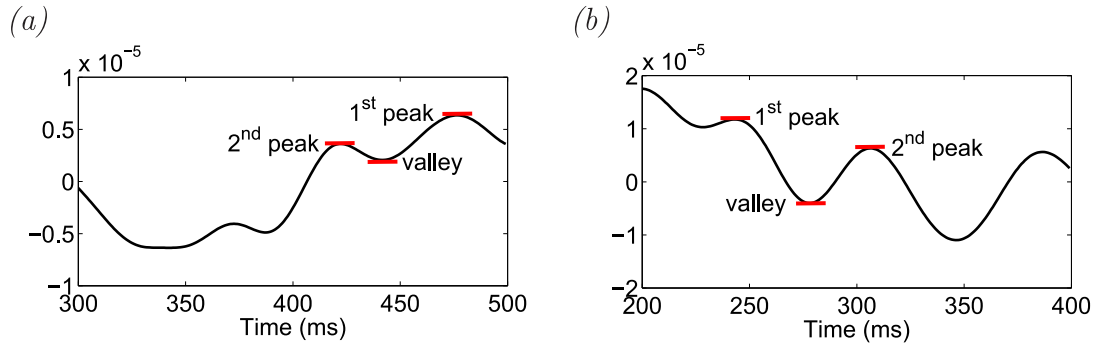


Figure 6.12: **Examples of EEG signals with and without the P300 present**. *(a)*: EEG signal with a P300 (two positive peaks, no negative trends). *(b)*: EEG signal without a P300 (negative trend, $\frac{d_1}{d_2} < 0.5$).

6.4.2 Application of Intrinsic Correlation to Cooperative P300-based BCI

The P300 brain response reflects the outcome of stimulus evaluation and internal decision-making processes [119]; however, its presence after a person is exposed to an expected stimulus (target) is not always guaranteed. The P300 used in BCI applications, such as word spellers, is therefore typically obtained by averaging EEG segments over a number of trials. For real-time applications, automatic detection of a single-shot P300 is imperative and can lead to practical cooperative real-world BCI applications. The EMD was applied in [120] to detect P300 in a single trial; however, the average sensitivity (57.36%) and specificity (52.63%) were not high. Intrinsic correlation is therefore employed here to detect single-shot P300 from a pair of individuals to reduce the time and number of trials normally required to establish an average P300, thus providing higher ITR. This approach is based on an assumption that P300 responses of two people simultaneously engaging in the same oddball paradigm are intrinsically cross-correlated.

In order to evaluate the performance of the proposed detection algorithm, it is essential to have prior knowledge of whether P300 of a subject was present after each target in the recorded data. To this end, the following three criteria are proposed to determine the presence of P300: (i) at least one positive peak must be present; (ii) a negative trend must not exist; and (iii) if two or more positive peaks do exist, the difference in the magnitude between the largest and second-largest peaks (d_1) must be higher than half of the difference in the magnitude between the largest peak and

the 'valley' located between the largest and second-largest peaks (d_2), $\frac{d_1}{d_2} > 0.5$.

Figure 6.12 *(a)* shows an EEG signal *with* P300 where: 1) at least 1 positive peak is present, 2) no negative trend exists, 3) the difference between the first and second largest peaks ($d_1 = 1^{st}\ peak - 2^{nd}\ peak$) was larger than half the difference between the first peak and the valley ($d_2 = 1^{st}\ peak - valley$), $\frac{d_1}{d_2} = 0.641 > 0.5$. Figure 6.12 *(b)* shows an EEG signal *without* P300 where: 1) a negative trend exists 2) the difference between the first and second largest peaks (d_1) was lower than half the difference between the first peak and the valley (d_2), $\frac{d_1}{d_2} = 0.345 < 0.5$.

The same experimental setting as in Section 6.3.3 (P300 reconstruction) was considered, except that EEG signals of Subject 1 were recorded from the Fz, POz and Oz electrodes. The recorded signals of both subjects were band-pass filtered to the range 1–20 Hz. The P300 ground truth of each subject was then constructed by averaging the signals recorded from the three electrodes over 10 trials. The ground truth was next used to determine the time span of P300 of each subject. The time span of P300 of Subject 1 was between 200–400 ms, while that of Subject 2 was between 300–500 ms. To detect the presence of P300 for both subjects and each trial, the 3-channel data of Subject 1 between 200–400 ms after a target, and the other 3-channel data of Subject 2 between 300–500 ms after the same target were used to construct 6-channel data, which were decomposed using NA-APIT-MEMD with 10 added WGN channels; 30 realisations of NA-APIT-MEMD were carried out. The α value was 0.2, and the number of direction vectors was 16 due to low power imbalances (less than 3 dB) between the data channels. Cross-correlation values between the spatially averaged primary IMFs of the signal channels were statistically compared against those between the primary IMFs of the noise channels (see Algorithm 6.2 for detail of the proposed two-person single-shot P300 detection algorithm).

The performance of the proposed two-person single-shot P300 detection algorithm was evaluated as described in [120]. By performing 30 realisations of this algorithm on 6 EEG signals recorded from two subjects after 10 targets, the number of true positive (TP, P300 was present in both subjects and detected), true negative (TN, P300 was not present in both subjects and not detected), false positive (FP, P300

was not present in both subjects but incorrectly detected), false negative (FN, P300 was present in both subjects but not detected), sensitivity ($\frac{TP}{TP+FN}$) and specificity ($\frac{TN}{TN+FP}$) were calculated, and shown in Table 6.2.

Algorithm 6.2: Two-person single-shot P300 detection using intrinsic correlation

Input P-channel EEG data of subject 1, $\mathbf{x}_1(t) = [x_1^1(t), x_1^2(t), \ldots, x_1^P(t)]^T$, and R-channel EEG data of subject 2, $\mathbf{x}_2(t) = [x_2^1(t), x_2^2(t), \ldots, x_2^R(t)]^T$ with the time length determined by the time span of P300 ground truth of each subject.

1. Construct (P+R+10)-channel data from EEG of two subjects and 10 adjacent WGN channels $\mathbf{n}(t) = [n^1(t), n^2(t), \ldots, n^{10}(t)]^T$. [1]

2. Perform NA-APIT-MEMD on the (P+R+10)-channel data.

3. Average primary IMFs (IMFs with maximum power) of P and R channels of $\mathbf{x}_1(t)$ and $\mathbf{x}_2(t)$, respectively, to construct spatially averaged IMFs of subjects 1 and 2, IMF_1 and IMF_2.

4. Split each spatially averaged IMF (IMF_1 and IMF_2) of length 200 ms into 25 overlapping windows of length 85 ms with 75 ms overlap. [2]

5. Calculate cross-correlation values between the window i of IMF_1 and the window j of IMF_2, $\rho^{IMF_1,IMF_2}(i, j, \tau)$, where $i = 1, 2, \ldots, 25$, $j = 1, 2, \ldots, 25$ and τ is the time lag.

6. Determine the maximum cross-correlation value of each pair of windows i and j, $\rho_{\max}^{IMF_1,IMF_2}(i, j) = \max(\rho^{IMF_1,IMF_2}(i, j, \tau))$.

7. Determine the final maximum cross-correlation value across all window pairs, $\rho_{\text{final max}}^{IMF_1,IMF_2} = \max(\rho_{\max}^{IMF_1,IMF_2}(i, j))$.

8. The 10 noise channels give 45 noise pairs to determine the maximum cross-correlation value.

[1] The number of adjacent WGN channels was 10, as this is sufficient to enforce the desired quasi-dyadic structure and thus reduce the degree of overlap between the IMF spectra.

[2] Note that the P300 response is typically obtained by averaging EEG signals over a number of trials, resulting in an average time span of P300 of approximately 150–200 ms. However, it has been empirically found here that the P300 in a single trial has a relatively short time span of approximately 85 ms, so that overlapping windows of length 85 ms were thus used in order to capture the P300 in a single trial.

9. Split the primary IMF (IMF with the same index as the primary IMF of subject 1) of each noise channel c, IMF_c, into 25 overlapping windows of length 85 ms with 75 ms overlap.

10. Calculate cross-correlation values between window i of primary IMF of noise channel c, IMF_c, and window j of primary IMF of noise channel d, IMF_d, $\rho^{IMF_c,IMF_d}(i,j,\tau)$, where $i = 1,2,\ldots,25$, $j = 1,2,\ldots,25$ $c = 1,2,\ldots,10$ and $d = 1,2,\ldots,10; c \neq d$.

11. Determine the maximum cross-correlation value between window i of primary IMF of noise channel c, IMF_c, and window j of primary IMF of noise channel d, IMF_d, $\rho_{\max}^{IMF_c,IMF_d}(i,j) = \max(\rho^{IMF_c,IMF_d}(i,j,\tau))$.

12. Determine the final maximum cross-correlation value across all window pairs of primary IMFs of noise channels c and d, $\rho_{\text{final max}}^{IMF_c,IMF_d} = \max(\rho_{\max}^{IMF_c,IMF_d}(i,j))$

13. Average 45 final maximum cross-correlation values obtained from 45 pairs of noise channels c and d, $\rho_{\text{ave}}^{\text{noise}} = \frac{\Sigma\rho_{\text{final max}}^{IMF_c,IMF_d}}{45}$.

14. By performing Steps (1)–(13), two scalar values, $\rho_{\text{final max}}^{IMF_1,IMF_2}$ and $\rho_{\text{ave}}^{\text{noise}}$, are obtained.

15. Perform 30 realisations of NA-APIT-MEMD in order to assess the statistical relevance of $\rho_{\text{final max}}^{IMF_1,IMF_2}$ and $\rho_{\text{ave}}^{\text{noise}}$, repeat Steps (1)–(13) for each realisation.

16. Perform the Z-test to determine a significant difference between 30 values of $\rho_{\text{final max}}^{IMF_1,IMF_2}$ and $\rho_{\text{ave}}^{\text{noise}}$.

17. If 30 values of $\rho_{\text{final max}}^{IMF_1,IMF_2}$ are significantly higher than 30 values of $\rho_{\text{ave}}^{\text{noise}}$ at a significance level of 0.05, P300 is considered present in both subjects.

Table 6.2: Performance of the proposed two-person single-shot P300 detection algorithm.

	Present	Not present
Detected	$TP = 112$	$FP = 61$
Not detected	$FN = 38$	$TN = 89$
	$Sensitivity = 74.67\%$	$Specificity = 59.33\%$

6.5 Summary

An extension of the MEMD algorithm, termed APIT-MEMD, has been introduced, in order to cater for power imbalances between data channels. This is achieved through the assessment of the statistical structure of multivariate data, and subsequent resampling of the direction vectors to ensure that their density matches data dynamics. The performance of the algorithm has been evaluated in terms of MSE and MMR in decomposing unbalanced synthetic multivariate data with and without the presence of adjacent WGN channels. It has been shown that the proposed algorithm outperformed conventional MEMD for certain degrees of power imbalances by using proper α values. The proposed algorithm has also been shown to outperform NA-MEMD in a noise-assisted mode of operation, for cases with significant power imbalance between data channels. Simulations on EEG data have also shown that NA-APIT-MEMD yielded substantially lower MSE in decomposing the P300, compared to NA-MEMD.

Intrinsic multiscale analysis [8] using NA-APIT-MEMD has been applied to cooperative SSVEP- and P300-based BCI, and financial signal processing. Intrinsic phase synchrony has been shown to effectively differentiate between SSVEP responses with different parameters (frequencies or phases) of two subjects. A two-person single-shot P300 detection algorithm has also been proposed. This approach employed intrinsic correlation to determine whether the maximum cross-correlation between EEG signals of two people was higher than that of noise, which can unveil the presence of P300 generated by two cooperating brains. Note that choices of parameters in this algorithm have been set empirically in order to optimally match the nature of P300 in a single trial, and that changes in parameter values might affect the results.

It has been observed that when performing either the APIT-MEMD or MEMD algorithm in a noise-assisted mode of operation on SSVEP and P300 signals, the number of WGN channels must be chosen cautiously, as [8] has shown that the higher number of noise channels, the faster the roll-off of a filterbank structure. For narrowband signals such as SSVEP, a filterbank structure with a fast roll-off is required so that such signals are contained in a single IMF with as little mode

mixing as possible. However, for signals with a wider bandwith such as P300, which are composed of several oscillatory components, a filterbank structure with slower roll-off may be required to contain those oscillations within the same IMF index. Finally, the APIT-MEMD is sensitive to parameter α which reflects the degree of imbalances across the data channels.

Chapter 7

Conclusions and Future Work

7.1 Conclusions

This thesis presents intrinsic data-association measures for quantifying physiological and neuronal couplings in human collaborative tasks, and their applications. The key motivator for this work is that such couplings are typically manifested at unique temporal scales and thus require data-association measures which allow for physically meaningful interpretation. Drawing upon ideas in the intrinsic multi-scale analysis framework and novel algorithms for the analysis of nonlinear and non-stationary signals, this thesis proposed several intrinsic data-association metrics which are suitable for quantifying inter-channel dependence in complex physiological and neuronal signals. In the process, several applications of the proposed algorithms to real-world data have been demonstrated, such as quantifying physiological couplings between choir members and pairs of surgeons, and quantifying neuronal coupling between participants while playing a multi-player cooperative game. In addition, an adaptive, data-driven algorithm for the analysis of unbalanced multivariate signals has been proposed. This chapter presents a brief overview of the contributions of the thesis and outlines the directions for future work.

- **Chapter 1: Introduction.**
  In the first chapter, the importance of scale-wise signal coupling analysis was first reviewed. Brief overview of the three proposed intrinsic data-association

measures (ICoh, ISC and N-IPS) and the APIT-MEMD was next provided. This chapter also reviewed relevant physiological and neuronal responses (HRV, respiration and EEG), the hyperscanning technique and the ear-EEG recording concept. The EMD and its variants were next introduced and linked to their application to the intrinsic multi-scale analysis framework for quantifying inter-channel dependence, where SST and MSST can also be employed to enhance time and frequency localisation in TF representations of signal coupling.

- **Chapter 2: Algorithms and Background.**

  This chapter first reviewed the concepts of stationarity of a random process and phase response of a filter, and next provided necessary details of the algorithms which were extensively employed in this thesis and are the foundations to the algorithms proposed here for the analysis of coupled nonlinear and non-stationary signals. Two adaptive, data-driven algorithms were elaborated for the analysis of univariate (EMD) and multivariate (MEMD) nonlinear and non-stationary signals. The NA-MEMD was also reviewed to show the noise-assisted mode of operation for MEMD, where a pre-defined structure within the IMFs is required, and was extensively employed in the thesis, since it produces multivariate IMFs with similar centre frequencies and bandwidths, thus preserving the physical meaning of the coupling analysis. The IPS was next described, since it is a novel intrinsic measure which was extensively employed and has been extended to introduce the N-IPS algorithm in Chapter 4 for empirically quantifying trends in synchrony which admit physically meaningful and straightforward interpretation. The SST and MSST algorithms were subsequently introduced in this chapter. These are algorithms for generating highly localised time-frequency representations and have been extended to introduce the ISC algorithm in Chapter 4 for generating precise time-frequency representations of signal coupling. This chapter finally provided background on the notions of bias and variance of an estimator, and background on matched filtering, Hilbert transform, and the matched filtering and Hilbert transform (MF-HT) algorithm for the extraction of HRV from ECG signals, extensively used in this thesis.

- **Chapter 3: Quantifying Cooperation in Choir Singing: Respiratory and Cardiac Synchronisation.**

  In this chapter, intrinsic phase synchrony and a data-association metric proposed in this thesis, termed intrinsic coherence (ICoh), were applied to identify scale-wise couplings in HRV and respiratory signals of a subset of choir members, the conductor and a subset of audience. The two measures have effectively revealed increases in synchrony in physiological responses (HRV and respiratory signals) among the subset of choir members from the rehearsal to the performance, especially in the HF band of the HRV signals. This is a signature of increased coordination between the performers, and this is for the first time that the involvement of physiological mechanisms mediating the SNS and PNS in cooperative activities has been quantified.

- **Chapter 4: Quantifying Team Cooperation Through Intrinsic Multiscale Measures: Respiratory and Cardiac Synchronisation in Choir Singers and Surgical Teams.**

  This chapter introduced a novel data-association measure, termed intrinsic synchrosqueezing coherence (ISC), and an extension of the IPS algorithm, referred to as nested IPS (N-IPS). The former algorithm is a combination of NA-MEMD and STFT-based M/-SST algorithms. It allows for generating highly-localised time-frequency representations of signal coupling. Its performance was evaluated against other combinations of algorithms in estimating degrees of synchrony in linear and nonlinear bivariate signals, and it exhibited highest average SNRs of TF representation of synchrony – 4.33 dB (linear) and 5.71 dB (nonlinear) higher SNRs than the second best combination (IIR BPF & F-M/-SST). It was next employed to produce TF representations of signal dependence in HRV and respiratory signals in a subset of bass singers of the same choir presented in Chapter 3. It has revealed distinct synchrony in both the physiological responses around 0.1 Hz in the LF band, which conforms with the finding in the previous chapter. The N-IPS was employed to empirically quantify trends in synchrony, i.e. the level of cooperation, which are physically meaningful and straightforward to interpret, of (i) subsets of soprano and bass singers of another choir while performing a 1-hour evensong; and (ii) a surgical

team during a 2-hour PCI procedure. The algorithm has effectively revealed marked increases and decreases in synchrony in HRV and respiratory signals of the soprano and bass singers respectively during songs and pauses. It has also revealed marked increases in trends in levels of cooperation between pairs of surgeons in response to certain types of glitches.

- **Chapter 5: Ear-EEG for Detecting Neuronal Synchrony in Continuous Cooperative Multi-person Scenarios.**
  In this chapter, the ISC algorithm presented in Chapter 4 was employed to evaluate the performance of a novel EEG recording concept, termed ear-EEG, against on-scalp EEG as an alternative data acquisition approach for the hyperscanning method in the task of identifying the unknown, most robust EEG subbands for neuronal synchrony detection for cooperative multi-player gaming. Both the recording modalities exhibited significant decreases and increases in neuronal synchrony respectively in the lower and upper theta bands, which are associated with attention and adaptive working memory. The lower theta band also has been shown to be the most robust neuronal marker for brain synchronisation, exhibiting: (i) the highest average correlation coefficient, $\rho = 0.42$, between the recording modalities, (ii) approximately 20% difference in the average proportions of the number of significant SCI values between the easy and hard tasks, and (iii) statistical difference in average significant SCI values between the easy and hard tasks at a significance level of 0.05.

- **Chapter 6: Adaptive-projection Intrinsically Transformed MEMD (APIT-MEMD) in Cooperative Brain-computer Interface Applications.**
  This chapter introduced an extension of MEMD referred to as APIT-MEMD, which caters for power imbalances between data channels. Its sampling scheme relocates projection vectors to their new positions adaptively determined by the first principal component of each sifting input reflecting the direction of the highest power imbalance. Its performance was evaluated against MEMD in reconstructing multivariate data with power imbalances with and without the assistance of WGN, and in P300 reconstruction, where its MSE was lower than

that of NA-MEMD by up to three orders of magnitude. The proposed algorithm exhibited lower MSE and MMR than MEMD in all the reconstructions. Applications of NA-APIT-MEMD in the intrinsic multi-scale analysis frameworks were demonstrated. The IPS using NA-APIT-MEMD was employed to differentiate between SSVEP responses with different parameters (frequencies or phases) of two subjects. The IPS effectively differentiated between SSVEP responses with different phases and allowed for higher ITRs. Intrinsic correlation using NA-APIT-MEMD was applied to detect the presence of P300 generated by two cooperative brains, and a two-person single-shot P300 detection algorithm was proposed, yielding enhanced sensitivity (74.67%) and specificity (59.33%) for two-person single-shot P300 detection.

7.2 Future Work

Future work in this area will involve:

- Work on the ISC algorithm will focus on the development of Panorama[1]-based SST and MSST algorithms in order to enhance the generation of TF representations.
- The result of the surgical synchrony analysis is only preliminary, and the N-IPS algorithm will be employed in the assessment of HRV changes in response to glitches within different surgical teams, to show how team familiarity impacts on patient outcomes, i.e. complications, reintervention rate, length of surgical or endovascular procedures and length of postoperative hospitalisation.
- Further development of APIT-MEMD will include clustering direction vectors into a number of different groups, depending on the number of principal components in the data correlation matrix, and an automated selection of this parameter based algorithm, e.g. on real-time tracking of the degree of impropriety.

[1]The Panaroma is the Fourier transform of the autoconvolution proposed in [121] for the generation of spectral representations capable of detecting deterministic sinusoidal components in correlated stochastic noise without knowledge of the sinusoidal frequencies or amplitudes.

- Further development of APIT-MEMD will include using all the principal components in the data correlation matrix to determine the locations and the number of clusters of direction vectors, and an automated selection of this parameter based algorithm, e.g. on real-time tracking of the degree of impropriety.

- Using the ISC algorithm to generate very precise TF representations of signal dependence is highly computationally expensive. To mitigate this problem, a post-processing technique will be employed to 'sharpen' moderately precise TF representations generated using the ISC algorithm.

- The performance of ear-EEG as an alternative for the hyperscanning technique will be further evaluated, using the ISC or other algorithms, against on-scalp EEG with as many electrodes on the scalp as possible to extensively justify the performance of ear-EEG.

- The APIT-MEMD will be employed to extract foetal ECG from mother's ECG, where power imbalances between ECG data channels will be determined by electrode locations on the mother's body.

- The proposed data-association measures could be applied to quantify physiological couplings in other group activities, such as rowing, team cycling and synchronised dancing.

- Neuronal couplings measured via ear-EEG between choir members and surgeons will be quantified using the proposed algorithms.

- The bias and variance of the ISC measure will be estimated.

References

[1] F. Babiloni and L. Astolfi, "Social neuroscience and hyperscanning techniques: Past, present and future," *Neurosci. Biobehav. Rev.*, vol. 44, no. 1, pp. 76–93, 2014.

[2] A. Hemakom, V. Goverdovsky, L. Aufegger, and D. P. Mandic, "Quantifying cooperation in choir singing: Respiratory and cardiac synchronisation," in *Proc. IEEE Int. Conf. on Acoustics, Speech and Signal Processing (ICASSP 2016), Shanghai, China, 20–25 March 2016*, (Piscataway, NJ), pp. 719–723, IEEE, 2016.

[3] B. Vickhoff, H. Malmgren, R. Åström, G. Nyberg, S.-R. Ekström, M. Engwall, J. Snygg, M. Nilsson, and R. Jörnsten, "Music structure determines heart rate variability of singers," *Front. Psychol.*, vol. 4, no. 1, pp. 334–1 – 334–16, 2013.

[4] C. Babiloni, F. Vecchio, F. Infarinato, P. Buffo, N. Marzano, D. Spada, S. Rossi, I. Bruni, P. M. Rossini, and D. Perani, "Simultaneous recording of electroencephalographic data in musicians playing in ensemble," *Cortex*, vol. 47, no. 1, pp. 1082–1090, 2011.

[5] C. Babiloni, P. Buffo, F. Vecchio, N. Marzano, C. D. Percio, D. Spada, S. Rossi, I. Bruni, P. M. Rossini, and D. Perani, "Brains in concert: Frontal oscillatory alpha rhythms and empathy in professional musicians," *Neuroimage*, vol. 60, no. 1, pp. 105–116, 2012.

[6] L. Astolfi, J. Toppi, G. Borghini, G. Vecchiato, R. Isabella, F. D. V. Fallani, F. Cincotti, S. Salinari, D. Mattia, B. He, C. Caltagirone, and F. Babiloni, "Study of the functional hyperconnectivity between couples of pilots during

flight simulation: An EEG hyperscanning study," in *Proc. Int. Conf. of the IEEE Engineering in Medicine and Biology Society, Boston (EMBC 2011), MA, 30 August–3 September 2011*, (Piscataway, NJ), pp. 2338–2341, IEEE, 2011.

[7] L. Astolfi, J. Toppi, G. Borghini, G. Vecchiato, E. J. He, A. Roy, F. Cincotti, S. Salinari, D. Mattia, B. He, and F. Babiloni, "Cortical activity and functional hyperconnectivity by simultaneous EEG recordings from interacting couples of professional pilots," in *Proc. Int. Conf. of the IEEE Engineering in Medicine and Biology Society (EMBC 2012), San Diego, CA, 28 August–1 September 2012*, (Piscataway, NJ), pp. 4752–4755, IEEE, 2012.

[8] D. Looney, A. Hemakom, and D. P. Mandic, "Intrinsic multi-scale analysis: A multivariate EMD framework," *Proc. R. Soc. A*, vol. 471, no. 2173, pp. 20140709–1 – 20140709–28, 2014.

[9] N. ur Rehman and D. P. Mandic, "Multivariate empirical mode decomposition," *Proc. R. Soc. A*, vol. 466, no. 2117, pp. 1291–1302, 2010.

[10] D. P. Mandic, N. ur Rehman, Z. Wu, and N. E. Huang, "Empirical mode decomposition-based time-frequency analysis of multivariate signals," *IEEE Sig. Proc. Mag.*, vol. 30, no. 6, pp. 74–86, 2013.

[11] M. P. Hlastala and A. J. Berger, *Physiology of Respiration*. Oxford, UK: Oxford University Press, 2nd ed., May 2001.

[12] W. Jänig, *Integrative Action of the Autonomic Nervous System*. Cambridge, UK: Cambridge University Press, 2006.

[13] D. U. Silverthorne, *Human Physiology: An Integrated Approach*. Pearson / Benjamin Cummings, 4th ed., 2009.

[14] G. Billman, "The LF/HF ratio does not accurately measure cardiac sympathovagal balance," *Front. Physiol.*, vol. 4, pp. 26–1 – 26–5, 2013.

[15] W. von Rosenberg, T. Chanwimalueang, T. Adjei, U. Jaffer, V. Goverdovsky, and D. P. Mandic, "Resolving ambiguities in the LF/HF ratio: LF-HF scatter

plots for the categorization of mental and physical stress from HRV," *Front. Physiol.*, vol. 8, pp. 1–12, 2017.

[16] P. R. Montague, G. S. Berns, J. D. Cohen, S. M. McClure, G. Pagnoni, M. Dhamala, M. C. Wiest, I. Karpov, R. D. King, N. Apple, and R. E. Fisher, "Hyperscanning: Simultaneous fMRI during linked social interactions," *Neuroimage*, vol. 16, no. 4, pp. 1159–1164, 2002.

[17] G. Dumas, J. Nadel, R. Soussignan, J. Martinerie, and L. Garnero, "Inter-brain synchronization during social interaction," *PLoS ONE*, vol. 5, no. 8, pp. 1–10, 2010.

[18] M. Naeem, G. Prasad, D. R. Watson, and J. A. Kelso, "Electrophysiological signatures of intentional social coordination in the 10–12 Hz range," *Neuroimage*, vol. 59, no. 2, pp. 1795–1803, 2012.

[19] H. H. Jasper, "The ten-twenty electrode system of the international federation," *Electroenceph. Clin. Neurophysiol.*, vol. 10, no. 1, pp. 371–375, 1958.

[20] L. Astolfi, J. Toppi, F. D. V. Fallani, G. Vecchiato, and F. Cincotti, "Imaging the social brain by simultaneous hyperscanning during subject interaction," *IEEE Intell. Syst.*, vol. 26, no. 5, pp. 38–45, 2011.

[21] F. Babiloni, F. Cincotti, D. Mattia, M. Mattiocco, F. D. V. Fallani, A. Tocci, L. Bianchi, M. Marciani, and L. Astolfi, "Hypermethods for EEG hyperscanning," in *Proc. Int. Conf. of the IEEE Engineering in Medicine and Biology Society (EMBC 2006), New York City, NY, 31 August–3 September 2006*, (Piscataway, NJ), pp. 3666–3669, IEEE, 2006.

[22] X. Cui, D. M. Bryant, and A. L. Reiss, "NIRS-based hyperscanning reveals increased interpersonal coherence in superior frontal cortex during cooperation," *Neuroimage*, vol. 59, no. 3, pp. 2430–2437, 2012.

[23] U. Lindenberger, S. Li, W. Gruber, and V. Müller, "Brains swinging in concert: Cortical phase synchronization while playing guitar," *BMC Neuroscience*, vol. 10, no. 22, pp. 1–22, 2009.

[24] E. Tognoli, J. Lagarde, G. C. DeGuzman, and J. A. Kelso, "The phi complex as a neuromarker of human social coordination," *PNAS*, vol. 104, no. 19, pp. 8190–8195, 2007.

[25] S. Acharya and S. Shukla, "Mirror neurons: Enigma of the metaphysical modular brain," *J. Nat. Sci. Biol. Med.*, vol. 3, no. 2, pp. 118–124, 2012.

[26] W. Klimesch, "EEG alpha and theta oscillations reflect cognitive and memory performance: A review and analysis," *Brain Research Reviews*, vol. 29, no. 1, pp. 169–195, 1999.

[27] U. Friese, J. Daume, F. Göschl, P. König, P. Wang, and A. K. Engel, "Oscillatory brain activity during multisensory attention reflects activation, disinhibition, and cognitive control," *Scientific Reports*, vol. 6, no. 1, pp. 1–11, 2016.

[28] W. Klimesch, H. Schimke, and J. Schwaiger, "Episodic and semantic memory: an analysis in the EEG theta and alpha band," *Electroenceph. Clin. Neurophysiol.*, vol. 91, no. 1, pp. 428–441, 1994.

[29] J. Fell, P. Klaver, H. Elfadil, C. Schaller, C. E. Elger, and G. Fernández, "Rhinal-hippocampal theta coherence during declarative memory formation: Interaction with gamma synchronization?," *Eur. J. Neurosci.*, vol. 17, no. 5, pp. 1082–1088, 2003.

[30] C. Summerfield and J. A. Mangels, "Coherent theta-band EEG activity predicts item-context binding during encoding," *NeuroImage*, vol. 24, no. 1, pp. 692–703, 2005.

[31] R. Fischer, J. Ferraro, and H. Lusted, "Apparatus and method for the measurement and monitoring of bioelectric signal patterns," May 17 2007. US Patent App. 11/549,862.

[32] D. Looney, C. Park, P. Kidmose, M. L. Rank, M. Ungstrup, K. Rosenkranz, and D. P. Mandic, "An in-the-ear platform for recording electroencephalogram," in *Proc. Int. Conf. of the IEEE Engineering in Medicine and Biology*

Society (EMBC 2011), Boston, MA, 30 August–3 September 2011, (Piscataway, NJ), pp. 6882–6885, IEEE, 2011.

[33] D. Looney, P. Kidmose, C. Park, M. Ungstrup, M. L. Rank, K. Rosenkranz, and D. P. Mandic, "The in-the-ear recording concept: User-centered and wearable brain monitoring," *IEEE Pulse*, vol. 3, no. 6, pp. 32–42, 2012.

[34] L. Fiedler, J. Obleser, T. Lunner, and C. Graversen, "Ear-EEG allows extraction of neural responses in challenging listening scenarios – a future technology for hearing aids?," in *Proc. Int. Conf. of the IEEE Engineering in Medicine and Biology Society (EMBC 2016), Orlando, FL, 16 August–20 August 2016*, (Piscataway, NJ), pp. 5697–5700, IEEE, 2016.

[35] V. Goverdovsky, W. von Rosenberg, T. Nakamura, D. Looney, D. J. Sharp, C. Papavassiliou, M. J. Morrell, and D. P. Mandic, "Hearables: Multimodal physiological in-ear sensing," *Nature*, vol. 7, no. 1, pp. 6948–1 – 6948–10, 2017.

[36] P. Kidmose, D. Looney, L. Jochumsen, and D. P. Mandic, "Ear-EEG from generic earpieces: A feasibility study," in *Proc. Int. Conf. of the IEEE Engineering in Medicine and Biology Society (EMBC 2013), Osaka, Japan, 3–7 July 2013*, (Piscataway, NJ), pp. 543–546, IEEE, 2013.

[37] J. H. Lee, S. M. Lee, H. J. Byeon, J. S. Hong, K. S. Park, and S.-H. Lee, "CNT/PDMS-based canal-typed ear electrodes for inconspicuous EEG recording," *J. Neural Eng.*, vol. 11, no. 1, pp. 046014–1 – 046014–11, 2014.

[38] M. G. Bleichner, M. Lundbeck, M. Selisky, F. Minow, M. Jäger, R. Emkes, S. Debener, and M. D. Vos, "Exploring miniaturized EEG electrodes for brain-computer interfaces. An EEG you do not see?," *Physiol. Rep.*, vol. 3, no. 4, pp. e12362–1 – e12362–4, 2015.

[39] V. Goverdovsky, D. Looney, P. Kidmose, and D. P. Mandic, "In-ear EEG from viscoelastic generic earpieces: Robust and unobtrusive 24/7 monitoring," *IEEE Sensors J.*, vol. 16, no. 1, pp. 271–277, 2016.

[40] H. Dong, P. M. Matthews, and Y. Guo, "A new soft material based in-the-ear EEG recording technique," in *Proc. Int. Conf. of the IEEE Engineering*

in Medicine and Biology Society (EMBC 2016), Orlando, FL, 16 August–20 August 2016, (Piscataway, NJ), pp. 5697–5700, IEEE, 2016.

[41] A. Casson, D. Yates, S. Smith, J. Duncan, and E. Rodriguez-Villegas, "Wearable electroencephalography. What is it, why is it needed, and what does it entail?," *IEEE Eng. Med. Biol. Mag.*, vol. 29, no. 3, pp. 44–56, 2010.

[42] K. B. Mikkelsen, S. L. Kappel, D. P. Mandic, and P. Kidmose, "EEG recorded from the Ear: Characterizing the Ear-EEG method," *Front. Neurosci.*, vol. 9, no. 438, pp. 1–8, 2015.

[43] P. Kidmose, D. Looney, and D. P. Mandic, "Auditory evoked responses from ear-EEG recordings," in *Proc. Int. Conf. of the IEEE Engineering in Medicine and Biology Society (EMBC 2012), San Diego, CA, 28 August–1 September 2012*, (Piscataway, NJ), pp. 586–589, IEEE, 2012.

[44] P. Kidmose, D. Looney, M. Ungstrup, M. L. Rank, and D. P. Mandic, "A study of evoked potentials from ear-EEG," *IEEE Trans. Biomed. Eng.*, vol. 60, no. 10, pp. 2824–2830, 2013.

[45] F. Farooq, D. Looney, D. P. Mandic, and P. Kidmose, "EarEEG based visual P300 brain-computer interface," in *Proc. Int. IEEE/EMBS Conf. on Neural Engineering (NER 2015), Montpellier, France, 22–24 April 2015*, (Piscataway, NJ), pp. 98–101, IEEE, 2015.

[46] A. Stochholm, K. Mikkelsen, and P. Kidmose, "Automatic sleep stage classification using ear-EEG," in *Proc. Int. Conf. of the IEEE Engineering in Medicine and Biology Society (EMBC 2016), Orlando, FL, 16 August–20 August 2016*, (Piscataway, NJ), pp. 4751–4754, IEEE, 2016.

[47] D. Looney, V. Goverdovsky, I. Rosenzweig, M. J. Morrell, and D. P. Manic, "Wearable in-ear encephalography sensor for monitoring sleep. Preliminary observations from nap studies," *Ann. Am Thorac. Soc.*, vol. 13, no. 12, pp. 2229–2233, 2016.

[48] T. Nakamura, V. Goverdovsky, M. J. Morrell, and D. P. Manic, "Automatic sleep monitoring using ear-EEG," *IEEE J. Transl. Eng. Health Med.*, vol. 5, no. 1, pp. 2800108–1 – 2800108–8, 2017.

[49] M. T. Curran, J.-K. Yang, N. Merril, and J. Chuang, "Passthoughts authentication with low cost earEEG," in *Proc. Int. Conf. of the IEEE Engineering in Medicine and Biology Society (EMBC 2016), Orlando, FL, 16 August–20 August 2016*, (Piscataway, NJ), pp. 1979–1982, IEEE, 2016.

[50] N. E. Huang, Z. Shen, S. R. Long, M. C. Wu, H. H. Shih, Q. Zheng, N.-C. Yen, C. C. Tung, and H. H. Liu, "The empirical mode decomposition and the Hilbert spectrum for nonlinear and non-stationary time series analysis," *Proc. R. Soc. A*, vol. 454, no. 1971, pp. 903–995, 1998.

[51] N. E. Huang, M.-L. C. Wu, S. R. Long, S. S. P. Shen, W. Qu, P. Gloersen, and K. L. Fan, "A confidence limit for the empirical mode decomposition and Hilbert spectral analysis," *Proc. R. Soc. A*, vol. 459, no. 2037, pp. 2317–2345, 2003.

[52] H. Liang, Q. H. Lin, and J. D. Chen, "Application of the empirical mode decomposition to the analysis of esophageal manometric data in gastroesophageal reflux disease," *IEEE Trans. Biomed. Eng.*, vol. 52, no. 10, pp. 1692–1701, 2005.

[53] Y. Zhou, W. Chen, J. Gao, and Y. He, "Application of Hilbert-Huang transform based instantaneous frequency to seismic reflection data," *J. Appl. Geophys.*, vol. 82, no. 1, pp. 68–74, 2012.

[54] X. Chen, Z. Wu, and N. E. Huang, "The time-dependent intrinsic correlation based on the empirical mode decomposition," *Adv. Adapt. Data Anal.*, vol. 2, no. 2, pp. 233–265, 2010.

[55] Z. Wu and N. E. Huang, "Ensemble empirical mode decomposition: A noise-assisted data analysis method," *Adv. Adapt. Data Anal.*, vol. 1, no. 1, pp. 1–41, 2009.

[56] G. Rilling, P. Flandarin, P. Gonçalves, and J. M. Lilly, "Bivariate empirical mode decomposition," *IEEE Signal Process. Lett.*, vol. 14, no. 12, pp. 936–939, 2007.

[57] N. ur Rehman and D. P. Mandic, "Empirical mode decomposition for trivariate signals," *IEEE Trans. Signal Process.*, vol. 58, no. 3, pp. 1059–1068, 2010.

[58] N. ur Rehman and D. P. Mandic, "Filter bank property of multivariate empirical mode decomposition," *IEEE Trans. Signal Proc.*, vol. 59, no. 5, pp. 2421–2426, 2011.

[59] H. C. Chang, P. L. Lee, M. T. Lo, Y. T. Wu, K. W. Wang, and G. Y. Lan, "Inter-trial analysis of post-movement beta activities in EEG signals using multivariate empirical mode decomposition," *IEEE Trans. Neu. Sys. Rehab. Eng.*, vol. 21, no. 4, pp. 607–615, 2013.

[60] C. Park, D. Looney, N. ur Rehman, A. Ahrabian, and D. P. Mandic, "Classification of motor imagery BCI using multivariate empirical mode decomposition," *IEEE. Trans. Neural. Syst. Rehabil. Eng.*, vol. 21, no. 1, pp. 10–22, 2013.

[61] N. ur Rehman, S. Ehsan, S. M. U. Abdullah, M. J. Akhtar, D. P. Mandic, and K. D. McDonald-Maier, "Multi-scale pixel-based image fusion using multivariate empirical mode decomposition," *Sensors*, vol. 15, no. 5, pp. 10923–10947, 2015.

[62] W. von Rosenberg, T. Chanwimalueang, D. Looney, and D. P. Mandic, "Vital signs from inside a helmet: A multichannel face-lead study," in *Proc. IEEE Int. Conf. on Acoustics, Speech and Signal Processing (ICASSP 2015), Brisbane, Australia, 19–14 April 2015*, (Piscataway, NJ), pp. 982–986, IEEE, 2015.

[63] A. Ahrabian, N. ur Rehman, and D. P. Mandic, "Bivariate empirical mode decomposition for unbalanced real-world signals," *IEEE Signal Process. Lett.*, vol. 20, no. 3, pp. 245–248, 2013.

[64] N. ur Rehman, M. W. Safdar, U. ur Rehman, and D. P. Mandic, "Dynamically-sampled bivariate empirical mode decomposition," *IEEE Signal Process. Lett.*, vol. 21, no. 7, pp. 857–861, 2014.

[65] A. Hemakom, A. Ahrabian, D. Looney, N. ur Rehman, and D. P. Mandic, "Nonuniformly sampled trivariate empirical mode decomposition," in *Proc. IEEE Int. Conf. on Acoustics, Speech and Signal Processing (ICASSP 2015), Brisbane, Australia, 19–14 April 2015*, (Piscataway, NJ), pp. 3691–3695, IEEE, 2015.

[66] H. Niederreiter, *Random number generation and quasi-Monte Carlo methods.* Philadelphia, PA: Society for Industrial and Applied Mathematics, 1992.

[67] J. Cui and W. Freeden, "Equidistribution on the sphere," *SIAM J. Sci Comput.*, vol. 18, no. 2, pp. 565–609, 1997.

[68] I. Daubechies, J. Lu, and H.-T. Wu, "Synchrosqueezed wavelet transforms: An empirical mode decomposition-like tool," *Appl. Comput. Harmon. Anal.*, vol. 30, no. 1, pp. 243–261, 2011.

[69] T. Oberlin, S. Meignen, and V. Perrier, "The Fourier-based synchrosqueezing transform," in *Proc. IEEE Int. Conf. on Acoustics, Speech and Signal Processing (ICASSP 2014), Florence, Italy, 4–9 May 2014*, (Piscataway, NJ), pp. 315–319, IEEE, 2014.

[70] A. Ahrabian, D. Looney, L. Stanković, and D. P. Mandic, "Synchrosqueezing-based time-frequency analysis of multivariate data," *Signal Process.*, vol. 106, no. 1, pp. 331–341, 2015.

[71] A. Ahrabian and D. P. Mandic, "A class of multivariate denoising algorithms based on synchrosqueezing," *IEEE Trans. Signal Process.*, vol. 63, no. 9, pp. 2196–2208, 2015.

[72] L. Stanković, "Time-frequency distributions with complex argument," *IEEE Trans. Signal Process.*, vol. 50, no. 3, pp. 475–486, 2005.

[73] A. Hemakom, K. Powezka, V. G. Goverdovsky, U. Jaffer, and D. P. Mandic, "Quantifying team cooperation through intrinsic multi-scale measures: Respiratory and cardiac synchronisation in choir singers and surgical teams," *R. Soc. Open Sci.*, vol. 4, no. 1, pp. 170853–1 – 170853–23, 2017.

[74] A. Hemakom, V. G. Goverdovsky, and D. P. Mandic, "Ear-EEG for detecting neuronal synchrony in continuous cooperative multi-person scenarios," in *Proc. IEEE Int. Conf. on Acoustics, Speech and Signal Processing (ICASSP 2018)*, in review, IEEE, 2018.

[75] A. Hemakom, V. G. Goverdovsky, D. Looney, and D. P. Mandic, "Adaptive-projection intrinsically transformed multivariate empirical mode decomposition," *Phil. Trans. R. Soc. A*, vol. 374, no. 2065, pp. 20150199–1 – 20150199–15, 2016.

[76] L. Cohen, *Time-Frequency Analysis: Theory and Applications*. Upper Saddle River, NJ: Prentice-Hall, Inc, 1995.

[77] M. Schwartz, W. R. Bennet, and S. Stein, *Communications Systems and Techniques*. New York, NY: McGraw-Hill, 1966.

[78] P. Flandrin, G. Rilling, and P. Gonçalvès, "Empirical mode decomposition as a filter bank," *IEEE Signal Process. Lett.*, vol. 11, no. 2, pp. 112–114, 2004.

[79] Z. Wu and N. E. Huang, "A study of the characteristics of white noise using the empirical mode decomposition method," *Proc. R. Soc. A*, vol. 460, no. 2046, pp. 1597–1611, 2004.

[80] P. Tass, M. G. Rosenblum, J. Weule, J. Kurths, A. Pikovsky, J. Volkmann, A. Schnitzler, and H.-J. Freund, "Detection of n:m phase locking from noisy data: Application to magnetoencephalography," *Phys. Rev. Lett.*, vol. 81, no. 15, pp. 3291–3294, 1998.

[81] E. T. Jaynes, *Probability Theory*. Cambridge, UK: Cambridge University Press, 1st ed., 2003.

[82] P. Stoica and R. L. Moses, "On biased estimators and the unbiased Cramér-Rao lower bound," *Signal Process.*, vol. 21, no. 4, pp. 349–350, 1990.

[83] P. M. Woodward, *Probability and information theory with applications to radar*. London, UK: Pergamon Press, 1953.

[84] G. L. Turin, "An introduction to matched filters," *IRE Transactions on Information Theory*, vol. 6, no. 3, pp. 311–329, 1960.

[85] T. Chanwimalueang, W. von Rosenberg, and D. P. Mandic, "Enabling R-peak detection in wearable ECG: Combining matched filtering and Hilbert transform," in *Proc. IEEE Int. Conf. on Digital Signal Processing (DSP 2015), Singapore, 21–24 July 2015*, (Piscataway, NJ), pp. 134–138, IEEE, 2015.

[86] D. Benitez, P. A. Gaydecki, A. Zaidi, and A. P. Fitzpatrick, "The use of the Hilbert transform in ECG signal analysis," *Computers in Biology and Medicine*, vol. 31, no. 5, pp. 399–406, 2001.

[87] K. E. Barrett, S. M. Barman, S. Boitano, and H. L. Brooks, *Ganong's Review of Medical Physiology*. McGraw-Hill Education / Medical, 23rd ed., May 2012.

[88] R. Q. Quiroga, A. Kraskov, T. Kreuz, and P. Grassberger, "Performance of different synchronization measures in real data: A case study on electroencephalographic signals," *Phys. Rev. E*, vol. 65, no. 4, pp. 041903–1 – 041903–14, 2002.

[89] L. Faes and G. Nollo, *Multivariate Frequency Domain Analysis of Causal Interactions in Physiological Time Series, Biomedical Engineering, Trends in Electronics, Communications and Software*. InTech, January 2011.

[90] H.-U. Strohmenger, K. H. Lindner, and C. G. Brown, "Analysis of the ventricular fibrillation ECG signal amplitude and frequency parameters as predictors of countershock success humans," *Chest*, vol. 111, no. 3, pp. 584–589, 1997.

[91] V. K. Murthy, T. M. Grove, G. A. Harvey, and L. J. Haywood, "Clinical usefulness of ECG frequency spectrum analysis," in *Proc. IEEE the Second Annual Symposium on Computer Application in Medical Care, Washington, DC, 5–9 November 1978*, (Piscataway, NJ), pp. 610–612, IEEE, 1978.

[92] G. K. Kanji, *100 Statistical Tests*. London, UK: SAGE Publications Ltd, 3rd ed., 2006.

[93] V. Radeka, "1/|f|noise in physical measurements," *IEEE Trans. Nucl. Sci.*, vol. 16, no. 5, pp. 17–35, 1969.

[94] M. K. Islam, A. Rastegarnia, and Z. Yang, "Methods for artifact detection and removal from scalp EEG: A review," *Clin. Neurophysiol.*, vol. 46, no. 1, pp. 287–305, 2016.

[95] M. A. Klados, C. Papadelis, C. Braun, and P. D. Bamidis, "REG-ICA: A hybrid methodology combining blind source separation and regression techniques for the rejection of ocular artifacts," *Biomed. Signal Process. Control.*, vol. 6, no. 3, pp. 291–300, 2011.

[96] M. H. Soomro, N. Badruddin, M. Z. Yusoff, and A. S. Malik, "A method for automatic removal of eye blink artifacts from EEG based on EMD-ICA," in *Proc. Int. Conf. of the IEEE 9th International Colloquium on Signal Processing and its Applications (CSPA 2013),Kuala Lumpur, Malaysia, 8–10 March 2013*, (Piscataway, NJ), pp. 129–134, IEEE, 2013.

[97] Y. Zou, V. Nathan, and R. Jafari, "Automatic identification of artifact-related independent components for artifact removal in EEG recordings," *IEEE J. Biomed. Health Inform.*, vol. 20, no. 1, pp. 73–81, 2014.

[98] A. Jafarifarmand and M. A. Badamchizadeh, "Artifacts removal in EEG signal using a new neural network enhanced adaptive filter," *Neurocomputing*, vol. 103, no. 1, pp. 222–231, 2013.

[99] C. Burger and D. J. van den Heever, "Removal of EOG artefacts by combining wavelet neural network and independent component analysis," *Biomed. Signal Process. Control*, vol. 15, no. 1, pp. 67–79, 2015.

[100] J. Hu, C.-S. Wang, M. Wu, Y.-X. Du, Y. He, and J. She, "Removal of EOG and EMG artifacts from EEG using combination of functional link neural network and adaptive neural fuzzy inference system," *Neurocomputing*, vol. 151, no. 1, pp. 278–287, 2015.

[101] S.-Y. Shao, K.-Q. Shen, C. J. Ong, E. P. V. Wilder-Smith, and X.-P. Li, "Automatic EEG artifact removal: A weighted support vector machine approach

with error correction," *IEEE Trans. Biomed. Eng.*, vol. 56, no. 2, pp. 336–344, 2008.

[102] J. Lawhern, W. D. Hairston, K. McDowell, M. Westerfield, and K. Robbins, "Detection and classification of subject-generated artifacts in EEG signals using autoregressive models," *J. Neurosci. Methods*, vol. 208, no. 2, pp. 181–189, 2012.

[103] S. Bhattacharyya, A. Biswas, J. Mukherjee, A. K. Majumdar, B. Majumdar, S. Mukherjee, and A. K. Singh, "Detection of artifacts from high energy bursts in neonatal EEG," *Comput. Biol. Med.*, vol. 43, no. 11, pp. 1804–1814, 2013.

[104] K. Mazzocco, D. B. Petitti, K. T. Fong, D. Bonacum, J. Brookey, S. Graham, R. E. Lasky, J. B. Sexton, and E. J. Thomas, "Surgical team behaviors and patient outcomes," *Am. J. Surg.*, vol. 197, no. 5, pp. 678–685, 2009.

[105] T. Manser, "Teamwork and patient safety in dynamic domains of healthcare: A review of the literature," *Acta. Anaesthesiol. Scand.*, vol. 53, no. 2, pp. 143–151, 2009.

[106] K. R. Catchpole, A. E. Giddings, M. Wilkinson, G. Hirst, T. Dale, and M. R. de Leval, "Improving patient safety by identifying latent failures in successful operations," *Surgery*, vol. 142, no. 1, pp. 102–110, 2007.

[107] A. Kurmann, S. Keller, F. Tschan-Semmer, J. Seelandt, N. K. Semmer, D. Candinas, and G. Beldi, "Impact of team familiarity in the operating room on surgical complications," *World J. Surg.*, vol. 38, no. 12, pp. 3047–3052, 2014.

[108] S. Arora, T. Tierney, N. Sevdalis, R. Aggarwal, D. Nestel, M. Woloshynowych, A. Darzi, and R. Kneebone, "The Imperial Stress Assessment Tool (ISAT): A feasible, reliable and valid approach to measuring stress in the operating room," *World J. Surg.*, vol. 34, no. 8, pp. 1756–1763, 2010.

[109] L. Hull, S. Arora, E. Kassab, R. Kneebone, and N. Sevdalis, "Assessment of stress and teamwork in the operating room: An exploratory study," *Am. J. Surg.*, vol. 201, no. 1, pp. 24–30, 2011.

[110] T. Adjei, W. von Rosenberg, V. Goverdovsky, K. Powezka, U. Jaffer, and D. P. Mandic, "Pain prediction from ECG in vascular surgery," *IEEE J. Transl. Eng. Health Med.*, p. in print, 2017.

[111] K. Catchpole, A. Mishra, A. Handa, and P. McCulloch, "Teamwork and error in the operating room: Analysis of skills and roles," *Ann. Surg.*, vol. 247, no. 4, pp. 699–706, 2008.

[112] L. Morgan, E. Robertson, M. Hadi, K. Catchpole, S. Pickering, S. New, G. Collins, and P. McCulloch, "Capturing intraoperative process deviations using a direct observational approach: The glitch method," *BMJ Open*, vol. 3, no. 11, p. 003519, 2013.

[113] R. Klimoski and S. Mohammed, "Team mental model: Construct or metaphor?," *J. Manag.*, vol. 20, no. 2, pp. 403–437, 1994.

[114] J. E. Mathieu, T. S. Heffner, G. F. Goodwin, E. Salas, and J. A. Cannon-Bowers, "The influence of shared mental models on team process and performance," *J. Appl. Psychol.*, vol. 85, no. 2, pp. 273–283, 2000.

[115] J. A. Cannon-Bowers and E. Salas, "Reflections on shared cognition," *J. Organ. Behav.*, vol. 22, no. 2, pp. 195–202, 2001.

[116] J. Polich, "Updating P300: An integrative theory of P3a and P3b," *Clin. Neurophysiol.*, vol. 118, no. 10, pp. 2121–2148, 2009.

[117] R. Kuś, A. Duszyk, P. Milanowski, M. Łabęcki, M. Bierzyńska, Z. Radzikowska, M. Michalska, J. Żygierewicz, P. Suffczński, and P. J. Durka, "On the quantification of SSVEP frequency responses in human EEG in realistic BCI conditions," *PLoS ONE*, vol. 8, no. 10, p. e77536, 2013.

[118] C. Jia, X. Gao, B. Hong, and S. Gao, "Frequency and phase mixed coding in SSVEP-based brain–computer interface," *IEEE Trans. Biomed. Eng.*, vol. 58, no. 1, pp. 200–206, 2011.

[119] S. N. G. Aston-Jones and J. D. Cohen, "Decision making, the P3, and the Locus Coeruleus-Norepinephrine system," *Psych. Bulletin*, vol. 131, no. 4, pp. 510–532, 2005.

[120] T. Solis-Escalante, G. G. Gentiletti, and O. Yanez-Suarez, "Single trial P300 detection based on the empirical mode decomposition," in *Proc. Int. Conf. of the IEEE Engineering in Medicine and Biology Society (EMBC 2006), New York City, NY, 31 August–3 September 2006*, (Piscataway, NJ), pp. 1157–1160, IEEE, 2006.

[121] S. C. Douglas and D. P. Mandic, "Autoconvolution and panorama: Augmenting second-order signal analysis," in *Proc. IEEE Int. Conf. on Acoustics, Speech and Signal Processing (ICASSP 2014), Florence, Italy, 4–9 May 2014*, (Piscataway, NJ), pp. 384–388, IEEE, 2014.

[122] H. Selye, "Stress and the general adaptation syndrome," *British Medical Journal*, vol. 1, no. 4667, pp. 1383–1392, 1950.

[123] R. Cardarelli, S. Elekdag, and S. Lall, "Financial stress, downturns, and recoveries," *IMF Working Paper*, vol. WP/09/100, pp. 1–58, 2009.

[124] R. Balakrishnan, S. Danninger, S. Elekdag, and I. Tytell, "The transmission of financial stress from advanced to emerging economics," *IMF Working Paper*, vol. WP/09/133, pp. 1–52, 2009.

[125] R. Cardarelli, S. Elekdag, and S. Lall, "Financial stress and economic contractions," *Financial Stability*, vol. 7, no. 2, pp. 78–97, 2011.

[126] M. Billio, M. Getmansky, A. W. Lo, and L. Pelizzon, "Measuring systemic risk in the finance and insurance sectors," *MIT Sloan School Working Paper 4774-10*, pp. 1–66, 2010.

[127] W. Er and D. P. Mandic, "Dynamical complexity analysis of multivariate financial data," in *Proc. IEEE Int. Conf. on Acoustics, Speech and Signal Processing (ICASSP 2013), Vancouver, BC, 26–31 May 2013*, (Piscataway, NJ), pp. 8732–8736, IEEE, 2013.

Appendix A

Areal Density

Trends in synchrony obtained using the proposed N-IPS algorithm offer physically meaningful and straightforward interpretation in signal dependence. This can also be further simplified by calculating the areal density (AD) – an area between a trend in synchrony and a corresponding baseline per unit of time. Figure A.1 *(a)* shows areal densities of trends in synchrony in the respiratory and HRV signals of the soprano and bass singers considered in Section 4.3.4. Observe that the areal densities increased during the songs (Sx, where x represents the song number) and decreased between 2 consecutive songs (Sx-Sy, where x and y represent the 2 consecutive song numbers), except for only 2 circumstances: (i) during Songs 1 and 2 (S1-S2), where areal densities of the trend in synchrony in the HRV signals of the soprano and bass singers remained relatively high, and (ii) during Songs 6 and 7 (S6-S7), where areal densities of the trends in synchrony in the sopranos' HRV signals and the basses' respiratory signals increased from the previous song (Song 6, S6). Note that 'S7 (pause)' represents the later period of Song 7 where several pauses occurred, and consequently the trends and the areal densities of the trends in synchrony decreased. For rigor, average areal densities of trends in synchrony in both signals of the sopranos and basses were also calculated, as shown in Figure A.1 *(b)*. The average areal densities exhibited distinct increases during the songs and decreases between the songs.

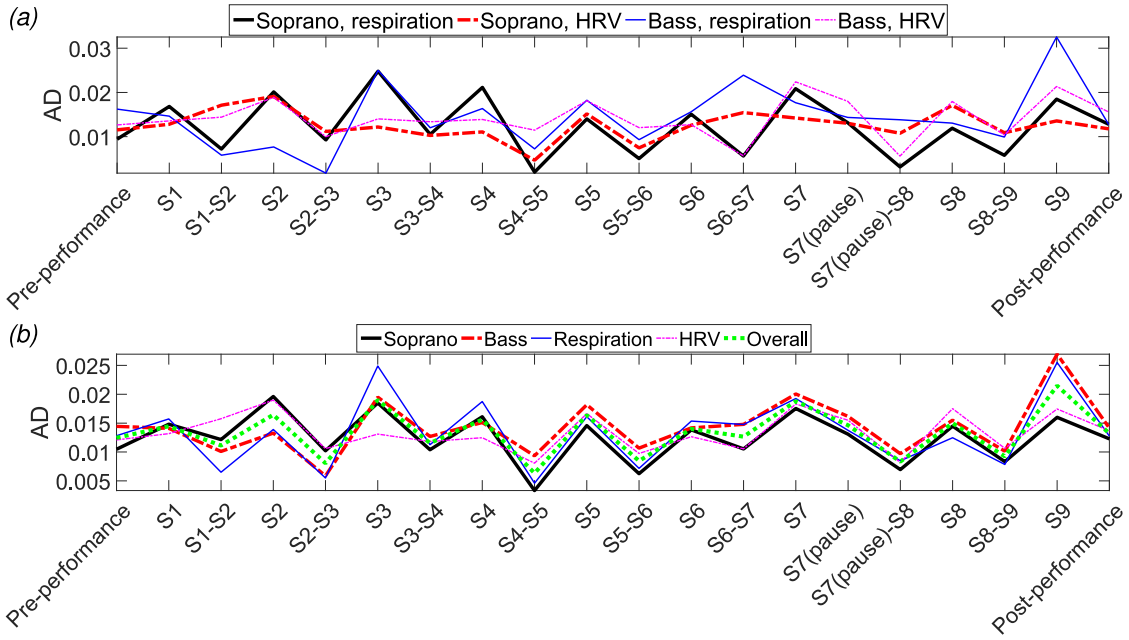


Figure A.1: **Areal densities of trends in synchrony**. *(a)* Areal density of trend in synchrony in the sopranos' respiratory signals (solid thick line), the sopranos' HRV signals (broken thick line), the basses' respiratory signals (solid thin line), and the basses' HRV signals (broken thin line). *(b)* Average areal density of trends in synchrony in both signals of the sopranos (solid thick line), both signals of the basses (broken thick line), the respiratory signals of both voices (solid thin line), the HRV signals of both voices (broken thin line), and all the signals (dotted thick line).

Appendix B

Supportive Performance Evaluation of Ear-EEG

The performance of ear-EEG against on-scalp EEG in another cooperative multi-player game called Ninjas has also been evaluated. The experiment consisted of 3 3-minute trials. During the first trial, Subject 1 was instructed to control a ninja character to run as fast as possible in 3 minutes, while Subject 2 was resting, listening to relaxing music and wearing a blindfold. For the second trial, the tasks were swapped between the subjects. After these two trials, both the subjects were instructed to cooperatively control the ninja characters to run at similar speed within a limited distance and complete as many laps as they could. Data acquisition and neuronal synchrony estimation were performed in the same manner as in Sections 5.2.2 & 5.2.3. Figure B.1 *(a)* shows a screenshot of the game, and Figure B.1 *(b)* shows correlation in neural synchrony *between the ear-EEG and on-scalp EEG recording*s. For this game, correlation in neuronal synchrony between the two modalities was highest in the subbands associated with attention – lower theta and lower alpha bands. This supports the results from the Bar Balancing game; through SCI estimation, both the recording modalities were capable of detecting joint attention between the couples.



(a) *(b)*

Figure B.1: **Game screenshot and correlation in neuronal synchrony between the recording modalities.** *(a)* Screenshot. *(b)* Correlation. Subjects 1&2 separately controlled the upper and lower ninjas to move back and forth. The EEG subbands associated with attention (lower theta and lower alpha bands) exhibited the highest correlation between the recording modalities.

Appendix C

Application of Intrinsic Phase Synchrony to Financial Signal Processing

In human sciences, stress is defined as a non-specific neuroendocrine response [122]. In an analogy to the sympatho-vagal balance in human stress research, whereby the sympathetic nervous system (SNS) accelerates body functions while the parasympathetic nervous system (PNS) slows them down, the 'biomarkers' of financial stress is considered here to be accelerations followed by recessions in stock indices. The market expansions are therefore interpreted similarly to the effects of the SNS activity in humans, and are characterised by investors' over-excitement, over-confidence, and heuristic approaches. Market recessions are then analogous to the effects of the PNS, whereby the financial slow-down is accompanied by a lack of confidence and a decrease in market efficiency.

During a financial crisis – a period when the financial system exhibits high levels of stress [123, 124, 125] – the term 'systemic risk' refers to a series of correlated defaults among financial institutions, occurring over a short time span and triggering withdrawal of liquidity and a widespread loss of confidence in the financial system as a whole. At the heart of the concept is the notion of 'contagion', a particularly strong propagation of failures from one institution, market, or system to another. Five different measures of systematic risk were proposed in [126], based on statistical relations among the market returns of hedge funds, banks, brokers and insurance companies. Using the correlations, cross-correlations, PCA, regime-switching models, and Granger causality tests, it was found that all the four sectors have become highly interrelated and less liquid over the past decade, an indicator of increased level of systemic risk in finance and insurance industries. These measures can also identify and quantify financial crisis periods.

Intrinsic phase synchrony was used here for the quantification of inter-dependence during financial crises, as financial systems often exhibit high levels of systemic risk, that is, they are contagious and, to an extent, dependent on one another. Four

stock market indices which represent the US economy over the last 25 years, between 1st January 1991 and 31st August 2015 were considered: (i) Dow Jones Industrial Average (DJIA), (ii) NASDAQ Composite, (iii) Standard & Poors 500 (S&P 500), and (iv) Russell 2000. The DJIA comprises 30 of the largest companies in the US across a range of industries except for transport and utilities; NASDAQ is an indicator of the performance of stocks in technology and of the growth in companies; S&P 500 consists of 500 large companies from a vast number of industries, each having market capitalisation of more than $5 billion; and Russell 2000 comprises a small-cap segment of the US equity market.

Five consecutive periods of different natures were identified, based on the interpretation of key geopolitical and socio-economic events which affected the US and world economies [127], as follows:

- **Period 1:** 1-JAN-1991 to 31-DEC-1999. Economic boom, followed by the 'dot-com' boom from 1997 to December 1999.
- **Period 2:** 1-JAN-2000 to 31-DEC-2003. Internet bubble burst and the economy crisis further deteriorated due to the 9/11 terrorist attack and its aftermaths.
- **Period 3:** 1-JAN-2004 to 31-DEC-2007. Recovery due to huge investment in undervalued stocks.
- **Period 4:** 1-JAN-2008 to 31-DEC-2011. Sub-prime mortgage and debt crises.
- **Period 5:** 1-JAN-2012 to 31-AUG-2015. Weak growth and recovery owing to the uncertainty in fiscal policy ('fiscal cliff'), increases in tax, and a slowdown in the housing sector.

The four financial time series were combined into a single quadrivariate signal, for which the intrinsic, data-adaptive scales were determined using the NA-APIT-MEMD with 10 adjacent noise channels. The α value for the NA-APIT-MEMD was 1 and the number of direction vectors was 64, to cater for high power imbalances (over 20 dB) between the four data channels. The PSIs between pairs of

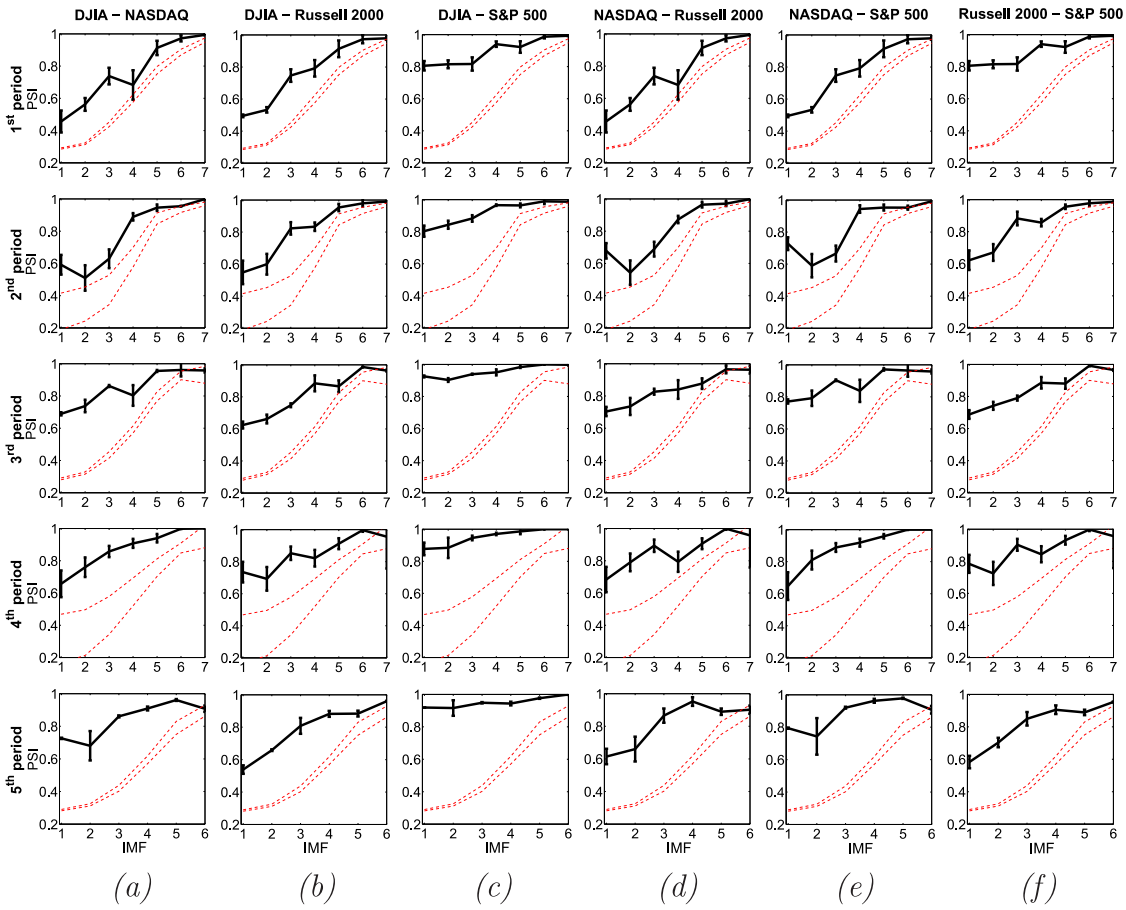


Figure C.1: **Intrinsic synchrony between individual stock indices.** The graphs show phase synchrony (PSI) between stock indices across different time scales (IMF index) for the five periods considered (black line), and the upper- and lower-bounds of confidence intervals (red lines). The IMFs [1, 2], [3, 4], 5, 6, 7 correspond respectively to the time scales of 1-5 days, 1 month, 1-3 months, 1 year, and 2 years. *(a)* DJIA against NASDAQ. *(b)* DJIA against Russell 2000. *(c)* DJIA against S&P 500. *(d)* NASDAQ against Russell 2000. *(e)* NASDAQ against S&P 500. *(f)* Russell 2000 against S&P 500. The PSI values outside the confidence intervals were statistically relevant estimates of synchronisation. The PSI values at IMF index 7 of the fifth period could not be estimated as they were monotonic functions.

the data channels at every IMF index were then calculated from 50 realisations of NA-APIT-MEMD, and the confidence intervals at each IMF index were calculated by benchmarking against the PSIs between pairs of noise channels (no synchrony). The PSI values between the financial time series within these confidence intervals were adjudged spurious.

Figure C.1 shows the PSI values between all pairs of stock indices at different IMF indices, estimated from 50 realisations of NA-APIT-MEMD. Observe that PSI values at IMF indices 6 and 7, which represent the periods of 1 and 2 years (long-term trends), in all the five periods were always higher than 0.8, indicating that all the

stock indices exhibited prominent synchrony in their long-term trends.

In all the five periods, the DJIA and the S&P 500 were also highly synchronised in: (i) short-term trading (periods of 1–5 days, represented by IMFs 1–2); (ii) short-term trends (periods of less than a month, represented by IMFs 3–4); and (iii) medium-term trends (periods of 1–3 months, represented by IMF 5). Notice from Figure C.1 that all the PSI values at IMFs 1–2 (short-term trading) during the dot-com bubble (1997–2000, the first period) and the Internet bubble burst (2000–2004, the second period) (except for the DJIA - S&P 500) were relatively low (lower than 0.6). However, during the third period (2004–2007) all of the stock pairs exhibited higher synchrony in short-term trading (IMFs 1–2) (all the PSI values were higher than 0.6). This indicates pronounced short-term dependence.

Observe that during the sub-prime mortgage crisis (2008–2011, the fourth period) all the PSI values (except for the DJIA - S&P 500) were, on the average, higher than those for the recovery and weak growth periods (the third and fifth periods, 2004–2007 and 2012–2015). This indicates the presence of systemic risk, where the markets are contagious and behave in the same way during the financial crisis.